Swimming behaviour of a flagellated alga in Newtonian and complex fluids

PhD Thesis

Ewan Rycroft

James Weir Fluid Laboratory
Department of Mechanical & Aerospace Engineering
University of Strathclyde, Glasgow

February 1, 2022

This thesis is the result of the author's original research. It has been composed by the author and has not been previously submitted for examination which has led to the award of a degree.

Signed: Ewan Rycroft

Date: January 2022

Abstract

Many microscopic swimmers in nature navigate through complex fluids, such as worm type swimmers in muds, and spermatozoa in cervical mucus. An understanding of the swimming response to such fluids is gaining increasing attention with the hope they will aid in the development of artificial microswimmers and in enhancing processes involving natural bioswimmers, such as fertility treatments. In this work, the swimming behaviour of a swimming green algae, *Dunaliella salina*, is examined experimentally. Fluids with different rheological properties have been used to study the effects of increasing viscosity, shear thinning properties and viscoelasticity of the surrounding medium on the algae swimming characteristics, such as velocity, beating frequencies and stroke velocities.

In a water-like medium akin to their natural environment, the algae were found to swim with a velocity of $V_{net} = 49.55\,\mu\mathrm{m\,s^{-1}}$ while beating at a frequency of $f_{BF} = 29.97\,\mathrm{Hz}$. With the addition of a viscous enhancing agent (Ficoll PM400) the algae swimming velocity followed an essentially monotonic decrease as viscosity increased, based on a power-law relationship ($V \propto \eta^{-1}$). This was attributed to the constant drag produced by the algae and limited variations in the stroke dynamics, which was confirmed by analysis of the power and recovery strokes.

Compared to the Newtonian cases, when the surrounding fluid exhibited shear thinning properties, achieved by addition of Xanthan gum, the swimmer displayed reduced stroke times for comparable displacements in the Newtonian cases. This lead to an overall boost in the recovery stroke over the power stroke. Polyacrylamide was used to analyse the

viscoelastic response of the algae. However, for this particular case it was apparent that due to the confounding effects of elasticity and shear thinning, it was difficult to define an elastic response.

Furthermore, the wall interactions of *Dunaliella salina* was quantified, with a preference to bounce from a wall observed. The approach dynamics to the wall were found to hold little influence on the escape, with only a slight tendency for increased reverse bounces at high approach angles and slower velocities.

Acknowledgements

First and foremost, I would like to extend my gratitude to my supervisors, Dr Mónica Oliveira and Dr Mark Haw, whose guidance, support, and encouragement were vital in my PhD journey. Thank you for always providing an open door and making time for a chat, even through the difficulties of Covid-19.

I would also like to thank Gemma for her help throughout the whole process, being there when I needed to discuss something through, working together when managing the laboratory and always keeping a positive outlook on everything. I wish you success wherever you end up after your PhD.

I would also like to extend my appreciation to all those who helped me at the start of my research journey, Vincenzo for introducing me to the algae protocols and illustrating the methods of upkeep and storage, Andreia for her tutorship on how to use the rotational and extensional rheometers, Joana for her time spent training me on fabrication methods and use of the microscope and further to anyone I have gained support from. Without you, my journey would have taken significantly longer. I would also like to extend my thanks to Debasish Das whose knowledge, guidance, and time spend building the simplified model of the swimmer is greatly appreciated.

To those in the office and laboratory for making a friendly working environment and keeping me entertained on those long days, I would like to say thank you. I also wish to extend my gratitude to the members of the Mechanical and Aerospace Department, providing assistance when needed and making my time in the department an enjoyable

one.

To my girlfriend, Emily, thank you for always being there for me and pushing me through when times were tough. Thank you for the much-needed distractions and countless weekend trips away in the van.

To Peter, Angus and Moritz, thank you for your support and much needed respite over lunches, breaks, and squash games. I'm very glad we all partook in this journey at the same time.

Finally, to my family, I am ever grateful for the support and guidance you have provided me over my years of study. Without your help, this journey would never have been possible.

Contents

List of Figures

List of Figures

List of Tables

List of Tables

Acronyms

C* . . . . . Critical Concentration

C. elegans . . . . . *Caenorhabditis elegans*

C. reinhardtii . . . . . *Chlamydomonas reinhardtii*

CCD . . . . . Charge-Coupled Device

CMC . . . . . Carboxymethylcellulose

D. salina . . . . . *Dunaliella salina*

De . . . . . Deborah Number

DFT . . . . . Discrete Fourier Transform

DHR-2 . . . . . Discovery Hybrid Rheometer 2

DOF . . . . . Depth of Focus

E. coli . . . . . *Escherichia coli*

El . . . . . Elastic Number

FFT . . . . . Fast Fourier Transform

FOV . . . . . field of View

Acronyms

FPS	Frames per second
MSD	Mean squared displacement
PAA	Polyacrylamide
Re	Reynolds Number
RES	Resolution
RFT	Resistive Force Theory
SR	Strouhal Number
TR	Trouton ratio
Wi	Weissenberg Number
XG	Xanthan Gum

List of Symbols

α . . . . . Apparent diffusion exponent

A_{loc_ind} . . . . . Local amplitude of individual alga

A_{net_ind} . . . . . Net amplitude of individual alga

A_{pow_ind} . . . . . Amplitude through power stroke of individual alga

A_{rec_ind} . . . . . Amplitude through recovery stroke of individual alga

A_{loc} . . . . . Local amplitude

A_{net} . . . . . Net amplitude

A_{pow} . . . . . Amplitude through power stroke

A_{rec} . . . . . Amplitude through recovery stroke

A_{rod} . . . . . Amplitude of rod prescribed in simple model

A_w . . . . . Wave amplitude

a . . . . . Area

a_B . . . . . Area of algae body

a_p . . . . . Area of a pixel

List of Symbols

α_{cy} . . . . . Carreau-Yasuda curve descriptor

C_N . . . . . Normal local resistance coefficient

C_T . . . . . Transverse local resistance coefficient

c_w . . . . . Travelling wave speed

De . . . . . Deborah number

δ . . . . . Channel depth

δ_z . . . . . Depth of focus

D_c . . . . . Characteristic length

D_{mid} . . . . . Filament midpoint diameter

D_o . . . . . Filament original diameter

D . . . . . Characteristic dimension

G . . . . . Elastic modulus

ε_H . . . . . Hencky strain

ε . . . . . Strain

F . . . . . Force in applied direction

F_B . . . . . Viscous body force acting on the algae

F_b . . . . . Force due to buoyancy

F_{drag} . . . . . Drag force

F_g . . . . . Force due to gravity

List of Symbols

F_{B_pow} . . . . . Power stroke body drag force

F_{prop} . . . . . Propulsion force

F_{B_rec} . . . . . Recovery stroke body drag force

FPS . . . . . Frames per second

$frame_{time}$ . . . . . Time between two consecutive frame

f_{rod} . . . . . Frequency of rod prescribed in simple model

f_{BF} . . . . . Beating frequency

f_{BF_ind} . . . . . Beating frequency of individual swimmer

$\dot{\gamma}_B$ . . . . . Body shear rate

$\dot{\gamma}_f$ . . . . . Flagella shear rate

$\dot{\gamma}_r$ . . . . . Shear rate at point r on plate

$\dot{\gamma}_{rot}$ . . . . . Rotational shear rate

$\dot{\gamma}_{trans}$ . . . . . Translation shear rate

El . . . . . Elastic number

g . . . . . Gravitational acceleration

h . . . . . Height between plates

i . . . . . Frame Number

K_α . . . . . Generalised diffusion coefficient

K . . . . . FFT harmonic

List of Symbols

k_w . . . . . Wave descriptor $k = 2\pi\lambda_w$

λ_r . . . . . Wavelength of red light

λ . . . . . Characteristic relaxation time

λ_{cy} . . . . . alpha Carreau-Yasuda relaxation time

λ_w . . . . . Wavelength

l_B . . . . . Body length

l . . . . . Channel length

L_F . . . . . Final distance between CaBER plates

l_f . . . . . Characteristic flagella length

L_O . . . . . Original distance between CaBER plates

l_p . . . . . Persistent length

l_{p_ind} . . . . . Persistent length of individual alga

l_{rod} . . . . . Length of rod prescribed in simple model

l_t . . . . . Tube length

M_X . . . . . Magnification

MSD . . . . . Mean squared displacement

m . . . . . Flow consistency index

M . . . . . Torque

M_m . . . . . Minimum torque limit

List of Symbols

N . . . . . Frames in track

n . . . . . Power-law index

n_{ri} . . . . . Refractive index

NA_{obj} . . . . . Objective numerical aperture

η . . . . . Viscosity

η_e . . . . . Extensional viscosity

η_∞ . . . . . Infinite shear viscosity

η_0 . . . . . Zero shear viscosity

ω_{BF} . . . . . Rotational beating frequency

ω_{rod} . . . . . Angular velocity of rod prescribed in simple model

ω . . . . . Angular velocity

ω_w . . . . . Wave frequency

p . . . . . Pixel size

P . . . . . Pressure

Q . . . . . Volume Flow Rate

r_B . . . . . Body radius

r_f . . . . . Flagella radius

r_t . . . . . Tube radius

Re . . . . . Reynolds number

List of Symbols

ρ . . . . . Density

ρ_f . . . . . Fluid density

r_n . . . . . Particle position

r . . . . . Plate radius

$\dot{\gamma}$ . . . . . Shear rate

σ . . . . . Stress in applied direction

σ_c . . . . . Maximum wall shear stress in circular channel

σ_t . . . . . Maximum wall shear stress in rectangular channel

t_s . . . . . Stroke time

t_{pow} . . . . . Power stroke time

t_{rec} . . . . . Recovery stroke time

τ . . . . . Time interval

t . . . . . Time

t_c . . . . . Characteristic time

t_p . . . . . Persistent time

t_{p_ind} . . . . . Persistent time of individual alga

t_w . . . . . Time spent at wall

θ . . . . . Swimming angle relative to the channel

θ_a . . . . . Swimming angle relative to algae swimming direction

List of Symbols

θ_A . . . . . Approach angle

θ_{cp} . . . . . Angle between Cone & Plate

θ_E . . . . . Escape angle

θ_{rod} . . . . . Angle of model flagella relative to horizontal

V . . . . . Velocity

V_A . . . . . Wall approach velocity

V_c . . . . . Characteristic velocity

V_E . . . . . Wall escape velocity

V_f . . . . . Flagella velocity

V_F . . . . . Fluid velocity

v_{in} . . . . . Instantaneous velocity

V_{loc_ind} . . . . . Local velocity of individual alga

V_{net_ind} . . . . . Net velocity of individual alga

V_{pow_ind} . . . . . Velocity through power stroke of individual alga

V_{rec_ind} . . . . . Velocity through recovery stroke of individual alga

V_{sign_ind} . . . . . Sign velocity of individual alga

V_{loc} . . . . . Local velocity

V_{net} . . . . . Net velocity

V_{net_shal} . . . . . Net velocity in shallow channel

List of Symbols

V_N . . . . . Normal local velocity

V_{pop} . . . . . Population velocity

V_{pop_shal} . . . . . Population velocity in shallow channel

V_{pow} . . . . . Velocity through power stroke

V_{rec} . . . . . Velocity through recovery stroke

V_{sign} . . . . . Sign velocity with recovery stroke taken as negative

V_{top} . . . . . Velocity of top plate

V_T . . . . . Transverse local velocity

V_w . . . . . Wall velocity

v_{x_in} . . . . . Instantaneous x Velocity between two consecutive frames

v_{y_in} . . . . . Instantaneous y Velocity between two consecutive frames

V_B . . . . . Alga body volume

w . . . . . Channel width

Wi . . . . . Weissenburg number

x . . . . . x spatial position in microchannel

x_{dist} . . . . . x wall distance travelled

y . . . . . y spatial position in microchannel

Z . . . . . FFT domain

z . . . . . FFT input signal

Chapter 1

Introduction

1.1 Chapter overview

In this chapter, the main topics and background knowledge drawn upon in this work are introduced. Initially, the chapter introduces the work conducted in this thesis, detailing the motivation and areas of interest. A description of swimming at the microscopic level follows, describing motility techniques and providing a definition of swimmer types (pullers vs pushers). A brief overview of the most relevant microscopic swimmers present in nature comes next, with details of low-Reynolds number swimming. Next, a look into the algae genus gives details into general algae classification, specifically looking at the algae utilised throughout this work, *Dunaliella salina*. Topics such as cell/flagellum structure, reproduction, and motility methods are all introduced and discussed. Finally, an overview of microalgae applications is conducted detailing processes such as food/supplement production, biofuels, biofertilisers and the production of microrobotic swimmers. Procedures utilising *Dunaliella salina* are given particular focus.

1.2 Motivation and overview of thesis

Across the natural world, many species rely on swimming at the microscopic scale. Organisms such as some algae species [1–3] and minute worms [4–6] rely on navigating to areas of favourable food or light, spermatozoa must navigate through cervical mucus to fertilise an egg [7,8] and cilia in the lungs and gut move in unison to remove mucus [9,10]. Due to the short length scales and relative low swimming velocities, microscopic swimmers are within the regime of low Reynolds number flows, consequently viscosity is dominant over inertial effects. Therefore, swimming at this scale is very different from that at the macroscale, as there is an inability to swim with reciprocating motion and an instantaneous fluid response to body motion is present.

A general understanding of these systems is key in utilising microorganisms for our benefit, such as commercial products ranging from the food to cosmetic industries and industrial applications including biofuels and bioindicaters [11–14]. Furthermore, if microorganisms motility methods can be replicated, it may lead to the production of artificial microswimmers. If these microbots become available at the commercial scale, a vast range of applications and possibilities open up, from targeted drug delivery, to microsensing, to micromanufacturing, to novel smart materials, the uses of such swimmers are vast [15–18].

Further to the general research for swimmers in a water-like media, research into the swimming response in complex fluids is of vital importance in many of the systems discussed. Many swimmers in nature navigate through complex fluids such as spermatozoa in cervical mucus [19,20] and worm type swimmers in complex muds [21]. Furthermore, for the generation of artificial microswimmer an understanding of the response to these complex fluids is needed for any system present in such a fluid. A key example is blood, which is shear thinning and would be of great importance in targeted drug delivery [22,23]. Complex fluids such as fluids that possess differing viscosities, shear thinning and viscoelastic properties have been shown to elicit non-trivial responses which may be able to be drawn upon to improve swimming efficiencies [19,24–28].

In recent years with improved microscopy and velocimetry methods interest in microscopic swimmers has increased with many works focusing on the swimming dynamics of microscopic organisms. Particular model swimmers are often referred to in these works, *Chlamydomonas reinhardtii*/*Dunaliella salina* single celled algae swimmers [24,29], *E. coli* a bacteria swimmer found in the gut [25,27,30], *C. elegans* a worm type swimmer [6,31,32] and spermatozoa which has great relevance in fertility treatment [19, 20, 33–35]. These swimmers each possesses different motility methods and their response to different fluid conditions varies greatly. Within the work that has been conducted thus far, a picture of the response to complex fluids is being built. However, a variety of responses have been displayed, thus significant questions are still present. The aim through this work is to aid in the understanding of microscopic swimming response to these complex fluids, and help add to the picture being constructed.

In this work, the swimming dynamics of a flagellated algae swimmer were characterised, first in the medium, a water-like solution (Chapter 4), then under Newtonian fluids with increasing viscosities (Chapter 5), fluids with shear thinning properties (Chapter 6) and finally viscoelastic fluids (Chapter 7). The swimmer of question in the study was *Dunaliella salina*, a swimming alga with a diameter of $\sim 14\,\mu m$. Its motility is provided by two arm like appendages which extend outwards from the top of the body, and beat in an almost breaststroke-like motion, propelling the swimmer forward.

A wide range of swimming dynamics were analysed and discussed using the methods discussed in detail in Chapter 3. Analysis with a camera of conventional frame rate (15 FPS) displayed the net swimming velocity, overall progression of the swimmer and the orientation. Using statistical methods such as histograms, windroses and the mean squared displacement (MSD) the swimmers' response to the different fluids was characterised. However, purely analysing the algae under a camera with conventional frame rate lost large parts of the swimming kinematics. Due to the restrictions of low-Reynolds number swimming the algae move forwards and backwards in two distinct phases (the power and recovery stroke) as they swim. Utilising a high speed camera and high magnification,

the beating dynamics such as the beating frequency and the velocities through the power and recovery stroke were captured, displaying responses that would be masked if purely using low frame rates.

An issue often present in experimental work into swimmers in complex fluids is fluids often possess different complex properties. One example is polymer solutions used to generate viscoelastic properties are often shear thinning and difficulty can be present when decoupling the response to each property. One method often drawn upon is calculating the effective shear rate of the swimmer (the average shear rate across the swimmer's body), allowing for an effective viscosity to be produced. This then allows for comparison between Newtonian and complex fluids. The hope is that through the methods conducted, greater knowledge into the individual response to such complex fluids for this alga will be recovered, and a definition of an effective viscosity can be characterised for this swimmer.

Furthermore, to the analysis of complex fluids, the swimmer's response to a solid boundary was examined (Chapter 8). The interaction with a wall for microscopic swimmers is of great importance for natural systems such as spermatozoa navigating the cervical canal [36–38], biofilm formation [39–41] and algae interaction with the surface barrier in oceans [42]. Further, industrial applications rely on these interactions, such as algae photoreactors which need to maintain a clear boundary to ensure sufficient light reaches the full population within [43]. It has also been shown that managing wall interactions of microswimmers can be used as a concentrating or filtration method, and have even been shown to move a mechanical gear [44–46].

The work conducted in this thesis placed *Dunaliella salina* in a shallow microfluidic channel, imposing quasi 2D conditions. This allowed for a detailed analysis of the controlling features when the algae came in contact with the solid boundary of the channel. Characteristics such as the approach and escape angles and velocities were defined, as well as the kinematics at the walls surface. Using these variables, a statistical analysis was conducted into the different forms of wall interactions. The hope that with this analysis the response to a wall can be predetermined by the approach conditions with the expectation

for this knowledge to be used in filtration or concentration methodologies.

1.3 Microswimmers

A microswimmer is an organism or device that is motile by means of self propulsion at the microscopic scale. A number of microorganisms utilise diverse motility techniques and posses the ability for controlled navigation as it allows them to relocate to areas of improved nutrition, light or away from hazardous effects such as temperature or high chemical levels as well as assisting in sexual reproduction processes. Recently, artificial microswimmers have been developed to mimic or evolve on the swimming techniques of natural microswimmers, with intended uses in sectors as diverse as medical, manufacturing and sensing [16–18].

There are many methods of propulsion at the microscopic scale in the natural world [47]. Some utilise the body of the organism to provide the forward propulsion, such as worm type swimmers. However, quite possibly the most common method of propulsion is by the means of flagella, which are whip-like appendages that protrude from the cell and are controlled by micromotors. There are two main types of flagella: prokaryotic and eukaryotic. Prokaryotic flagella utilise rotary movement to rotate a helical protrusion, whereas eukaryotic flagella use a complex sliding filament system to drive responses along the whole flagellum [48]. Examples of prokaryotic swimmers are *Escherichia coli* (*E. coli*) which use many flagella all over its surface [25, 27, 30] and *Vibrio choleraes* which rotate one flagellum similar to a corkscrew [49]. In contrast, examples of eukaryotic swimmers include green algae such as *Chlamydomonas* and *Dunaliella* who use two flagella beating in a breaststroke-like motion [24, 43, 50]. Other forms of flagellated swimmers are motile by the means of Cilia, which have the same structure as flagella but are typically shorter and are distributed across the cell body in their thousands. *Paramecium* and *Volvox* are types of algae that use cilia as a motility method [9, 10, 48, 51–53].

In terms of artificial microswimmers, motility techniques are just as broad. Examples of these swimmers include scallop type swimmers that have one simple mechanical hinge that can only move through complex fluids [54], and chains of beads [55] that are motile by flexing the beads along the chain. These systems are commonly controlled by magnetic actuation, which allows for fine precise control at a distance from the swimmers. Another method of artificial swimming is janus particles [56, 57]. Janus particles surfaces have two or more distinct physical properties such as chemical structure, response to water (hydrophobic/hydrophilic) or magnetic properties. Utilising the difference in structures, these particles can be given active motion dependent on the immersed fluid or magnetic field [58, 59].

Swimmers are generally categorised dependent on their interaction with the fluid and are classed are either pullers or pushers [60–62]. As can be seen in Figure 1.1, puller swimmers draw the fluid around them, in towards the body in the longitudinal direction and expel it in the transverse direction. Whereas pusher swimmers expel the fluid in the longitudinal direction, drawing the fluid in from the transverse direction. The induced flow field can be modelled as a symmetric force dipole or stresslet [63]. In regard to a puller swimmer, a negative stresslet would be assumed and positive for a pusher. Hydrodynamic interactions will thus vary depending on swimming type, with attraction or repulsion forces depending on orientation and swimmer type. This has been shown to have significant influences on the viscosity of swimming suspensions, with pushers seeming to reduce viscosities [64, 65] and pullers increasing it [66–70]. Examples of pusher type swimmers are *E. coli*, or Spermatozoa and examples of puller swimmers are algae swimmer such as *C. reinhardtii* and *D. salina*. However, while these types of swimmers are generally classified as puller swimmers, they oscillate between pusher and puller like behaviour between their power and recovery stroke as they move backwards and forwards through the fluid. In some cases this type of swimming is referred to as neutral swimming [60, 62].

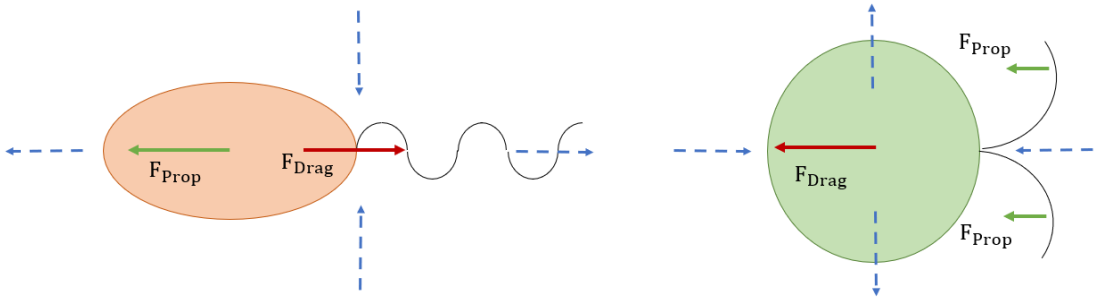

Figure 1.1: Schematic diagram noting a fluid's response to pusher (orange body) and puller (green body) swimmers. Green and red arrows represent the propulsions and drag forces on the swimmer's body and appendages, and blue dashed arrows depict the direction of fluid motion. Image adapted from Podar et al [71]

1.3.1 Swimmers in nature

Across the natural world, many organisms utilise the mechanisms of microscopic swimming to either provide motility to their body or the movement of other substances. The ability for an organism to achieve motility is an evolutionary trait, with the obvious advantage of the capability to move to areas of benefit to the organism and away from areas of harm. The type of swimming motion to provide progression is not universal with different species utilising different appendage formation and numbers to provide the propulsive force. Some of the most common and well known microscopic swimming organisms are described below:

- *E. coli*
  - *E. coli*, a bacterium common in human and animal intestines, has several flagella which are connected to a rotary motor. Each filament has a diameter of approximately 20 nm and length of 10 µm. Rotating in an anti-clockwise direction, the flagella bundles and the cell swims along in a straight path. When one or a number of flagella start to rotate clockwise, the bundle is disrupted causing an abrupt change in direction. This type of motion is called a run and tumble trajectory, with the run representing the straight part of the motion and tumble

representing the sharp change in direction [25, 27, 30].

- Spermatozoa
  - Spermatozoa propel themselves towards the egg using a rollicking spin in precession. As well as the tail rotating, the head also rotates, resulting in an almost drilling like motion of the spermatozoa through the fluid. The length of a spermatozoa flagellum varies by species, but for a human it is approximately 40 µm [7, 8].
- *Chlamydomonas reinhardtii*/*Dunaliella salina*
  - *Chlamydomonas reinhardtii* (*C. reinhardtii*) and *Dunaliella salina (D. salina)* are morphologically similar algae that use the same method of propulsion. Both are approximately 14 µm in diameter and swim with two flagella beating in an asymmetric almost breaststroke like motion. Two strokes are present, a power stroke where the flagella extend bending towards the base of the body and a recovery stroke where the flagella fold and return to their initial position producing less drag than the power stroke [2, 24, 50].
- *C. elegans*
  - *C. elegans* is a small, multicellular roundworm, which due to the wealth of biological research into the species is seen as a model system for low Reynolds number experimentation. *C. elegans* move by producing travelling waves using 95 muscles through its body. It has a length scale of 1 mm but despite their large size in convention to other microswimmers, *C. elegans* still display low Reynolds number swimming. An advantage of their larger size is flow fields around their bodies can be more accurately obtained [6, 32, 72].
- *Paramecium*

– *Paramecium* is a ciliated microorganism that is covered with thousands of cilia that beat in time with each other. Cilia can also be found in the lungs and airways of humans, with their job to remove mucus and other forgiven particles up and out of the airway [53].

1.3.2 Swimming at low Reynolds numbers

Swimming at the microscopic level is very unlike the swimming kinematics experienced by a swimmer at the macroscale. A key defining feature of microscopic swimming is the Reynolds number (Re), defined as the ratio of inertial to viscous forces

$$Re = \frac{Inertial\ Forces}{Viscous\ Forces} = \frac{\rho V D}{\eta} \tag{1.1}$$

where V is the velocity, ρ is the density, η is the viscosity and D is a characteristic dimension. At high Reynolds numbers, inertial forces dominate while at low Reynolds numbers, viscous forces have the greater impact.

Generally a human swimming in water would experience a Reynolds number in the order of $\sim 10^4$. However, for a microscopic organism, the characteristic Re is typically $\ll 10^{-1}$, often in the region of between 10^{-3} to 10^{-5}, due to their slow swimming velocities and small bodies [73]. Therefore, viscous forces dominate and inertial effects can typically be ignored.

Additionally, the frequency-based Reynolds number can be used to assess unsteady flow effects. Conventionally, the frequency-based Reynolds number is defined as

$$Re_{freq} = \frac{\rho D^2 f_{BF}}{\eta} \tag{1.2}$$

where f_{BF} is the frequency. For *C. reinhardtii* (Section 1.3.1), an alga microswimmer the beat frequency can be approximated to 50 Hz [24, 67] and therefore the frequency-based Reynolds number of a typical microswimmer can be calculated as $Re_{freq} \approx 0.03$.

Consequently, it can be assumed the flow is steady. In the case of a typical bacterium such as *E. coli* (Section 1.3.1) ω_{BF} would replace the frequency and denote the rotational frequency at which the flagella rotate.

To gain further information on swimming at the microscopic level in Newtonian fluids, the Navier-Stokes (Equation 1.3) and continuity (Equation 1.4) equations can be modified to produce the Stokes equation

$$\rho(\frac{dV}{dt} + (V \cdot \bigtriangledown)V) = \eta \bigtriangledown^2 V - \bigtriangledown P + F_B \tag{1.3}$$

$$\bigtriangledown \cdot V = 0 \tag{1.4}$$

where P is the fluid pressure, F_B takes into account in the momentum equation the forces applied, V is the velocity, ρ is the density and η is the viscosity [53, 74]. The Navier-Stokes equation can be nondimensionlised using V_c, D_c and t_c as reference scaling for velocity, length and time

$$\tilde{D} = \frac{D}{D_c} \tag{1.5}$$

$$\tilde{V} = \frac{V}{V_c} \tag{1.6}$$

$$\tilde{t} = \frac{t}{t_c} \tag{1.7}$$

where V_c, D_c and t_c are the characteristic dimensions variables for velocity, length and time and reduce the terms to dimensionless values. The tilde $\tilde{}$ denotes a variable as dimensionless.

This follows that the spatial derivatives will naturally follow the nondimensional coordinates thus

$$\tilde{\bigtriangledown} = \frac{\bigtriangledown}{1/D} \tag{1.8}$$

$$\tilde{\bigtriangledown}^2 = \frac{\bigtriangledown^2}{1/D^2} \tag{1.9}$$

and the pressure and force terms can then be defined as

$$\tilde{P} = \frac{P}{\eta\, V_c/D} \tag{1.10}$$

$$\tilde{F_B} = \frac{F_B D_c^2}{\eta V_c} \tag{1.11}$$

Rearranging the unsteady conventional Navier-stokes equation into its nondimensionalised form gives

$$\frac{Re}{Sr}\frac{d\tilde{V}}{d\tilde{t}} + Re\tilde{V}\cdot\tilde{\bigtriangledown}\tilde{V} = \tilde{\bigtriangledown}^2\tilde{V} - \tilde{\bigtriangledown}\tilde{P} + \tilde{F_B} \tag{1.12}$$

where Sr is the Strouhal number defined as $Sr = (t_c V_c)/D$. It describes the forcing timescale in relation to the flow timescale and is related to the oscillating flow mechanics.

Given the typically low Reynolds number experienced by microswimmers, the Navier-Stokes equations reduces to the so-called Stokes equation (also known as the creeping flow equation).

$$\bigtriangledown P = \eta\, \bigtriangledown^2 V + F_B \tag{1.13}$$

The Stokes equation is a linear time-independent equation, and consequently symmetric under time reversal. This leads to a number of important properties that affect the fluid flow around a microswimmer. Firstly, it is pseudo steady-state [74]. The lack of a time derivative infers that temporal changes can only be introduced by moving boundary conditions, such as the flagellum, to which the fluid responds immediately. Secondly, it is

linear. The Stokes equation implies the solution of the flow field around complex structures can be assembled by superposition.

As the Stokes equation is linear and time reversible, it gives rise to motility reversibility. Therefore, for microswimmers it is not possible to achieve net motion by using reciprocating strokes under Stokes conditions. The significances of the reversibility is known as the "scallop theorem" coined by Purcell in a famous lecture in 1976 [73] in relation to the swimming motion of a scallop which uses one degree of freedom reciprocating strokes, and thus would not be motile in low Reynolds number fluids.

The first to prove it was possible to swim in an incompressible Newtonian fluid in the absence of inertia (low Reynolds numbers) and under the Stokes equation was Sir Geoffrey Taylor. He demonstrated that an infinite waving sheet generating travelling waves could indeed swim through such fluids [75, 76]. Taylors planar sheet oscillated following the prescribed form according to

$$y(x,t) = A_w sin(k_w c_w - \omega_w t) \tag{1.14}$$

where A_w is the travelling wave amplitude, ω_w is the wave frequency, $k_w = 2\pi/\lambda_w$, λ_w is the wavelength, $c_w = \omega_w/k_w$ is the travelling wave speed and k is the wave number.

Through this analysis, Taylor found the travelling sheet to move forward at a velocity of

$$V = \omega_w A_w^2 \frac{k_w}{2} \tag{1.15}$$

When oscillations were introduced, a point of interest to note is that the sheet would propel itself in the opposite direction to the travelling wave [75, 77].

Following on from Taylor's work, many expanded and refined the work conducted such as the resistive force theory (RTF), devised by Gray and Hancock [78] who, by analysis of spermatozoa cells and Taylor's sheet, stated the hydrodynamic forces an organism would experience would be proportional to the local body velocity

$$F_B = C_N V_N + C_T V_T \tag{1.16}$$

where C is the local resistance coefficient per unit length and N and T are the normal and tangential components. Therefore, it states the total thrust produced by the flagellum can be obtained by the integral of the propulsive force over the body or flagellum length. The drag-based thrust is therefore defined by the anisotropy between the normal and tangential resistance coefficients.

For *Caenorhabditis elegans* (*C. elegans*) a worm-like swimmer, using slender rod approximations it the ratio was found to equal 1.5 [79, 80]. When wall effects were incorporated, the resistance coefficient ratio was found to alter and has been found to reach values greater than 2 [81].

Microswimmers are not solely restricted to swimming in simple Newtonian fluids, with many swimmers thriving in complex fluids such as muds, gels and bodily fluids [19, 31, 35]. Often these fluids display shear thinning and viscoelastic behaviour. Fluid elasticity reinserts a history-dependent element that is removed by low-Reynolds number swimming, as the elasticity adds a relaxation timescale [82]. This added time dependence allows for motility through elastic fluids by one degree of freedom reciprocating motion, such as a scallop would use. While this technique has never been observed in the natural world, the concept has been proven both numerically and by experimental means [83].

As well as reciprocating motility through viscoelastic solutions, it has also been shown that it is possible for strain rate-dependent viscosities to allow for motility at low Reynolds numbers. Qui et al. showed that by controlling the movement rates of a scallop-like swimmer in low-Reynolds numbers fluids which were shear thinning or shear thickening, motility could be achieved. This was due to local changes in viscosity of the fluid induced by different shear rates exerted by the scallop [54].

With the addition of complex rheology, further dimensionless numbers are of importances. This work will draw on a couple of these numbers: the Deborah and Weissenberg

numbers.

The Deborah (De) number is a dimensionless quantity relating how over a given time frame a viscoelastic fluid will behave. It is defined as the ratio between the characteristic time of the fluid and the characteristic time of the flow, ($De = \frac{\lambda}{t}$) where λ is the characteristic relaxation time and t, a characteristic timescale. For Newtonian fluid flows $De = 0$, and for purely elastic solids $De \to \infty$ [84].

The Weissenberg number, coined after Karl Weissenberg, is a comparison of elastic and viscous forces providing a metric of non-Newtonian effects. It defines the degree of anisotropy or orientation generated by deformation. In simple shear, it is defined as the shear rate multiplied by the relaxation time [84] $Wi = \frac{Elastic\,Forces}{Viscous\,Forces} = \dot{\gamma}\lambda$.

Furthermore, for reciprocal swimmers, it has been shown that the addition of Brownian motion can enhance diffusivity compared to normal diffusion [85]. This was shown at time scales larger than that of rotational diffusion, breaking the symmetry of the back and forward strokes. Therefore, for these swimmers under the influence of Brownian motion, utilising reciprocal motion can lead to enhanced diffusion under certain conditions which can be biologically advantageous.

1.4 Algae

The term "algae" (singular Alga) is a broad term that has no formal definition or taxonomic meaning; however, it is generally used to describe a group of photosynthetic organisms that are primarily aquatically based [86, 87]. Depending on the definition, the number of algae species can range from 30,000 to 1 million, with 72,500 species being the quantity reported by Michael Guiry [88] based on the current species documented on AlgaeBase. Each species can be distinguished and defined by the morphology of their features such as number of cells, size, compositions, etc.

Algae have a relatively simple reproductive and vegetative structures, in comparison to more high-level land plants, as they lack complex tissues such as stems, roots, leaves and

vascular tissues. Depending on the species, algae reproduce by asexual or sexual means [87]. However, in certain species reproduction can be achieved using either, depending on the situation. Algae thrive in a wide range of environments, but they are most commonly found in freshwater, marine or terrestrial habitats. Moreover, algae have evolved to live in harsher habitats such as environments with high salinity, extreme temperatures and limited resources. For example, *Verdigellas* genus have been found at depths between 60 m and 120 m, and *Dunaliella salina* which can live in very high salinity waters [87].

Algae can be divided into two distinct groups: macro and microalgae. Macroalgae or multicellular algae consist of many cells, have an asexual reproduction structure and can grow up to 60 m in length, as in the case of kelp [87]. Microalgae range in size from a couple of micrometres to a few hundred micrometres for the biggest of the species, with most microalga species being unicellular.

Microalgae are vitally important to the aquatic food chain, as they are the primary producer, feeding everything up to the biggest ocean mammals. Furthermore, it is estimated that 70% of the world's oxygen is produced by phytoplankton, which is essential for ensuring the earth atmospheric balance [89].

1.4.1 *Dunaliella salina*

This research focuses on the swimming behaviour of a microalgae species known as *Dunaliella salina (D. salina). D. salina* are part of the *Dunaliella* genus, which is made up of 22 unique species [90]. The *Dunaliella* genus was first reported in 1838 by Michael Felix Dunal who, on an expedition on behalf of the Académie des Science (Paris, France), found that the red colouration in saltern brines was not caused by chemicals or the brine shrimp, as had been assumed, but by a unicellular bi-flagellate microalga *D. salina* [91]. Although later studies suggested the majority of red colouration is caused by a red halophilic *Archaea*. Later, after further research, Emaniol C. Tedorescu collated all relevant studies and formed a formal description of the genus *Dunaliella* [92]. All species in the *Dunaliella* genus belongs

to the *Chlamydomonadales* family [90]. The defining features of the genus are the lack of rigid cell walls and their reproduction structure, which occurs by longitudinal division or by fusion of two motile cells to form a zygote.

The *Dunaliella* Genus is a very diverse species which inhabit a range of diverse environments such as marine, halophilic and freshwater [91]. *D. salina* are part of the halophilic group within the genus, meaning they thrive in high salt concentrations. This is due to their ability to produce glycerol to compensate for the high salinity, in some cases as high as 5 M NaCl [92]. Due to this fact, *D. salina* are usually found in salt fields around the world.

1.4.1.1 Cell structure

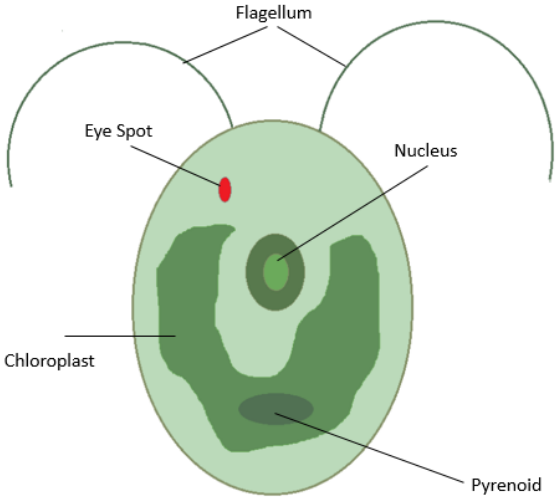

Figure 1.2: Simplified schematic diagram of the cell structure of *Dunaliella salina*, with labels indicating the main cell structures.

Dunaliella salina is a singular celled organism, its internal cell make-up is morphologically similar to the *Chlamydomonas* Genus. However, they are surrounded by a glycocalyx rather than a cell wall, a mucilaginous glycoprotein coating of variable thickness. Its role

is to act as a cellular barrier, provide some rigidity and is also key in the adhesion process during sexual reproduction [93].

A simple diagram of the cell structure of *D. salina* can be viewed in Figure 1.2. Within the cell, there is a nucleus which contains the organism's DNA. This is surrounded by the nuclear envelope, which controls the movement of materials in and out of the nucleus. Towards the bottom of the cell is a simple chloroplast shaped like a cup. The main function of the chloroplast is to help with the photosynthetic processes. In addition, it has the secondary function of accumulating large quantities of β-carotene. Other organelles present in the cell are the vacuoles, which have a range of functions from food storage to containing waste and the Golgi apparatus, which sorts, packages and modifies proteins post or pre passing through the outer membrane [90, 94].

Located close to one of the alga flagellum is a structure that plays a vital role in phototaxis, the movement towards favourable light conditions (Section 1.4.1.2.1). It is constructed of mostly carotenoids and is called the eye-spot. The eye-spot is light sensitive and when suitable light signals are sensed (not too dark or light) the flagellum closest (cis-flagellum) will beat less while the further away flagellum (trans-flagellum) will increase its beating, turning the organisms towards the desired light conditions. The opposite is also true for unideal light conditions [95].

Dunaliella salina are one of the few algae in the world to be able to adapt to drastic salinity changes. They manage this by the use of glycerol and glycerine betaine as an intracellular osmotic metabolite. To control the levels of salinity entering the cell, *D. salina* produces glycerol from starch as well as maintaining a cell membrane with a low permeability to glycerol. Together, this allows the cell to maintain its osmotic balance, and enzymatic activity, and thus is the reason why *D. salina* can live in high saline environments. [93, 96, 97].

The cell shape of *D. salina* is not uniform and varies between each individual cell. However, they do conform to some defining characteristic; the length of a *D. salina* cell is within the range of 5 to 25 µm and its width from 3 to 15 µm [98]. *D. salina* cells

have been found to be bottom-heavy, meaning each cell's centre of mass is offset from its centre of buoyancy [99]. Significantly, this leads to a tendency for the algae to orientate in the opposite direction to gravitational forces and therefore swim upwards. This is known as gravitaxis, which is beneficial for the algae as conventionally there is more light and nutrients closer to the surface of the water. *D. salina's* cell shape depends greatly on its stage of growth and environmental conditions and can range from ovoid, spherical, pyriform, fusiform or ellipsoid [98]. They are capable of thriving in a number of different environmental conditions due to its adaptability. Thus, it has a very high tolerance to fuel oil spills when compared to other similar algae [100].

D. salina have two flagella of length between 1 and 1.5 times that of the body. They have a diameter between $200 - 400\,\text{nm}$ [101, 102], and so can be assumed as a slender body due to their very high aspect ratio. Each flagellum conforms to the so called $9 + 2$ flagella structure [93]. Within each flagellum is a bundle of 9 fused pairs of protein filaments called microtuble dublets surrounding two single microtubles in the centre, as shown in Figure 1.3. This structure is known as the axoneme. Connecting the flagellum to the body is the basal body, serving as a base and growth site for the flagellum. The outer of the two microtuble pair is connected to the axomen by a protein called Nexin, with the other connected to numerous motor proteins utilising ATP. Upon activation of the ATP, the microtubles can slide along one another, generating an internal shear. This motion across the 9 doubles creates the whip-like motion of the flagellum [24, 50, 93, 101].

D. salina can go through either sexual or vegetative reproduction, depending on environmental conditions. Vegetative reproduction occurs by longitudinal division of the motile cell, with the chloroplast dividing at the preprophase. This is the most common form of reproduction for *D. salina*, but under favourable conditions, *D. salina* can also reproduce by isogamous sexual reproduction. In this case, two cells come together and form a cytoplasmic bridge and fuse together to form a Zygote. This zygote has a hard outer shell and can survive in very harmful and unfavourable conditions. After a resting stage, or when conditions are suitable, the zygote germinates and can release up to 32

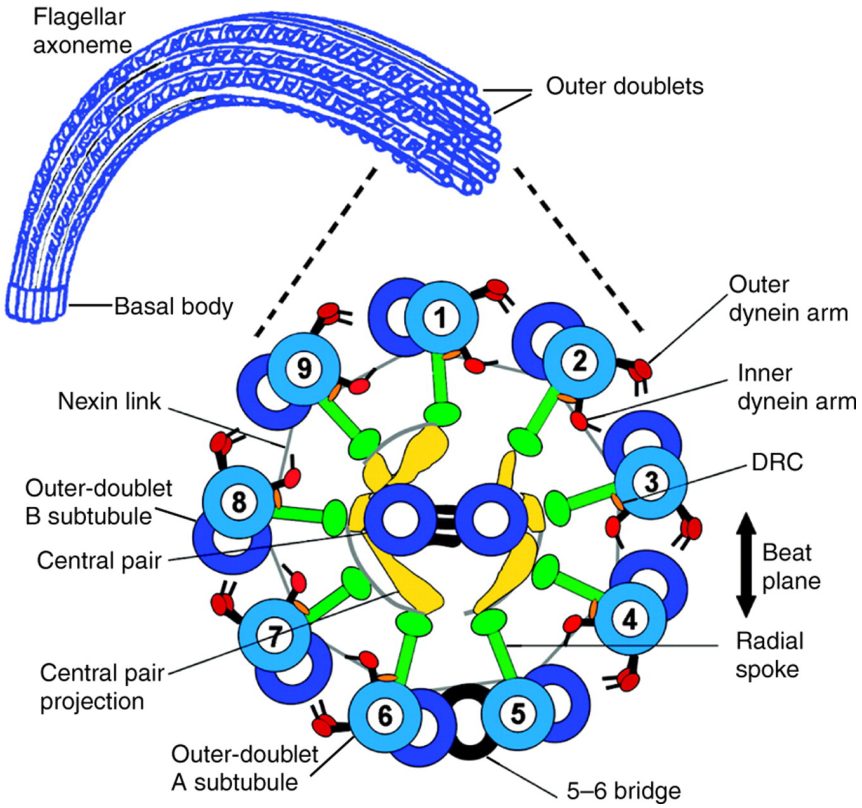

Figure 1.3: Digram of 9+2 flagellum structure present in *D. salina's* flagellum, consisting of peripheral ring of 9 microtubular structures and 2 central microtubules. Image reproduced with permissions from Lindemann et al. [51].

haploid daughter cells through a tear in the cell envelope. Sexual reproduction is very rarely observed in laboratory grown cultures, but is more common in the alga's natural environment [86, 91, 103].

1.4.1.2 Dunaliella swimming

Active motility is a desirable characteristic for *D. salina* as it allows it to optimize its positions through their microhabitat, whether that be photic, chemical, gravitation or thermal stimuli to name but a few [104, 105]. To achieve motility, *D. salina* has two eukaryotic flagella that beat in a motional likened to a travelling wave at a frequency

between 25 and 50 Hz [50, 106]. This motion can be broken down into two distinct strokes: the power stroke, during which the flagella move from the top of the stroke back to the body and the recovery stroke, during which the flagella return to their original position at the head of the algae. Figure 1.4 shows the differences between the two strokes, with the power stroke extending further away from the body, perpendicular to the swimming direction, to produce the greatest possible force. During the recovery stroke, the flagella are distinctly closer to the body than in the power stroke [74]. Due to the nature of fluid mechanics at the microscopic level, the power stroke produces the entirety of the forward motion, with the recovery stroke actually propelling the cell in a rearward direction relative to the net swimming bearing [24, 107]. However, this retardation is significantly less than the forward movement provided by the power stroke. These swimming kinematics allow the algae to swim through a water-like medium at velocities of around $50\,\mu\mathrm{m\,s^{-1}}$ [106]. Backwards swimming is also possible where the flagella move in an undulatory motion, but this is very rare [87].

The beating of the two flagella is at times not symmetric and can become asynchronous. This is thought to be the primary driver in turning events of the swimmer, with one flagellum beating with a greater dominance [109]. Furthermore, unsynchronised strokes can lead the algae to rotate in an anti-clockwise direction around their longitudinal path, tracing a helical path at $1 - 2\,\mathrm{Hz}$ [50, 87, 95]. A schematic of this type of motion can be visualised in Figure 1.5.

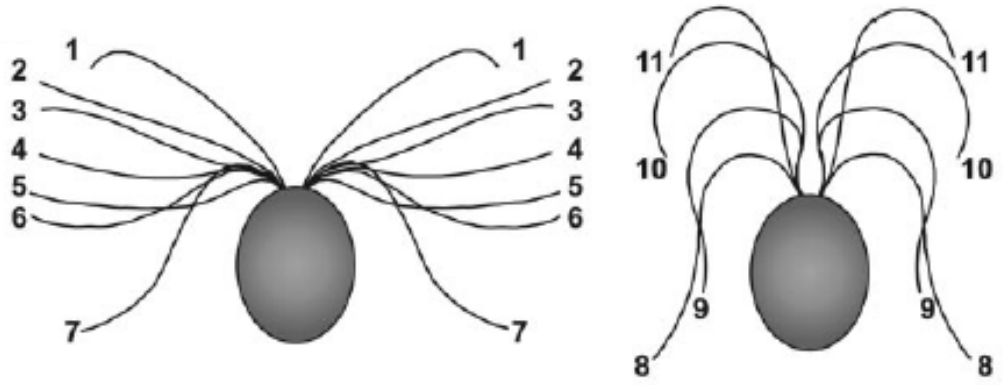

Figure 1.4: Diagram of an approximate beat cycle of a puller algae such as *D. salina*. The beat is split into two distinct strokes, the first, a power stroke (1-7) during which the flagella extend downwards in a wide arc, followed by the recovery stroke (8-11) during which the flagella return to its original position close to the head. In the power stroke, the body moves forwards, and recovery rearwards, relative to the overall direction of travel. Image reproduced with permissions from Weibel et al. [108].

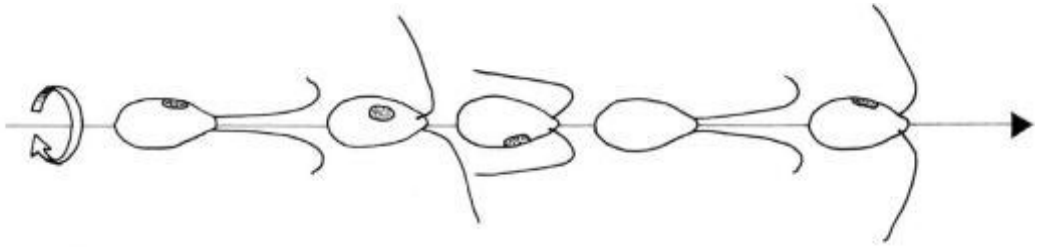

Figure 1.5: Schematic of longitudinal rotation exhibited on occasion in puller swimmers. Image reproduced with permissions from Barsanti et al. [87].

1.4.1.2.1 Taxis When the alga's movement occurs in response to an external stimulus, the resultant movement is called a taxis effect. Common taxis effects that are experienced by *Dunaliella salina* include [50, 74, 110, 111]:

- Phototaxis
  - Swimming directed motion based on the response to light (either too much or too little)
- Chemotaxis
  - Swimming directed motion based on the presence of chemicals (e.g. spermatozoa's movement towards an egg during fertilization [112])
- Gravitaxis
  - Swimming directed motion based on the response to gravity (as *D. salina* is bottom heavy, they tend to orientate themselves in an upwards direction)
- Gyrotaxis
  - Swimming directed motion based on a combination of gravitational and viscous torques. This tends to lead the algae to orientate themselves around regions of downwelling in a fluid [113, 114]

1.4.1.3 *D. salina* vs *C. reinhardtii*

Throughout this work, comparison will be drawn between *Dunaliella salina*, which is used in this work, and *Chlamydomonas reinhardtii*, which is often used for motility analysis and is seen as the model microscopic puller algae swimmer. Morphologically, the two algae are very similar, with similar dimensions and stroke gaits. However, there are subtle difference between the two that should be accounted for [50].

D. salina and *C. reinhardtii* are both members of the same family of alga species. Therefore biologically, they are closely related and share many similar traits. Morphologically the two algae are almost identical. However, one noticeable difference between the two is the absence of a cell wall in *D. salina*, which adds rigidity to the cell and can influence how the body reacts to changes in environmental conditions [50].

While both have two flagella and are classed as puller type swimmers, the beating patterns of the two swimmers are different. *C. reinhardtii* beats with a stroke more akin to a breaststroke like movement with a wide power stroke followed by a tight inward recovery stroke. The distal tip of the flagella moves with greater longitudinal and lateral motion relative to the body through the strokes. In contrast, *D. salina* move their flagella in a stroke that resembles more of a travelling bending wave that moves outwards from the body. The distal end of the flagella moves primarily in the lateral space, with less motion in the longitudinal direction than *C. reinhardtii* [50]. Furthermore, in the recovery stroke, the flagella come closer to the cell body. *D. salina* tend to have relatively longer flagella compared to body length, with flagella sometimes as large as 1.5 times their body length, whereas *C. reinhardtiis* flagella are similar to their body diameter. *C. reinhardtii* beat their flagella between 50 and 60 Hz [24, 67], greater than *D. salina*, which exhibits a beating frequency of between 25 and 50 Hz [50, 106]. *C. reinhardtii* swims at a greater velocity than *D. salina*, (approximately double) possibly as a result of the increased beating frequency [24, 50].

1.5 Applications of microalgae

The applications of algae are widespread, with many diverse uses of different species being discovered and utilised. The first uses of microalgae date back to the Chinese and Japanese, who collected and used algae as a food source over 2000 years ago [11]. In the present day, algae are used in many products and applications, with new processes and uses still being discovered. The range of possibilities is virtually unlimited for microalgae as by changing

cultivation conditions and by the large species diversity, a wide assortment of products can be created. Furthermore, their high protein production by weight can lead to very high yields and efficiencies.

1.5.1 Food and nutritional supplements

Microalgae are a very effective producer of nutritional supplements that can be used in both human or animal feeds. Depending on the alga and its conditions they can be manipulated to produce large quantities of carbohydrates, proteins, enzymes and fibres, as well as a range of vitamins and other minerals. The Asian market consumes the most microalgae products, commonly in the forms of nutritional supplement. In modern times, *chlorella* and *spirulina* are the most dominant microalga species in the market, mainly due to their high protein content, nutritional value and easy manipulation during growth [11, 115].

One use of marine microalgae is the production of complex polyunsaturated fatty acids (PUFA's). Polyunsaturated fatty acids, such as omega-3 and 6, have been shown to possess health benefits such as improved joint health, and relieving the symptoms of rheumatoid arthritis [11, 116]. Higher order plants and animals do not have the required complex enzymes to produce complex fatty acids with greater than 18 carbons, and commonly PUFA's are obtained from fish and fish oils. However, safety issues have arisen recently due to the increased toxins in fish. Furthermore, using fish oil as additives can be limited due to the unpleasant taste, smell and poor oxidative stability. For certain applications, fish oil is not applicable, as it is composed of a number of different mixed fatty acids that cannot be separated easily. With these uncertainties and the unsustainable overfishing of fish populations, algae could become a leading source of PUFA's [117].

Another useful pigment produced by microalgae is β-carotene, which can be converted into vitamin A through oxidization in the liver. Moreover, it is known to have anti-oxidising effects, which are thought to give health benefits by reducing cell damage from free radicals [98]. Some studies have suggested health benefits of β-carotene in reducing the risk

of developing cataracts, cancers, cardiovascular disease as well as reducing cholesterol [118]. However, research into the benefits of β-carotene in serious disease prevention have shown mixed results and further work is still needed to confirm or deny the true health benefits of β-carotene [119,120]. β-carotene as well as having nutritional value is also a yellow/orange pigment that is used to enhance the colour of margarine, fresh fish and egg yolks to name but a few [121].

Many generic foods also have some levels of β-carotene in them, including some fruits, vegetables and fungi. However, the concentrations of β-carotene are relatively low, especially when compared with microalgae. It is possible to synthesise β-carotene from bixin and crocetin as their structures are very similar, and the same intermediates can be used [122]. However, synthetic β-carotene isomers composition contains only 1-cis whereas natural β-carotene is composed of 9-cis [94]. Therefore currently, microalgae are the leading and best commercial source of natural β-carotene [98]. Under the correct conditions, *D. salina* can produce a very high (up to 14%) dry weight of carotenoids concentration [123,124] and is a leader in β-carotene production.

1.5.2 Cosmetics

Products produced by microalgae can also be used in the cosmetic industries. Pigments and other components are used as cosmetic agents, such as antioxidants, thickening agents and water-binding agents [125]. Generally, microalgae are used in face and skin products, but can also be used in sun and hair products.

1.5.3 Glycerol production

Glycerol is used worldwide and has uses in the pharmaceutical, cosmetic, and food industries [126]. Commercially, glycerol is mainly produced from petrochemical sources. However, as the price of petrol chemicals increase and environmental pressure intensifies, the commercialisation of glycerol produced from microalga is becoming more viable [127].

D. salina is a very effective producer of glycerol as it uses it as an osmotic balance, accumulating large quantities (up to 50%) [98] which can be harvested under the correct conditions. In these processes, after the removal of glycerol or β-carotene in the *D. salina* cells, the remaining substance contains around 40% proteins [98]. The base protein is similar to that of plants like the soybean with low cysteine, methionine and high lysine. Thus, the remaining proteins and fatty acids, can still be used as a supplement or as a meal on its own [128].

1.5.4 High-value molecules

A number of further products that can be harvested from microalga have been discussed. A brief summary and description of further uses, as well as specific alga products, can be found in Table 1.1.

As mentioned previously algae have a high diversity of different species, because of this, many species are still fairly unexplored and unresearched. Research of new species could lead to new novel materials generated from this natural source or refinements of current procedures.

Table 1.1: Common microalgae used in industrial and commercial sectors with typical products extracted for use in these industries. Adapted with permissions from [12].

Microalga	**Products**	**Application areas**	**Basin/Reactors**
Spirulina platensis	Phycocyanin, biomass	Health food, cosmetics	Open ponds, natural lakes
Chlorella vulgaris	Biomass	Health food, food supplement, feed surrogates	Open ponds, basins, glass-tube PBR
Dunaliella salina	Carotenoids, β-carotene	Health food, food supplement, feed surrogates	Open ponds, lagoons
Haematococcus pluvialis	Carotenoids, astaxanthin	Health food, pharmaceuticals, feed additives	Open ponds, PBR
Odontella aurita	Fatty acids	Pharmaceuticals, cosmetics, baby food	Open ponds
Porphyridium cruentum	Polysaccharides	Pharmaceuticals, cosmetics, Pharmaceuticals	Tubular PBR
Isochrysis galbana	Fatty acids	Animal nutrition	Open ponds
Phaedactylum tricornutum	Lipids, fatty acids	Nutrition, fuel production	Open ponds, basins
Lyngbya majuscule	Immune modulators	Pharmaceuticals, nutrition	Open ponds
Spirulina platensis	Phycocyanin, biomass	Health food, cosmetics	Open ponds, natural lakes

1.5.5 Biofertiliser

Certain types of microalgae can be manipulated to be used as a biofertilizer and soil conditioners [129]. Most of the cyanobacteria group have atmospheric nitrogen-fixing capabilities. Nitrogen in soils is the second-greatest influence on plant growth after water levels. Often cyanobacteria are used in rice cultivation, with their ability to reduce nitrogen and generally improve soil quality a great benefit to rice farmers.

1.5.6 Bioindicators

Microalgae can be very useful in use as bioindicators when examining the ecotoxicity of anthropogenic compounds on environments. The fluctuations in alga's characteristics can be analysed and used to decipher the conditions of the environment. In comparison to other organisms that can be used for the same process, algae tend to have a greater sensitivity as well as the ability to grow in harsher conditions. The Dunaliella Genus is one of the best options for use as a bioindicator as it lacks a cell wall, meaning a potential barrier to the substance is removed. It has been shown that *D. salina* are a good indicator of mutagenic phenols [130].

1.5.7 Biofuels

With the overuse of fossil fuels and their effect on the climate, the need to find new energy sources has been readily increased in the last few decades. Thus, many new technologies have been examined to evaluate their potential. One of these that holds promise is the growth of algae to produce biofuels. Many institutions, governments and companies have invested into the research of this topic, with the most notable being Exxon who have placed a significant investment into the research of algae biofuels [131, 132].

The use of algae for biofuel production presents a very attractive alternative to conventional biofuels, with many advantages over a more conventional crop. As microalgae do not produce complex structures such as stems and Xylem, a greater percentage of en-

ergy is used for lipid production, the substance that can be converted to biofuels, than a common land plant. In actual fact, it has been reported that in the right conditions some algae species can produce up to $70 - 80\%$ dry mass of lipids that can be used for biodiesel [133,134]. Moreover, the waste dry mass from the biodiesel process is in the form of rich proteins that can be used in the food and cosmetic industries in the same methods as mentioned previously [13, 14].

Furthermore, as algae are an aquatic organism, they are not constrained to conventional fertile farming land for growth. Therefore, these lands can be used for feed crops. In addition, as algae growth is not reliant on fertiliser, a shift towards algae biofuels production would reduce the amount of potentially toxic fertilizers use worldwide.

Table 1.2: Typical crop yield of conventional biofuel crops alongside the crop yield of microalgae for production of biofuels. Table adapted from [133].

Crop	**Oil Yield (L/ha)**	**Land Area needed (Mha)**	**Percent of existing US cropping area (%)**
Corn	172	1540	846
Soybean	446	594	326
Canola	1190	223	122
Jatropha	1892	140	77
Coconut	2689	99	54
Oil Palm	5950	45	24
Microalgae 30% oil Biomass	58700	4.5	2.5
Microalgae 70% oil Biomass	136900	2	1.1

Table 1.2 shows the differences in crop yield between conventional crops and microalgae. It can be seen microalgae have much higher oil yield and therefore reduced cropping area. As a photosynthesising organism, algae take up carbon dioxide through the energy generation process. Therefore, captured carbon dioxide can be recovered from conventional power plants and used for algae growth. It has been shown that an increase in carbon

dioxide around algae ponds can speed up growth [133].

Nevertheless, despite all the supposed reported benefits of biofuel generation through microalgae, there are some fundamental issues still remaining before it can be economically viable and pose a serious challenge to conventional biofuels and ultimately fossil fuels [14]. The main challenge is reducing the cost of biofuel production to a competitive level. At the present moment, the price per barrel for algae biofuels ranges from 300-2600 US$ compared to $\approx$ 74 US $ as of 9/2021, per oil barrel [135]. Other issues that are still present are: contamination of suspensions, oil extraction difficulties and high water usage. These issues present huge engineering and technological challenges to improve efficiencies and costs throughout the entire systems from biological to structural components [14]. If these challenges can be overcome and the whole system refined to allow for a price per barrel similar to that of oil, then algae biofuels could become the new norm throughout the world.

1.5.8 Microrobotic swimming

The development of artificial microswimmers is an area that is gaining much attention in the last few years [136]. The idea of using a microscale robot to swim and reach areas difficult to reach by conventional means has been around for years, with it being coined in popular culture and films such as the "fantastic voyage". However, now the reality of such devices is starting to become promising, with many developments in the recent past. The hope is that these swimmers can have applications in micromanufacturing, targeted drug delivery and sensing applications to name a few [16,17]. The minimal invasive nature of artificial microswimmers is especially sought after for the medical industry as it can reduce recovery time, infection risks, drug side effects, and post-operative pain from current procedures [18].

A number of different artificial microswimmers have been developed or conceived, with a variety of solutions relating to motility. Generally speaking, most utilise magnetic fields to wirelessly control and power the microstructures. However, the process of developing the

"ideal" artificial swimmer is still in its infancy and is still needing more scientific input [15].

The first man-made microswimmer device was devised by Whitesides [137] and co-workers, who constructed chemically powered millimetre scaled swimmers who swam at the free surface. This was followed by, Dreyfus [138] in which a linear chain of colloidal magnetic particles was fabricated. These chains were linked by short DNA segments and could oscillate and rotate depending on an input of an external rotating magnet. Recently, artificial microswimmers have focused on magnetically actuated beads and rotating helix's [139–142]. As well as displaying a full range of swimming motions, these swimmers have also been shown to break through artery blockages, which could give great benefits for the medical sector [143].

Microswimmers found in nature have been an inspiration to a number of microartificial robot designs [144] and biomimicry as a tool can be incredibly valuable. This field is constantly developing and attributing to finding new solutions in artificial microswimmer development. The flagellum has been one of the most studied features when it comes to artificial microswimmers, such as Dreyfus's work into self-assembling magnetic beads based on the form of a natural flagellum [138]. Further, the helical tail of a pusher microswimmer has also been mimicked in a rigid helical tail that could be actuated to move though fluids [58].

Furthermore, the continued evaluation and depiction of natures microswimmers is still a key area in the development of effective and efficient motile micro/nanorobots. As well as research in simple Newtonian fluids, it is just as vital to examine the effects of complex fluids and flows on natural microswimmers to better understand the response to such fluids. This research can lead to interesting and unanticipated discoveries that can help further the state of artificial microswimmers. This is true when examining the artificial microswimmers in the human body as many of the fluids in the body are complex in nature exhibiting shear dependant properties or viscoelasticity, e.g. blood which is both shear thinning and viscoelastic [22].

1.5.9 Micromixers

As microswimmers swim through a fluid, they move the surrounding fluid, mixing it, albeit at a very small scale. With enough biomass and time, it is feasible that swimmers could be used as micromixers, mixing solutions without conventional stirrers. There is potential for either natural swimmer or artificial to fulfil this role. There is some research into microalgae and other small scale swimmers that show they can be a significant contributor to ocean mixing and nutrient transport [145–147].

1.5.10 Smart materials

A further use of microscopic swimmer could lead to the development of controllable smart materials. Materials that possess novel properties that can be controlled by outside input could process of great us in many industries. An example may be controlled rheological properties by the alignment or cell structure of microscopic swimmers, with external commands directing their movement. This may be desirable in drilling fluids where it is desirable for large changes in fluid rheology dependent on the situation [148].

Chapter 2

Literature review

2.1 Chapter overview

In this chapter, the most relevant literature in the subjects related to this work are discussed. Initially, a general overview of swimming in complex fluids followed by specific insight into works conducted on swimmers in Newtonian viscous, shear thinning and viscoelastic fluids are conducted. Finally, an overview of work focused on wall interactions is concluded, giving the reader the background knowledge into related works.

2.2 Literature overview

The ability for microscopic swimmers to navigate through fluids possessing complex rheology has much relevance in both the natural world, and in the development of artificial microswimmers [16, 143]. Interest in the effects of complex fluids on natural swimming organisms dates back to the 1970s, when bacteria were examined under fluids of different viscosities [149]. Recently, with the enhancement of microscopy and velocimetry experimental techniques, together with great advances in computational techniques and computer power, there has been an increased interest in the dynamics under such conditions. Research has primarily focused on a few model species such as spermatozoa, *E. coli* and *C.*

reinhardtii [8, 19, 24, 27, 34, 35]. Despite the various advances and increased interest in the topic, the picture of microscopic swimming in complex fluids is still very much incomplete. Across the range of different swimming types and locomotion, no single model can describe every organism's reaction to complex fluids, and it has been shown both experimentally and theoretically that swimmers can be affected very differently by complex fluids depending on the swimmer's shape, swimming gait and fluid properties [72].

In the following sections, recent advances in the understanding of swimming in Newtonian and complex fluids is summarised, primarily focussing on the effects of viscosity, shear thinning properties and viscoelastic fluid properties.

2.3 Swimming in viscous fluids

The viscosity of a swimmer's medium has far-reaching effects on a swimmer's motility. The flagella provide a propulsive force as a result of drag based thrust to move the swimmer forward, and the drag on the body is primarily related to the viscous drag imposed by the fluid [77]. Swimmers in nature are motile is a wide range of fluids that can posses very different viscosities, from water to highly viscous muds and mucuses [10, 21, 150]. Furthermore, swimmers can experience viscous changes, which are often controlled by temperature [151]. An understanding of how a swimmer interacts with viscosity gives an important insight into the swimmer's gait and information on the individual stroke dynamics. Further, it provides a key input and comparison for analysis in more complex fluids.

Swimmers in solutions of different viscosity have shown varied responses to increases in the medium viscosity, with contradictory results seen across different swimmers [30, 35, 149, 152–155]. One of the earliest works into varying fluid rheology on swimming dynamics was carried out by Schneider and Deoetch in 1974 in which a range of motile bacteria species in solutions of varying viscosities were investigated [149]. They found all the species examined showed an increase in swimming velocity in more viscous fluids. With further increases

in viscosity, the velocity increase would reach a local maximum and thereafter decreased. This dynamic was unexpected due to the increases in drag forces related to the increases in viscosities. The study attributed the velocity increase to the conformation of the flagella helix, affecting the efficiency of propulsion.

Further studies have also shown this velocity increase in other bacteria suspensions [156]. In *E.coli*, the viscosity has been seen to affect the flagella bundling due to the reduced rotational velocity [30,157], altering the swimming pattern from a run and tumble to one more akin to random walk. This was seen as a possible mechanism of increased swimming velocity, as the swimmers paths showed increased linearity.

A further explanation to this velocity increase discussed is the apparent metabolising of viscosity enhancing polymers. In the works studying this phenomenon, the polymers used as viscosity enhancers were dialysed, removing impurities the bacteria could potentially be feeding on [27, 30]. Thereafter, the increases in velocity seen at higher viscosities ceased to show, which suggests the bacteria were attaining extra metabolic activity from the impurities within the polymers.

Numerical models have also been proposed based on existing theories to quantify the velocity enhancement in bacteria species. Magariyama and Kudo produced a model, based on the resistive force theorem [77], with the addition of two viscosities that depend on swimmer characteristics and interactions with polymer molecules [157]. It was found that the extra viscosity improved the propulsion efficiency, which reduced the flagella rotation rate, providing an explanation for the increase in swimming velocities found in *E. coli* [30, 157]. Further to this work, Pande and Merchant [153] suggested microswimmers with an elastic degree of freedom could exhibit varied responses depending on the ratio of the relaxation time of the swimmer's elastic component and the swimming stroke period.

Other pusher swimmers have also been examined in fluids of different viscosities. In terms of human spermatozoa, dynamics such as rolling rate, waveform and trajectory have been shown to be significantly altered by viscosity [35]. However, this did not result in notable variations in velocity, which remained constant when comparing high and low

viscosity solutions. *C. elegans*, a worm type swimmer that is commonly found in highly viscous muds, have been found to display a monotonic decrease in velocity with increases in viscosity in a number of studies [6,21,26,31]. The swimmer's gait (frequency, amplitude, and wavelength) was also found to decrease with the increases in viscosity conforming to the rate of velocity decrease.

Puller organisms with two distinct flagella have also been studied in terms of the influences of viscosity on each flagellum. Studies of *Vibrio alginolyticus*, which possesses two types of flagellum (lateral and polar) on a single cell, have shown that each flagellum exhibits different responses to viscous influences. By removing the flagellum not under scrutiny in turn, the researchers were able to isolate the response of each individual flagellum. When swimming using purely the lateral flagellum, a speed boost was observed, whereas swimming using the polar flagellum yielded a monotonic decrease in velocity with increasing viscosity [158]. *Prorocentrum minimum*, a marine dinoflagellate with two flagella which beat in distinct patterns, have been seen to follow a monotonic decrease in velocity under the effects of increasing viscosity [155]. It was reported that the motion of the transverse flagellum seemed to determine the velocity decrease.

As is apparent, each individual organism has its own response to viscous fluids and can conform to different methods under the influences of viscosity. *D. salina* is morphologically different to the afore noted swimmers, with the two distinct flagella unlikely to get tangled and a larger body size. However, these effects should not be ruled out and the chemical composition of the medium should be carefully considered. Experiments involving *C. reinhardtii* have shown its swimming velocity to vary as a function of viscosity, with velocity scaling by a decreasing power-law as the viscosity is increased. This seems to indicate the algae are swimming at a constant thrust, such that the thrust produced by the flagella remains constant across viscosities [24, 67, 107]. Therefore, indicating that the gait of the swimmer in more viscous Newtonian fluids decreases in line with the induced viscous drag.

It should be noted that viscotaxis is a different form of transport motion that occurs as a result of viscosity gradients across a solution [159, 160]. Viscotaxis has been observed in

a number of species in nature, such as *Spiroplasma* and *Leptospira* which have been found to navigate positive viscosity gradients to areas of higher viscosities, where their swimming is improved [161].

2.4 Swimming in complex fluids

Various research has been undertaken to quantify the effects of fluid shear thinning rheology and elasticity on various species of microorganisms and other forms of microswimmers. Experimental tests have been carried out on natural and swimmers, and macro scale-up models [6,24,27,31,162,163]. Furthermore, theoretical and mathematical models have been presented to gain insight into these complex effects [164–168]. Despite the recent ongoing interest into the effects of complex fluids on microscopic swimming, many questions are still present.

When conducting experimental investigations into the swimming kinematics of microswimmers, the majority of work focusses on live organisms, with a few using artificial apparatus. Experiments with live microorganisms can introduce a range of challenges due to their unpredictability and scale, but can produce results of the utmost relevance. Conventional methods involve microscopy of the microorganism's body, tracking its movement. Recent advances include obtaining time-resolved images of the flagella using high-speed cameras [24, 31, 169, 170] as well as tracking the swimmer in three dimensions [171].

Analysing of artificial microswimmers in complex fluids reduces some of the uncertainties and challenges that come with natural swimmers. However, due to challenges producing an artificial microswimmers to scale, very few works concerning artificial microscopic swimmers at a very small length scales are present. To overcome this, often scale-up models are used. To approximate dynamic similarity, highly viscous fluids are used to reducing the Reynolds number to values similar to those experienced by small scale microorganisms. Such experiments have been particularity useful in the understanding of helical flagella [162, 163], travelling waves along long elastic tails [172, 173] and helping

with the production of artificial microswimmers.

2.4.1 Effective shear rates

To compare the response of swimmers in complex fluids to Newtonian solutions, an effective shear rate is often defined from characteristic dimensions and velocities of that particular swimmer. This then gives an effective viscosity that can be compared across Newtonian and non-Newtonian solutions. Across the literature, the general accepted method to define an effective shear rate is to characterise the shear produced by the body and that produced by the characteristic propulsion method (such as the algae flagella or body wave of *C. elegans*) and take an average between the two. Calculating a shear rate for the body is generally straight forward due to the simple body shape, often with evidence being found for similarly shaped objects such as a falling sphere [174, 175]. However, an estimation for the appendage shear rate can often be more challenging as these features have more complex trajectories and shapes. Some methods of this effective shear rate calculation for different works follows:

- For *C. reinhardtii* [24], the body shear rate has been defined as a ratio of the average velocity of the body and the body diameter, $\dot{\gamma}_B = |V_{loc}|/2r_B \sim 15\,\mathrm{s}^{-1}$ where V_{loc} is the average velocity through both the power and recovery stroke and r_B is the cell radius. The characteristic beat shear rate was defined as the beating frequency, which for *C. reinhardtii* in its medium is $f_{BF} \approx 50\,\mathrm{Hz}$. The average of the two was taken to give an effective shear rate of $32.5\,\mathrm{s}^{-1}$ in the medium [24].

- For *C. elegans* [6] the body shear rate has been defined as $\dot{\gamma}_B = V_{loc}/l_B \sim 0.35\,\mathrm{s}^{-1}$ where V_{loc} is the forward velocity and l_B the length of the body. *C. elegans* move by producing a travelling wave and thus the appendage shear rate was defined as $\dot{\gamma}_{appendage} = (2f_{BF}A_w)/r_B \sim 15\,\mathrm{s}^{-1}$ where f_{BF} is the beating frequency, A_w amplitude of the beat and r_B is the diameter of the body. Again, the average of the two

characteristic shear rates was taken and gave an approximate average effective shear rate of $7.7\,\mathrm{s}^{-1}$ [6].

- For a macro scale-up experiment using a spinning helical coil [163], the translation and rotational shear rates of the head were estimated from, $\dot{\gamma}_{trans} = V_{loc}/2r_B$ and $\dot{\gamma}_{rot} = \omega_{BF}$ respectively. At the tail in rotation, the shear rates altered to become $\dot{\gamma}_{rot} = \omega_{BF}2r_B/l_B$. A novelty in this type of experimental process was that the frequency of the swimmer could be mechanically controlled, giving a frequency based comparison, independent of the effective viscosity.

Assigning a characteristic shear rate is a challenging topic that is often overlooked by cases in the literature. The outcome of a characteristic shear can be pivotal to the overall findings of an experimental work and can change significantly the findings of the work, especially if trying to understand whether a swimmer is more or less effective in a fluid that displays shear thinning properties, as often is the case [6, 24].

2.4.2 Swimming in shear thinning fluids

Experimental observations focussing on purely shear thinning fluids (i.e. with no elasticity) are arguable less frequent than in viscoelastic fluids. However, from the few experimental studies, a contradictory picture is present in terms of the effects on different swimmers.

For *C. elegans* [6, 170], through experimental observations, it was found that there were no significant differences between the velocities and observed kinematics between the control (Newtonian) and shear thinning solutions. Despite this, when the flow fields were examined, substantial differences were found for the two fluids. Structural differences were observed in the dominant body vortex at the head and tail of the organism. The shear thinning properties lead to an increase in circulation in these areas as well as decreasing the average fluid velocity at the head and increasing it near the tail. However, when immersed in a shear thinning colloidal suspension, the average velocity of the swimmer increased compared to that in the comparable Newtonian solutions [176]. It was postulated that at

the fast moving head, the swimmer was feeling close to the solvent viscosity, meaning that the swimmer was effectively moving in a fluid akin to water.

Further, *E. coli* have been shown to swim faster in a shear thinning viscoelastic solution [27, 177] than in corresponding Newtonian fluids. These works aimed at separating the effects of the two rheological properties and while they faced challenges in this they attributed the majority of the bacteria speed up to the shear thinning properties of the fluid. A two viscosity model was suggested, with the head feeling higher viscosities compared to the flagellum, which experienced relatively lower viscosities. Further, it has been discussed that the bacterium flagella simply passed by the polymers, not influencing their stretching profiles and thus feeling a viscosity akin to the solvent viscosity [27].

For a Mechanical helix immersed in a highly viscous fluids, it displayed an increase in velocity by a factor of up to 50% in the shear thinning cases, with the largest increase observed in a fluid with a power-law index of 0.6 [163]. It was argued that the speed increase was due, not to changes in viscosity between the head and tail of the swimmer, but due to confinement-like effects as a result of viscosity stratification around the swimmer.

Theoretical models of the effects of shear thinning fluids have mainly focused on small amplitude models. Under the effects of varying viscosities dependent on shear rate, work has sought to understand the influence on different body types and compositions [17]. Variations of Taylor's swimming sheet and the squirmer model have all been analysed and as with the experimental results, a varied picture is observed. Analysis of a waving sheet under a pseudoplastic fluid have shown it is possible to either enhance or hinder the propulsion velocity of the sheet by varying the sheet's kinematics [164–166]. This is also true in the squirmer model, which has shown the velocity in relation to Newtonian cases is heavily dependent on the surface actuation [178].

2.4.3 Swimming in viscoelastic fluids

The effects of viscoelasticity on microscopic swimmers is a further fluid property that has been widely examined. It should be noted that many fluids in the works analysed also have shear thinning properties and while the work primarily focuses on viscoelasticity, often a shear thinning response can also be present.

The run and tumble motion of *E. coli* has been examined in detail under the effects of complex fluids in the medium, with a marked change in the swimming dynamics reported [25,27]. It has been found that polymer solutions induced changes to the swimming patterns compared to the Newtonian cases. The polymer solutions reduced the tumbles in the stroke, enhancing linearity of the swimming paths. The cells "wobble", the oscillatory change in the organism's direction, was also found to reduce with increased in complex solution concentration. Furthermore, *E. coli's* velocity was found to increase with increasing polymer concentrations despite the increase in viscosity (roughly $10\,\mu m\,s^{-1}$ to $25\,\mu m\,s^{-1}$). Through further analysis, it was shown that suppression of the tumbling was primarily as a result of the fluid viscosity while the enhancement in swimming speed was mainly due to fluid elasticity [25, 30, 177].

For *C. elegans*, varying the types of viscoelastic fluids has yielded different velocity responses [31]. When a comparison was drawn between Newtonian swimming and that in a viscoelastic fluid Carboxymethyl cellulose (CMC), velocities were almost identical up to a defined viscosity, where after the velocities started to diverge and reduced by up to 35% in the viscoelastic case compared to Newtonian. Xanthan gum was used as a shear thinning control to eliminate the possibility of shear thinning properties impacting the swimmer's response and ensure it was purely viscoelastic effects being examined [31]. Upon analysis of the swimmer's bending wave speeds, it was found that the wave speeds were essentially identical for both viscoelastic and Newtonian cases. One possible explanation posed by the researchers was related to the extensional viscosity of viscoelastic fluids. When the streamlines around the organism's body were examined, they showed a distinct hyperbolic

point close to the body, at this point the flow was purely extensional and therefore generated elastic viscous stresses that were of greater order than Newtonian viscous stresses. Thus, the hypothesis was that the reduction in swimming speeds was primarily down to the sudden increase in elastic stresses in regions of high-velocity gradients, such as hyperbolic points [31].

Following on, differences in polymer molecular weights were examined, with the transition between the semi-dilute and concentrated region analysed [26]. When the motility of the organisms was examined, a surprising result was observed, in the semi-dilute solution the swimming velocities were relatively constant, reducing slightly with an increase in viscosity. Unexpectedly, above the critical concentration, swimming velocities increased by up to 65% despite the increased viscosity. As the concentration was further increased, the swimming velocity ultimately diminished due to the organism's finite power output. It was argued that the kinematics of the swimming motion induced a structural anisotropy which then led to an increase in the effective resistance coefficients C_N/C_T (where C_N and C_T are the normal and tangential resistance coefficients) compared to the semi-dilute case, leading to the enhancement in velocity [26]. Further work argued the an apparent slip in the polymers close to the swimmer caused the velocity increase [179].

For *C. reinhardtii*, a clear separation in swimming dynamics between Newtonian viscous and viscoelastic solutions has been seen [24], with the viscoelastic case showing reduced swimming velocities compared to that in viscous fluids of similar viscosities (when compared using an effective viscosity). In the Newtonian case, when the viscosity was increased, the beat slowed down as would be expected, but the stroke pattern did not change. However, in the viscoelastic case, the stroke pattern experienced a significant alteration, and the beat frequency was found to be much higher than in comparable viscous cases. This lead to an apparent variation in stroke velocities with the recovery stroke remaining remarkable unaffected by increasing solution concentration, thus decreasing the overall efficiency of the entire swimming stroke.

Numerical simulations of the gait taken from the experimental work interestingly

showed that the viscoelastic gait was more effective. Further, the elastic memory effect was found to enhance both the power and recovery stroke with larger stresses present in the tangential direction relative to the normal swimming direction [167]. However, this did not translate into a velocity enhancement compared to the Newtonian cases, which was attributed to the recovery stroke gaining a large enhancement in velocity over the power stroke and extensional thickening of the fluid by the tips of the flagella [168].

A helical screw in polymeric solutions has shown that at a $De = 1$ an enhancement of swimming velocities was found of $\times 1.15$ [162]. The solutions used were Boger fluids to reduce any influences from shear thinning or shear thickening effects. Either side of this De peak, the velocity ratio reduced down to unity at $De = 0$ and $De = 2$. These findings are similar to observations of a flexible filament in an Oldroyd-B fluid [180] and of a helical filament [181] again using the Oldroyd-B model.

Utilising a macroscopic version of Taylors swimming sheet, an approximate comparison with theoretical models has been drawn [182]. In the set-up, an elastic sheet was wrapped in a cylinder and by propagation of transverse waves around the cylinder the sheet "swam" in a circle. Once immersed in a Boger fluid, the sheet was found to swim quicker than the Newtonian counterpart, contrary to theoretical models of Tayors sheet [150]. However, the normal stress coefficients were seen to vary compared to that in the Oldroyd-B model used in the theoretical work, and further confinements of the system were suggested as possible explanations of the reported difference.

Janus particles, propelled by local concentration gradients, have also been used to assess the influence of fluid elastic properties [56]. It was found that in such fluids the rotational diffusion would increase by two orders of magnitude. An increase that could be described by the Weissenberg number and the subsequent relaxing of the fluid microstructure surrounding the particle.

To further quantify and interpret experimental results, many studies into analytical and theoretical analysis have been undertaken. Again, a varied picture is captured. For a finite waving sheet based on Taylor's model [76], an increased efficiency was found. This has also

been shown to be true for helical bodies [180,181]. On the other hand, for a small amplitude waving sheet and cylinder, fluid elasticity has been shown to hinder motility [150,183]. One metric that has been shown to be key in the viscoelastic fluid response is the body flexibility, which can have significant effects on the overall outcome [184].

2.4.4 Overview

The main question often asked in terms of complex fluids, is whether the addition of complex rheology will enhance or reduce the swimming velocity. Despite, the levels of work on the subject, the overall conclusions are varied with some studies finding an increase, some a decrease and others no changes whatsoever. This is also backed up with numerical results, which also show a range of result depending on the conditions. The main experimental results are presented in Table 2.1 with their respective findings. Overall, there is still a vast quantity of work to conduct before a complete picture of the effects of complex fluid on small length scale swimming is fully understood.

Table 2.1: Overview of experimental results of low-Reynolds number swimming in complex fluids. [1] Fluids also displayed shear thinning properties, [2] A velocity enhancement was also found but only in a singular solution.

Publication	**Type of fluid**	**Type of swimmer**	**Conclusion**
B. Qin (2014) [24]	Viscoelastic[1]	*C. reinhardtii*	Velocity reduction
X. Shen (2011) [31]	Viscoelastic[1]	*C. elegans*	Velocity reduction
D. Gagnon (2013) [26]	Viscoelastic[1]	*C. elegans*	Velocity enhancement
A. Patterson (2015) [25]	Viscoelastic[1]	*E. coli*	Velocity enhancement
V. Martinez (2014) [27]	Viscoelastic[1]	*E. coli*	No change [2]
B. Liu (2011) [162]	Viscoelastic	Mechanical helix	Velocity enhancement
J Gomez (2016) [56]	Viscoelastic[1]	Janus Particle	Velocity enhancement
M. Dasgupta (2013) [182]	Viscoelastic[1]	Angular sheet	Velocity enhancement
S. Gomez (2016) [163]	Shear thinning	Mechanical Helix	Velocity enhancement
D. Gagnon (2014) [6]	Shear thinning	*C. Elegans*	No change
J. Park (2016) [176]	Shear thinning	*C. Elegans*	Velocity enhancement

2.5 Interactions with walls

Microscopic swimmers often come into contact with walls and solid boundaries, either in their natural environment or in processes in which they are being utilised. An important example of wall interactions is bacteria entrapment near boundaries, which is vital in the production of biofilms, an architectural colony of microorganisms. Depending on type and situation, biofilms can be beneficial or harmful [39–41]. In industrial processes, the wall interactions of microorganisms in bioreactors can lead to reduced efficiencies if there is a build-up of organisms at the walls surface [43]. Another example of interactions with a domain boundary is that of spermatozoa coming into contact with the walls of the female oviduct on their passage towards egg fertilisation [36–38]. Furthermore, in the pursuit of microbots that can be placed within a blood vessel in the human body, the method of interaction with solid surfaces will be key to develop efficient swimmers to navigate these

systems [185]. The complex interactions between walls and swimmers can lead to variations in the efficiencies, and dynamics of these systems affecting cell motility greatly.

Specifically for *D. salina*, wall contact does not occur to a great extent in nature. However, the industrial use of *D. salina* in bioreactors relies heavily on transparent and clear walls to maintain efficiency and ensure the whole population receive sufficient light for growth. Therefore, it is desirable for this type of swimmer not to cluster at the walls surface in this application, and understanding such interaction may help in reducing such clustering.

The presence of walls can have a significant impact on organisms swimming kinematics, even at a distance away from the walls. Hydrodynamically, the velocity field around the swimmer is different from that in bulk to satisfy the introduction of the boundary. Furthermore, short range interactions are present close to the wall and can occur when part of the swimmer's flagellum or body is sufficiently close to the wall. As is the case with most microscopic interactions, the type of interaction and outcome with the boundary can vary widely depending on the swimmer type, type of contact, boundary morphology and other dynamics [44, 186].

As a body approaches a wall, it has been observed that the viscous drag will increase [77]. An increased drag might lead to the assumption of reduced swimming velocities by a boundary. However, as swimmers rely on drag based thrust, the effects can be more complex. When Taylor's sheet was analysed close to a boundary, depending on the wave form, the sheet was seen to move faster, slower or at the same pace as if the boundary was not present [77]. This reaction was due in part to the resistance coefficients (C_N/C_T) being affected in different ways. While both were generally increased due to the presence of the wall, the ratio between the two changed. For swimmers operating at a constant power, the presence of a boundary generally leads to a decrease in swimming velocities [43] which has been attributed to their inability to produce additional work to overcome the increase in viscous drag, with changes in normal and tangential forces not being sufficient to overcome increased viscous drag.

Short range interactions have also been shown to have great importance on the reorientation of the cell at the wall [45]. Generally, pushers and pullers are seen to react in distinct ways when short range interactions are present [44, 45, 187, 188]. However, the exact response depends greatly on the morphology of the swimmer, swimming method and wall shape.

For pusher cells, the dynamics close to the wall tend to orientate the swimmer to become attracted to the wall, and they tend to swim parallel to its surface. Of particular interest is *E. coli*, which once at a wall surface are seen to change their swimming motion from a straight trajectory to a trajectory of circular patterns. The presence of the boundary induces a torque on the bacteria, resulting in the circular motion around the wall [187–189].

For puller swimmers, surface interactions tend to induce rotation of the cell such that they bounce away from the wall [44, 45]. In *C. reinhardtii* in particular, it has been shown for flagellum contact to be critical in the scattering from a solid boundary, with hydrodynamic effects only playing a secondary role. The size and length of the flagellum have significant influence on the scattering angle and type of interaction. Furthermore, the longitudinal body rotation has been seen to aid in puller swimmers 'escaping' from a wall [186].

Chapter 3

Methodology

3.1 Chapter overview

In this chapter, the details of the experimental methodologies are discussed. The main purpose of the experiments were to visualise the algae such that their swimming dynamics could be recovered. Initially, the process of growing and storing the algae is detailed, specifically looking at the algae medium and storage hut. Next there is a section on the procedures used for the rheological characterisation of the medium, which is followed by a section on the microfluidic devices used as a platform to visualise the algae with the fabrication methods discussed. Finally, the experimental set-up is discussed with an overview of the image analysis processes adopted to analyse the captured images.

3.2 Growth of *Dunaliella salina* for experimental use

From the first in-depth studies of the Dunaliella geode carried out by Teodoresco [190] and Hamburgher [191] in 1905, the species has been used in wide-ranging scientific works [91]. It has been a valuable, adaptable species for experimental observations. From initially examining commercial uses and determining valuable pigments [11, 115, 119, 126, 192], to wastewater treatment [193], to defining osmoregulatory [194, 195], to ascertaining biofuel

potential [98, 131, 134], and as a model microscopic swimming organism [29, 43, 50] the Dunaliella geode has been used extensively in a laboratory setting. Key to the success of any laboratory-based work is maintaining the algae in an environment that provides the best conditions for growth. The primary basis when constructing these settings is to produce conditions as similar as possible to the environments the algae would often live in, providing a growth medium that mimics the fluids found in their normal habitat and a light source to mimic the sun. The following section describes the processes and methodology of the algae storage, growth, disposal and general upkeep required to maintain a healthy population.

The initial suspensions of algae were purchased from the Culture Collection of Algae and Protozoa (CCAP) [196]. From the initial base solution, the algae were left to grow and decanted into a new growth medium to stimulate future growth. The specific species purchased from CCAP was *Dunaliella Salina* 19/18, originally from hypersaline brines in Western Australia [197].

3.2.1 Growth medium

D. salina are a halophilic organism, and are known for their adaptability, with a foremost trait being their ability to balance osmotic pressure through the production of glycerol [98,194,195]. Therefore, it is feasible to cultivate them in a wide range of salty media with the caveat of different growth rates depending on the medium properties [198]. Examples of possible media that have been used to store and grow *D. salina* are Artificial Seawater Medium, F2 Medium, Hejazi and Wijffels modified medium and modified Johnson medium [29, 124, 199]. In this work, the Hejazi and Wijffels modified medium was used.

The purpose of a culture medium is to maintain normal function of the organisms suspended within. For the medium to achieve its function, the addition of certain chemicals is essential, each with its own specific function and benefit to the organism.

For *D. salina*, the medium should contain a source of inorganic carbon for the process of

cell photosynthesis, which can be achieved by adding a glucose or sodium bicarbonate [200]. Without the proper levels of carbon within the medium, the process of photosynthesis cannot occur or is heavily reduced, leading to limited energy production, consequently hindering normal cell functions [201]. It is possible for carbon to be replenished from the ambient air, but this process can be slow and unreliable within a laboratory environment.

Another key chemical for uptake by the algae is monophosphate, which is of vital importance in the formation of DNA, cell energy, and cell membranes [202]. Monophosphate can be introduced by the addition of a phosphorous source, with optimal phosphorous concentrations typically ranging between 0.02 and $0.025\,\mathrm{g\,l^{-1}}$ (as higher concentrations can lead to alga flocculation [203]). Further, nitrates, chlorides, sulphites, magnesium and calcium ions are also all-important additions to maintaining proper cell function [200, 204].

Trace element solutions (purchased from CCAP) is a combination of chemicals and minerals such as zinc, cobalt, copper, molybdenum and manganese that can be added to the medium. Although this addition is not necessarily key to organism's survival, it is a common addition if the medium is composed of technical grade salts, i.e. salts of lower purity than food grade salts or seawater [98].

The pH of the medium should also be controlled depending on the specific organism housed within, with a neutral to slightly alkaline pH often being the target [98].

3.2.1.1 The Hejazi and Wijffels modified medium

For the cultivation of *D. salina* in this work, the Hejazi and Wijffels modified medium (HWMM) was used to store and grow the algae [205]. A full description of the experimental protocol used to prepare the medium can be viewed in Appendix A. Table 3.1 summarises the main chemicals and minerals within the HWMM and their key function for normal algae growth.

Throughout the process, the utmost care was taken to avoid foreign bodies or other unwanted contaminates spoiling the medium. This was controlled by sterilising the medium,

Table 3.1: Chemicals and their function within the Hejazi and Wijffels modified culture medium.

Chemical composition	**Function**
Sodium Chloride [NaCI]	Provide halophilic environment and uptake of Chloride ions
Sodium Nitrate [$NaNO_3$]	Uptake of nitrate ions
Magnesium Sulphate Heptahydrate [$MgSO_4$ $7H_20$]	Uptake of Magnesium and Sulphate ions
Potassium Chloride [KCI]	Uptake of Chloride ions
Calcium Chloride Dihydrate [$CaCI_2$ $2H_2O$]	Uptake of Chloride ions
Sodium Bicarbonate [$NaHCO_3$]	Inorganic carbon source
Tris-base [THAM]	Controls pH and provides nutrients [206]
Trace elements solution	Uptake of iron, zinc cobalt, copper, molybdenum and magnesium
Boric acid [$H3BO_3$]	Maintain normal cell function [207]
Hydrochloric acid [HCI]	Maintain pH in medium
Monosodium Phosphate [$NaHPO_4$]	Reduce precipitation issues

and all relevant materials before and after use by autoclaving at 121 °C for 30 minutes. Once completed, the medium was stored in a fridge and disposed of after $\sim$ 6 months to avoid deterioration of its chemical properties.

3.2.2 Algae storage

When not in use, the algae were stored in a home-built algae hut, as seen in Figure 3.1. Approximately 50 mL of the algae/medium algae was stored in Pyrex conical flasks without any form of mixing as *D. salina* are very good swimmers and do not tend to clump, cluster or form chains [50]. To avoid foreign contamination and unwanted substances, the flasks were sealed with cotton wool and tin foil. This allowed the transfer of gasses through the seal to account for atmospheric changes from photosynthesis, but provided a barrier for

larger containments.

Figure 3.1: Wooden algae hut used to store and grow algae suspensions. The design was such to reduce the influence of light from sources other than the growth lamps.

To provide a replacement for the natural light source of the sun, two 55 W white florescence light bulbs were placed next to the algae hut. To control the intensity of the light source the distance from the suspensions was adjusted to meet the required level (between $1600 - 2000$ lux [2]) and the surrounding algae hut blocked any unwanted light pollution. The correct light intensity can have wide-ranging effects on the swimmers, too little and the algae cannot produce enough energy, and too high an intensity can stress the algae causing them to cluster and other unwanted behaviours [208, 209]. To mimic the day/night cycle of the sun, the lights were set to a 12-hour light/dark cycle. The cultures were maintained at room temperature.

Dunaliella salina are a relatively inert organism and pose very little danger to human health. They are categorised as a Generally Recognised as Safe (GRAS) organism and therefore, working with the algae required few additional safety measures in this regard in addition to standard experimental good practice [210, 211].

3.2.3 Algae upkeep

The growth of the algae is limited by resources within the medium and therefore required periodical replenishment. To ensure continual growth in the suspensions and to reduce the number of dead cells, the suspensions were replenished on a bi-weekly basis. Replenishment involved adding a small (5 mL) volume of a 4-week-old suspension to 50 mL of the fresh medium inside a new conical flask. To avoid contaminates the flasks were cleaned and autoclaved before the process was carried out. The full experimental procedure is discussed in detail in Appendix B.

Algae used in the experimental work were taken from suspensions in between weeks 2 and 4 of their growth. This had three main benefits: firstly, the "ages" of the algae remained fairly constant and gave a good spread of the algae population, secondly, the concentration of the suspensions was reasonably uniform, reducing complex alga-alga interactions expected in highly concentrated suspensions and finally, it reduced the number of unwanted dead cells in the system.

Disposal of the algae and growth medium was carried out by the in-house waste disposal services within the university. As the algae are classified as GRAS no specific disposal measures had to be taken in this regard. However, due to the chemicals within the medium and organic materials, the suspensions had to be disposed of according to the appropriate safety procedures. To ensure the algae were dead before disposal, they were placed in a dark cupboard for 2 months after use. Further, the suspensions were autoclaved before being handed over to chemical waste services.

3.3 Rheology of modified media

3.3.1 Rheology fundamentals

In this work, defining the rheological properties of the fluids the algae were immersed in was key in ascertaining the swimming response to individual fluid dynamics. The principles

of both shear and extensional rheology were drawn upon. A brief description of these rheological fundamentals follow, preceded by a detailed description of the experimental approaches.

3.3.1.1 Shear rheology

Shear rheology works under the principle (in the simplest terms) of the relationship between force and deformation. With the addition of the conformation of the fluid, the relationship develops to the relation between stress and strain. Stress, the tensile force per unit area acting on the cross-sectional area of a material. Strain, the tensile deformation of the specimen which can be thought of as the fractional change in length.

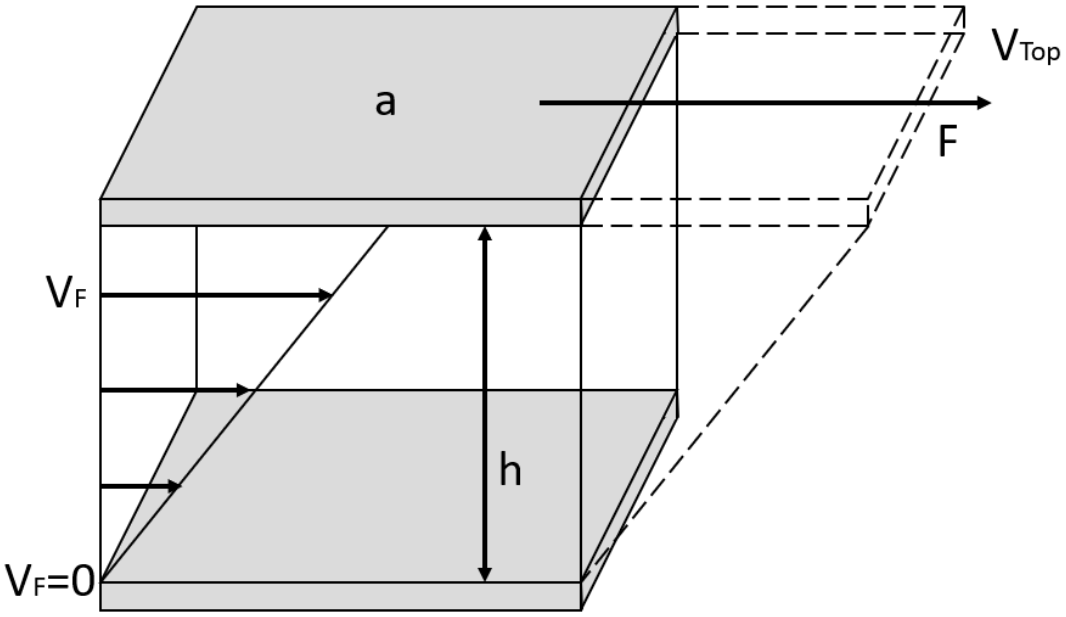

Figure 3.2: Schematic of simple shear flow with stationary bottom plate and top plate moving at a constant velocity (V_{top}), assuming zero wall slip, the fluid in-between at a height h experiences a simple shearing flow.

For a fluid placed between two parallel plates, with a stationary bottom plate and top plate moving with a constant velocity as in Figure 3.2 [212] (often described as simple

shear), and assuming zero slip at the walls, the stress is defined as the force per area to maintain the constant velocity of the upper plate

$$\sigma_{yx} = \frac{F}{a} \tag{3.1}$$

where F is the force and a the area. σ_{yx} is the stress, with the subscript yx indicating the stress is a shear stress.

In terms of shear rate, for a fluid under simple shear as just descried will continually deform under the applied shear stress. Therefore, the shear rate is defined as the rate of change of velocity between two layers of fluids

$$\dot{\gamma} = \frac{V_F}{h} \tag{3.2}$$

where $\dot{\gamma}$ is the shear rate, V_F the velocity of the fluid and h the gap between the upper and lower plates.

For a rheometer with a certain gap (h) the velocity at the stationary plate can be assumed to conform to no slip conditions and thus $V_F = 0\,\mu\mathrm{m\,s^{-1}}$. As the velocity is linearly dependent on the position across the gap due to laminar steady shear, the shear rate is considered constant across the gap, and thus for the system described in Figure 3.2 can be described as $\dot{\gamma} = \frac{V_{top}}{h}$. Where V_{top} is the velocity of the top plate.

Equations 3.2 and 3.1 can be combined to generate the constitutive model for Newtonian fluids, the basis for all classical fluid mechanics [213, 214]

$$\sigma_{yx} = \eta \frac{dy}{dt} = \eta\dot{\gamma} \tag{3.3}$$

where η is the shear viscosity.

Viscosity, in its simplest term, is a measure of a fluid's resistance to flow. At a molecular level, changes in viscosity are as a result of interactions between different molecules within the fluid. The viscosity determines the energy required to move a fluid.

In the examples above, the case is related to a simple shear in a single plane. However, as materials respond differently to different types of stresses in 3 dimensions, tensor notation must be added [214–216]. Thus, the constitutive equation of an incompressible Newtonian fluid is as follows

$$\hat{\sigma} = \eta\hat{\dot{\gamma}} \tag{3.4}$$

where the $\hat{}$ accent notates a tensor.

To define the state of stresses within a material, a 3-dimensional stress tensor is used representing both the force and areas magnitude and direction. A graphical representation of the stress tensor can be viewed in Figure 3.3. With the subscripts referring to the face or plane and direction of the force respectively.

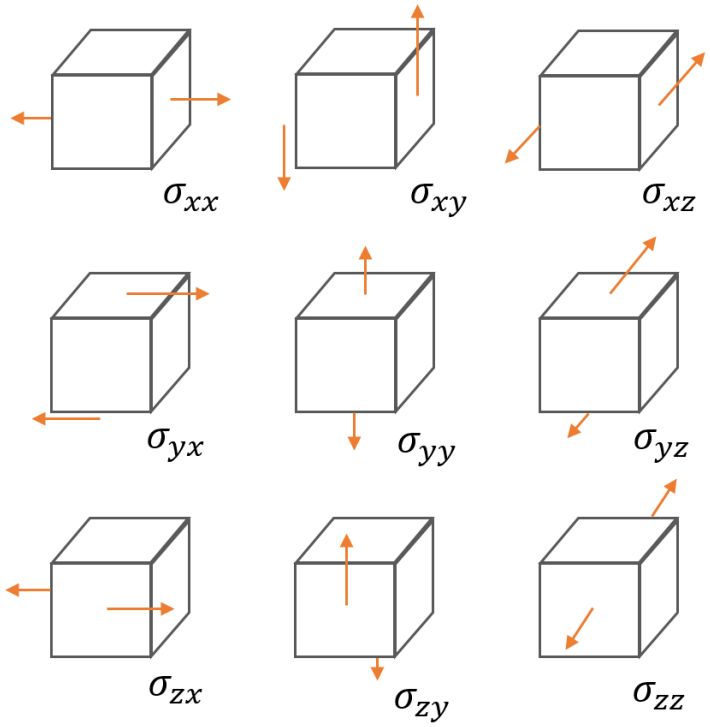

Figure 3.3: Directional stress acting on an infinitesimal cube. Image adapted with permissions from Macosko et al. [214].

$$\hat{\sigma} = \begin{bmatrix} \sigma_{xx} & \sigma_{xy} & \sigma_{xz} \\ \sigma_{yx} & \sigma_{yy} & \sigma_{yz} \\ \sigma_{zx} & \sigma_{zy} & \sigma_{zz} \end{bmatrix} \tag{3.5}$$

For a simple shearing fluid, Figure 3.2 shows a stress in the x plane relating to a stress in the yx component of the tensor, generating a shear deformation. However, the pair of stresses are unbalanced, and a net torque is present in the system. To balance the torque, a second stress must be added in the xy component of the tensor with an equal magnitude. Thus, giving the stress tensor of a simple Newtonian fluid

$$\hat{\sigma} = \begin{bmatrix} 0 & \sigma_{xy} & 0 \\ \sigma_{yx} & 0 & 0 \\ 0 & 0 & 0 \end{bmatrix} \tag{3.6}$$

This is an acceptable representation of a Newtonian fluid. However, complex fluids such as viscoelastic fluids can generate normal stresses and therefore, the most common stress tensor for simple shear is

$$\hat{\sigma} = \begin{bmatrix} \sigma_{xx} & \sigma_{xy} & 0 \\ \sigma_{yx} & \sigma_{yy} & 0 \\ 0 & 0 & \sigma_{zz} \end{bmatrix} \tag{3.7}$$

where the normal forces are represented by the stress in the diagonal coordinates.

3.3.1.2 Rotational rheometers

To examine and define the shear rheological properties of fluids, different methods such as capillary and microfluidic rheometers can be used. However, the most common type of rheometer used to perform these measurements are rotational rheometers which use different geometries to rotate the fluid and read its response. Common geometries include, parallel plates, cone and plate, concentric cylinders or vane geometries [214]. In this

work, two geometries were utilised, the parallel plates and the cone and plate. For these geometries, the fluid is placed between two plates and depending on the rheometer type one or both of the plates will impose a deformation or stress to the fluid, reading the opposing value (stress or deformation) to define the fluid's properties. Thus, the two types of rotational rheometers are named stress or strain controlled.

Stress controlled rheometers combine an actuator and transducer on the same shaft, imposing a defined stress onto the sample and reading the changes in deformation. On the other hand, a strain-controlled rheometer will have the motor and transducer on separate shafts, imposing a defined strain and measuring the normal force of the fluid [213]. The main differences between the two types of rheometers are seen in Table 3.2 with a schematic diagram in Figure 3.4.

Table 3.2: Primary differences in stress and strain controlled rheometers. [3] Temperature control often difficult due to multiple rotating shafts

	Controlled stress Rheometer	**Controlled strain Rheometer**
Design	Actuator and transducer on single shaft	Actuator and transducer on separate shafts
Sample influence	Affects motor control	No influence on motor control
Limitation	Friction and Inertia	Transducer range and sensitivity
Short time response	Limited	Relatively good
Normal Stress measurement	Limited	Relatively accurate
Cost	Relatively less expensive	Relatively more expensive
Temperature control	Relatively easy	Difficult[3]

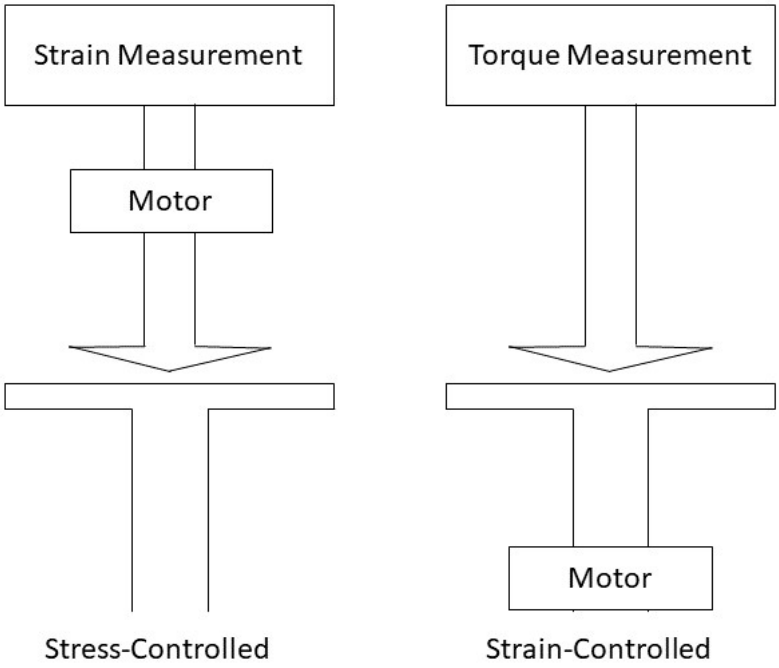

Figure 3.4: Schematic diagram of stress-controlled and strain-controlled rheometers. Stress-controlled consists of a transducer and actuator on a single shaft, while in strain-controlled, these are separate.

3.3.1.3 Extensional rheology

An extensional flow is defined as a fluid that is stretched or squeezed. Pure extensional flow is shear free flow with zero terms in the off-diagonal components of the stress tensor i.e. with stresses acting only in the perpendicular direction (also called the normal stresses). There are three types of pure extensional flow, uniaxial elongation, planar elongation and biaxial extensional flow as seen in Figure 3.5 [214].

Primarily this work will focus on uniaxial elongation as it is the method used by the measuring apparatus. In simple uniaxial extension, the strain tensors are represented as follows

$$\dot{\gamma} = \begin{bmatrix} 2\dot{\varepsilon} & 0 & 0 \\ 0 & -\dot{\varepsilon} & 0 \\ 0 & 0 & -\dot{\varepsilon} \end{bmatrix} \tag{3.8}$$

where $\dot{\varepsilon}$ is the strain rate. Measuring the properties of elongational flow can be challenging due to the very rapid and large deformations within a fluid element. Different methods can be used to achieve and characterise extensional flow depending on the nature of fluid. Examples include an extensional viscosity fixture or filament stretching rheometers [217, 218]. However, both these systems require medium to high viscosity samples. In this work, the solutions were examined with a capillary break up extensional rheometer, a device that monitors the break-up dynamics of a fluid filament under the effects of capillary action. This technique gives information on the relaxation spectrum of the fluid, giving an associated relaxation time.

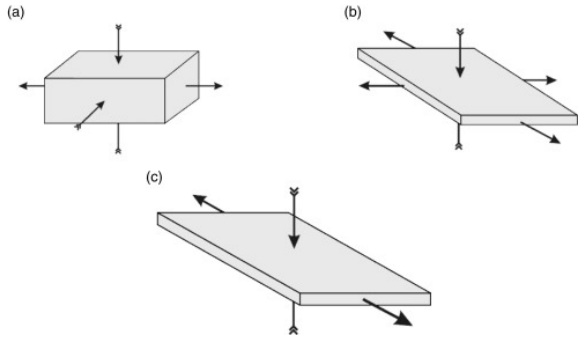

Figure 3.5: Schematic representation of the three different types of extensional flow: (a) Uniaxial, (b) biaxial and (c) planar elongation extensional flow (Equation 3.8 only valid for (a)) . Image reproduced with permissions from Ahmed et al. [219].

3.3.1.4 Complex rheology

Across the diverse complex fluid spectrum, there are many complex rheological phenomena with examples including: viscoelasticity, shear thinning, shear normal stress and extensional thickening. These phenomena are described as complex rheological properties, as

they exhibit time-dependent or non-linear features (Non-Newtonian).

Simple rheological fluids (Newtonian), such as water or air, are comprised of small molecules that do not easily deform or rotate and imposing a flow onto these fluids does not move the fluid away from an equilibrium configuration. At least not at measurable time scales. The complex fluid rheology shown by Non-Newtonian fluids arises from their complex molecular and microscale structure. These molecular structures can deform, rotate and break causing non-linearity and time-dependent responses. This work involved experiments with shear thinning (inelastic) fluids and viscoelastic fluids, in addition to Newtonian fluids at different viscosities.

3.3.1.4.1 Generalised Newtonian fluids Generalised Newtonian fluids show a shear rate dependent viscosity, a viscosity that varies depending on the imposed shear rate on the fluid [216]. Furthermore, generalised fluids show time independence in deformation, with the constitutive equation being written as

$$\sigma = \eta(\dot{\gamma})\dot{\gamma} \tag{3.9}$$

There are two different types of simple generalised fluids, shear thinning and shear thickening, depending on their response to an imposed stress. A fluid is described as shear thinning when its viscosity decreases with imposed shear stress, also known as pseudo-plastic. Many complex fluids show shear thinning properties such as polymer solutions with polymer chains lining up with the direction of an imposed flow, reducing viscosity. For shear thickening, the viscosity increases with imposed shear stress, also known as dilatants. Generally, this behaviour is found in suspensions. Common models for describing generalised Newtonian fluids are the power-law model and the Carreau-Yasuda model. Descriptions of these models can be found in Appendix C.

3.3.1.4.2 Viscoelastic fluids A fluid that is described as viscoelastic behaves both like a solid and viscous liquid. The definition of how "viscoelastic" a fluid is, is a measure

of how close to an elastic solid a fluid behaves [216, 220, 221]. An elastic solid behaves as if it has a perfect memory and through a deformation process will return to its original shape once the force is removed. Whereas Newtonian viscous fluids, have no memory and when any force is removed will retain their conditions at the time the force is removed. Therefore, a viscoelastic fluid cannot be described by a simple shear stress and shear rate relationship. For an incompressible elastic solid, the stress is proportional to the strain, whereas in a Newtonian fluid the stress is proportional to the strain rate. Therefore, for a simple viscoelastic fluid, the constitutive law must encompass both these principles. The time evolution is represented by a relaxation character of the fluid stresses.

3.3.2 Medium modifying agents

To alter the properties of the medium to be able to study the effect of specific rheological characteristics on the algae swimming behaviour, small quantities of various agents were dissolved within the medium to create solutions with the desired characteristics.

3.3.2.1 Ficoll PM400

Ficoll PM400 (Figure 3.6) is a high molecular weight ($Mw \sim 400\,000$) sucrose polymer and was used as a viscosifier, increasing the viscosity of the solution while keeping the solution Newtonian. The highly branched molecules and high content of hydroxyl groups makes it highly soluble in aqueous media (up to 50% w/w) [222].

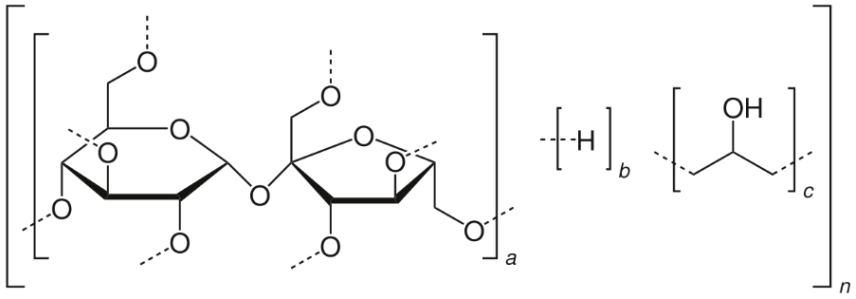

Figure 3.6: Ficoll chemical structure. Image reproduced with permissions from Sankaranarayanan et al. [223].

3.3.2.2 Glycerol

Glycerol (Figure 3.7), is a commonly used viscosifier. It forms a simple polyol compound and comes as a viscous liquid [126,224,225]. In this work, it was utilised only in a restricted number of experiments as an alternative to Ficoll PM400 (Appendix E).

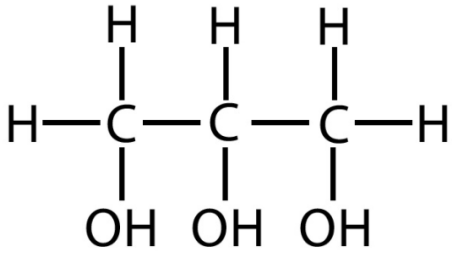

Figure 3.7: Glycerol chemical structure. Image reproduced with permissions from Lazar et al. [226].

3.3.2.3 Xanthan Gum

Xanthan Gum (XG) (Figure 3.8) is a long-chain heteropolysaccharide which once dissolved gives a solution of highly shear thinning properties. It possesses an insensitivity to salt, pH and temperature variations [227–229]. In the food industry, Xanthan gum is often used as a thickener as its high shear thinning properties are extremely useful for fluids contained in bottles or that must be held in place on food substances, but easily squeezed out or

swallowed e.g. ketchup and salad dressings [230, 231]. At low concentrations, Xanthan Gum shows no viscoelastic properties, which allows the effects of shear thinning on the swimmer to be analysed separately from the effects of viscoelasticity [6, 229, 232].

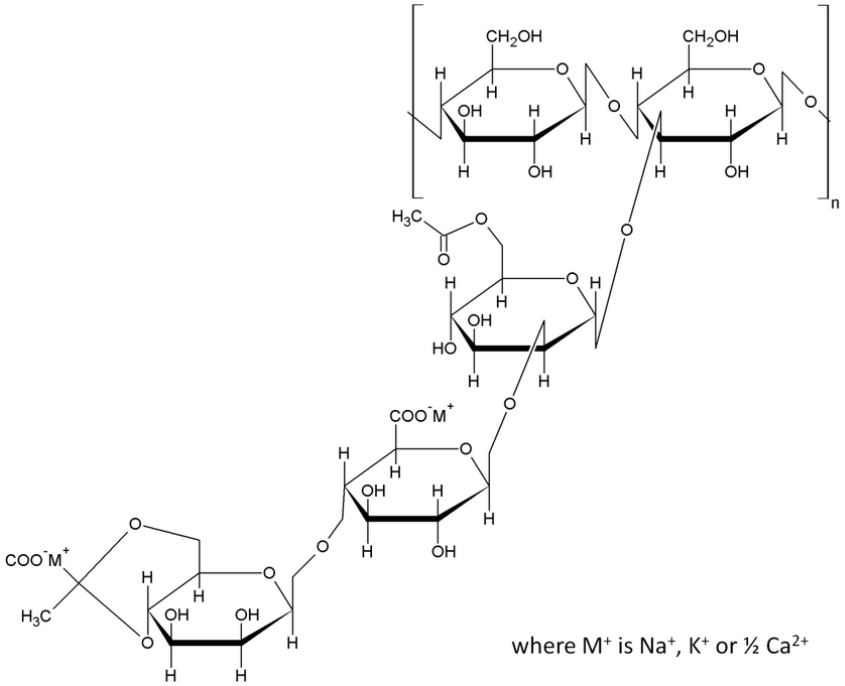

Figure 3.8: Xanthan Gum chemical structure. Image reproduced with permissions from Quinten et al. [233].

3.3.2.4 Polyacrylamide

Polyacrylamide (Poly(acrylamide/sodium acrylate) [70:30] PAA) was used to introduce viscoelastic properties for the swimmer to navigate in (Figure 3.9). Chemically, PAA is formed from a free radical polymerization reaction of the monomer acrylamide [234–236]. A high molecular weight polymer (18 million) was used to enhance the elastic properties of the medium. PAA is a granular medium that can be dissolved into water under mixing.

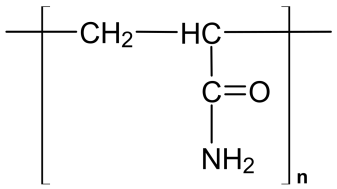

Figure 3.9: Polyacrylamide chemical structure. Image reproduced with permissions from Worsfold et al. [237].

3.3.2.5 Preparation of solutions with modifying agents

The preparation of the solutions involved dissolving the required agents within the medium through a simple magnetic mixing process. To avoid damage from the magnetic stirrer to the alga cells, the chemical agents were not added directly into the algae suspensions. Instead, a solution with the rheological agents added to the original medium (HWMM) without algae was created initially and then mixed with the algae suspensions. This solution was prepared using double the desired concentration of the modifying agent which was then added to the alga mixture at a ratio of 1 : 1 attaining the desired rheological properties without damaging the algae.

All concentrations were calculated in a weight by weight (w/w) percentage using an OHAUS analytical scale (OHAUS^{TM}). To ensure there was no substantial damage to the polymers and that all solutions were created under the same conditions, the solutions were mixed at low mixing speeds (75RPM) over an extended period of $\sim$ 24 hours [238, 239].

Mixing of the algae suspension and solution with added rheological agent was performed by rotating and/or inverting the fluid container periodically until the suspension was homogeneous. In addition, prior to each experiment, mixing by this method was carried out to mitigate any settling effects.

Fluids were stored in plastic containers in a fridge held at 5 °C. This was to reduce the effects of degradation from excess and changes in heat and light sources. Solutions over 2 months in age were disposed of and replaced to stop the effects of degradation altering the rheological properties [240]. Additionally, rheological characterisation of the solutions

were undertaken regularly before experiments to guarantee consistency across the fluids.

3.3.3 Experimental shear rheology

In this work, fluid characterisation under shear was conducted using the discovery hybrid rheometer 2 (DHR-2) produced by TA instruments, a stress-controlled rheometer. A schematic of the rheometer can be seen in Figure 3.10, with a description of the key components following:

- Drag-cup motor
  - A brushless motor and light cup on the driving shaft used to drive the shaft.
- Magnetic thrust bearing
  - Provides stiff "frictionless" axial support of the drive shaft.
- Radial Air bearings
  - Provides stiffness and support in the radial direction.
- Optical encoder
  - Determines the angular displacement and the velocity, i.e. shear, rate with high resolutions
- Normal force transducer
  - Highly sensitive load cell for normal force calculation

Figure 3.10: DHR-2 Rotational rheometer

3.3.3.1 Rheometer geometries

As mentioned, the two geometries used through this work were the parallel plate and cone and plate. Parallel plates geometries consist of two parallel plates, with one in rotation. Whereas the cone and plate geometry, as the name suggests, consists of a cone at a constant angle and one parallel plate. A schematic diagram of the two geometries can be seen in Figure 3.11. The advantage of the cone is it produces a constant shear across the diameter of the plate, which is not possible in a parallel plate, where a correction procedure must be applied to overcome the error. These plates come in a variety of diameters with the general convention of the larger the diameter, the better sensitivity due to the increased surface area. Depending on the of type of geometry, the calculations of the shear rate, shear stress and consequently the shear viscosity change as shown in Table 3.3, where the symbols definitions are ω is the angular velocity, Θ_{cp} is the angle between cone and plate, M is the torque and r is the radius of the plate. For the parallel plates, the correction factor is the bracketed terms in Table 3.3 [213]

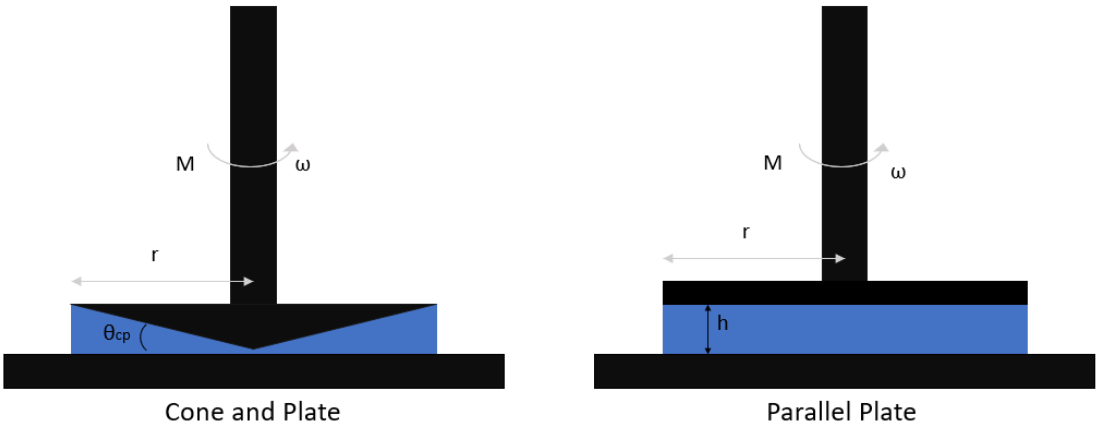

Figure 3.11: Schematic of cone and plate and parallel plate geometries with fluid sample in place. Labels denote relevant variables of importance for each.

Table 3.3: Defining variable equations for different plate types.

	Cone & Plate	**Parallel plate**
Shear stress	$\sigma = \frac{3M}{2\pi r^3}$	$\sigma = \frac{2M}{\pi r^3}(\frac{3}{4} + \frac{d\ln M}{4d\ln\dot{\gamma}r})$
Shear rate	$\dot{\gamma} = \frac{\omega}{\Theta_{cp}}$	$\dot{\gamma}_r = \frac{r\omega}{h}$
Shear viscosity	$\eta = \frac{3M\Theta_{cp}}{2\pi\omega r^3}$	$\eta = \frac{2M}{\dot{\gamma}_R}\pi R^3(\frac{3}{4} + \frac{d\ln M}{4d\ln\dot{\gamma}r})$

3.3.3.2 Rheometer limits

All rheometers have sensitivity limits, with manufacturers specifying a minimum and maximum torque value dependent on the machine's sensitivity and range. Upper limitations can also be related to the onset of inertial instabilities and sample loss. Shear rate limits can be calculated and depend on the minimum torque values given by instrument manufacturers, geometry type and radius and viscosity of the sample [28, 242]. For the cone and plate, the minimum measurable viscosity is defined as

$$\eta = \frac{3M_m}{2\pi\dot{\gamma}r^3} \tag{3.10}$$

and for the parallel plate as

$$\eta = \frac{2hM_m}{\pi\omega r^4} \tag{3.11}$$

where M_m is the minimum measurable torque of the rheometer, which for the DHR2 in steady shear was 5 nN m [241].

It is often conventional to consider the minimum calculations with a factor of uncertainty as experimental set-up, sample loading and rheometer deterioration (dust on encoder etc.) can add uncertainties [28].

The maximum measurable torque of the system used was defined as 200 mN m [241]. However, before reaching this limit it is likely that inertial instabilities will set in, in particular for low viscosity solutions used. The onset of inertial instabilities can be approximated

using the following equations for the two geometries used

$$\eta = \frac{\omega \Theta_{cp}^2 \rho r^2}{6} \tag{3.12}$$

for the cone and plate and

$$\eta = \frac{\omega \rho h^2}{6} \tag{3.13}$$

for parallel plate geometry. When reporting viscosity measurements both limits will be added to the graphs as can be seen in Figure 3.12 as an example.

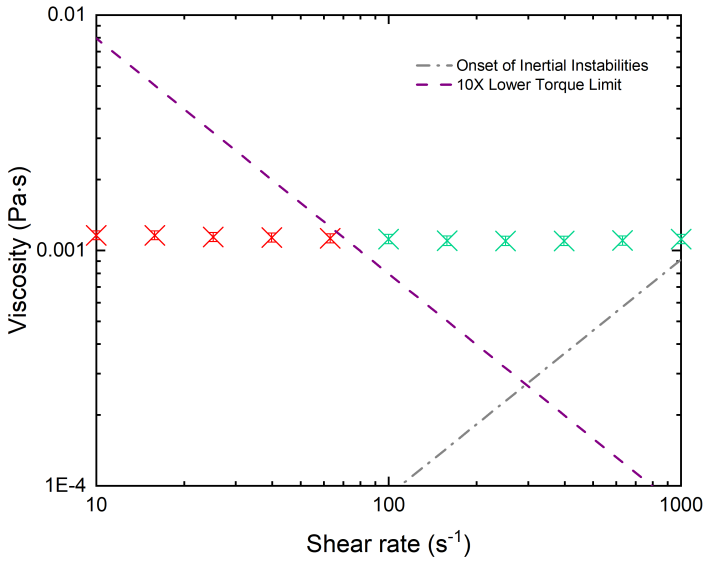

Figure 3.12: Example of rheometer limits displayed on shear viscosity graph. Lower limit is represented by the purple line and upper limit referring to the onset of inertial instabilities by the grey line. Red points show discarded data as it falls below the lower limit.

3.3.3.3 Experimental processes DHR-2

The steady shear viscosity dependence on the shear rate was measured for all fluids used in the work. The flow curves were obtained by imposing an incremental step of shear rate (controlled by stress) over time. The resultant deformation was then recorded and shear viscosity calculated. To accept the result at that specific step, a process called steady state sensing was used which ensured the fluid had reached steady state before a measurement was taken i.e. the result would have to remain within 5% of the previous measurement for 30 s for 3 consecutive iterations. The resultant measurements could then be plotted as a flow curve showing how the shear viscosity varied with shear rate as in Figure 3.12, for the Newtonian medium. The measurements of the medium properties were conducted using a 60 mm diameter cone and plate geometry with an angle of 1°. Given the size of the algae particles within the suspensions, a parallel plate geometry of diameter 40 mm was used with an appropriate gap separation (400 µm), for exploratory measurements with the algae suspensions. Three repeats of each fluid were carried out using a new sample each time, all tests were conducted at 20 °C, and a solvent trap was used to reduce the effects of evaporation.

The rheological uncertainty was defined as a combination of the percentage error across repeat experiments, an approximate rheometer reading error (1%) and a mixing uncertainty which was related to slight variation in weights from the desired quantities. (Rheology error (%) = repeat error (%) + rheometer uncertainty (1%)+mixing uncertainty (%)) Due to the sensitivity of the rheometer and analytical scales used for the weighing of solutions, the rheological error was relatively low.

3.3.4 Experimental extensional rheology

In this work, a capillary break up extensional rheometer (CaBER, HAAKE™) was used to characterise the viscoelastic fluid response under uniaxial extension. The CaBER consists of two smooth coaxial disks, a motor to provide fast axial step strain to the sample and a

laser to measure the diameter of the formed filament.

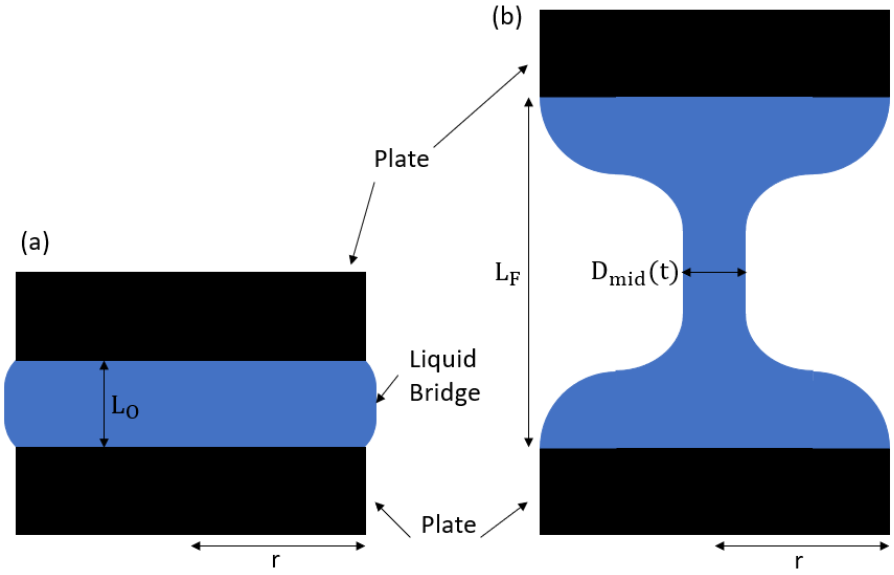

Figure 3.13: Representation of the CaBER with the plates in the initial position (a) and final position (b) showing a cylindrical filament in the central region typical of a viscoelastic fluid. The diameter of the filament over time is measured using a laser micrometre, from which the maximum relaxation time can be calculated.

The sample is placed between the two plates, forming a liquid bridge as shown in Figure 3.13 (a). The plates are subsequently separated over a short space of time to a prescribed distance (Figure 3.13 (b)) by the step strain motor. This forms an unstable hourglass shaped filament between plates in a viscoelastic fluid. This filament undergoes a self-driven uniaxial extensional flow in which the capillary forces are balanced by viscous and elastic tensile stresses [243]. A typical example of a filament thinning showing the different stages can be viewed in Figure 3.14.

In the relaxation process, the filament profile is assumed to remain spatially self-similar, and thus the dynamics can be characterised by measuring the time evolution of the mid-point diameter (D_{mid}) measured by a laser micrometer and from this the extensional strain rate can be calculated [243, 245]

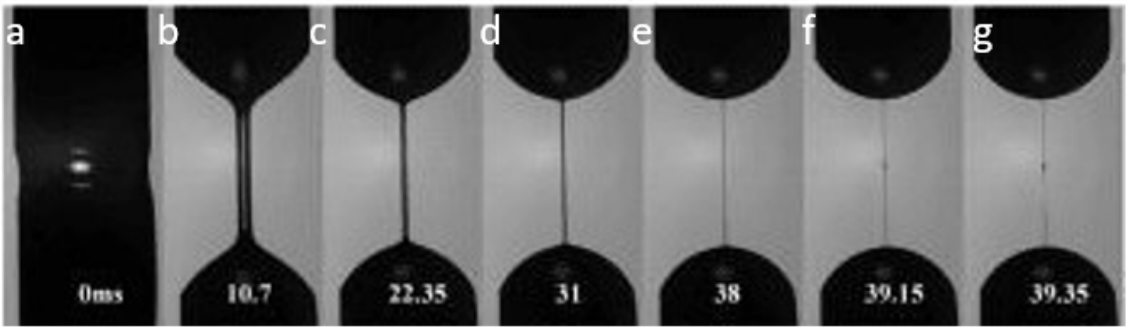

Figure 3.14: Schematic of the different stages of capillary break up: (a) plates in their initial position with liquid bridge (b-f) plates in final positions and capillary driven drainage (g) break up of filament. Image reproduced with permissions from Vadillo et al. [244].

$$\dot{\varepsilon} = -\frac{2}{D_{mid}(t)}\frac{dD_{mid}(t)}{dt} \tag{3.14}$$

Further, the Henckly strain (ε_H)

$$\varepsilon_H = \ln\frac{L_F}{L_O} \tag{3.15}$$

can be imposed by controlling the final (L_F) and original (L_O) separation between plates.

Combining the stress and strain, an apparent uniaxial extensional viscosity can be found

$$\eta_E = \frac{\sigma_{xx} - \sigma_{yy}}{\dot{\varepsilon}} \tag{3.16}$$

The ratio of the extensional viscosity to the shear viscosity is known as the Trouton ratio, Tr

$$Tr = \frac{\eta_E(\dot{\varepsilon})}{\eta_o(\dot{\gamma})} \tag{3.17}$$

For a Newtonian fluid, the Trouton ratio is constant and equal to 3 for axisymmetric flow i.e. the extensional viscosity is 3 times greater than shear viscosity, but for viscoelastic

fluids the extensional viscosity can be orders of magnitude greater than the shear viscosity. For a Newtonian fluid, the filament diameter decays linearly with time, while for a viscoelastic fluid it decreases with time exponentially [243]. A simple fit of the diameter evolution in the linear region of exponential thinning yields the material's maximum relaxation time λ [213, 245], corresponding to the longest relaxation for an ideal fluid.

$$D_{mid}(t) = D_o(\frac{GD_o}{\sigma})^{\frac{1}{3}} e^{\frac{-t}{3\lambda}} \tag{3.18}$$

To determine the maximum relaxation time of the polymer solutions discussed in this work, 6 mm plates were used with an initial gap between the plates of $L_O = 3$ mm. The final gap was varied depending on the solution used, but was typically approximately $L_F = 12$ mm. The resultant filament thinning was analysed, and a fitting process was undertaken over the linear viscoelastic region of $ln(\frac{D_{mid}}{D_o})$ vs time to define the relaxation time. Ten plus stretch profiles were examined in the CaBER for each fluid, using a new sample each time, and the average determined.

3.4 Microfluidic platforms

Within this work, to provide a controllable platform for the algae swimming and dynamics to be observed, microchannels made of polydimethylsiloxane (PDMS) were utilised. These channels with a width of $w \sim 400$ µm and depth of $\delta \sim 84$ µm allowed for a controlled environment to visualise the algae with protection from the influence of environmental factors. Furthermore, they allowed for the algae to be observed in the fluids with no additional agents such as surfactants needed for thin film devices. However, the use of such channels did present issues such as the presence of walls and 3D swimming. The channels were manufactured in-house with a procedure described in the following section.

Microfluidic devices can be controlled and modified to suit many diverse needs and fields, and have been extensively used in biophysics, fluid dynamics, medical works and

many more [246–248]. To create the microfluidic channels used throughout this work, photolithography [249,250] was used to produce the mould, and soft-lithography [251–253] was used to create the channels. This allowed for a relatively cheap, repeatable and accurate method of producing channels that could be manufactured in-house.

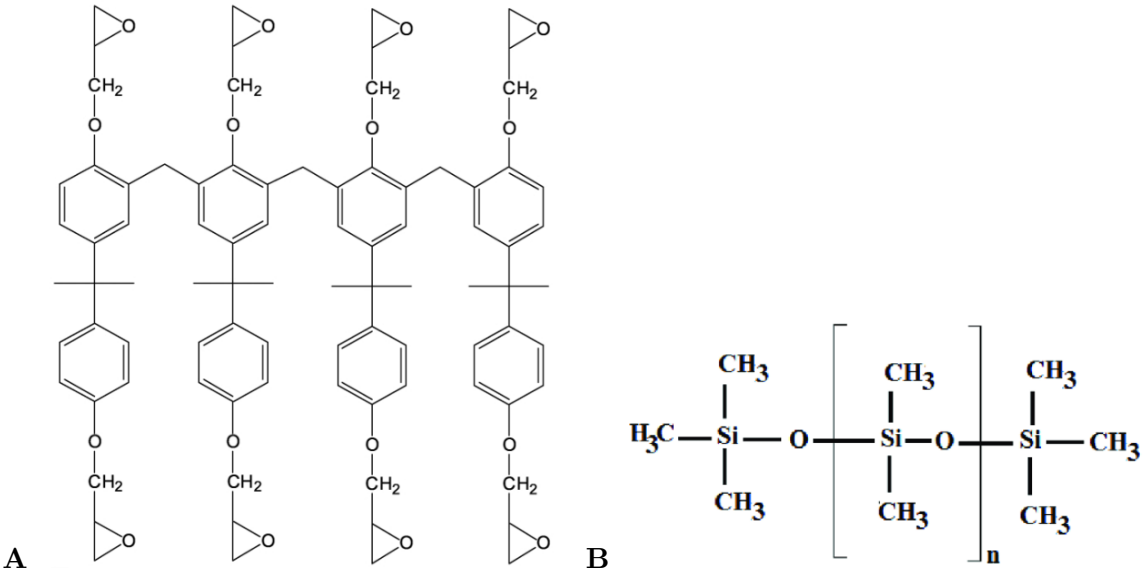

Figure 3.15: (A) SU8 [254] (B) PDMS [255] chemical structure.

The process of fabricating channels to be used in the experimental process followed a number of steps, which are described as follows:

1. Design of a geometry in CAD to be reproduced onto a physical mould
2. Produce a photo mask from CAD design
3. Use photo mask to produce SU8 epoxy resin mould using photolithography
4. Fabricate PDMS block with channels imprints from mould using soft-lithography
5. Make access ports and bond PDMS to glass slide to complete channels

Straight channels with a rectangular cross-section were used in all experiments carried out in this work. The channels were produced from a previously developed geometry, mask and mould and thus, these steps (1-3) were not required to be completed in this work. A brief description will still follow for reference [256, 257]. Steps 4-5 for the fabrication and bonding of the PDMS channels were carried out as needed for the experiments. The channels were fabricated in a clean environment with forced ventilation to reduce contaminates during the process.

3.4.1 Geometry design

The specifications of the particular geometries were designed on a conventional computer aided design program, for example AutoCAD (Autodesk). The design defines the transparent areas of the mask representing the channel dimensions and opaque sections defining the limits and the areas around the channels. The channel geometry should encompass an entrance and exit section where the fluid inlet and outlet can be punctured through the final PDMS block. A set of typical straight geometry designs with different widths can be viewed in Figure 3.16.

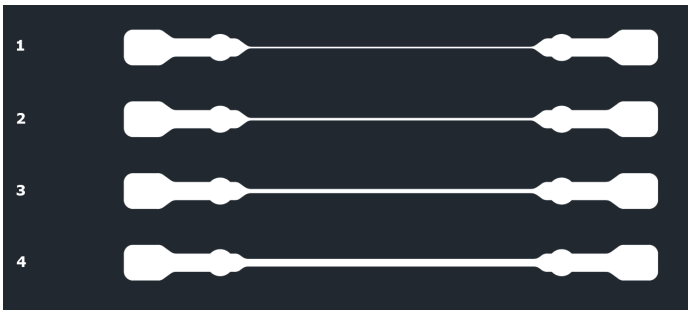

Figure 3.16: CAD drawing of a microfluidic mask showing geometries of microfluidic channels to be produced. The mask consists of 4 straight channels with varying widths, with sections for inlets and outlets to be punched.

Once the design has been completed, a chrome mask can be produced where the channel regions are left transparent. The mask used in this work was manufactured by an

outsourced company (Selba S.A. Switzerland) and can be viewed in Figure 3.17.

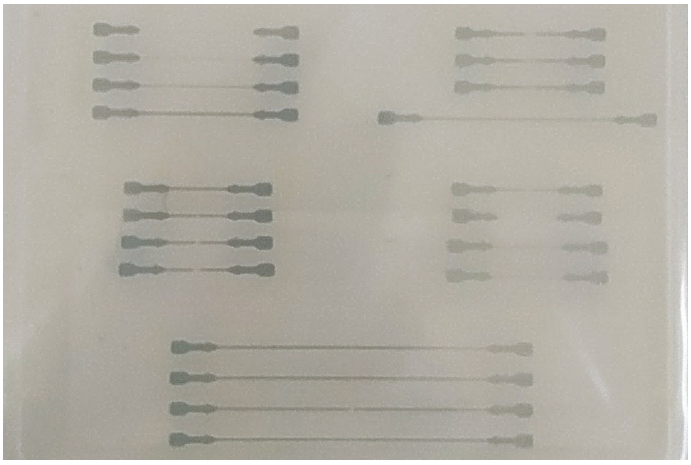

Figure 3.17: Transparent photo mask with various geometries. Straight geometries were used for research conducted in this work.

As with the mask, the production of the SU8 mould was outsourced and once completed, it was used multiple times to create the PDMS channels in house. As any defect in the mould will be reproduced in all following channels, this stage is highly critical. In very simplistic terms, the process commences with a silicon wafer spin-coated with a layer of SU-8 a negative photoresist [256, 257]. The depth of the layer of SU-8 relates to the eventual desired channel height. The mould with mask placed on top is exposed to a UV light source, allowing the regions of exposed SU-8 through the mask to cross-link and polymerise. The non-cured resin is then removed using a SU8 developer, leaving the portions of the exposed SU8 in the desired channel geometries. Further details with greater complexity of the process can be found here [257]. A simplified schematic diagram is displayed in Figure 3.18 (A) and mould used in this work in Figure 3.18 (B).

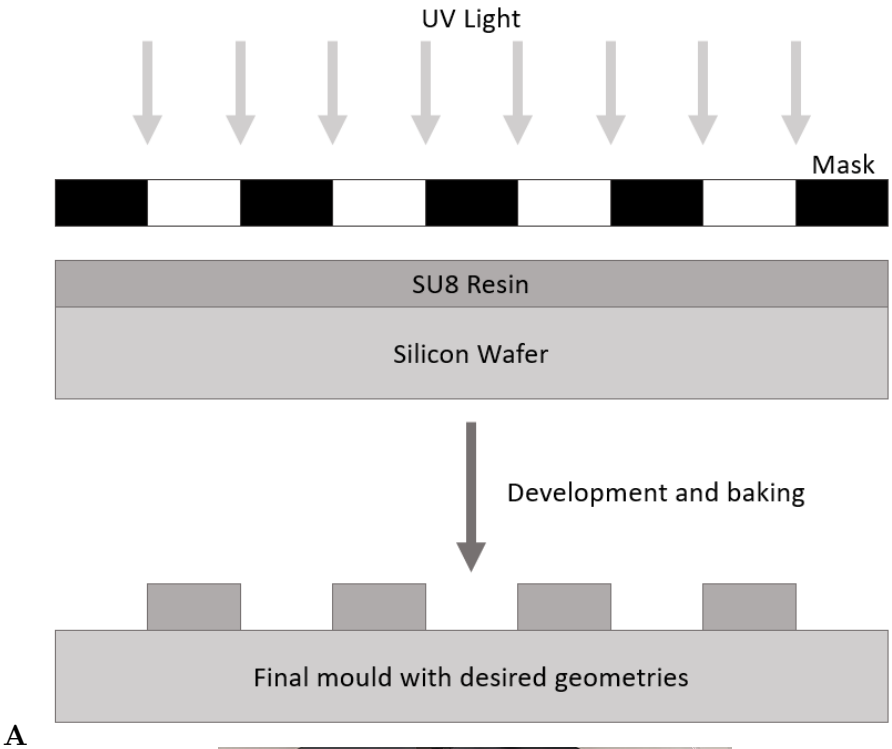

A

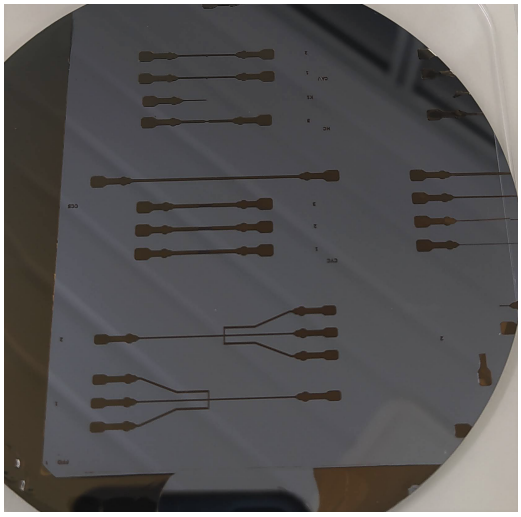

B

Figure 3.18: (A) Simplified schematic diagram of photo-lithography principle to fabricate SU8 mould showing UV exposure through mask polymerising exposed sections of SU8 and the final geometry (B) Final mould used to create the PDMS microchannel geometries.

3.4.2 PDMS microchannel fabrication

Soft-lithography was utilised to create the microfluidic channels by forming PDMS onto the mould, imprinting the channel dimensions. PDMS, arguably the most common material for microchannel manufacture, was preferred over others as it has many advantages. These include: its optical transparency over a large range of wavelengths, its permeability meaning gasses can be squeezed out of the channel, its relative low cost, its chemical inertness, and its biocompatibility [258].

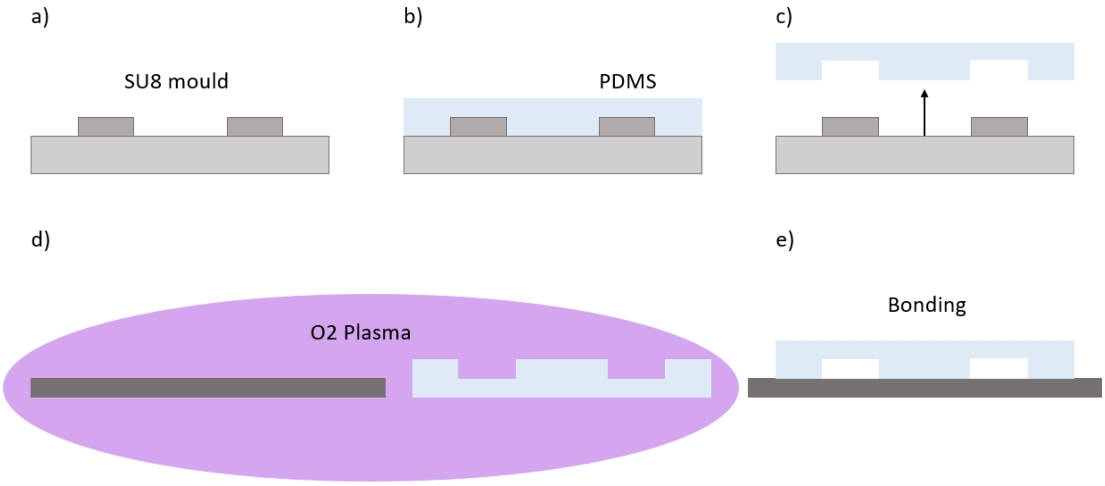

Figure 3.19: Steps involved in PDSM channel fabrication: (a) Mould preparation and cleaning (b) PDMS is poured onto mould (c) PDMS is removed from mould, leaving channels imprinted on thesurface (d) Oxygen Plasma (e) PDMS bonding to glass slide.

The process of PDMS channel fabrication from the SU-8 mould is discussed in detail below and shown schematically in Figure 3.19.

1. Preparation

   The preparation process consisted of the cleaning of both the mould (shown in Figure 3.19 (a)) and work bench surfaces to avoid any small particulates corrupting the integrity of the final device. The mould was washed using isopropanol and dried using compressed air, surfaces wiped with conventional surface cleaner and an aluminium

foil ring placed around the mould to contain the polymer. The mould was then covered and left in a clean petri dish.

2. Mixing

   The PDMS was mixed with a curing agent at a ratio of 9:1 using a mixer (THINKY ARE-250 CE) for a pre-determined period, 2000RPM for 5 minutes followed by a deaerating phase at 1600RPM for 1 minute. After mixing, the PDMS solution was poured into the mould (Figure 3.19 (b)).

3. Degassing

   The mould with PDMS was then degassed using a desiccator and vacuum pump to remove any air bubbles trapped within the PDMS mixture during the mixing or pouring process.

4. Curing

   The mixture was then cured in an oven for 30 minutes at a temperature of 80 °C.

5. PDMS block

   After the mould and PDMS layer had cooled down, the PDMS was removed from the mould (Figure 3.19 (c)), with the PDMS layer now having the features of the microchannels imprinted on its lower surface.

   In some instances, rather than removing the whole mould, a section of channel desired was cut from the PDMS, leaving a vacant space around the desired channel which could be used in future channel production. This was beneficial if only 1 geometry was needed from the whole mould, as it saved PDMS and reduced time.

   The detached section of PDMS with the desired geometries was cut into a rectangular shape to fit onto a glass slide and inlet and outlet holes punched using a mechanical puncher (Harris Uni-core 1 mm puncher). Care was taken to remove waste PDMS from the punching and through the whole process to maintain cleanliness within the microchannels.

6. Bonding

   Prior to the bonding process, the PDMS blocks were washed with isopropanol and dried with compressed air. Scotch tape was used to clean the surfaces and to cover while the bonding process was prepared. The same procedure was carried out with the glass slide the PDMS was to be bonded to.

   An issue that arises when using PDMS is its low adhesion to glass [259]. To provide a stronger bond, an oxygen plasma system was used to 'excite' both glass and PDMS. Oxygen plasma removes hydrocarbons from the materials surface. The resultant exposed silanol and hydroxyl groups left on the surface of the PDMS and glass respectively, once brought into contact with each other form a very strong Si-O-Si covalent bond [257].

   Before placing the PDMS and glass into the oxygen plasma chamber (Figure 3.19 (d)), the plasma system process was run with an empty chamber to remove impurities. The oxygen plasma process comprised of three alternate cycles of vacuum and oxygen inflow. This was followed by plasma generation at a stable chamber oxygen pressure of 0.2 mbar, The Plasma was present for a duration of 75 s at 50 W with a frequency of 40 kHz. Once the plasma process was finished, the glass slide and PDMS were brought together for the permanent bonding (Figure 3.19 (e)) and placed in the oven at 80 °C for 10 minutes to strengthen the bond and complete the procedure. Once cooled, the channels were ready to be used.

   The sealed channels were stored in covered Petri dishes with scotch tape covering the inlet and outlet holes. Channels were replaced and fabricated as needed, as particulates would build up within the channel through continual use.

3.4.3 Channel properties

The channels used in this work were ~ 3 cm long with a rectangular cross-section of width $w \sim 400$ µm and depth $\delta \sim 84$ µm, giving an aspect ratio of 4.76. Examples of a PDMS

chip and the channel cross-section with dimensions are displayed in Figure 3.20 (A) and (B) respectively. Due to slight irregularities in the mould, the channel did not represent a true rectangular cross-section with slight deviations seen in the corners. These sections were not considered in the analysis of the results and thus should not have a significant bias on the results.

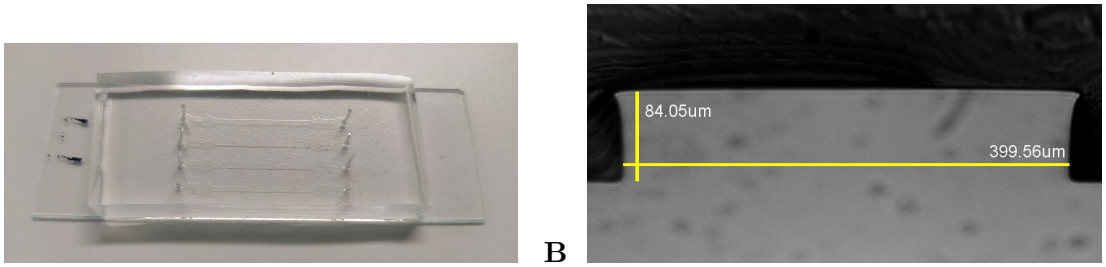

Figure 3.20: (A) Final produced PDMS channel consisting of four straight geometries. Inlets and outlets are present at the start and end of the channel. (B) Cross-section of channel with width and height annotated.

3.5 Experimental set-up

The generic experimental set-up is described below. It primarily describes the set-up used to determine the swimming velocity of the algae, but the set-up is very similar in all experimental cases with the necessary changes in camera and objectives discussed in Section 3.6.3. An overview of the system is shown in Figure 3.21 with the main components as follows:

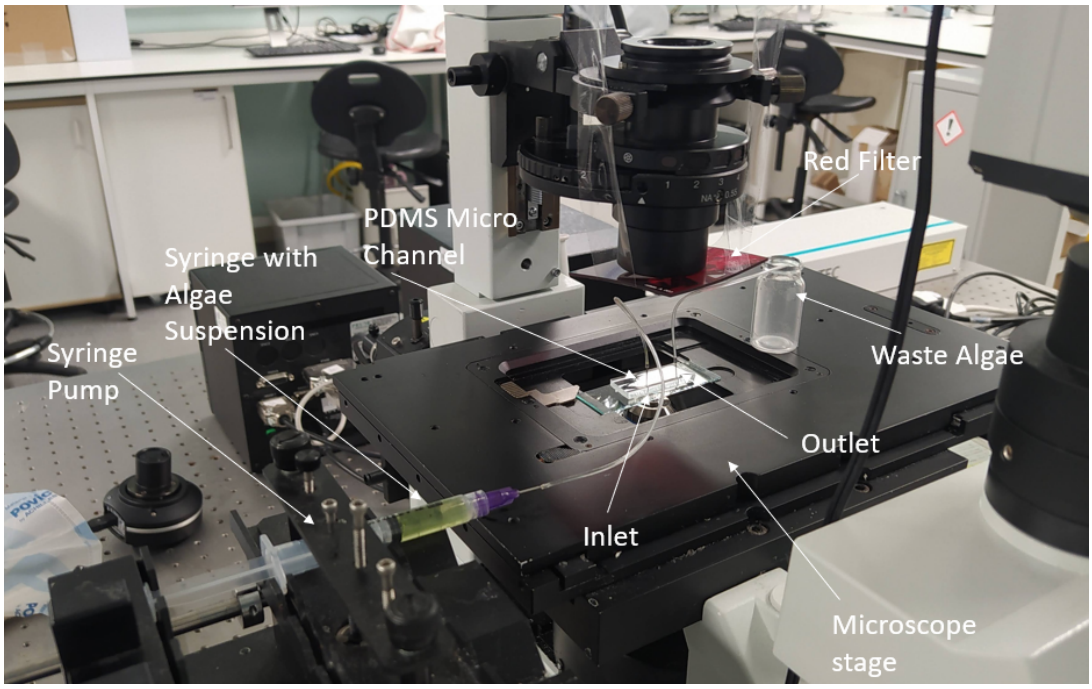

Figure 3.21: Standard experimental set-up of the experimental apparatus with labels denoting major components.

- Microscope stage and imaging system used to visualise specific section of the channel.
- Syringe pump used for injection of the alga cells at a controlled rate.
- PDMS channel used as a visualisation platform to monitor the algae swimming behaviour.
- Channel tubing used to transfer the algae from the syringe to the channel and from channel to the waste container.
- Waste container to collect the algae after experimental use.
- Red filter to reduce phototaxis movement of the algae.

3.5.1 Imaging system

In this work, an Olympus IX71 inverted microscope (Olympus-Global) was used to visualise the swimmers in the microchannel. Using brightfield microscopy, the algae motion could be easily visualised with videos captured to characterise their swimming behaviour. The videos were then post-processed to extract the relevant data, as discussed in Section 3.6. Different cameras, processes and systems were used to fulfil different requirements of each swimming characteristic examined.

Brightfield microscopy is one of the most elementary methods for observing dark microscopic specimens. It works by passing light through a condenser, through the specimen (in the case here the swimming algae), through an objective magnifying the light and finally to an ocular lens or camera. As the light passes through the specimen, it is absorbed by the dense areas of the sample creating a contrast that allows an image of the sample to be viewed [260, 261]. The path the light travels through the system can be viewed in Figure 3.22.

As mentioned, *D. salina* are phototactic, meaning they sense and swim towards light stimuli (Section 1.4.1.2.1). *D. salina* only sense certain wavelengths of light ($\sim 400 - 550\,\text{nm}$) [29, 262, 263] and are not influenced by wavelengths corresponding to red light. Therefore, to reduce this stimulus during experiments, a red filter was placed over the microscopic light and all external lights within the room were switched off. The filter blocked other wavelengths of light, so the algae were only illuminated by that of a wavelength of approximately $\lambda_r = 600\,\text{nm}$, allowing for enough light for visualisation without introducing phototactic biased swimming.

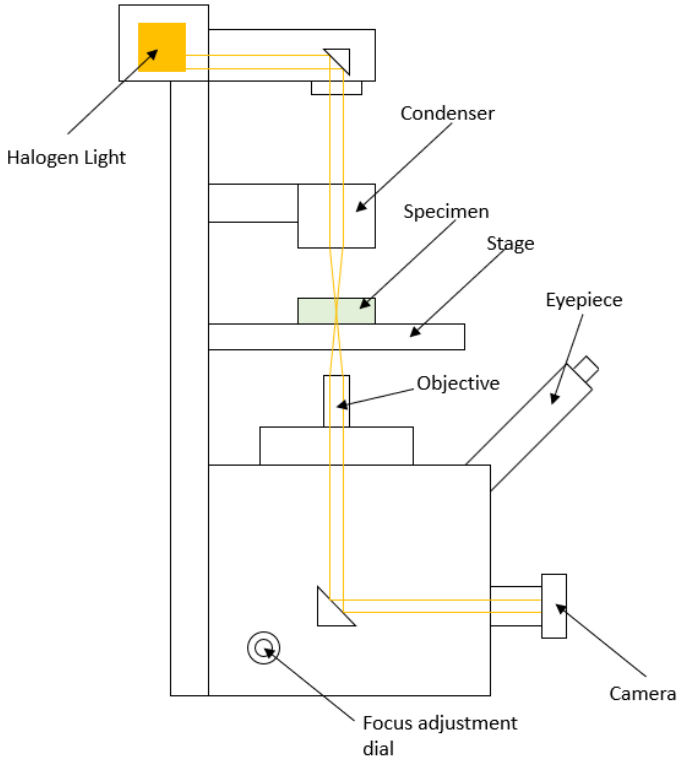

Figure 3.22: Representation of the optical path taken in brightfield microscopy. The set-up is similar to the path taken in the Olympus IX71 used throughout this work [43].

3.5.1.1 Cameras

Two different cameras were used to capture the images, depending on the specific needs of each type of experiment. To visualise the algae swimming in the fluid for classification of the net velocity and orientation, a CCD camera was used (CCD Olympus XM 10 monochrome camera). The camera has a resolution of 1376×1032 pixels at a frame rate of $FPS = 15\,\text{Hz}$ with a large range of shutter speeds ($0.1\,\mu\text{s}$ to $160\,\text{s}$). When examining beating frequencies and stroke dynamics, a high-speed camera (Mikrotron MC1310 high speed camera) was utilised as the conventional frame rate given by the CCD camera was not sufficient to capture the motion of these behaviours. The Mikrotron MC1310 has a resolution of $1280 \times$

1024 pixels and can employ frame rates up to $FPS = 46000\,\text{Hz}$, although the maximum frame rate used in this work was $FPS = 500\,\text{Hz}$.

In the analysis discussed in the following chapters, data captured with the conventional frame rate is classed as net global data and high speed camera as local data. Low frame rate ($FPS = 15\,\text{Hz}$) videos were captured over a duration of 1 minute and for high speed videos ($FPS = 500\,\text{Hz}$) due to data storage capacity, were 3 seconds long or 1500 frames. For repeatability, 10 plus videos were taken and analysed for each experimental case.

3.5.1.2 Microscope objectives

The choice of microscope objective is pivotal in proper microscopy and in producing a suitable image to be analysed, with objectives magnifying the sample by a factor, often a multiple of 10. Generally, microscope systems will have further magnification in the ocular lens or adapter lens (or camera). Depending on the objective, the resolutions, field of view (FOV) and depth of focus (DOF) will change with improved resolution coming at the expense of a reduced FOV and DOF and vice versa [264].

The resolution is defined as the shortest distance between two points that can be distinguished, the field of view as the area of visualisation and, the depth of focus as the distance in the z direction between the nearest and furthest plane where an object remains in focus [260, 265].

The resolution can be calculated from [266]

$$RES = \frac{\lambda_r}{2NA_{obj}} \tag{3.19}$$

where λ_r is the wavelength of the light illuminating the sample and NA_{obj} is the numerical aperture of the objective.

As for the depth of focus, it can be calculated by [267]

$$\delta_z = \frac{n_{ri} \cdot \lambda_r}{NA_{obj}^2} + \frac{e \cdot n_{ri}}{NA_{obf} \cdot M_X} \tag{3.20}$$

where n_{ri} is the refractive index of the fluid between the microfluidic device and the objective lens, p is the pixel size, and M_X is the magnification of the objective lens.

For the experimental processes undertaken within this work, 10X and 40X were both utilised to take advantage of their particular resolution, DOF and FOV. For net velocity and beat frequency calculations, where a large quantity of data was important for statistical relevance, and resolution was less significant, the 10X objective was used. In these cases, a high resolution was not critical as the algae were visualised as particles to be tracked by its centroid position and as such the relevant data could be captured from lower resolution images. However, when capturing individual stroke velocities (i.e. power and recovery stroke), a higher resolution was required and thus the higher magnification objective used (40X). Further, a 63X objective was used to visualise the flagella, which has a diameter of approximately 200 nm. The main characteristic of the three objectives can be viewed in Table 3.4.

Table 3.4: Types of objectives used within this work and their respective resolutions, DOF and FOV for Olympus camera (values will change slightly with Mikrotron).

Objective	**Process**	**Resolution** (µm)	**DOF** (µm)	**FOV** (µm)
10X	Net velocities and beat freq	1.4	15.12	$\sim 890 - 660$
40X	Individual stroke dynamics	0.53	2.03	$\sim 225 - 165$
63X	Flagella motion	0.46	1.46	$\sim 142.9 - 104.8$

The focal point of the system was always maintained on the mid-plane of the channel, i.e. the half depth. To achieve this, first the system was focused on the lower wall then on the top wall of the channel and using the micrometre scale on the focusing dial the half distance was calculated. Despite the low depth of focus compared to channel depth ($\delta \sim 84$ µm when using the 10X objective, the tracking software could still pick up unfocused algae. Unfortunately, this introduced disadvantages such as algae interaction with lower and upper walls relative to the z direction were captured, as well as only the 2D projection

of the algae 3D motion.

When capturing images with the higher magnification on an individual algae bases, the system was focused "on the fly" as the DOF was significantly lower, and it had to be modified for each alga.

3.5.2 Algae injection

For injection of the algae into the channels and refreshing alga through repeat experiments, a syringe pump was used (Phd 22/2000 Programmable Syringe Pump, Harvard Apparatus). While this task could have been carried out manually, the use of the syringe pump increased control and ensured the algae were subjected to constant controllable shear stresses. Furthermore, the maximum shear stress experienced could be managed so it remained below a damaging threshold. This is discussed in more detail in Section 3.5.2.1.

The algae were transported to and from the PDMS channel by the means of flexible Tygon plastic tubing with an internal diameter of 490 µm. At the ends of the tubing a metal connector was fixed, which could then be inserted into the microchannel inlets and outlets. As well as delivering fluid to the channel, the tubing was also used to remove the fluid and deposit it in a waste disposal container. The fluid within this container was disposed of by the aforementioned disposal methods (Section 3.2.3) at the end of the experimental procedure.

Once the algae suspension was injected and any prevalent air bubbles were removed, the channel pressure was equalised. The system was then left to settle for a period of time and once flow rate reduced to a negligible value a video of the swimmers was captured.

3.5.2.1 High stress conditions

Dunaliella salina are susceptible to damage under high shear stress conditions, with the possibility of broken flagella, deformation or death if the stress on the swimmer is significantly high. This can severely alter their natural dynamics, biasing the analysis. To avoid

this, the flow rates exerted on the algae were monitored to ensure stresses were kept well below the minimum value where signs of damage could become present.

Dimitrios et al. [268] measured the effects of shear stress on *D. salina* suspensions, for the use in cultivation. These results were applied to give an estimation of shear rate that should be avoided. It was found that above 15 Pa the cells started to lose motility and becoming immobile from the high stresses.

Throughout the experimental process, a prescribed safety factor of $\times 10$ was combined with the onset of non-motility to ensure all procedures did not damage the algae irreversibly. Thus, the maximum flow rate imposed by the syringe pump was $0.001\,\mathrm{mL\,min^{-1}}$.

To calculate this value, the maximum shear stress which would be found at the walls of both the tubing and the channel were calculated using the following calculations. Initially using the Hagen-Poiseuille Equation [269], the pressure drop per unit length was calculated in the circular tubing

$$\frac{\Delta P}{l_t} = \frac{8\eta}{\pi r_t^4} Q \tag{3.21}$$

and for the channel cross-section

$$\frac{\Delta P}{l} = \frac{12\eta Q}{w\delta^3} \tag{3.22}$$

where r_t is the radius of the tube, l_t is its length, δ the channel depth, ΔP is the applied pressure, Q is the flow rate and η viscosity. For the calculation, the most viscous solution used in the work was assumed to represent the most extreme case. This was 40 mPa s for Ficoll at 20%. Further details of the fluid rheology can be found in section 5.2.

For the circular tubing, the relevant dimensions were radius $r_t = 245\,\mu\mathrm{m}$, while for the rectangular cross-section, the dimensions were $w = 400\,\mu\mathrm{m}$ and $\delta = 84\,\mu\mathrm{m}$.

With the maximum flow rate of $Q = 1.667 \times 10^{-11}\,\mathrm{m^3\,s^{-1}}$, the shear stress for the tubing and channel was approximated from [270]

$$\sigma_t = \frac{r_t \Delta P}{2 l_t} \tag{3.23}$$

and

$$\sigma_c = \frac{0.5 \delta \Delta P}{l} \tag{3.24}$$

Therefore, for the most extreme case, the maximum wall shear stress the algae would experience was found to be $\sigma_t = 0.058\,\text{Pa}$ in the circular tubing and $\sigma_c = 1.42\,\text{Pa}$ in the channel. Both cases fall well below the critical value of 15 Pa suggested by Dimitrios et al [268] and the prescribed safety factor.

As well as in the tubing and channels, an area where high stresses can be present is the entrance and the exit of the channel, where the metal connector makes contact with PDMS. While no simple calculations can be made for the stress at this area through the experimental processes, the end of the metal connector was made sure to be raised from the base of the channel to avoid a contraction region for the flow to be accelerated in. With this and the relative margins of errors, it is assumed that the algae were not affected significantly by the shearing flow imposed through the experimental processes.

3.5.3 Alga to alga Interactions

Alga to alga interactions were a factor within the results that needed to be controlled, as only individual motion was being analysed within this work. With the algae swimming in the channel, on occasion two or more would meet and thus interrupt the swimming track. Dilute alga suspensions were used within the channels to avoid the likelihood of cell to cell interactions as there is sufficient displacement between cells.

Using the dimensions of the channel and relative algae number, an approximation of the percentage of channel taken up by the algae can be found. The channels used in the work had a width of $w \sim 400\,\mu\text{m}$, a depth of $\delta \sim 84\,\mu\text{m}$ and a length of $l \sim 890\,\mu\text{m}$ within

the viewing frame of reference. This gave a channel volume of approximately $0.0299\,\mathrm{mm}^3$ in the field of view. Assuming an algae width of $14\,\mu\mathrm{m}$ and shape to be spherical and with approximately 20 algae in the reference frame. The volume taken up was found to be $2.875 \times 10^{-5}\,\mathrm{mm}^3$ which translated to the algae taking up $\sim 0.1\%$ of the channel's volume.

During the post analysis, any algae seen to interact or pass another swimmer were not representative of natural individual swimming and therefore the tracks stopped upon contact.

3.6 Image processing and tracking

The image analysis and tracking procedures were carried out using ImageJ, a Java based image processing software, and MATLAB. The aim of the image analysis post-processing was to remove all stationary sections within the video and threshold the images so just the algae remained as dark objects. A plugin for imageJ, wrMTrck [271, 272] was then used to track the individual swimmers and quantify their positions in time, with the output being exported to MATLAB, where the swimming characteristics could be determined.

The video files were processed in ImageJ in an 8-bit stack format. A video stack comprises a series of temporally related images in a single file, i.e. all images have been acquired sequentially across different points in time. Each image within the stack is defined as a slice or frame and must have the same size and bit-depth as other images.

The first stage of the process required a conversion factor to be applied to the image to convert the distance from pixels to micrometers. To define the correct scaling from the images, a precise microscopic ruler was visualised under the same experimental conditions to calculate a scaling factor, which was input into the software. It should be noted that the scale factor was different depending on the cameras and objectives used, and thus this process was carried out for all camera/objective combinations.

Once scaled correctly, the images were cropped to remove the areas of the video outside the area of interest, such as the blank spaces outside the channel walls. This would free up

computer processing power, as the areas outside the channel need not be analysed. When characterising individual strokes, the area was cropped around the swimming organisms path.

Stationary objects, such as the walls, dirt on the camera lens, dead algae or other particulates were removed using a Z projection subtraction [272]. A Z projection generates an image from a stack containing the pixels of which intensity remains unchanged across the entirety of the stack, giving an image of all non-moving parts. The resultant Z projection was then subtracted from each slice within the frame individually using the image calculator tool, leaving a video stack comprised of only moving objects (Figure 3.23).

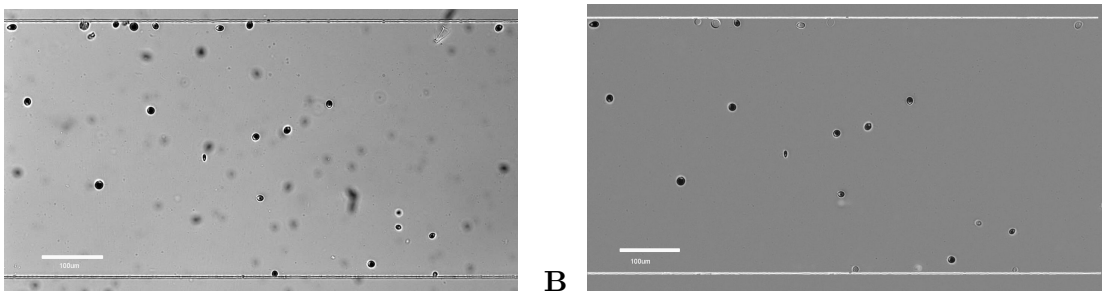

Figure 3.23: (A) Typical image taken from XM10 Olympus camera with algae represented by dark spots and lines respecting channel walls (B) Corresponding image after Z-projection subtraction (removing stationary objects and leaving motile algae). The walls of the channel usually removed, have been redrawn for reference.

For the tracking software to determine the swimming algae the image must be converted to a binary format i.e. black and white, with the swimming algae in black and rest of the image white (Figure 3.24). A thresholding process was used to achieve this.

The threshold process employed two threshold values, an upper and lower limit. Any pixels with an intensity between these limits were defined as the foreground and assigned as black. The rest of the pixels falling outside the limits were assigned as the background and white. ImageJ either allows this process to be carried out manually or automatically (where the software examines the corresponding intensity histogram and assigns the values for each individual image, dependent on a function defined). For the majority of images,

an automatic process was relied upon. A common function utilised was the maximum entropy function based on the Kapur-Sahoo-Wong Method [273].

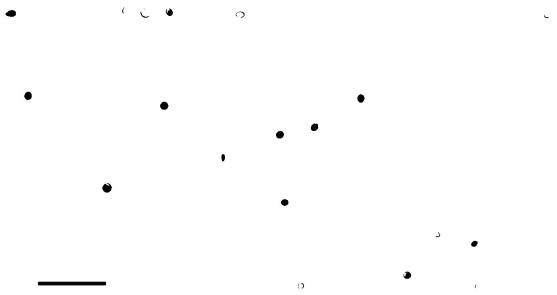

Figure 3.24: Image having undergone threshold process converting to a binary format

Finally, a binary process to fill any holes remaining within the system was applied to the video stack. This process took an area surrounded by black pixels from the thresholding process and filled the vacant pixels within this area. For example, it was possible for the thresholding to pick up the outline and not the centre of an alga, leaving a doughnut shape. For the tracking analysis, a full spherical structure was needed, therefore this step was completed to create the desired features.

Upon completing of the image processing procedures, videos with black circles representing the motile algae should be present (Figure 3.24 (A)). The definition between algae and background could then be determined by the tracking software and positional data across the image stack captured.

3.6.1 Algae tracking

Once the videos were in the correct configuration for the software to determine the swimmers, the videos were analysed using wrMTrck, a plugin for ImageJ. WrMTrck, developed by Pedersen [272], is a tracking software primarily designed for worm type swimmers but can be utilised for many other types of tracking. The plugin lets users select a variety of variables, that can be viewed in Figure 3.25, which defines the objects the system will

track. This includes a minimum and maximum area, maximum velocity, minimum track length and others. This allows for other moving particulates, or other objects not removed through the image processing set-up to be discounted from the analysis, granting the user high levels of control.

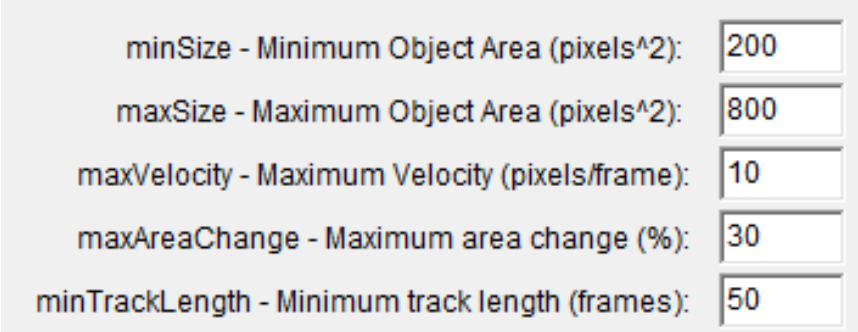

Figure 3.25: Example settings used within wrMTrck to track algae. Values are approximate and varied depending on circumstance.

The x and y position of the algae and identification of the tracks were compiled on a frame by frame basis, which were saved as a .dat file to be read and used in the next stage of the analysis. Other outputs from the software included an overview of track numbers by the individual algae on a threshold image giving the user a reference for the tracked algae. Further, a still image of the paths taken by the swimmers was also generated as well as a summary of the algae data which included data such as the average length, time in frames and other specific statistics.

Once the videos were compiled through the wrMTrck code, it was imperative to review the videos and remove any unwanted tracks or features that could have been tracked accidentally through the software. These could include: dead algae (algae that had deceased and become non-motile but still retained their body shape), spinning algae (algae that were seen to spin in the same spot which could be caused by flagella damage or being stuck), alga to alga interactions (when two or more algae crossed paths and the track jumped between alga).

The final positional data was then processed through a specific MATLAB code, depending on the purpose and type of analysis desired. The code read the x and y positions and calculated relevant desired values, which could then be exported for further post-processing. For example, in a standard tracking experiment set-up the positional data was read, and velocities, orientations and other statistical data was provided as output for each individual alga and for the population as a whole. This data was taken further and analysed to produce statistical data (averages, MSDs, etc) and to produce graphs such as histograms and windroses for better interpretation of the results.

3.6.1.1 Algae tracking experimental uncertainty

Inherently within the experimental system, errors were present in the calculations of centroid positions due to pixel resolution and slight underlying flow. To define this error, an approximate non-swimming value was calculated and any alga found to be swimming under this value were seen as non-swimmers and removed from the analysis. The point of non motility was defined as

$$Non - swimming\, value = 5 \times \frac{a_p}{a_B} \times r_B \times FPS + V_f \tag{3.25}$$

where a_p is the area of a pixel, a_B the area of the alga body, r_B the alga body radius and V_f the underlying fluid flow velocity. This relates to the percentage change related to 5 pixels out of place per frame, plus an approximation of underlying flow that could be present. The maximum underlying experimental flow was assumed to be $1.5\,\mu m\,s^{-1}$ from experimental observations and tracking tracer particles within the systems. Thus, from Equation 3.25, for the conventional camera this produced an uncertainty of $\pm 2.76\,\mu m\,s^{-1}$, which was then rounded up to $\pm 3\,\mu m\,s^{-1}$.

3.6.2 Beat frequency calculation

The beating frequency (frequency to complete power and recovery stroke) is an important metric in characterising puller alga's swimming dynamics and can give specific insight into the different effects a fluid has on the body and flagella. *D. salina* beat at a frequency of 25 Hz [106], greater than the frame rate of a conventional camera. Thus, a high speed camera must be utilised to capture the beating.

To quantify the beating frequency, there are two conventional methods, one focuses on the body and the second focuses on the flagella. Both are described in the following:

Firstly, relating the beat frequency of the body, makes use of low Reynolds number swimming and tracks the body of the swimmer. As the body moves forwards in the power and backwards in the recovery stroke, relative to their overall swimming direction, capturing this motion a frequency can be drawn.

Secondly, the flagella of the swimmer can be captured and analysed. To visualise an individual swimmer's flagella over a period long enough to gain experimental data, either the algae must be held stationary (trapping) [274, 275] or the swimmer must be confined to a single plane in a thin film device [24]. Trapping methods vary, but the conventional methods include trapping between two glass slides [276], optical tweezers [274] and using a small pipet with negative flow to trap the body [275]. All methods have advantages and disadvantages, and use often depends on the equipment available within a laboratory.

For the research undertaken in this work, data was primarily gathered through body tracking, with flagella tracking utilised to define flagella characteristic lengths and provide confirmation of the body tracking method.

3.6.2.1 Body Tracking

To track the body at the high frame rates needed to quantify the beating frequency, the Mikrotron MC1310 camera was used with a frame rate of $FPS = 500$ Hz. The determination of the frame rate is significant, too low and data can be lost from the analysis and

too high can bring in unwanted noise into the system. A frame rate of $FPS = 500\,\text{Hz}$ was decided upon as it encompassed a ratio of 20 times that of the beating frequency defined in the literature and in theory, each stroke should be covered by 10 frames assuming an equal distribution in stroke dynamics.

The experimental set-up matched that of the conventional camera velocity tracking, with the only difference being the use of a high-speed camera. Once the data had been collected, analysed with the positions and velocities of the swimmers defined, the results were then analysed using a Fast Fourier transform (FFT) algorithm. The FFT algorithm converted the signal from the time domain, into a frequency domain where the dominant frequency of the system can be identified. More details of this approach are discussed in Section 4.2.3.3.

Utilising a higher magnification objective, the individual stroke dynamics could also be recovered using this camera. Examples of the data that could be captured included the body velocities, time and amplitude in each of the two strokes (power and recovery).

3.6.2.2 Flagella method

The other method mentioned is analysis of the individual flagella of the algae. This method was used to define the characteristic length of the flagella and stroke, but not as a method of determining the beating frequency.

To capture images of an alga's flagella, a droplet of the algae suspension was placed on a glass slide using a micropipette and a cover slip was placed on top. The weight of the cover slip trapped large algae between the glass slide and cover slip, allowing for visualisation of the flagella with phase contrast microscopy and high magnification (63X).

Phase-contrast microscopy is an optical technique that translates minuscule changes in the phase of the light path into changes in amplitude. Flagella are clearly visible with a sharp contrast using phase contrast, where they may not be in brightfield microscopy.

Figure 3.26 shows a schematic of the light path through a phase contrast microscope. The difference from conventional brightfield microscopy is the light travels through a condenser annulus and phase plate within the objective. Wave fronts passing through the annulus are then diffracted in phase by structures present in the specimen, in the case here the flagella. This light passes through the objective where a phase plate, which matches that condenser annulus is housed. This segregates the diffracted and undiverted light, creating a contrast between specimen structures. Phase contrast is a powerful tool to enhance the contrast of the specimen being examined [277].

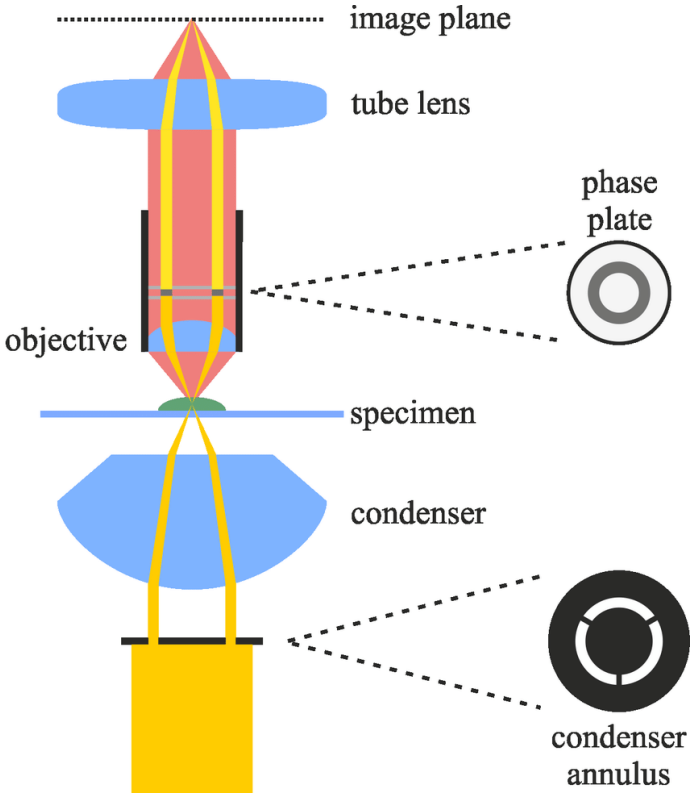

Figure 3.26: Schematic of light path of phase contrast microscopy. Condenser annulus focuses the light on the specimen structures, which diffracts the light as it hits it. This diffracted light is then segregated from the undeviated light in the phase plate, creating a contrast between specimen and background. Image reproduced with permissions from [278].

As used here, the flagella method possessed some draw backs, hence the body method was preferred to quantify the beating frequency of *D. salina*.

Analysis using the flagella method can only be carried out on an individual alga. Therefore, to achieve statistical quantifiable data, the process must be completed numerous times, a time intensive manual process. Further, as for the case described, the algae were trapped using two effective walls, influencing the algae stroke. Upon investigation of the flagella in confinement, it was apparent they went through different phases, where the flagella became attached to the walls and either stopped moving or beat with unconventional motions. Finally, evaporation issues could occur with the set-up inducing minute flows through the system [50].

Therefore, with the lack of statistical data available through the flagella method, it was primarily utilised to characterise flagella stroke dimensions. This is not to say this method is not valid for characterising beating dynamics, but with the current set-up the issues were significant for the body method to be preferred.

3.6.3 Example tracking data

To capture the detailed components of an alga's swimming velocities and stroke dynamics, three different experimental set-ups were utilised. For the net swimming, a conventional camera utilising a frame rate of $FPS = 15\,\text{Hz}$ and objective of 10X magnification. This gave the greatest field of view and timescale to capture the largest proportion of swimming algae. To quantify the beating frequency a higher frame rate was needed ($FPS = 500\,\text{Hz}$) and in an attempt to maintain the number of algae tracked the 10X objective was utilised. However, to capture the individual stroke positions, a higher magnification was needed to reduce noise in the system. Thus, the 40X objective with high speed camera was used, which allowed for the capture of the stroke dynamics but meant that only a single alga at a time could be tracked due to the reduced field of view. The beating frequency could also be captured using this method and was validated against the lower magnification calculations

to ensure consistency between the two methods.

Table 3.5: Different experimental set-ups for defining full body motion of *D. salina*. The approximate number of data points references the number of positional data entries captured for the full population of swimmer in that method across the full experimental processes.

Captured Data Type	Objective	FPS	Video Time	Approx. no. of Alga Tracks Analysed	Approx. no. of Data Points Analysed
Net Swimming	10X	15	1 min	100	15000
Beat Frequency	10X	500	3s	50	50000
Local Dynamics	40X	500	3s	10	10000

Therefore, for the full quantification of the algae cell swimming in a particular fluid, three different experimental set-ups had to be drawn upon. These methods for capturing the variety of stroke dynamics are detailed in Table 3.5. In general the data was captured over one or two days with selected points repeated after at least a month of the first capture to ensure consistency was maintained across algae samples.

Chapter 4

Swimming in the conventional medium

4.1 Chapter overview

In this chapter, the swimming dynamics of *D. salina* in their conventional medium are characterised. Initially, the chapter focuses on the swimming dynamics of a single organism, swimming in the medium with no rheological additives. This introduces the statistical methods utilised and gives an insight into the basic swimming dynamics. The analysis focuses on the swimming of the alga captured with a conventional frame rate ($FPS = 15\,\mathrm{Hz}$) and moves onto analysis of the beating and stroke dynamics captured with a high speed camera ($FPS = 500\,\mathrm{Hz}$). Once established, the chapter undertakes this analysis on a full population of swimmers, reporting the swimming dynamics of *D. salina* within its conventional media.

4.2 Individual alga swimming dynamics

4.2.1 Medium properties

In their natural environment, *D. salina* feed and rely on several nutrients and substances to maintain proper function within the cell as discussed in Section 3.2.1. The growth medium the algae are immersed in is designed to provide these nutrient conditions (Hejazi and Wijffels modified culture Medium [205]). However, due to the presence of the various chemical additives, both the density and viscosity of the medium increase slightly to that of purified water (Table 4.1). In terms of rheology, the medium still exhibits Newtonian behaviour as shown in Figure 4.1. The density and viscosity of the medium will vary with the number of algae present, so will be related to the current stage of algae growth [64, 66–70]. However, these changes due to algae presence are not critical in this study, as dilute suspensions are used, and only individual behaviour is analysed.

Table 4.1: Density and viscosity variations of the medium and purified water. The inclusion of chemicals and salts increase both the density and viscosity slightly from the base of purified water. All measurements taken at room temperature (20 °C).

Solution/Suspension	**Density** ($\mathrm{kg\,m^{-3}}$)	**Viscosity** ($\mathrm{Pa\,s}$)
Purified Water	0.9982 [279]	1.0016 [279]
HWMM Medium	1041 ± 0.4	1.14 ± 0.05

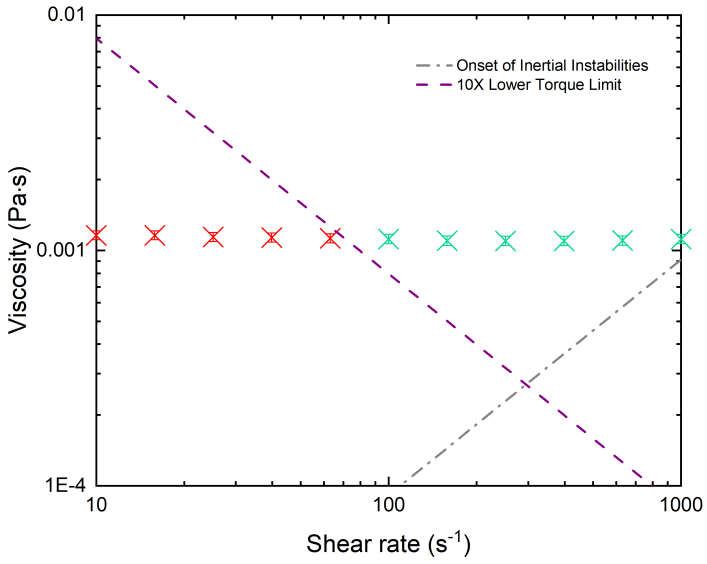

Figure 4.1: Flow curves showing the steady shear viscosity of the medium without the presence of any other agents or suspended algae. The medium displays Newtonian behaviour. The minimum measurable torque represented by the purple dashed line is calculated from Equation 3.10, and the onset of inertial instabilities by the grey dashed is line calculated from Equation 3.12 with values outside these limits being discarded from the results (red data points). The average viscosity is taken as the average of the data points lying within rheometer limits (green points). Error bars relate to the experimental error in rheological measurements (Section 3.3.3.3).

4.2.2 Individual net motion

For the first stage of the chapter, the analysis of a single alga moving in the medium is conducted for illustrative purposes, introducing the statistical methodologies. The alga highlighted in Figure 4.3 was chosen for this analysis as it provides a good illustration of typical swimming locomotion that is representative of the full population.

For the section that follows, the different analysis methods are detailed, which are characterised into two regimes. Initially, the net (global) motion, which describes dynamics calculated through methods using a conventional frame rate camera ($FPS = 15\,\mathrm{Hz}$). In

these calculations, the back and forth motion of the algae is not captured as the frame rate is not sufficient. The local motion then describes the dynamics captured using increased frame rates ($FPS = 500\,\text{Hz}$) where the full stroke is defined and both the power and recovery strokes are visualised.

The reference frame of the channel is displayed in Figure 4.2 with the origin $(0, 0)$ set at the top left-hand corner, with x positive from the left to right and y positive from the top to bottom of the channel. In all instances the channel was visualised in its mid-plane.

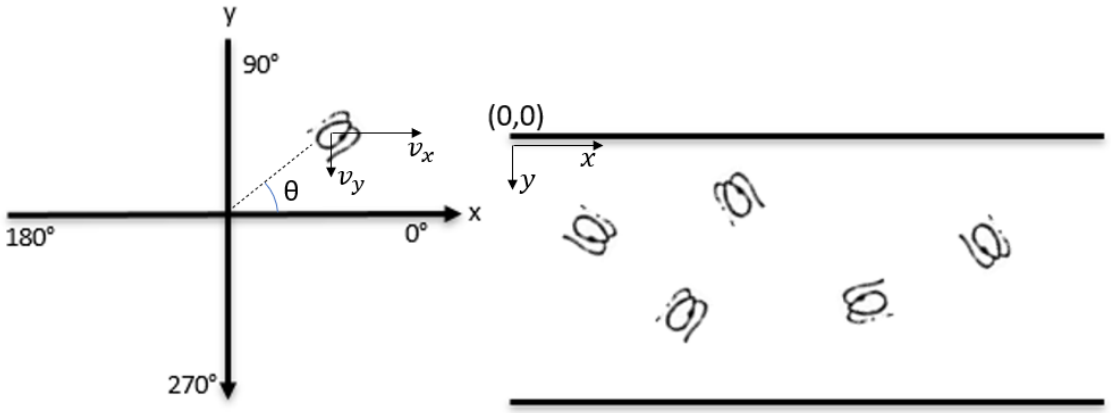

Figure 4.2: Definition of swimming orientation with 0° related from left to right horizontal motion within the channel and increasing anti-clockwise. Note, positive x is defined left to right and y from top to bottom. Origin of the channel is noted with $(0, 0)$.

4.2.2.1 Net track and position data

The path the singular alga in question undertook can be viewed in Figure 4.3. It starts as it entered the viewing frame at the left of the channel and follows the alga as it swam from left to right then upwards until it was passed by another alga (alga 24 in Figure 4.3) which resulted in the termination of the track. The $x - y$ positions of the alga for each frame was captured as it swam through the channel, as discussed in Section 3.6. In total, the track consists of 119 position co-ordinates over a time frame of roughly 8 seconds.

The video capture rate of this analysis was 15 frames per second ($FPS = 15\,\text{Hz}$) in this initial section of the analysis. From the track it can be seen that the alga possesses motility, navigating with relative ease from the left to the right of the image frame. Although only an individual alga was analysed at this stage, and the data was captured over a short time frame, the swimmer does not show any form of run and tumble motion. The cell swims in an almost fixed direction for the majority of the track with no sudden changes of movement which would be related to the tumble stage of this prescribed swimming type. From the limited data it would be seen that the swimmer navigates with a persistent random walk [67, 107, 280].

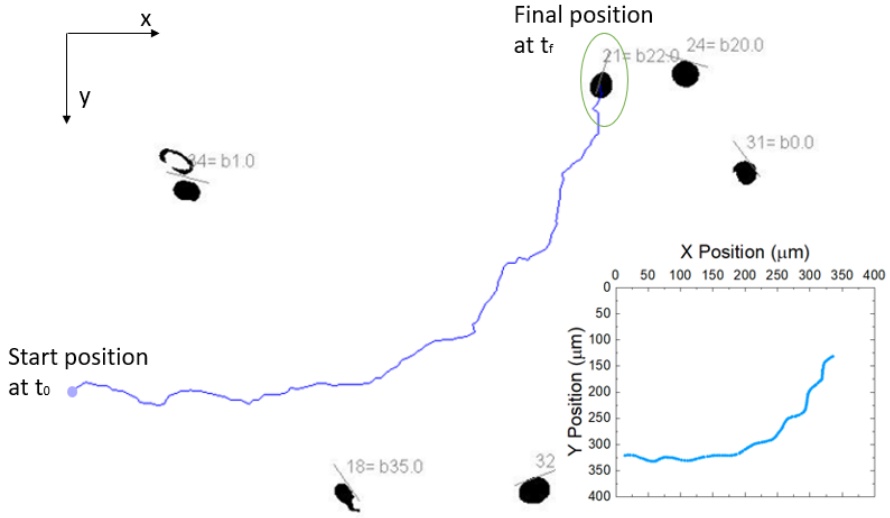

Figure 4.3: Still image of single algae motile in microfluidic channel. The track of alga 21 is plotted, which is analysed for characterisation of net individual motion. Inset shows positional data of the track which is used for the analysis steps.

4.2.2.2 Net swimming velocity

The next phase of the analysis was to take the positional data captured from the experimental video to calculate and process the velocity data of the swimmer. The net velocity was calculated on a frame by frame basis by calculating the x and y velocity components

across consecutive frames along the track. The magnitude of the two velocities was then taken to define the alga swimming velocity

$$v_{in} = \sqrt{v_{x\_in}^2 + v_{y\_in}^2} \tag{4.1}$$

where v_{in} is the instantaneous velocity between frames. v_x_in and v_y_in are the components of the alga's instantaneous velocity in the x and y direction

$$v_x = \frac{x_{i+1} - x_i}{\triangle t} \tag{4.2}$$

and

$$v_y = \frac{y_{i+1} - y_i}{\triangle t} \tag{4.3}$$

where x_i and y_i are the x and y positions of the centroid of the alga in frame i and $\triangle t$ is the time between frames, $\triangle t = 1/FPS$ (in this case $FPS = 15\,\mathrm{Hz}$).

The mean of all the instantaneous velocities across the track for a single alga was calculated to give the average net swimming velocity

$$V_{net\_ind} = \frac{1}{N-1} \sum_{i=1}^{N-1} (v_{in})_i \tag{4.4}$$

where N is the number of frames in the particular track, 119 for the individual case analysed and V_{net_ind} is the average velocity for the individual swimmer. For this particular alga its swimming velocity was found to be $V_{net\_ind} = 56.33\,\mu\mathrm{m\,s^{-1}}$, a relatively fast velocity in comparison to its body size, translating to approximately 4 body lengths per second. The distribution of the swimmer's instantaneous velocities (v_{in}) across its full track is displayed in Figure 4.4 and describes how the velocity of the alga varies within this particular track. It shows a distribution either side of the mean velocity, showing that the swimmer has a variation in its velocity. Some variations will be related to the beating cycle (Section

1.4.1.2) as the instant the position is captured relative to the point the alga is on in its swimming stroke will impact the instantaneous velocity.

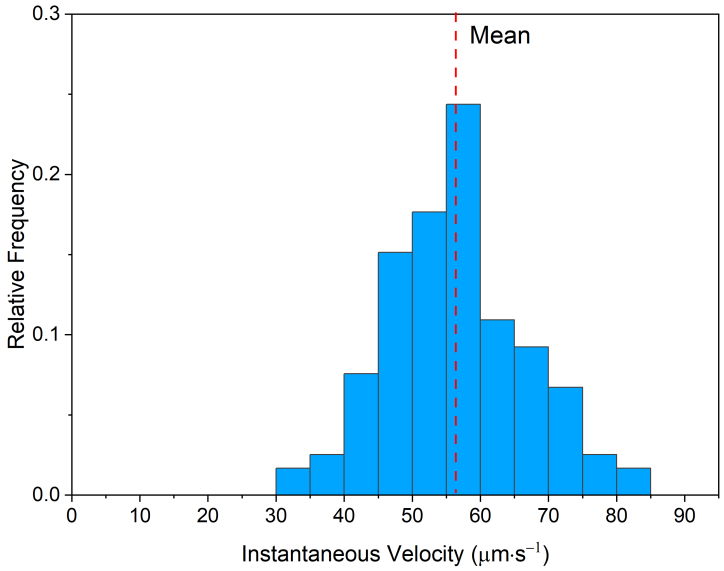

Figure 4.4: Instantaneous velocity data (v_{in}) of a single swimming alga represented across a relative frequency histogram with bins of size $10\,\mu\mathrm{m\,s^{-1}}$. Each individual point relates to a velocity calculated between two reference frames. The mean corresponds to the calculated mean of all instantaneous velocities for this particular track, $V_{net\_ind} = 56.33\,\mu\mathrm{m\,s^{-1}}$.

4.2.2.3 Swimming orientation

Further to the analysis of the swimming velocity, the preferential direction of the swimmer can be another characteristic definition of swimming motion. This analysis was conducted by compiling the swimming direction into a "windrose", a method used to show any preferential direction of a swimmer while also linking the velocity to the orientation. The swimming direction was calculated from the x and y velocity components, with the angle defined as anti-clockwise from the positive x direction in the channel.

The swimming angle was calculated following

$$\theta = 360 - tan^{-1}\frac{v_{y\_in}}{v_{x\_in}}\,(v_{x\_in} > 0)\,\&\,(v_{y\_in} > 0) \tag{4.5}$$

$$\theta = -tan^{-1}\frac{v_{y\_in}}{v_{x\_in}}\,(v_{x\_in} > 0)\,\&\,(v_{y\_in} < 0) \tag{4.6}$$

$$\theta = 180 - tan^{-1}\frac{v_{y\_in}}{v_{x\_in}}\,(v_{x\_in} < 0) \tag{4.7}$$

where θ is the swimming direction of the alga with the reference defined in Figure 4.2.

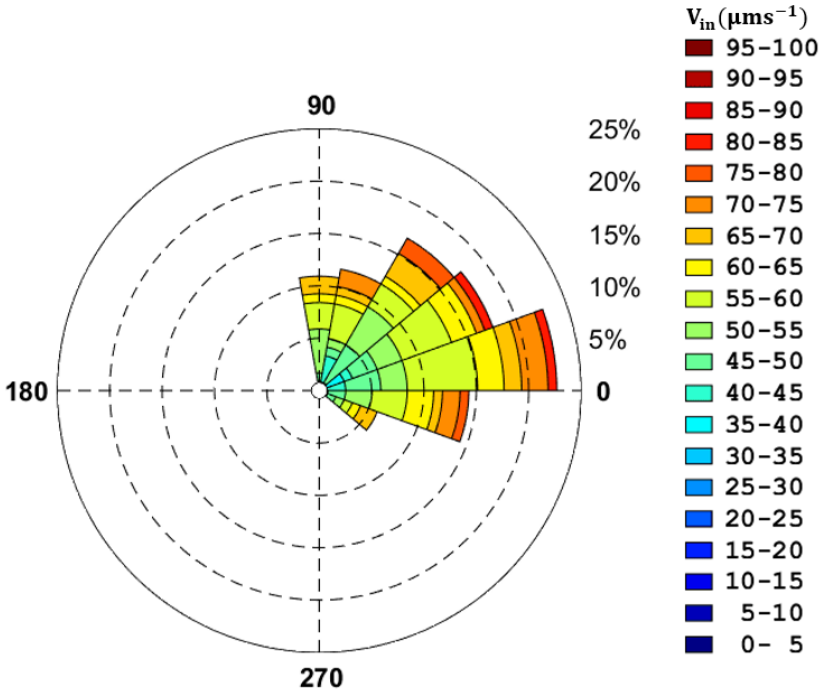

Figure 4.5: Individual swimmer windrose displaying direction of travel split into orientation bins and instantaneous swimming velocity denoted by colour relating to scale on the right. The dashed circles indicate the percentage of track present in that specific bin in increasing intervals of 5%. The track of this single alga moves with a mostly positive x direction with a slight directed motion in the positive y direction as seen in Figure 4.3.

The windrose of the single alga is shown in Figure 4.5 (corresponding to velocity data

in Figure 4.4), which shows a clear preferential direction of the alga, swimming across the channel from left to right in the positive x direction with a degree of positive y directed movement as seen in Figure 4.3. In this case the swimmer's direction remains mostly constant with no major turning events or other such stark deviations from its track. From this combination of data, it can be seen the velocity of the swimmer does not alter depending on its orientation [281].

4.2.2.4 Mean squared displacement

The mean squared displacement (MSD) is a powerful analysis tool often used in biophysics for the determination of particle displacements over time and the nature of their motion. For a given single particle, the 'mean' displacement is taken over many repeat instances of a time interval. Calculating the MSD's dependence on the time interval then shows the mode of diffusion and gives an effective diffusion coefficient [282–287]. The MSD for the cases discussed in this work was calculated from the following

$$MSD(\tau) =< (r_n(t+\tau) - r_n(t))^2 > \tag{4.8}$$

where $r_n(t)$ is the position of the particle at a certain time, $r_n(t+\tau)$ is the position after a time interval. The average ($<>$) denotes a time-average taken across values of τ i.e. for a track of 50 frames, the lowest value of τ will produce 49 MSD values which are averaged to increase reliability and thus give a single MSD for each value of τ.

Once calculated, it is possible to fit the MSD with τ to a power-law to define crucial information regarding the nature of the swimming dynamics observed

$$MSD = K_\alpha \tau^\alpha \tag{4.9}$$

where α is the apparent diffusion exponent, a measure of the nature of the system and K_α is a generalised effective diffusion coefficient. Once calculated, the MSD can give information

on the type of movement, that being whether the particles being analysed movement is freely diffusive, bounded or transported [283]:

- $\alpha = 1$ a freely diffusive particle such as a particle undergoing purely Brownian motion will exhibit a linear MSD as a function of the time interval. This motion is a pure random walk with no preferential particle direction.
- $\alpha > 1$ if the plot exhibits an increasing slope, the particle is exhibiting directed active motion. This could be an underlying flow or a swimming particle.
- $\alpha < 1$ if the plot plateaus, then the motion of the object is seen to be constrained. An example might be a particle undergoing Brownian motion constrained within a microfluidic channel.

For a swimming alga, a MSD that increases faster than linear, e.g. $\alpha > 1$, would be expected as they are active swimmers with preferential forward motion [282].

Figure 4.6 shows the MSD data for the single swimmer as a function of the time interval (τ). It shows clear active motion with an ever-increasing upward trend of the MSD curve as the time interval is increased, indicating active motion. The MSD curve is fitted to Equation 4.9 with time intervals between 0 s and 3.2 s, which corresponds to the ballistic region [67, 288, 289]. As the analysis focuses on swimming in the ballistic region, the diffusion is controlled by the velocity squared since the direction of the swimming is predominantly in a linear direction. This can be seen (for the case of the single swimmer) by the effective diffusion coefficient of 2947 and exponent of 1.959. Therefore, at time intervals of less than 3.2 s, the alga's movement is heavily active, with motion very close to a straight directed line and thus indicative of purely ballistic behaviour.

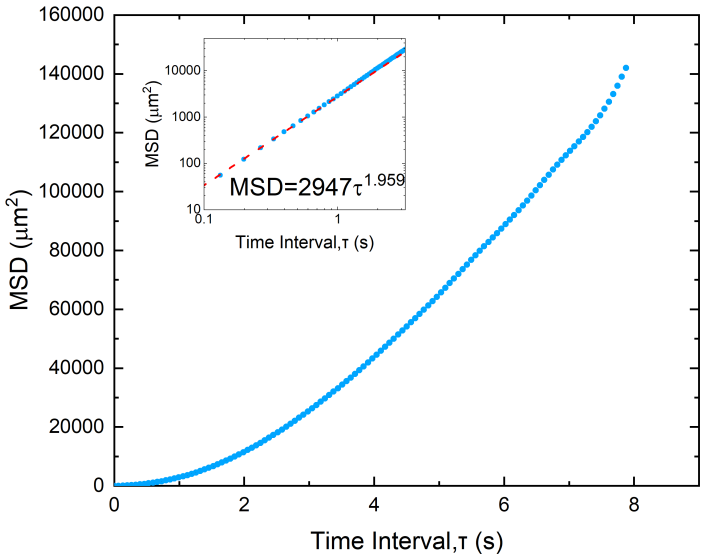

Figure 4.6: MSD over time interval (τ) for a single swimmer. The MSD is calculated for each time interval and time-averaged across points of equal time intervals. MSD shows heavily active motion with the algae swimming close to a straight directed line. The insets displays a log-log plot at lower time intervals with a power-law fit as shown by the equation represented by the red dashed line.

4.2.2.5 Persistent random walk

The swimming motion of *D. salina* fits well to a persistent walk model, sometimes also described as a correlated random walk [107]. This model is commonly assigned for microscopic swimming organisms. The persistent random walk model adds a "memory" to the conventional random walk model, where the direction of the particle is taken at random from its previous position [290]. This "memory" term is prescribed by assigning a probability for the swimmer that each step tends to the same direction as the step previous. The initial directed motion diminishes over time and a uniform distribution will be observed over long time periods. The persistent random walk model is independent of the back and forth motion of *D. salina* (Section 1.4.1.2) which is not represented within the model.

At very short timescales, the swimmer will present an almost fixed direction corresponding to a ballistic regime characterised by the exponent (α) in the MSD time-interval dependence being close to 2 (Equation 4.9). This regime ends when the probability of the swimmer turning becomes significant. For a puller alga, the turning process has been shown to be as a result of the two flagella becoming asynchronous for a short period of time [67, 107, 280].

It is possible to fit the MSD of a swimmer displaying this motion to the persistent random walk model. The persistent model consists of a persistent length l_p and time t_v

$$MSD(\tau) = l_p^2 \frac{\tau}{t_v} - 0.5 l_p^2 (1 - e^{\frac{-2\tau}{t_v}}) \tag{4.10}$$

where τ is the time interval and $\tau \ll t_v$. These persistent characteristics are related to the turning events of the swimmer. For the MSD below t_v the motion tends to be mostly in a fixed direction and above tends towards random motion ($\alpha \to 1$) from Equation 4.9 [67]. Unfortunately, for the analysis contacted in this work the MSD could not be fitted to the persistent random walk model as the confinements of the channel were less than the lengthscales needed for the model. Furthermore, the minimum track length was taken as 50 frames, meaning no data above this value was calculated for the MSD and therefore, details of the longer lengthscale interactions lost. Thus, the majority of the analysis will likely fall this the ballistic region of the MSD as discussed previously.

4.2.3 Individual localised motion

4.2.3.1 Local track and positional data

As mentioned in Section 1.4.1.2, the swimming motion of *D. salina* is not simply linear, with the algae moving only in the anterior direction. Rather, the swimming stroke of *D. salina* and other puller type flagellated swimmers is split into two idiosyncratic strokes [94, 98]. During the power stroke, the body of the swimmer moves forward and in recovery it moves

backwards.

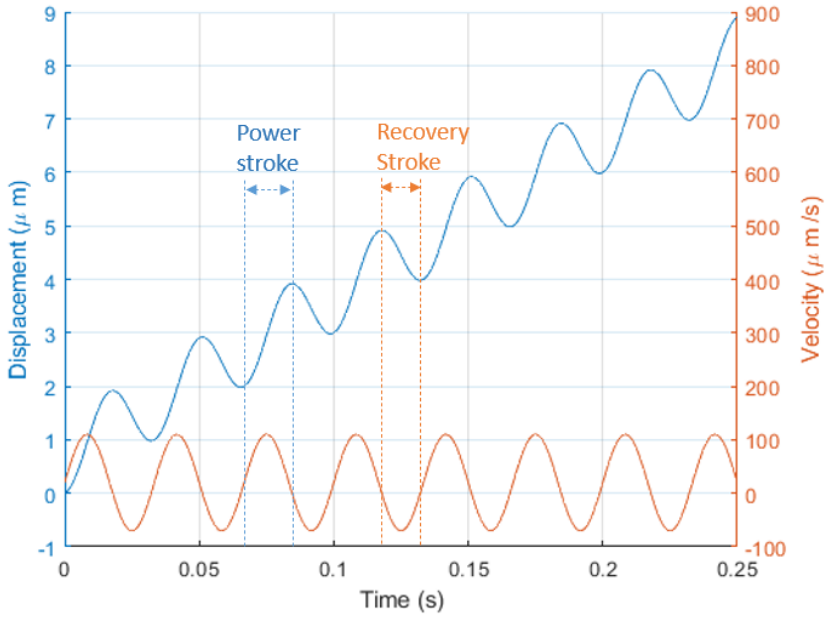

Figure 4.7: An example of how *D. salina* achieves a positive net motion in relation to time. Data is taken from fabricated idealised values. The velocity oscillates in time following an approximate sin wave with a bias towards the power stage of the stroke. Translating the velocity behaviour to the amplitude, shows the swimmer moves forward further during the power stroke than it moves backwards during the recovery stroke, resulting in a net positive motion.

Figure 4.7 displays a simplified theoretical representation of how a swimmer's velocity and amplitude varies over time. The velocity of the swimmer fluctuates over the power and recovery strokes, which in turn moves the swimmer in the direction related to that particular stroke. The power stroke is more effective than recovery, and thus the swimmer moves a greater distance through the power stroke than the recovery stroke. The swimming gait can be viewed as "two steps forward, one step back" approach [24]. For the purpose of the analysis, the power stroke is defined as the portion of the beat cycle where the swimmer is moving forwards and the recovery when moving rearwards relative to the overall direction of travel. While *D. salina* can exhibit a slightly asynchronous beat pattern, notably during

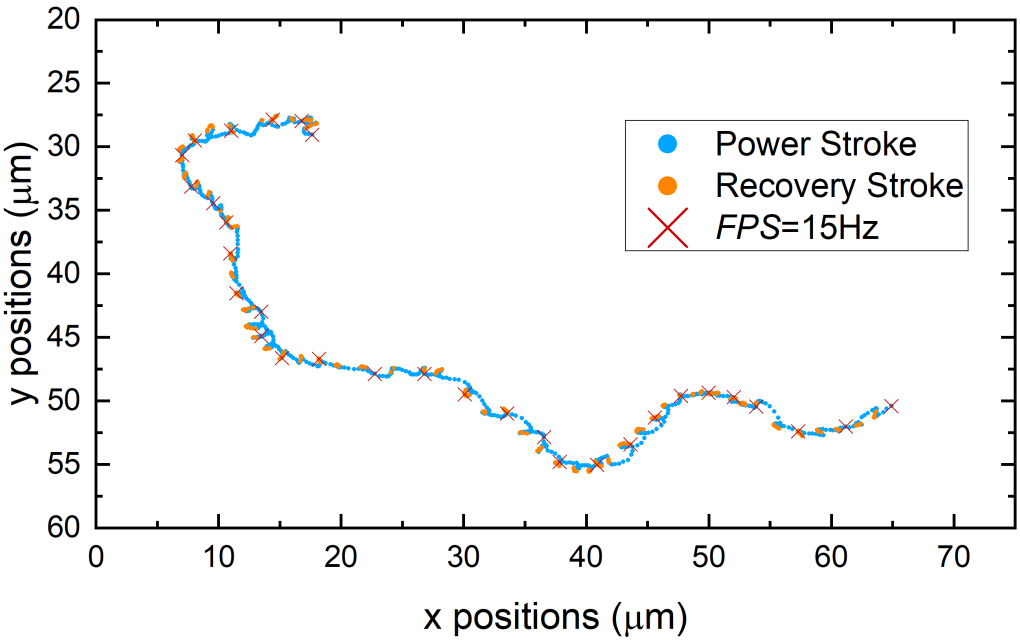

Figure 4.8: Localised track of an individual alga, with the start point in the bottom right corner and finishing at the upper left. Blue circles represent the power stoke, orange the recovery stroke and the red crosses denote the track if $FPS = 15\,\text{Hz}$, showing the hidden stroke dynamics. The track is composed of 1000 frames covering 2 seconds.

a turning event (i.e. individual flagellum beat out of sync with each other), an entirety synchronous beating pattern is assumed for this analysis.

For local analysis of the individual swimmer a different alga must be taken from the net analysis as video capture simultaneously using both the conventional frame rate and high-speed camera needed for the localised motion was not possible. However, all experimental conditions were maintained, and the algae possessed similar swimming kinematics.

The track of the specific single alga analysed can be viewed in Figure 4.8. It is composed of 1000 frames, covering 2 seconds of movement ($FPS = 500\,\text{Hz}$). Compared to the motion at the global net scale (red crosses in Figure 4.8) the track can be seen moving both forwards and backwards, with the points representing the power stroke represented by a blue circle, while those in the recovery, an orange circle. The track initiates from the right of the channel moving right to left with a notable turning event at the end of the track where the

alga starts to swim in the opposite direction.

The power and recovery strokes can also be visualised using the windrose format. Figure 4.9 comprises the velocity and orientation data from the linear section of the track where the movement is predominantly in the x direction ($x > 20\,\mu m$ Figure 4.8). Despite the overall motion being in the negative x direction ($90° < \theta < 270°$) the windrose shows a portion of the motion in the posterior direction ($90° > \theta > 270°$) corresponding to the recovery stroke of the swimmer. It is clear from the graph that the swimmer spends the majority of its time in the power stroke, with greater velocities in this phase.

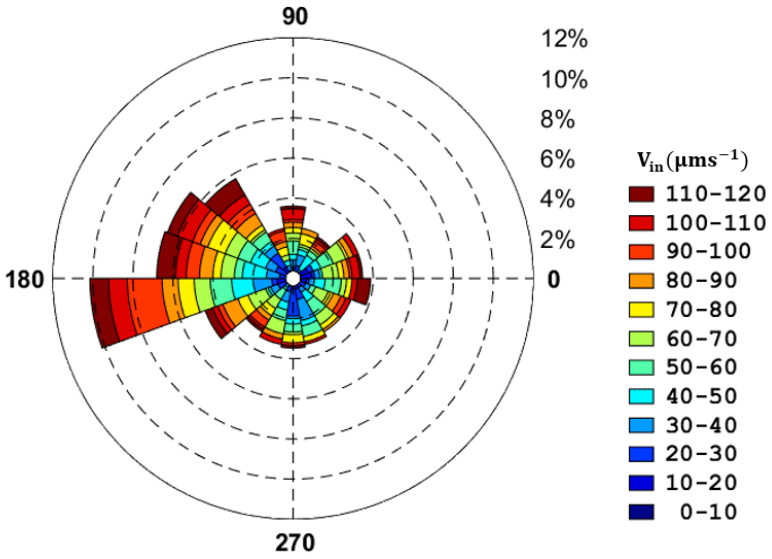

Figure 4.9: Localised windrose across a section of the track where the predominant net directed motion of the track is in the negative x direction (see Figure 4.8). The velocity of the swimmer is denoted by colour relating to the instantaneous velocity on the scale on the right. Dashed circular lines correspond to relative frequency of swimming orientation, which are displayed in bins of 20°.

4.2.3.2 Local swimming velocity

The instantaneous swimming velocities at the local scale are calculated by the same methods as described in Section 4.2.2.2 for the quantification of the net swimming velocity.

The only variations in the calculation is the reduction in the frame time as the frame rate of the camera is increased from $FPS = 15\,\text{Hz}$ to $FPS = 500\,\text{Hz}$, and thus the frame time reduces to $\triangle t = 0.002\,\text{s}$. Further, as the swimmer moves backwards and forwards, a definition between the power and recovery strokes is required with v_{in} being assigned as negative in the recovery stroke. This is defined when the swimmer is moving rearwards relative to its overall direction of travel such that when $270 > \theta_a > 90$, $v_{in} = v_{in} \times -1$ where θ_a is the swimming angle with the reference frame relative to the directed motion of the swimmer, such that 0° is related to V_{net} travel (green arrow in Figure 4.10).

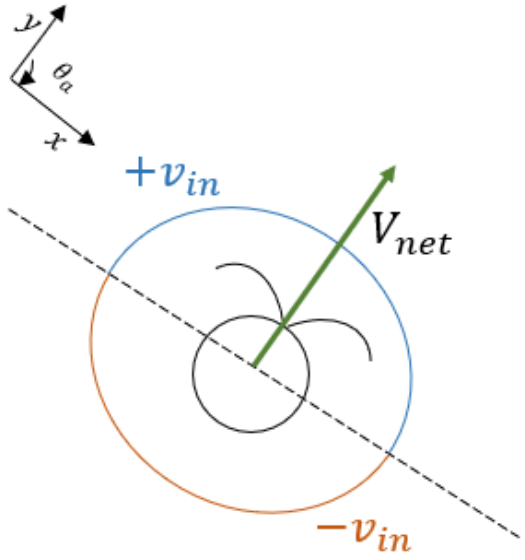

Figure 4.10: Schematic diagram of the definition of recovery stroke, where v_{in} is assigned as negative when $270 > \theta_a > 90$.

Thus, when moving forward relative to the net directed motion, the alga was seen to be in the power stroke and if moving in the reverse direction in the recovery stroke. The process of calculating the net directed motion was repeated every 50 frames to account for changes in direction of the alga.

Taking the velocity over a specific time frame produces a velocity spectrum in the time

domain, which can be viewed in Figure 4.11 where a quasi-sinusoidal curve is presented. When the velocities are positive (above red reference line , $v_{in} = 0\,\mu\mathrm{m\,s^{-1}}$) the swimmer is seen to be in the power stroke and when negative, in the recovery stroke.

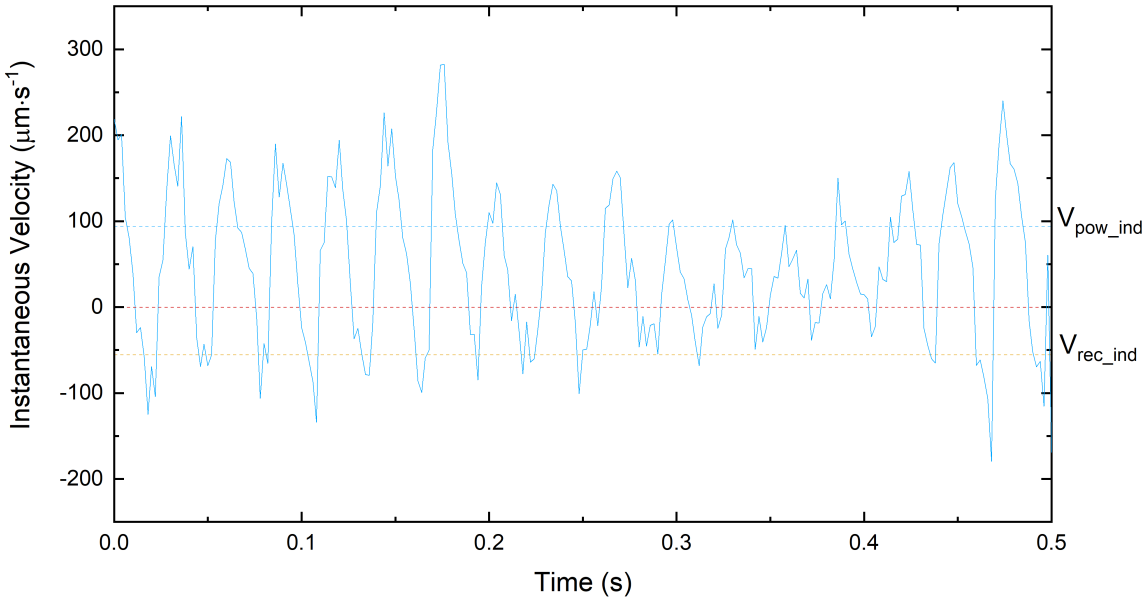

Figure 4.11: Instantaneous swimming velocity as a function of time of a single swimmer. The power and recovery strokes are clearly visible with the power stroke notated by positive velocities (above red reference line) and recovery by negative. The average velocity for the power (blue) and recovery (yellow) strokes are notated by dashed coloured lines. The inverse of the wave period is defined as the beating frequency.

Taking the average of the positive velocities, the average velocity across the power stroke can be recovered and for the recovery stroke the negative velocities. For this single swimmer, the average velocity in the power stroke was found to be $V_{pow\_ind} = 93.67\,\mu\mathrm{m\,s^{-1}}$. A value much greater than the net average swimming velocity. In the recovery stroke, the average velocity was $V_{rec\_ind} = -55.69\,\mu\mathrm{m\,s^{-1}}$. As expected, the recovery velocity is less than that produced in the power stroke, resulting in a velocity ratio between the power and recovery of 1.68.

Computing a 'signed average' velocity where the instantaneous velocities are averaged as in Equation 4.4, treating the recovery stroke velocity values as negative, and conducting

an average across the full spectrum of v_{in}, returns a value relative to the net velocity calculated at lower frame rates. In the case described, this signed velocity was seen to be $V_{sign\_ind} = 47.6\,\mu m\,s^{-1}$. This velocity is similar to the net velocity, which was found to be $V_{net\_ind} = 56.33\,\mu m\,s^{-1}$ for the analysis of a single swimmer. It should be noted that two different algae were taken for this analysis, hence the variation in velocities.

If the magnitude (treating all values of v_{in} as positive) of the instantaneous velocities are applied to Equation 4.4 a short timescale complete velocity is found (V_{loc_ind}). This velocity should be much greater than the net velocity, as it essentially encompasses the swimmer's entire stroke. However, will be less than the power velocity as it includes the recovery portion of the stroke. For the individual swimmer, this velocity was found to be $V_{loc\_ind} = 81.92\,\mu m\,s^{-1}$.

A table of all the comprised velocities is described in Table 4.2, with the relative velocity values for the single swimmer also included. Furthermore, a simple schematic diagram of velocity definitions can be viewed in Figure 4.12. Other defined parameters will follow the same subscript notation, such as the amplitude of the body moving through the stroke.

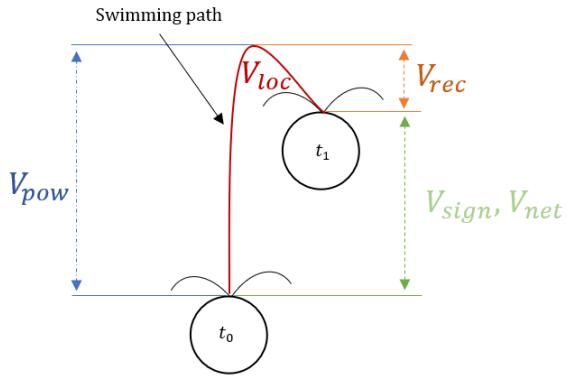

Figure 4.12: Simple schematic diagram of characteristic velocity definitions. With t_0 and t_1 indicating the start and finish of one complete stroke.

Table 4.2: Velocity definitions of a swimming alga for both local and global net data analysis. All definitions are in terms of individual swimmer tracked through current analysis. However, the same definitions will be carried through to the analysis of the full population minus 'ind' subscript, which in this case indicates the velocities averaged over a single track.

Velocity Name	**FPS** (Hz)	**Description**	**Individual value**	**Abbreviation**
Instantaneous velocity	N/A	Instantaneous velocity between frames	N/A	v_{in}
Net velocity	15	Frame by frame average velocity	$56.33\,\mu m\,s^{-1}$	V_{net_ind}
Local velocity	500	Local velocity encompassing full path length	$81.92\,\mu m\,s^{-1}$	V_{loc_ind}
Signed velocity	500	Local velocity with recovery being negative	$47.6\,\mu m\,s^{-1}$	V_{sign_ind}
Power velocity	500	Velocity though power stroke	$93.67\,\mu m\,s^{-1}$	V_{pow_ind}
Recovery velocity	500	Velocity through recovery stroke	$-55.69\,\mu m\,s^{-1}$	V_{rec_ind}

4.2.3.3 Beating frequency

For Newtonian media in the absence of inertia, the response of the body to the flagella motion is instantaneous such that as soon as the flagella initiate a stroke the body will follow [24]. Therefore, the back and forth motion can be related to a beating frequency of the body and thus flagella, where the frequency refers to the swimmer completing one power and one recovery stroke.

To extract the beating frequency from the data of instantaneous velocities with time (as shown in Figure 4.11) a fast Fourier transform (FFT) was performed.

A fast Fourier transform is an algorithm that converts a signal from the time domain

into frequency. It is a particularly useful tool in signal analysis and can even decompose a signal consisting of multiple different frequency inputs.

The FFT algorithm computes the discrete signal or the discrete Fourier transform (DFT) of the inputted signal [291, 292]. The DFT is written as follows

$$x(k) = \sum_{z=0}^{Z-1} x(z) e^{\frac{-j2\pi Kz}{Z}} \tag{4.11}$$

where Z is the size of the domain. Each value is multiplied by e to some function of z and summed for that given z. To calculate the full DFT, the number of operations increases with z to the order of Z^2. The FFT algorithm determines the DFT of a signal significantly faster than computing it directly, reducing the number of computations from Z^2 to $N \log_2 Z$. To achieve this, a FFT process rapidly computes the DFT by factorising the DFT matrix in a product of mostly zero factors reducing the complexity and computation requirements of the DFT [293].

The resultant FFT signal in the frequency domain is represented in Figure 4.13. The beat frequency was taken as the frequency at the maximum peak of the signal, thus the beating frequency was found to be $f_{BF\_ind} = 33.03\,\text{Hz}$, meaning that every 0.03 s the alga completed a stroke.

It might be expected that the power and recovery strokes attribute the same proportion of time to the full stroke. However, this is not the case, with the power stroke taking a much greater proportion of a single beat. This can be visualised in Figure 4.11, with the period of positive velocity for the power stroke clearly greater than negative. Quantitatively, taking velocities in the positive direction as the power stroke and negative in recovery, for this individual alga it spent 69.1% of the stroke in the power phase and 30.9% in the recovery, across the data set.

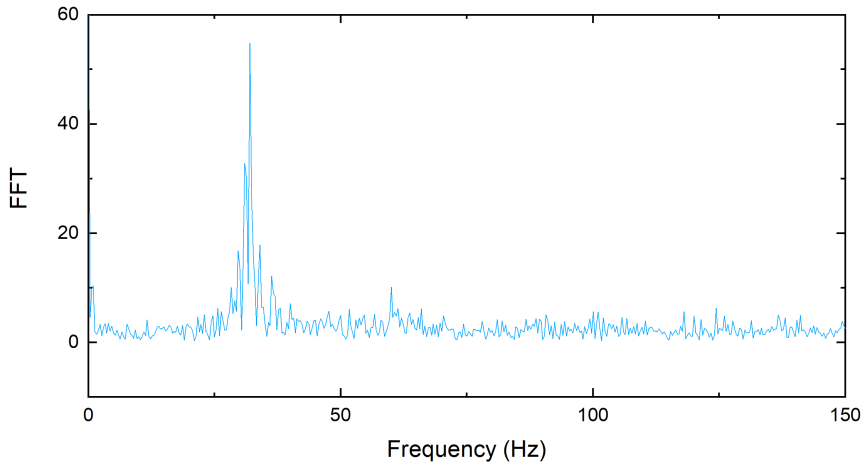

Figure 4.13: FFT frequency taken from time domain plot in Figure 4.11. The distinct peak represents the calculated beating frequency for that particular swimmer.

4.2.3.4 Stroke amplitude

The stroke amplitude or the distance travelled through the swimming stroke is another key defining feature. For the single swimmer it moved forward on average $A_{pow\_ind} = 1.96\,\mu m$ in the power stroke and backward $A_{pow\_ind} = 0.52\,\mu m$ in the recovery.

In total, across the full dataset of 1000 frames (and 2 seconds), the swimmer swam 163.84 µm. This relates to an average stroke amplitude of $A_{loc\_ind} = 2.48\,\mu m$ which includes the full proportion of the stroke (both power and recovery) relating to the localised velocity (V_{loc_ind}). Whereas, if purely observing the net global motion, the net displacement per stroke was found to be $A_{net\_ind} = 1.44\,\mu m$.

4.2.3.5 Local mean square displacement

With the additional data captured at the local timescale, it is possible to apply the mean squared displacement methods detailed in Section 4.2.2.4 and produce a localised MSD. Figure 4.14 shows the theoretical movement of *D. salina* and the regions the swimmer will go through, including the back and forth motion followed by the persistent model regime [107, 290]. Initially the first ballistic region is reached which is at very small timescales,

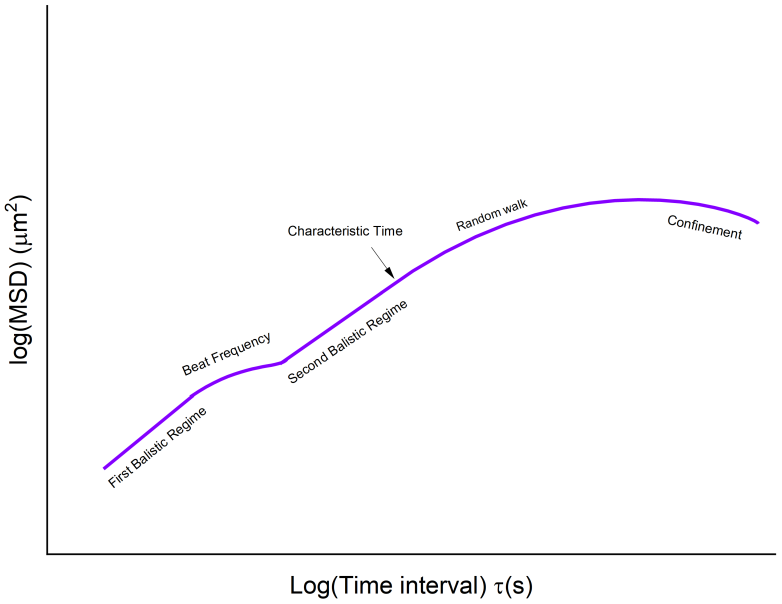

Figure 4.14: Approximate model of a flagellated puller swimmer's MSD with τ, denoting different regions dependent on time interval. Initially, the first ballistic region is captured relating to the instantaneous velocity. This transitions to the second ballistic region at an interval related to the beating frequency. The second ballistic region is characterised by the net velocity. With sufficient turning events, the swimmer will display random walk like behaviour and if under confinement α will fall below 1 [107, 290].

$\tau \ll t_s$. In this region, the individual strokes can be defined. Due to the small timescales the motion of the swimmer is mostly linear, hence the MSD takes the form of the power-law with an exponent close to 2.

The first ballistic region ends as the time scales nears the inverse of the beating frequency. At this value the MSD stops its sharp incline as the effects of the whole beating stroke are encompassed by the increased time scale. An approximation of the beating frequency can be taken from the plateau of this region.

The next region after the time interval has passed the inverse of beat frequency is the second ballistic region, where the MSD increases rapidly again. As the time scale increases the back and forth motion is not visible and it becomes too great to capture. This region

and above has been defined as the net motion of the swimmer in this work. Again, this region can be fitted to a power-law due to its ballistic nature.

After a certain time, the swimmer will likely make a turning event. This is defined by the characteristic time. With significant turning events taking place with a sufficiently large system, it enters a new region likened to a random walk. Here the MSD is linear and the stochastic nature of the swimmer's turning and tumbling is captured. If the swimmer is in a confined container, then α will fall below 1.

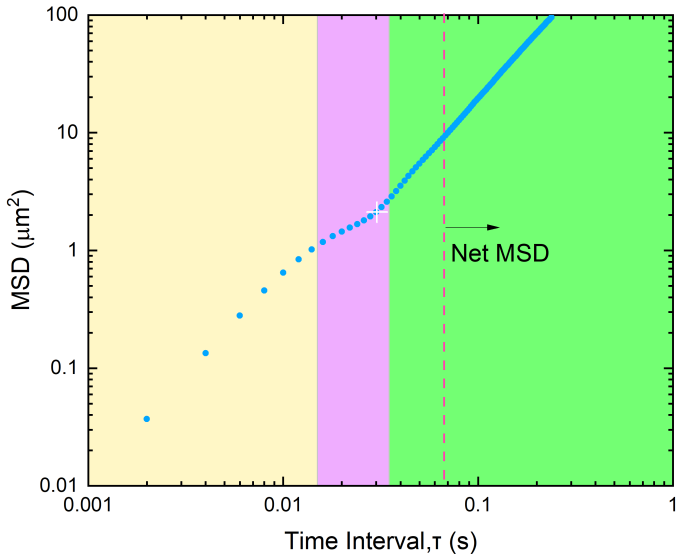

Figure 4.15: Local MSD with τ of individual swimmer. MSD shows two distinct regimes with transition period (pink background) in between characterised by the beating frequency of the swimmer. Below the transition period the swimmer is characterised by local motion (yellow background) and above the net motion of the swimmer (green background). The white cross represents the beating frequency calculated using FFT methods and the Pink dashed vertical line the start point of the net MSD taken as its lowest time interval based on a frame rate of 15FPS in the global net measurements.

Figure 4.15 shows the MSD consisting of the data set of the full $500FPS$ data across the range of time intervals analysed. Compared to the net MSD, the localised MSD extends the

data to lower time intervals with the data above a time reference of 0.067 s characterising the same data represented in the net MSD.

Fitting the two regimes to a power-law and taking their exponents as in Section 4.2.2.4 gives an effective diffusion coefficient of 2537 and exponent of 1.788 in the localised region. The net motion fits to a coefficient of 1344 and exponent of 1.845. Thus, showing highly ballistic motion in both the regimes analysed.

Whether this method is an appropriate method for calculating the beating frequency is debatable. The beat frequency (calculated through FFT methods, Section 4.3.2.1) is represented in Figure 4.15 by a white cross. Clearly it lies within the transition region, but defining a specific point would require further understanding.

4.2.4 Conclusion

In this section, the methods of analysis have been introduced in regard to the swimming properties of an individual swimming alga. The net swimming velocity was seen to be $V_{net} = 56.33\,\mu\mathrm{m\,s^{-1}}$ with other methods such as track analysis, windroses and MSDs all utilised to quantify the swimming dynamics. A high-speed camera was utilised to captured the full back and forth swimming dynamics *D. salina* utilise to progress through the medium they are suspended within. From this data, dynamics of the individual power and recovery strokes and the beating frequencies were quantified and analysed. For the individual alga it was seen to swim with a much greater velocity if the full strokes were encompassed ($V_{loc} = 81.92\,\mu\mathrm{m\,s^{-1}}$) and the power stroke was seen to be 3.76 times more efficient than the recovery stroke for a single stroke in terms of the displacement covered in each stroke.

4.3 Analysis of algae population in medium

The following section focuses on the full population of the swimming algae, taking the analysis from the preceding section and applying it to each individual swimming track.

Thereafter, if required, the average across the population is conducted to quantify the dynamics of *D. salina*. Thus giving better statistics and giving more representative data of the swimming behaviour of the algae. Observations for this stage were undertaken with the algae simply swimming in their medium, a water-like solution in terms of viscosity. Dilute suspensions were considered and alga to alga interactions were removed from the analysis so purely individual motion akin to the analysis of the previous section for a single alga was undertaken.

4.3.1 Net motion of full population

4.3.1.1 Swimming velocity

The instantaneous swimming velocity of the algae was calculated on a frame by frame basis across the entire populating as described in Section 4.2.2.2. The resultant set of instantaneous velocities were then averaged as in Equation 4.4 across the full spread of the population, where in this case $N = 19363$. Interacting algae and unnatural swimming tracks were removed from this data, i.e. spinning, trapped or non-motile.

With no external influences and zero net underlying flow, an average net swimming velocity of $V_{net} = 49.55\,\mu\mathrm{m\,s^{-1}}$ was seen across a large population of algae (176 alga). This can also be translated to approximately 4 body lengths per second. Values in the literature range depending on the situating and definitions, but the consensus is a swimming velocity of approximately $50\,\mu\mathrm{m\,s^{-1}}$ for *D. salina* [43,106]. Therefore, it can be said that the results are in agreement with the literature.

The histogram of the instantaneous velocities (Figure 4.16) follows an approximate bell curve, with the majority of swimming velocities close to the average velocity of $V_{net} = 49.55\,\mu\mathrm{m\,s^{-1}}$, with the tails reducing to the maximum and minimum velocities. The peak distribution of the histogram is between $55 - 57.5\,\mu\mathrm{m\,s^{-1}}$, slightly higher than the average velocity as the histogram shows a biased weighting to swimming at the slower end relative to the histogram peak compared to the faster.

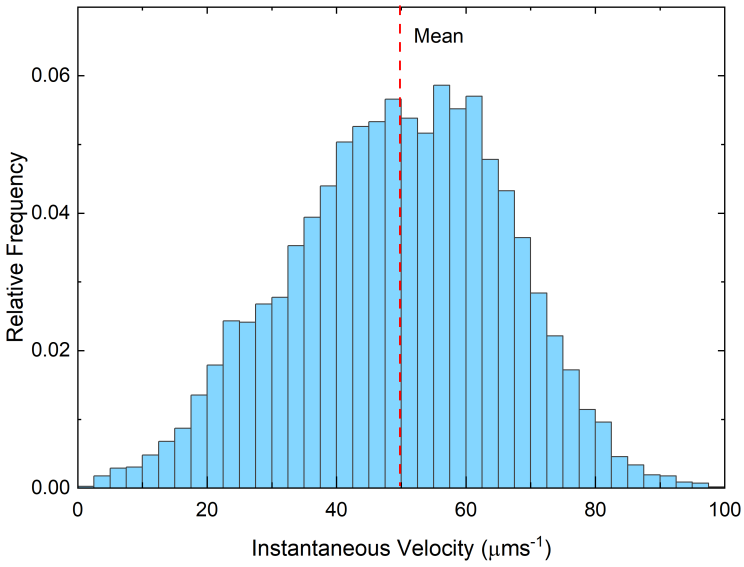

Figure 4.16: Swimming velocities represented as a histogram showing the spread of instantaneous velocities (v_{in}) of the entire population of swimmers active in just the medium. The peak is slightly greater than mean velocity with velocities decreasing either side of the peak, creating a slightly skewed bell curve. The plot consists of 19363 individual points analysed from 176 algae tracks.

The Standard deviation for the entire population was calculated as 16.5 $\mu m\,s^{-1}$. This high spread in velocities is related partly due to the time in the stroke the positional reference is captured, along with variability in the algae physiology and characteristics across the whole population. Further, only 2D motion was captured in the x, y plane and motion in the z direction was not quantified.

As well as analysis of the instantaneous velocity spread (Figure 4.16) it is also helpful to understand the difference across individual swimmers in the population. A histogram analysis of individual algae swimming velocities (Figure 4.17) reveals similar results to the previous analysis (Figure 4.16). Again, a peak around the average swimming velocity is clear, with the swimmers either side following an approximate bell curve. From the histogram, it can be seen that the swimmers generally swam with an average velocity

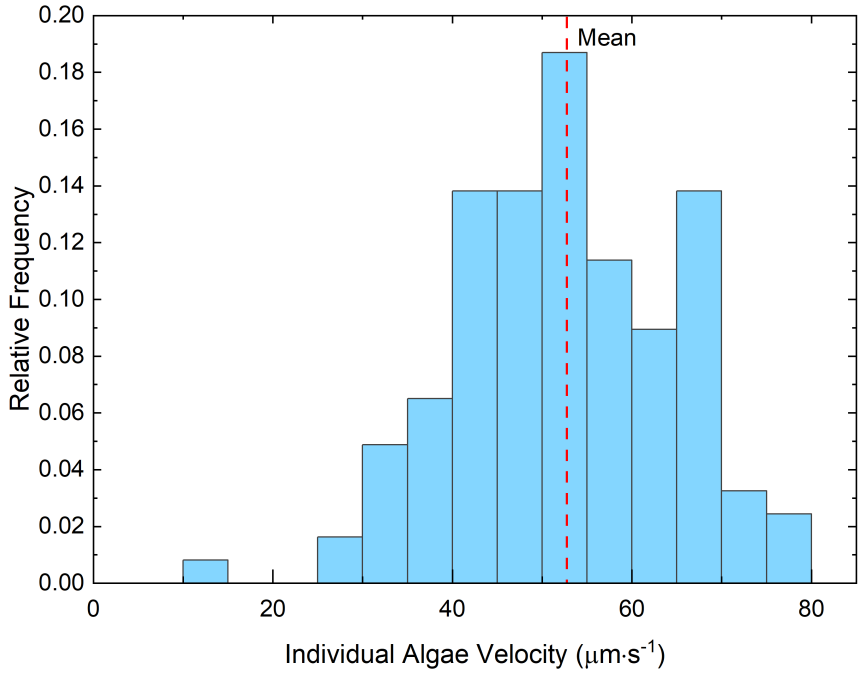

Figure 4.17: Individual swimming velocity histogram, comprised of the average velocity of each swimming alga's track (176 tracks). The distribution follows as similar trend seen in Figure 4.16 with a peak close to the mean value, albeit with less spread in the data as the variations in v_{in} are masked by the individual swimming velocity

greater than $25\,\mu m\,s^{-1}$ and are unlikely to swim at an average velocity of higher than $80\,\mu m\,s^{-1}$.

The average of each individual swimming algae velocity was found to be $V_{pop} = 52.69\,\mu m\,s^{-1}$, slightly higher than the net velocity (V_{net}). An individual average is expected to be higher as this calculation gives a preferential bias to algae that stay in the frame for a shorter period. Naturally, faster swimmers will tend to swim in and out of the frame compared to slower swimmers, hence the slightly higher velocity seen in this average. Both methods of calculating the velocity are suitable to report.

Comparing the two different methods of analysing of the velocities, both have advantages and disadvantages and give a different insight into the nature of the swimmers. Averaging across the full instantaneous velocities gives an average across the whole pop-

ulation and shows a bulk spread negating any bias dependent on track length. However, some inconsistencies within the data (frame jumps) can arise, although these are small in the scale of data analysed and should even out over the track. This is the main method used for reporting swimming dynamic averages throughout this work. The method of comparing an average of individual velocities while introducing a bias to shorter track lengths gives extra details into the spread of velocities across the population. For the uncertainty of the swimming velocity, the population standard deviation is used as it gives a better representation of the spread in the swimming dynamics.

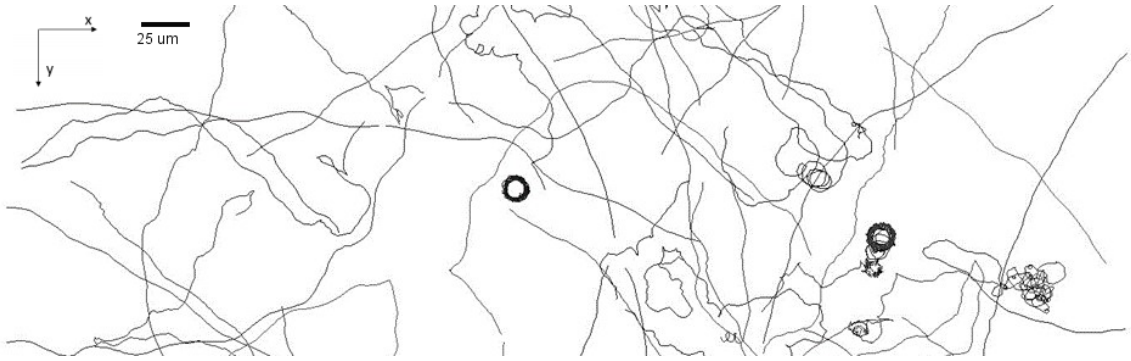

Figure 4.18: Example of algae swimming tracks. An apparent persistent random walk method of motility seems present on examination. Note, tracks that follow a continuous circle and do not progress from starting point, are deleted from the analysis.

4.3.1.2 Swimming orientation

Figure 4.18 shows typical swimming paths of the *D. salina* in the microchannel. Qualitatively, observations show an apparent persistent random walk motion (section 4.2.2.5) with swimming paths that are generally straight with no sharp 'tumbles' that would be present in run and tumble motion (Section 2.4.3).

When the swimming directions of the algae are analysed in a windrose format (Figure 4.19), a general random distribution of swimming velocities is observed with no preferential direction. Thus, it can be said there is no correlation between swimming velocity and orientation, with a fairly uniform spread of velocities with regard to swimming angles in

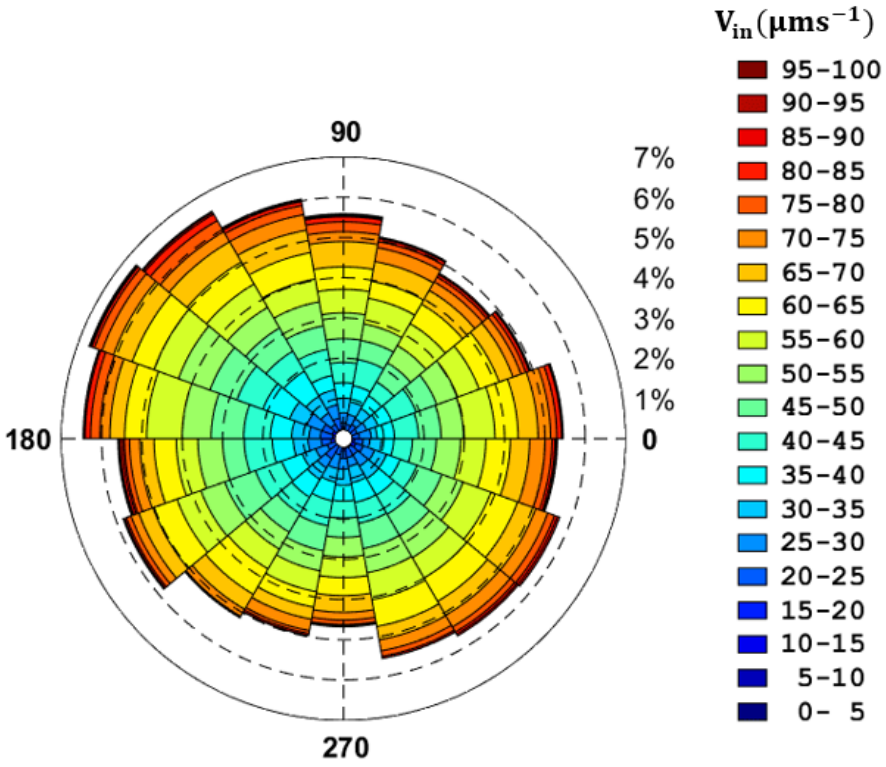

Figure 4.19: Windrose showing orientation and instantaneous velocity across population of swimmers in the medium. The percentage values relate to the relative frequency of that particular swimming direction and the scale to the instantaneous velocity.

the discussed analysis.

4.3.1.3 Net mean squared displacement

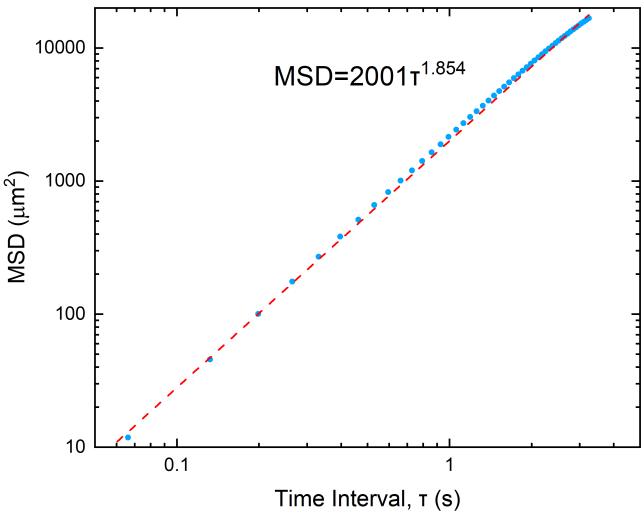

Figure 4.20: (A) Log-log representation of mean squared displacement (MSAD) as a function of the time interval of algae population in the medium. A maximum times interval of 3.2 s is taken, which corresponds to the minimum frame interval of tracks. Data follows a power-law trend comparable with ballistic active motion. The red dashed line denotes the simple power-law fit (Equation 4.9).

The net MSD of the full population, as calculated in Section 4.2.2.4, gives further quantitative understanding into the swimming motion of *D. salina*. To account for the full variation in population, an ensemble average MSD is performed. This averages the calculated individual MSD values at the related time intervals (τ) across the algae population and thus combines them into a singled averaged plot encompassing the full proportion of the swimming tracks.

The net MSD (Figure 4.20) shows the MSD across small time intervals in the ballistic region of the alga's swimming motion. To ensure continuity, the maximum time interval was taken as $\tau < 3.2\,\mathrm{s}$, as this was the minimum track length for data recorded. This corresponds to 50 frames. The data fits well to a power-law (Equation 4.9) giving an

effective diffusion coefficient of 2018 and exponent of 1.89.

4.3.2 Local motion of full population

The following section describes the local motion of the algae population, characterising the back and forth motion and the individual power and recovery strokes. The analysis methods used are as described in Section 4.2.3.3.

4.3.2.1 Beat frequencies

For a swimming alga with no external influences, in their medium with no added agents, the average beating frequency was found to be $f_{BF} = 29.97 \pm 2.82\,\text{Hz}$ across all the alga population (50 tracks/75000 frames). This frequency relates to a time per stroke of $t_s = 33.37\,\text{ms}$. The beating frequency of *D. salina* has been reported in literature as between 25 and 50 Hz [50, 106], with the analysis carried out here falling within this value. However, this value is not reported very regularly within the literature for *D. salina*, with limited references stating the above range.

In some cases the frequency of *D. salina* is approximated to the frequency of another model swimmer *C. reinhardtii* which swims with at a frequency of $50 - 60\,\text{Hz}$ [24, 67]. Clearly it can be seen this is not a suitable assumption or association to make and the beating frequency of *D. salina* is considerably reduced compared to *C. reinhardtii*.

A significant finding of the beating frequencies is related to the spread or standard deviation, which is noteworthy as it is comparatively small compared to the velocity. A histogram comparing the beat frequency spread and velocity spread can be viewed in Figure 4.21. Hence, the majority of an algae population beat at very similar frequencies, which does not translate or relate to the overall velocity of the swimmer.

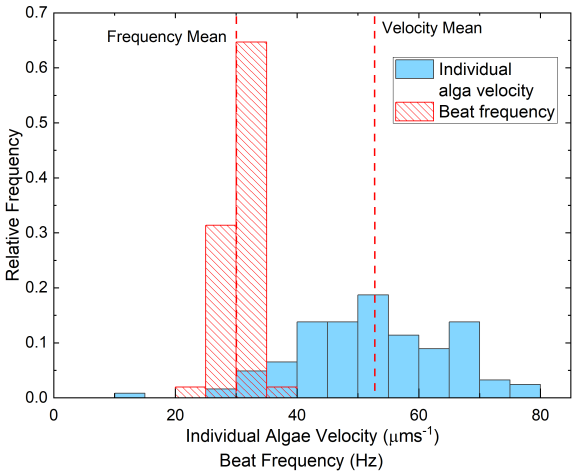

Figure 4.21: Distribution of individual algae velocities and beating frequencies. Velocities display a greater spread than the beating frequency, showing a dependency for the algae to poses remarkably similar beating frequencies independent of velocity.

4.3.2.2 Stroke dynamics

The analysis of the stroke dynamics is conducted as described in Section 4.2.3.2.

Time *D. salina* was found to spend on average 72.02% of their time in the power stroke, giving an average time per power stroke of $t_{pow} = 24\,\text{ms}$. Conversely, they spent 27.98% of their stroke in the recovery stage, with an average time per recovery stroke of $t_{rec} = 9.3\,\text{ms}$. The stroke is weighted in a way that favours the power stroke, which is significant for the swimmer as an increased efficiency in power over the recovery stroke is desirable to achieve the most effective stroke and increased net motion. However, this is not a method of breaking the time reversibility of Newtonian low Reynolds number flows (Section 1.3.2).

Velocity As the nature of the stroke of *D. salina* is weighted to provide the best forward momentum, the power stroke velocity would be expected to be much greater than recovery. In a water-like medium, *D. salina* moved forward in their power stroke with an average body velocity of $V_{pow} = 97.32\,\mu\text{m}\,\text{s}^{-1}$. In the recovery stage of the stroke,

the average velocity was found to be $V_{rec} = -61.04\,\mu m\,s^{-1}$ where the negative implies movement in the posterior direction to the overall swimming direction. The ratio between the power and recovery stroke velocity was seen to be 1.6 in favour of the power stroke.

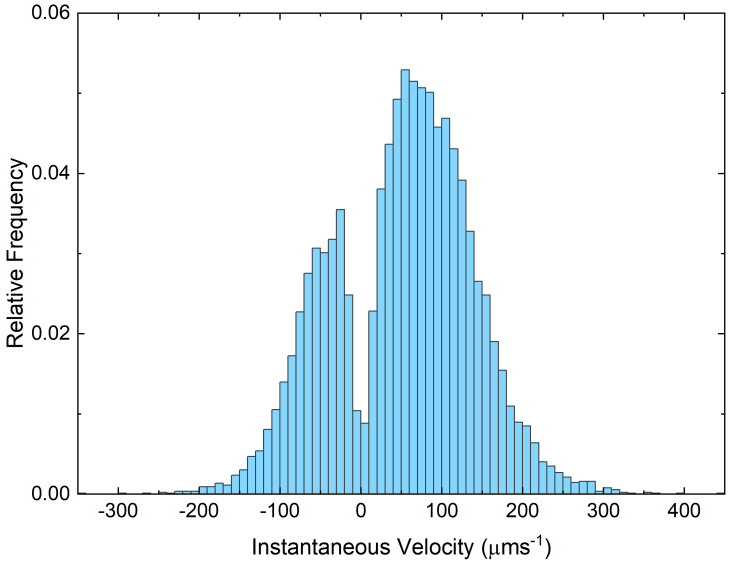

Figure 4.22: Velocity (v_{in}) histogram across power and recovery strokes, with positive velocities relating to the power stroke and negative to recovery.

Figure 4.22 shows the velocity histogram distribution for the power and recovery strokes. From the reference at $0\,\mu m\,s^{-1}$, the two strokes follow a similar distribution with a sharp increase up to a peak then a reduced tail to the extreme velocities. The relative velocity enhancement of the power stroke compared to recovery is clear, with the swimmer moving significantly faster overall through the power stroke for a much greater length of time. The standard deviations for power and recovery stroke was seen to be $\pm 57.9\,\mu m\,s^{-1}$ and $\pm 43.02\,\mu m\,s^{-1}$ and for the overall localised data, $\pm 86.69\,\mu m\,s^{-1}$.

Taking purely the net velocity of the swimmer, the average was found to be $V_{net} = 49.55\,\mu m\,s^{-1}$. However, if both portions of the stroke are examined together, the average swimming velocity was found to be $V_{loc} = 87.2\,\mu m\,s^{-1}$. Thus, these swimmers cover

significantly more distance than it might appear when using conventional methods.

Comparing the local signed velocity to the net velocity measured at a conventional frame rate outputs only slight variations between the two methods. The net velocity using the conventional camera was found to be $V_{net} = 49.55\,\mu\mathrm{m\,s^{-1}}$ and signed velocity with high frame rate camera $V_{sign} = 52.7\,\mu\mathrm{m\,s^{-1}}$. It should be noted that these values are taken from different algae populations, but the similarities between these values give backing to the localised velocity methods.

Amplitude The body amplitude represents the distance travelled in each portion of the alga's beat cycle. The same definition and subscripts as velocities are utilised for the amplitudes with velocity definitions defined in Section 4.2. As with all other calculations in this section, the values are taken across the whole population and thus may vary depending on individual algae. In the power stroke *D. salina* where found to move forward on average $A_{pow} = 2.34\,\mu\mathrm{m}$ and rearwards $A_{rec} = -0.57\,\mu\mathrm{m}$ in recovery giving a resultant net gain of $A_{net} = 1.77\,\mu\mathrm{m}$ per stroke. As with the other analysis, the power stroke is dominant in relation to the recovery stroke. For an average stroke the swimmer moves 4.1 times further in the power than the recovery stroke, a credit to the effectiveness of their swimming stroke.

Summary A summary table of the relevant beating parameters of *D. salina* in the medium can be seen in Table 4.3.

Table 4.3: Swimming characterises (time, velocity, amplitude) of *D. salina* swimming in the medium, calculated by different descriptors descriptor in Table 4.2

Characteristic / **Descriptor**	**Time** (ms)	**Velocity** ($\mu\mathrm{m\,s^{-1}}$)	**Amplitude** (μm)
Net	33	49.55	1.77
Signed	N/A	52.70	N/A
Local	N/A	87.20	2.91
Power	24	97.32	2.34
Recovery	9.3	−61.04	−0.57

4.3.2.3 Local mean squared displacement

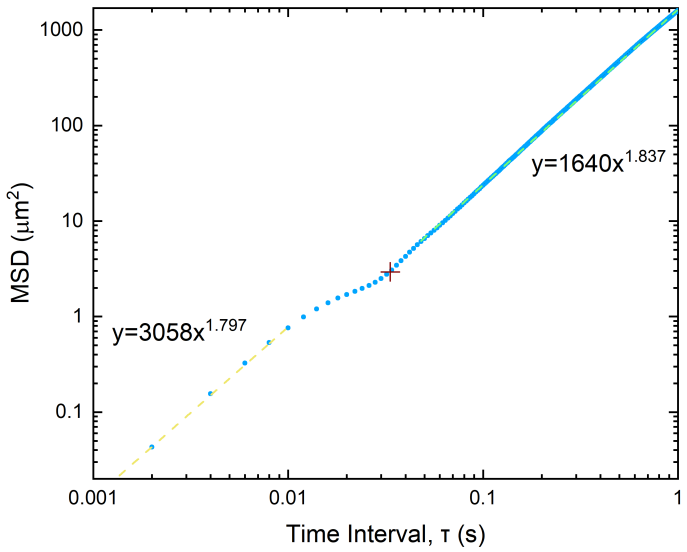

Figure 4.23: Local MSD across population of algae in the medium. Two regimes represented by yellow and green power-law fit with transition region related to the beating frequency. The red cross corresponds to the beating frequency calculated in Section 4.3.2.1.

The localised MSD again shows the two regimes discussed in Section 4.2.3.5, with the beating frequency the defining feature of the transition region. The fit of the two regimes shows ballistic behaviour is present in both regions. The red cross shows the beating frequency as found in Section 4.3.2.1 and appears to be towards the upper end of the transition period.

4.3.3 Viscous body drag

The nature of low-Reynolds number swimming simplifies drag calculations for the body. As inertia effects are not present, all forces can be assumed to be instantaneous and diminish instantaneously. Further, the only forces acting on the body of the swimmer are the drag based thrust provided by the flagella, buoyant force (sometimes known as Archimedes

force), gravitational force and viscous drag of the body. The body of the swimmers is too large to be affected significantly by Brownian motion [294]. Both buoyancy force and gravitational force can be cancelled out and assumed negligible, as shown below:

The buoyant force is defined as

$$F_b = \rho_f V_B g \tag{4.12}$$

where ρ_f is the density of the fluid medium and V_B the volume of the body. Given the equivalent diameter of the cell is 14 µm, the resultant buoyant force is ~ 1.4 pN which is equivalent to the weight of the cell (~ 1.5 pN [295]). Therefore, these cancel and thus, the swimmer is seen as essentially neutrally buoyant.

As a result, the two relevant forces acting on the body of the swimmer are the propulsion caused by the drag of the flagella as they move through the stroke and opposing this, the viscous drag of the body (force dipole). These force act in the opposite directions and reverse during the stroke stages (power and recovery).

If a spherical body is assumed, the viscous drag can be calculated using

$$F_B = 6\pi\eta r_B V_{loc} \tag{4.13}$$

where η is the viscosity of the suspension media, r_B is the equivalent radius taken from the average of the minor axis of the algae and V_{loc} is the average local velocity of each alga. The velocity is taken as the average velocity inclusive of the power and recovery and thus the drag is calculated in terms of the full stroke.

For the swimmer in their water-based medium, an estimated viscous body drag was calculated to be $F_B = 12.7 \pm 1.26$ pN. The individual strokes display viscous drag forces of $F_{B\_pow} = 14.1 \pm 1.26$ pN and $F_{B\_rec} = 8.86 \pm 1.4$ pN for power and recovery strokes respectively. The differences in the velocity of the power and recovery strokes is the reasoning behind the variation in viscous body drag between strokes.

As *D. salina* can be modelled as a force dipole, it is possible to assume the viscous drag force will be equal and opposite to the propulsion force generated by the two flagella. For *C. reinhardtii* the propulsion force has been measured as $23 \pm 5\,\mathrm{pN}$ using force sensors and trapping methods [275]. The method of calculation for this value is much more accurate than utilised in this work, but it can still be related. The variation between swimmers is likely a result of the increased velocity *C. reinhardtii* swim with, which is a result of their high beat frequency and different stroke dynamics.

4.3.4 Conclusion

The swimming dynamics of a population of *D. salina* in a water-based medium has been analysed in this section. Numerous methods were utilised to characterise both the net swimming dynamics and individual stroke dynamics. The average velocity of *D. salina* was found to be $V_{net} = 49.55\,\mu\mathrm{m\,s^{-1}}$ a value in concert with the literature. *D. salina* was found to beat at a frequency of $f_{BF} = 29.97\,\mathrm{Hz}$ substantially less than the morphologically similar *C. reinhardtii*. To achieve its forward motion, the power stroke of *D. salina* must have a greater efficiency than the recovery stroke. This value was calculated to be 4.1 times with the amplitude through the power stroke greater than recovery by this multiplication, which is a result of an enhanced stroke pattern in the power stroke.

Chapter 5

Swimming in viscous fluids

5.1 Chapter overview

The following chapter details the effects of viscosity on the swimming behaviour of *D. salina*. The same processes as descried for the population in the medium (Section 4.3) was carried out across the spectrum of viscosity ranges measured ($0.0014 - 0.04\,\mathrm{Pa\,s}$). For each viscosity concentration, the quantity of the data captured follows the approximate values described in Table 3.5. For some concentrations only the net swimming data was captured. Further to using Ficoll as a viscosifying agent, glycerol was used to increase the medium viscosity. However, this was found to influence the osmotic pressure within the algae and render the algae non-motile. A summary of these results can be found in Appendix E.

5.2 Viscosity modifying agent

The viscosifying agent used to enhance the viscosity of the medium was Ficoll PM400 (Sigma-Aldrich), a non-toxic, non-ionic, sucrose polymer that is known to increase viscosity without substantial density change or effects on organism behaviour aside from the swimming changes due to viscosity [24, 151, 152]. Ficoll maintains the mediums Newtonian properties independent of the concentration. It was provided in a dry powder and

was combined with the aqueous medium and slowly mixed to create the desired solution concentration as described in Section 3.3.2.5. As Ficoll is extremely hydrophilic, solutions of high concentrations could be produced, up to 50% [222]. The maximum concentration used in this work was 40% which was diluted down to 20% for the experimentations.

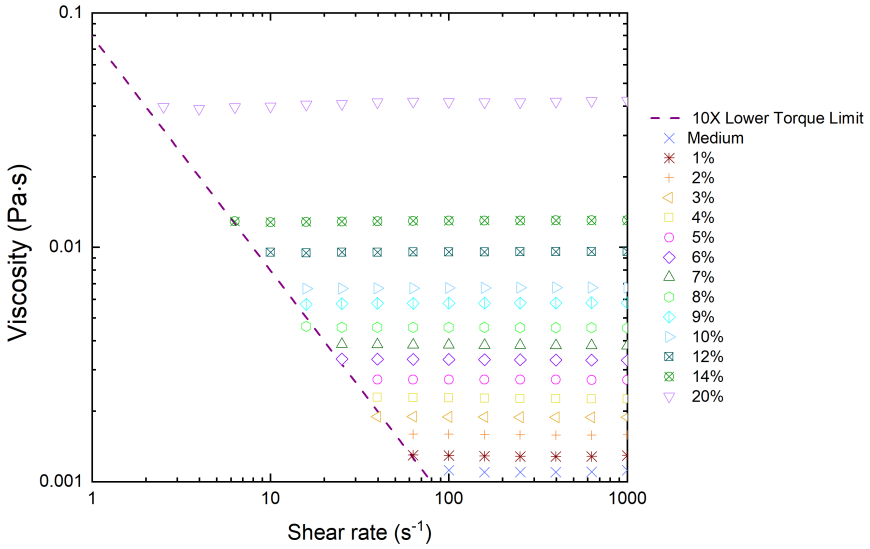

Figure 5.1: Flow curves showing the steady shear viscosity of Ficoll solutions used to vary the medium viscosity. All solutions show Newtonian behaviour, and an increase in viscosity is observed as concentration increases. Legend refers to Ficoll concentration percentage. The minimum measurable torque represented by the purple dashed line is calculated from Equation 3.10.

Rheological characterisation of the Ficoll solutions were conducted as described in Section 3.3.3.3 for a range of concentrations up to a maximum of 20%. Figure 5.1 shows the steady shear viscosity data for the modified media for Ficoll concentrations, with Figure 5.2 showing the average viscosity against the concentration. The viscosity ranged from 0.0014 Pa s in the medium with no addition of Ficoll to 0.04 Pa s for 20% Ficoll, with the increase of viscosity with concentration clearly non-linear. All fluids used in the experiments reported in this chapter exhibited a Newtonian behaviour.

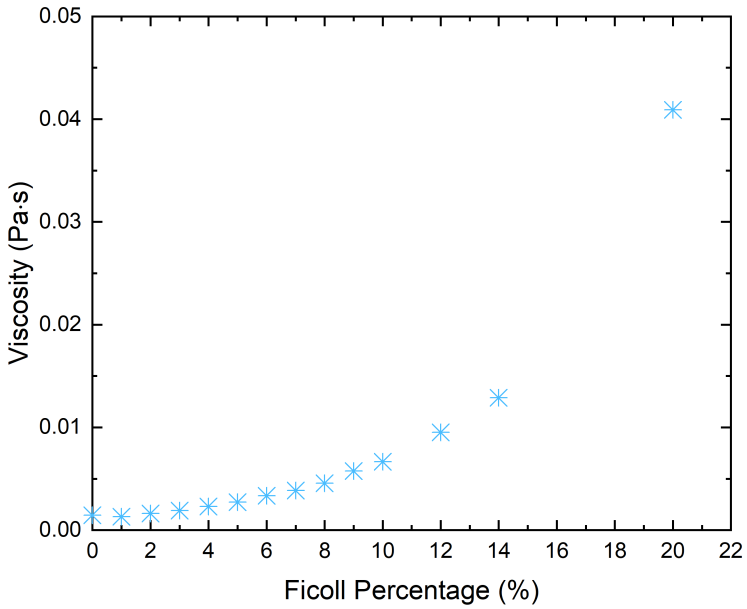

Figure 5.2: Average Ficoll viscosities taken across a range of steady state shear rate values plotted against the Ficoll concentration of the solution. The viscosity increases with a non-linear trend.

5.3 Reduced nutrient swimming

By the addition of Ficoll and other rheologically active agents, the concentrations of salts and other nutrients in the medium would naturally be reduced. For example, introducing 20% Ficoll to the medium reduces the nutrients and salts available to the algae by this percentage. To ensure any changes in swimming dynamics were primarily as a result of the mediums rheological properties and not as an effect of changes to the mediums additives, validation experiments were carried out. While the effects of salts and nutrients of the medium has been extensively researched [96, 198, 296] in regard to the growth of an algae culture, the effects this has on the swimming dynamics is unknown to our knowledge, especially for *D. salina* .

To provide insight into these effects, a new medium was prepared with de-ionised water used to reduce nutrient concentrations to a value that would be experienced at the greatest

concentration examined (Ficoll 20%). With the algae suspended in the reduced medium, the standard experimental procedures for velocity and beat frequency were conducted. For the effects of the changes in the medium nutrients to be negligible or not affect the algae, the final results should have matched or been similar to that of the medium.

Under the conditions of a reduced medium, *D. salina* swam with a velocity of $48.67\,\mu\mathrm{m\,s^{-1}}$ and exhibited a beating frequency of 31.64 Hz. Both of the captured dynamics were within the error for algae swimming within the medium with full nutrients. Thus, it was felt that the effects of different fluid nutrient levels did not have a large notable influence on the swimming dynamics of *D. salina* in the short time of the experiential window. If larger length scales were examined the reduced nutrients may eventually have a clearer effect on the algae, but for the experimental process conducted here this was not the case.

5.4 Net viscous swimming dynamics

5.4.1 Swimming velocities

As has already been discussed in Section 2.3, the effects of viscosity on a swimmer are not necessarily trivial and can be heavily dependent on the swimmer's motility method. For *D. salina*, the net swimming velocity (V_{net}, taken as an average of v_{in} data as in Section 4.2.2.2) response to varying concentrations of Ficoll in the medium is displayed in Figure 5.3. For the viscosities examined, the swimming velocities exhibited an essentially monotonic decreasing trend with increasing viscosity. The decrease in velocity scales proportionally to the inverse of viscosity following an approximate power-law $V \propto \eta^{-1}$ as shown in the inset of Figure 5.3, a response also observed in *C. reinhardtii* [24,67]. Such a relationship suggests that *D. salina* operate at a constant thrust [67]. This would tend to the assumption that the added viscosity impacts the power and recovery stroke similarly, and no significant changes in the stroke gait are apparent, apart from the viscosity induced velocity reductions. Further, any change in velocity is purely down to viscous effects on the flagella and body. However, only net movement is represented by this measurement

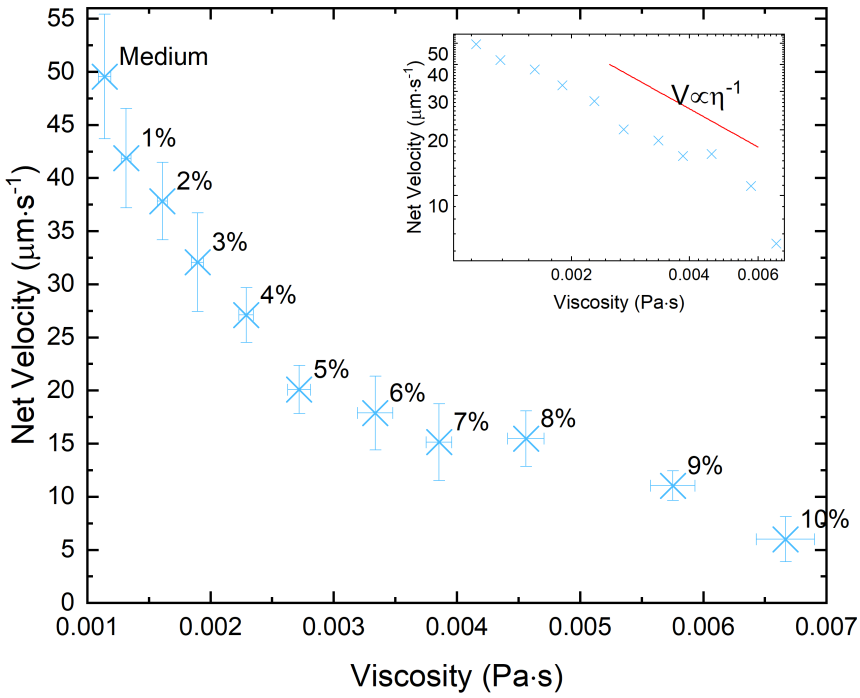

Figure 5.3: Swimming velocity (V_{net}) across population suspended in various Ficoll concentrations. Velocity decreases essentially monotonically with increasing viscosity. Data labels correspond to the percentage of Ficoll. Error bars in x show uncertainty in rheology measurement and y error bars correspond to the standard deviation taken from the individual variations across the full population, representing the variation in swimming velocity across the population. Inset shows data on a log-log scale, with a power-law with exponent of -1 also plotted.

of the velocity, and it does not incorporate the back and forth motion of a beating stroke. This will be discussed in more detail in Section 5.5.1.

Through the use of probability distribution functions, the spread and ranges of swimming velocities can be examined and compared in more detail across viscosity ranges. A log normal fit is applied to the instantaneous velocities for each concentration to allow comparison between cases. Figure 5.4 shows at low viscosities, a wide spread of velocity distributions is observed with a high standard deviation. The peak of the curve is relatively low with a fairly symmetric curve. As the viscosity is increased, the distribution fit shifts towards lower velocities with the distributions becoming narrower. At the highest

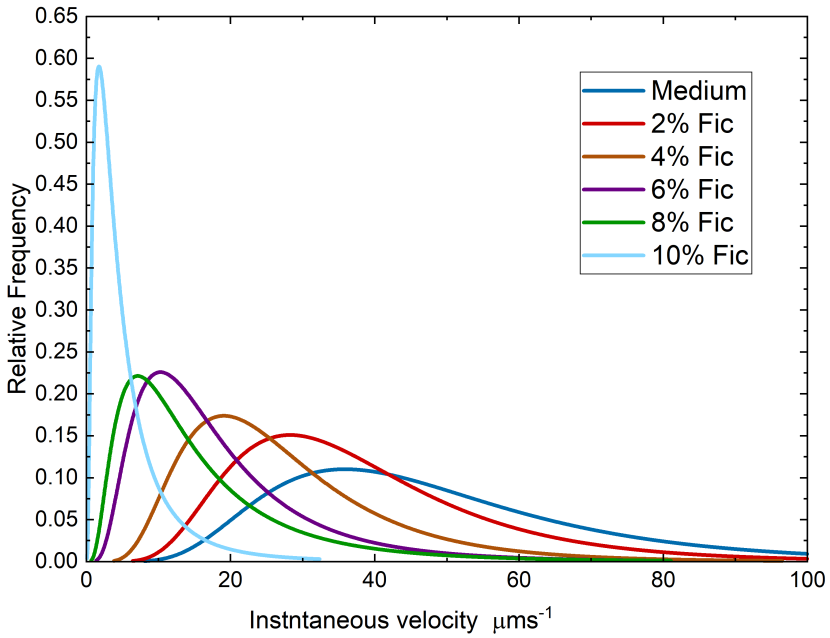

Figure 5.4: Log normal distribution of instantaneous velocities (v_{in}) across populations of swimmers in differing viscous solutions, with concentration percentage of Ficoll denoted in legend. As viscosity is increased, algae tend towards, much reduced motility with decreased spread in velocity distributions.

viscosities measured, the velocity distributions display a very narrow tall peak with a tail of a very small number of algae swimming. All other viscous concentrations follow a similar expected trend, not shown on the above graph due to limited space.

5.4.2 Limitation of the algae swimming at high viscosities

Under conditions of high viscosity, the swimming velocity is greatly reduced, approaching effective non-motility as shown in Figure 5.5. However, a point of viscous non-motility, where the active motion of the entirety of the population has ceased due to the large viscous forces is not found.

The point at which the algae cease to move is of interest and can pose relevance in certain systems and give further detail into stroke dynamics, such as a stall force being

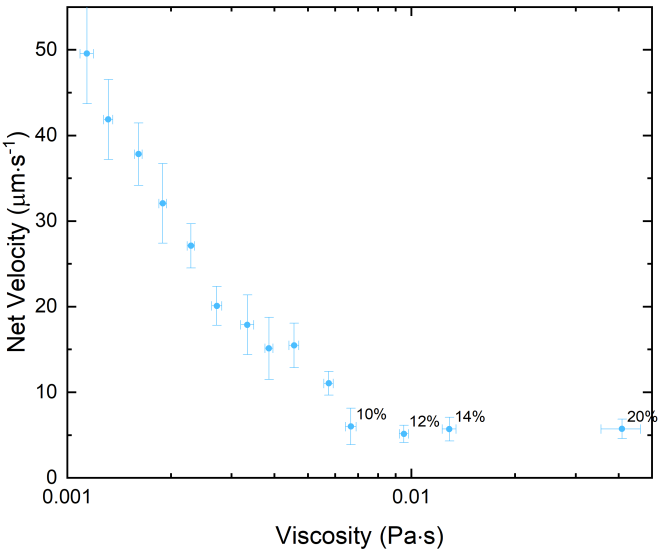

Figure 5.5: Swimming velocities in relation to viscosity with the inclusion of high viscous solutions showing apparent viscous plateau region. Note the log scale on x axis. Error bars correspond to rheological error and standard deviation across population.

present. In the analysis thus far, algae are classed as non-swimmer and have been removed from the analysis that swim below the non-swimming value ($< 3\,\mu m\,s^{-1}$) defined in Section 3.6.1.1. This is the primary reason for the plateauing region seen in Figure 5.5, as for the higher viscosities a greater number of swimmers were removed from the data leaving only those swimming slightly above the non-swimming value (Figure 5.6). Therefore, there is a difficulty in producing solid conclusions for these swimming velocities as there velocity is close to the experimental error.

Figure 5.6 shows the breakdown of the percentages of algae swimming at certain velocities across the Newtonian solutions analysed. For the general analysis of the swimmers, algae represented in red and blue were discounted and viewed as non-swimmers. If this metric is taken it has very little effect on the low viscosity ranges, but at the higher viscosities the number of active swimmers is greatly reduced. An apparent critical point of

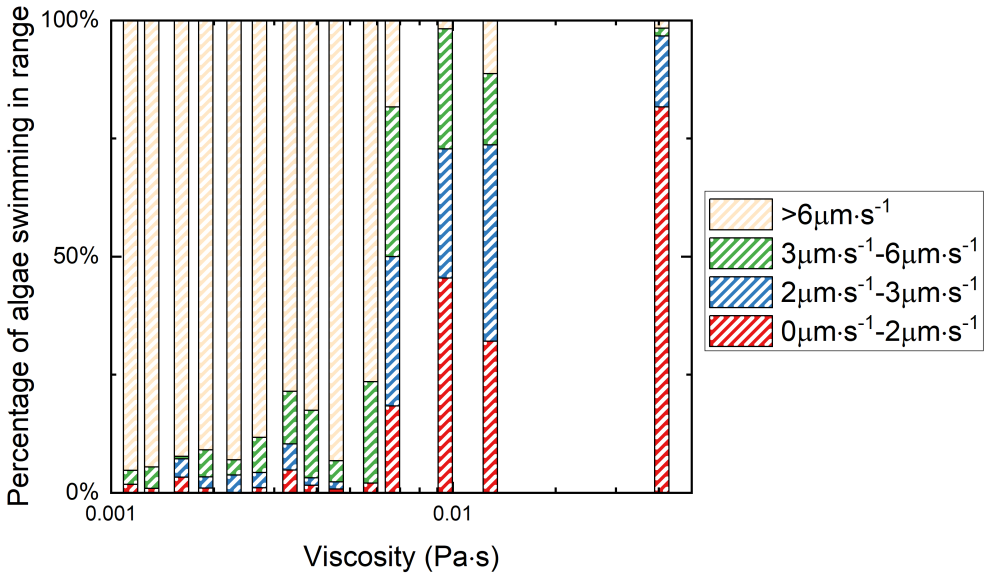

Figure 5.6: Percentage of algae swimming at different velocities. Legend represents range of net swimming velocities.

non-swimming is observed at a viscosity of 5.5 mPa s. This could be seen as a stall point or a point of viscous forces becoming too great, but it is not possible to conclude this for certainty since by this point velocities have reduced to a level close to the experimental limit of uncertainty [297].

Figure 5.7 gives an overview of swimming velocity when a different value the of minimum swimming velocity is defined as a threshold. All velocities exhibit a decrease as all tracked algae are included in this data, such as algae that might be dead or exhibiting unconventional swimming (spinning etc). For the lower viscosities, the change in non-swimming value makes little difference relative to the swimming velocity. However, this metric has the biggest effect on swimmers at the higher end of the viscosity spectrum. In this region, a gradual drop in the swimming velocities is observed in the cases analysed with decreases in the minimum swimming value. This could lead to the proposition that the swimmer is still following a viscous drag power-law decrease and the high viscosities do not affect their swimming stroke in any critical manner. Again however, nothing can

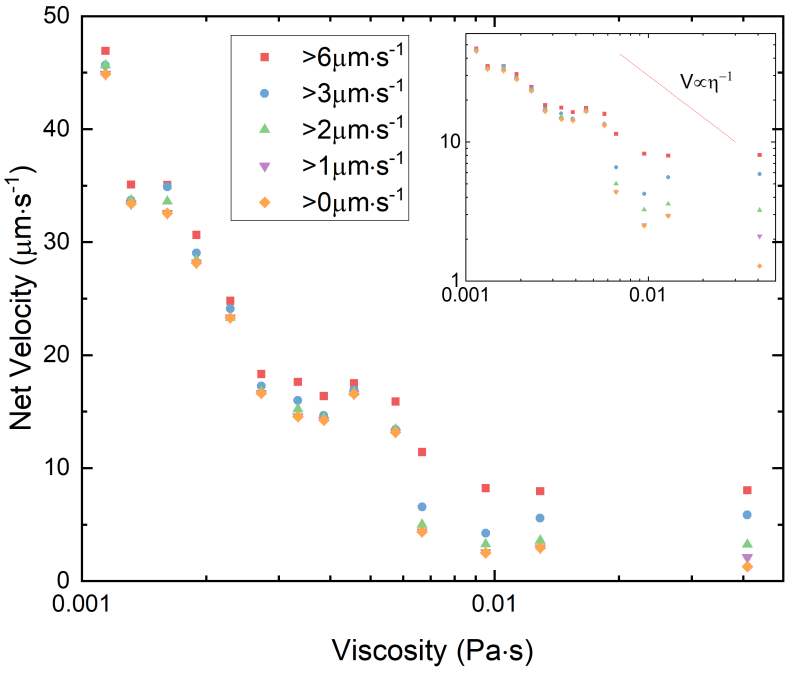

Figure 5.7: Net swimming velocities as a function of viscosity with varying threshold velocities considered defining non-swimming velocity (i.e. only algae swimming above this threshold are considered). Inset shows the same data in log-log scale.

be stated definitely due to the relative uncertainties at high viscosities.

One notable conclusion from this data is that despite the high viscosities there is still motility, albeit very slow and potentially not in a great number of swimmers [297]. This shows a clear point of non-motility across the population is not apparent and despite a number of algae becoming non-motile there is not a viscous limit that applies to the entire population for the range of viscosities analysed. However, more insight at a detailed level with enhanced optics to lower experimental uncertainties would be needed to increase the understanding.

5.4.3 Swimming orientation

The effects of viscosity have been found to alter the orientational preference and the swimming behaviour of some swimmers. Qu et al. [30] and Patterson [25] found that increasing viscosities altered the standard run and tumble patterns of *E. coli*. This was attributed to increased flagella bundling due to low rotation speeds at high viscosities. To examine the effects of viscosity on *D. salinas* orientation, the swimming paths and preferential direction were examined across viscosity ranges.

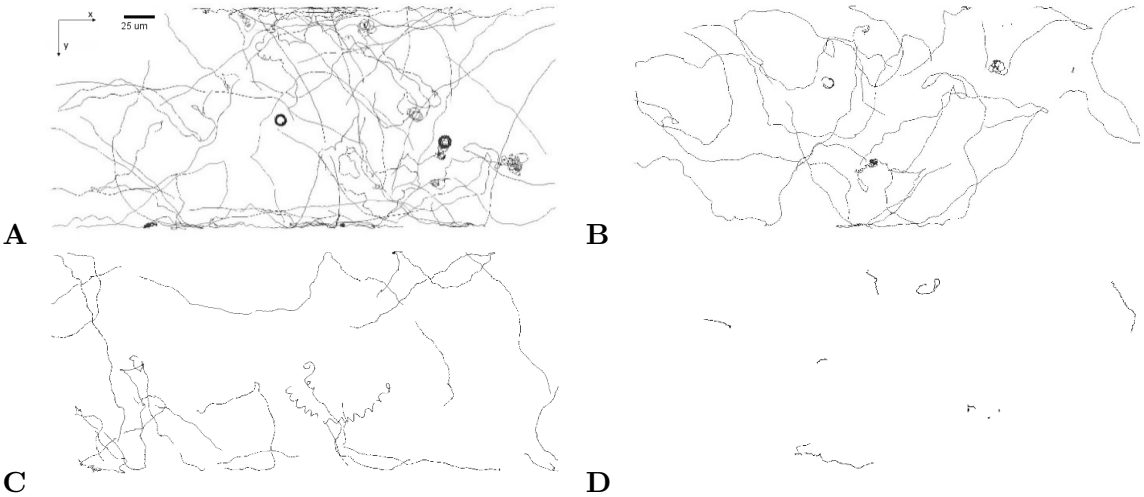

Figure 5.8: Example of paths of swimming algae with increasing viscosity in medium. A-D corresponds to $0\%, 4\%, 8\%, 12\%$ respectively. As viscosity increases, path lengths are reduced for the same time interval as the velocity decreases, but the overall nature of the swimmer's walk remain similar. Scale bar (A) is consistent across B-C.

When considering the effects of viscosity on the preferential orientation of *D. salina*, no clear orientational preference or change in swimming paths were observed. Qualitatively the swimming paths show an indication of persistent random walk across viscous ranges (Figure 5.8). The paths across all viscosities follow a stochastic motion, with no tendency for population migration or any significant changes in their swimming nature.

To examine swimming direction in a more quantitative approach, the swimming angles across the full population were analysed and compared. These can be viewed in Figure 5.9.

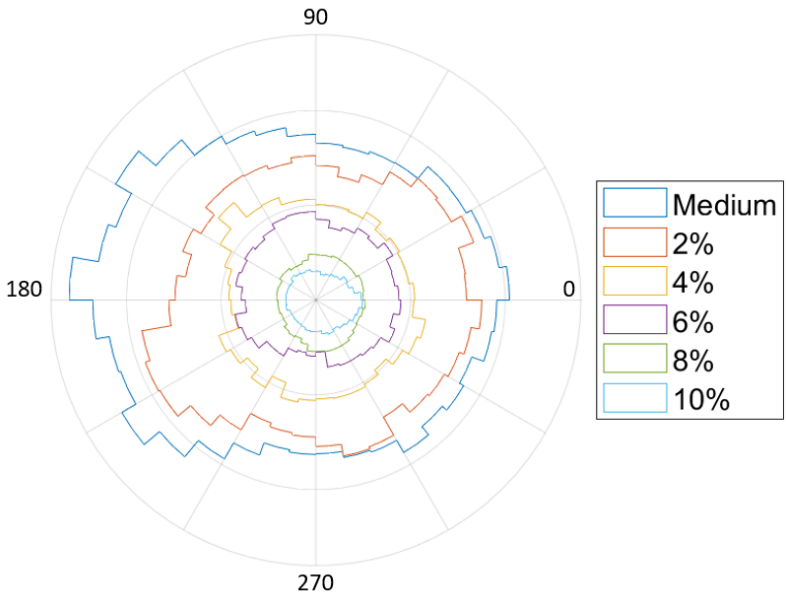

Figure 5.9: Swimming distribution of algae orientation in different viscosities. Each curve has been assigned an arbitrary multiplication value to separate different viscosities to allow the data to be plotted on the same graph and thus are not comparable. Legend corresponds to Ficoll concentrations.

The majority of cases show symmetric swimming, indicating little preference to favour a specific direction.

In some viscosities, a slight preference to swim parallel to the channel is noticeable. When eliminating underlying flow through the channel, as discussed in Section 3.5.2, challenges were present in the high viscous cases as the swimmer velocities were closer to any underlying flow velocity. This phenomenon is especially apparent in the highest viscosity cases shown in the Figure 5.9 (10%) where there is a tendency for the algae to swim parallel to the channel. Therefore, these orientation observations were attributed to the experimental set-up and any potential underlying low velocity flows with the channel and not a physical interaction between alga and viscosity. Taking this into consideration, it can be said for *D. salina* changes in viscosity have no distinguished effect on the preferential swimming direction for the cases examined.

5.4.4 Net mean square displacement

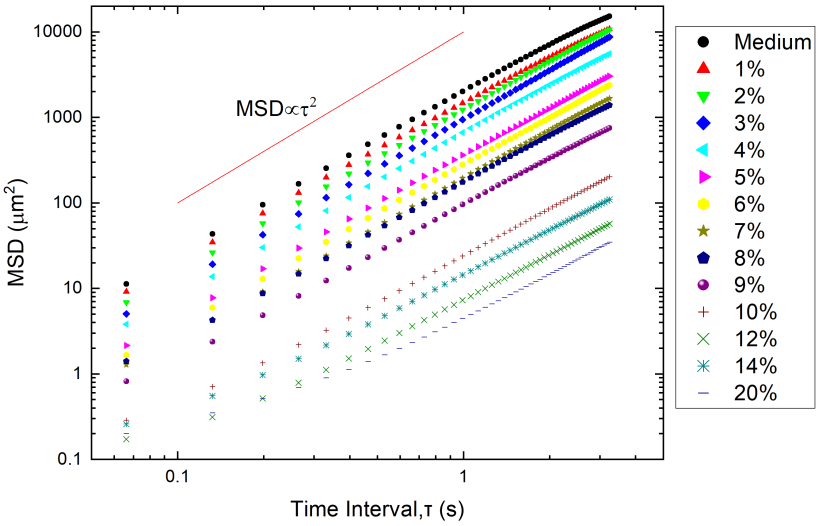

Figure 5.10: Net Mean Square Displacement across Ficoll concentrations, which are notated in legend. Red line show a power-law representing straight line directed active motion.

Comparison of the net mean squared displacement as in Section 4.2.2.4, across viscosity ranges allows the effective diffusion of the swimmer to be compared, both in terms of displacement travelled and type of swimming. As shown in Figure 5.10 the effective diffusion of the swimmer decreases with an increasing Ficoll concentration (viscosity).

As all tracks exhibit active motion with no significant deviation they can all be fitted well to a power-law (Equation 4.9). The power-law fits can be viewed in Table 5.1. For the higher viscosity cases, the lowest time intervals are removed from the power-law fit, as the uncertainty due to the noise of the signal was sufficient to skew the results. Therefore, the lowest time intervals are removed ($0.066\,\mathrm{s} - 0.132\,\mathrm{s}$ for $10 - 14\%$ and $0.066\,\mathrm{s} - 0.0594\,\mathrm{s}$ for 20%).

Across viscous ranges a principally monotonic decrease in the effective diffusion coefficient is observed in-line with previous observations and velocity analysis (Figure 5.3).

Table 5.1: Power-law fit of local MSD with effective diffusion coefficient and exponent extracted from the fit (Equation 4.9)

Fluid Concentration	**Power-law fit**	**Diffusion Coefficient**	**Diffusion Exponent**
Medium	$y = 2018x^{1.89}$	2018	1.890
1%	$y = 1424x^{1.844}$	1424	1.844
2%	$y = 1237x^{1.898}$	1237	1.898
3%	$y = 950x^{1.921}$	950	1.921
4%	$y = 664.8x^{1.903}$	664.8	1.903
5%	$y = 360.7x^{1.877}$	360.7	1.877
6%	$y = 278.8x^{1.882}$	278.8	1.882
7%	$y = 195.5x^{1.878}$	195.5	1.878
8%	$y = 175x^{1.824}$	175	1.824
9%	$y = 95.6x^{1.812}$	95.6	1.812
10%	$y = 24.2x^{1.738}$	24.2	1.738
12%	$y = 7.39x^{1.564}$	7.39	1.564
14%	$y = 14.52x^{1.616}$	14.52	1.616
20%	$y = 4.63x^{1.335}$	4.63	1.335

For the majority of solutions the swimmer is seen to be in the ballistic region indicated by high diffusion exponents and coefficients related to the velocity squared. However, at higher viscous regions (above 10%) the diffusion exponent drops across these three cases. This point of separation from the norm could be a potential limit of swimming where the viscous forces are altering the swimming paths or possibly more likely the data becoming unreliable due to noise in the system.

5.5 Local swimming dynamics

5.5.1 Viscous body drag

The drag on the body of microscopic swimmer was estimated for all viscous solutions as in the calculations carried out in Section 4.3.3.

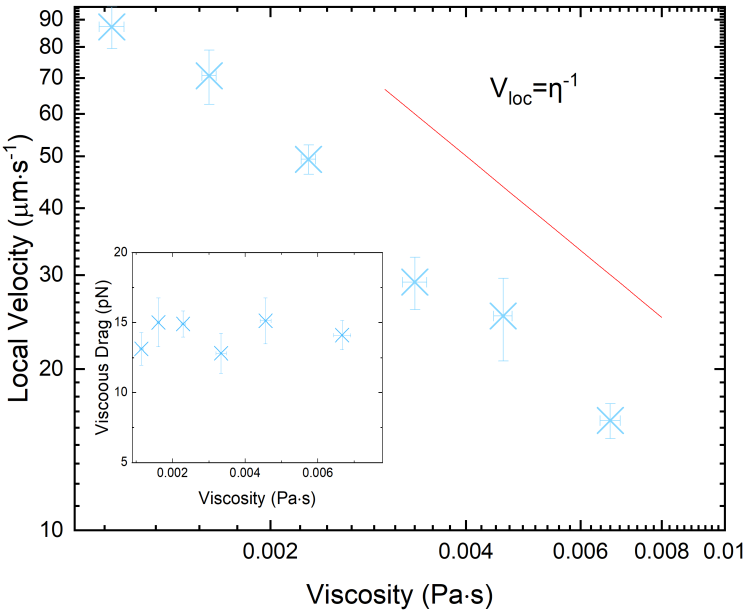

Figure 5.11: Local velocity (V_{loc} as defined in Section 4.2.3.2) as a function of viscosity. The velocity decreases with a power-law with power of -1 implying that the algae maintain constant thrust through viscous solutions. Error bars take into consideration the standard deviation of population velocity and rheological error. Inset displays viscous drag with increasing viscosity. Body drag remains constant across viscosities.

Figure 5.11 shows the change in local velocity across the viscosity range. As the viscosity is increased, the velocity decreases following a power-law of $V_{loc} = \eta^{-1}$, showing viscosity and velocity are inherently linked and scale together. This confirms that *D.salina* are producing constant thrust despite the changes in viscosity as discussed in Section 5.4.1. The viscous drag calculation is shown in the inset of Figure 5.11 reaffirming this.

Constant thrust swimming has been reported in a number of cases for swimming algae [24, 67]. However, often a net velocity is used to report the viscous drag. While a constant viscous drag is reported the full back and forth nature of the stroke is not analysed. For such puller swimmers the overall net velocity is not representative as the swimmers move through the fluid with a higher velocity at the local beat scale than the net velocity captured with a conventional camera. Therefore, using the net velocity of the swimmer is not a suitable approximation to use for calculating viscous drag, as it does not encompass the full swimming gait. It is likely if both power and recovery strokes scale in-line with each other with increasing viscous forces, a constant thrust will be still be presented. However, any viscous drag calculations using a net velocity will under-represent the produced force.

The consequences of *D. salina* propelling itself at constant thrust confirms several questions about the swimming stroke. It shows that the thrust produced by swimming stroke is not affected by viscosity, and remains constant for the range of viscosities examined. Further, it would seem that the swimmer cannot change its swimming stroke to counteract a change in viscosity and maintains its stroke no matter the surrounding fluid for the range of viscosities examined.

5.5.2 Flagella response

An analysis of the effect viscosity has on the beating of a swimmer is not as simple as the preceding analysis of the body. Understanding the effects of viscosity on the beating frequency and relation between the later, and velocity can give an increased understanding in both Newtonian and complex fluids.

To understand the effects of viscosity on the beating frequency, it is first needed to comprehend the flagellum beating pattern employed by *D. salina*. The relative scale of the flagellum is small in comparison with the body, with flagellum diameter approximately 200 nm. The length of the flagellum is very similar to the body diameter and generally lies in between 1 and 1.5 body lengths. A cylindrical shape moving through a fluid does not

follow the same viscous drag laws as a sphere [107, 298]. Furthermore, the beat pattern of the flagella is a complex motion developed over millennia to presumably produce the most effective stroke possible, with the aim to enhance the power stroke over the recovery stroke.

The stroke of *D. salina* can be viewed in Figure 5.12. Often likened to breaststroke like motion, however the motion of *D. salina* is notably different, utilising a technique that can be compared to a travelling wave progressing across the flagellum. During the recovery stroke, the flagellum is brought close to the body with the proximal portion of the flagellum extending forwards out from the body. Through this motion, the tip of the flagellum moves closer to the body. At the moment the proximal portion reaches its peak is the point of switching between recovery and power stroke. At this point, a wave travels along the flagellum towards the distal end, almost in a whip like fashion. This is the main provider of forward motion during the stroke. Through this motion, the tip extends back out in a lateral direction in relation to the body of the swimmer, with very little longitudinal motion. This complex motion means it is not applicable to perform the same viscosity calculation as with the body and further detailed analysis of the flagellum dynamics would need to be undertaken to get an accurate description of wave form and flagellum dimensions [50].

The analysis of the stroke seen in Figure 5.12 has been captured with the body held stationary, and all descriptions are relative to the body. While not analysed in detail at the flagellum level, there is no indication that a change in viscosity will alter the swimming stroke in any considerable way [24].

To capture the thrust generated by the flagella, slender body theory can be used to understand drag locomotion. This theory is commonly known as resistive force theory (RFT) and was first presented by Gray and Hancock [78]. RFT provides the flagella forces corresponding to the normal and tangential motion by the local flagella velocity and coefficients as discussed in Section 1.3.2.

Lighthill further provided theoretical estimations for the resistance coefficients of both

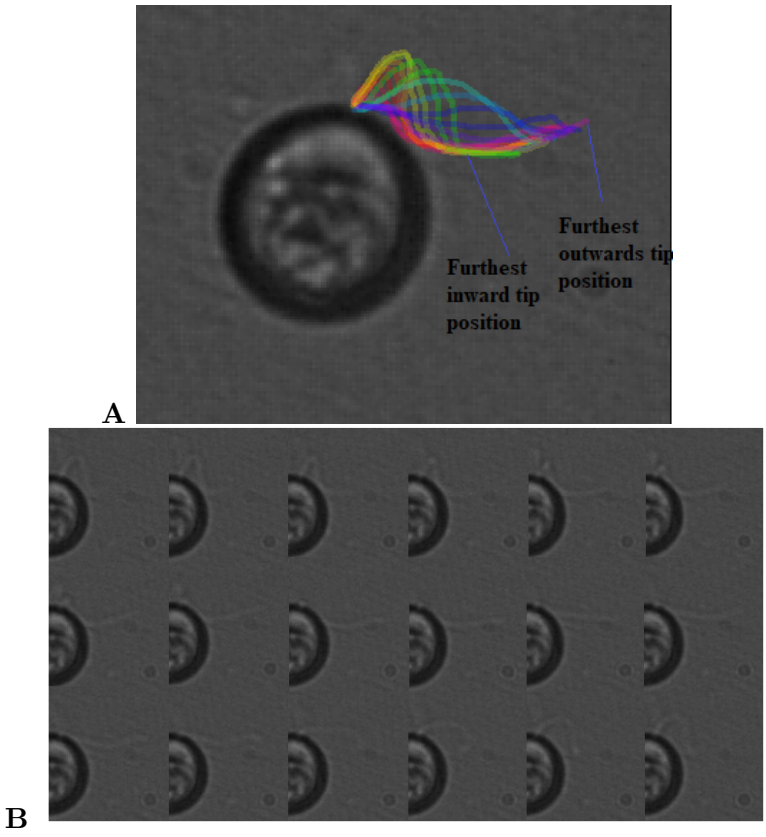

Figure 5.12: (A) Overlay of an approximate algae beat. The onset of the power stroke commences when the flagellum is represented as yellow and recovery when purple. (B) Flagella through a single stroke with frame by frame capture of a single beat with 2 ms between each image. Power and recovery strokes can be visualised with flagella moving in and closer to the body in the recovery stage and out and away from the body in the power.

the normal and tangential forces by analysing a distribution of the stokeslet by the centre-line of a flagellum [79]. The resistance coefficients were described as

$$C_N = \frac{4\pi\eta}{\ln(\frac{2l_f}{r_f}) + \frac{1}{2}} \tag{5.1}$$

$$C_T = \frac{2\pi\eta}{\ln(\frac{2l_f}{r_f})} \tag{5.2}$$

where l_f is the characteristic length often taken as $l_f = 0.09 \times \lambda_w$, λ_w is the wavelength of a flagellum wave and r_f is the flagellum radius [77, 155, 276].

For *D. salina* with a wavelength taken as the average equivalent body length of 14 µm and $r_f = 200\,\text{nm}$ the coefficients can be calculated as

$$C_N \simeq 3.2\eta \tag{5.3}$$

$$C_T \simeq 1.4\eta \tag{5.4}$$

Applying the above equations into equation 1.16 gives the thrust generated by the flagella linearly increases with increasing medium viscosity, if the relative flagella velocity and stroke pattern remains constant. Assuming constant thrust as mentioned previously, it becomes apparent that the relative flagella velocity must decrease linearly to maintain the constant thrust.

5.5.3 Beat frequencies

The same methodology as described in Section 4.2.3.3 of capturing the beating of the algae was applied to the swimmers for a range of viscosities, with a fast Fourier transform performed on the instantaneous swimming velocity with time to quantify an effective beat frequency. Appendix D shows example representative velocity functions within the time domain for selected viscosities. The velocity functions show a clear increase in the stroke period as viscosity is increased. Further, the amplitude of the waves decreases with the increase in viscosity, in-line with the dynamics observed at the global net scale.

Figure 5.13 shows the effects of the beating frequency calculated through FFT, with increases in viscosity. As with the overall swimming velocity, the beating frequency decreased as the viscosity was increased. This relates to an increased stroke period observed in the velocity time graphs (Appendix D). The decrease is not as dramatic as velocity, decreasing

with a dissimilar trend. While velocity followed an approximate power-law ($V_{loc} \propto \eta^{-1}$), the beating frequency follows a power-law of ($f_{BF} \propto \eta^{-0.375}$). For the range of viscosity, covered the frequency decreases from 30 Hz in the medium to approximately 10 Hz at the highest viscosity measured, over a 10-fold viscosity increase.

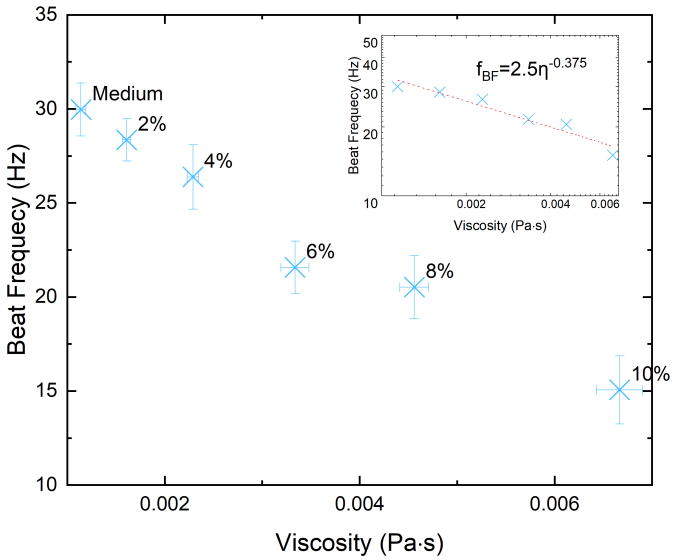

Figure 5.13: Beating frequencies of the algae in relation to changes in suspension viscosity. A general decrease in beating frequency with increasing viscosity following a power-law is observed. Error bars in x axis relate to uncertainty in rheological measurements, and y axis error bars correspond to the standard deviation of algae measure. Inset shows log-log scale with power-law fit.

5.5.4 Stroke dynamics

Time: With increasing viscosity, the time spent in each individual stroke increased in-line with the decreasing beating frequency observed. This can be viewed in Figure 5.14 (A) where the time to complete each stroke is shown across differing viscosities. For the viscosity range.

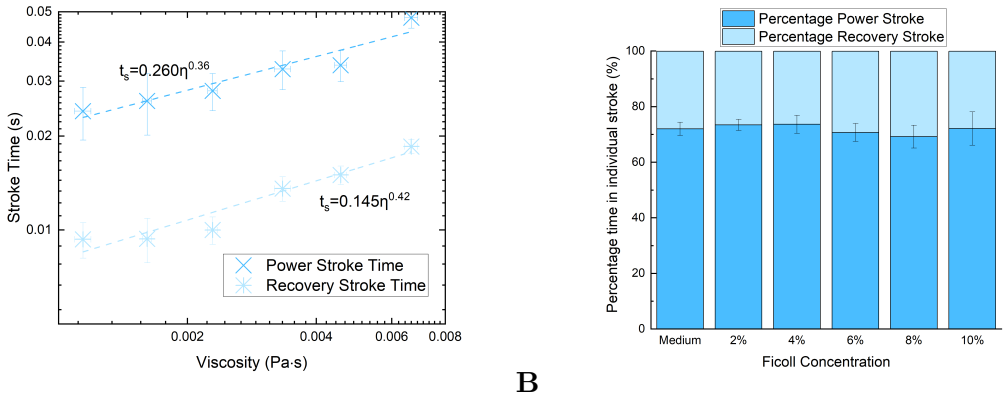

Figure 5.14: (A) Average time to complete power and recovery stroke across the viscosity range studied displaying little variation in response between strokes. (B) Percentage of time spent in each stroke across fluids of differing viscosities. Error bars correspond to standard deviation in variation in stroke times.

As mentioned previously, in the water like medium the algae spent the majority ($\sim 2/3^{rds}$) of the stroke in the power stroke. With an increase in viscosity of the medium the ratio between the strokes remained remarkable comparable as shown in Figure 5.14 (B). Within the experimental error, it can be said that viscosity seems to have the same influence on each individual stroke under this metric.

Velocity: The power and recovery strokes react in concert to viscous influences with both strokes following a power-law function close to $V_{pow} \propto \eta^{-1}$ (Figure 5.15 (A)), within the value of errors of the experimental set up. Thus, implying that both strokes follow constant thrust with changes in viscosity. This is backed up by viscous based drag calculations (Figure 5.15 (C)) where there is little variation across solutions in the averaged value. The power stroke induces an increased viscous drag on the body than the recovery stroke due to the higher average velocity.

The velocity ratio between the strokes as seen in Figure 5.15 (B) displays a constant ratio across all viscosities measured, with the power stroke average velocity $\sim 1.6\times$ greater than the recovery stroke.

Amplitude: With increasing viscosity, the amplitude of each individual stroke de-

creases (Figure 5.16 (A-B)). Due to the different nature of the scaling of the velocity and time per stroke, the stroke amplitude scales with a power-law of $A_{loc} \propto \eta^{-0.687}$. This is a function of the increasing time per stroke and decreasing velocity within the stroke. The ratio between the stroke remains mostly constant no matter the viscous change (Figure 5.16 (C)).

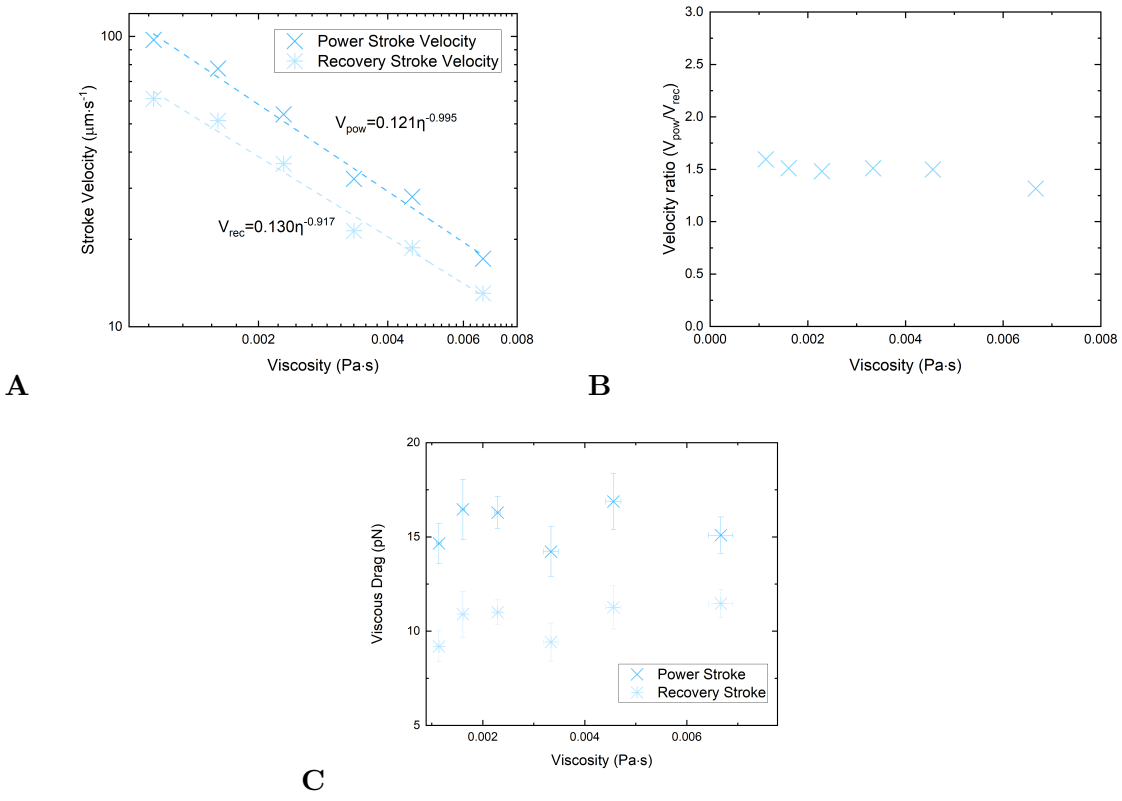

Figure 5.15: (A) Average Individual stroke velocities (V_{pow}&V_{rec}) through increased viscous influences. Velocity in the power stroke is significantly higher in all cases relative to the corresponding recovery stroke. (B) Ratio of Power and Recovery stroke with increasing viscosity. Across the viscous ranges, the velocity ratio between strokes remain constant. (C) Viscous drag of the body in power and recovery stroke, which remains constant through changes in rheology. Error bars relate to rheological error and standard deviation across population analysed.

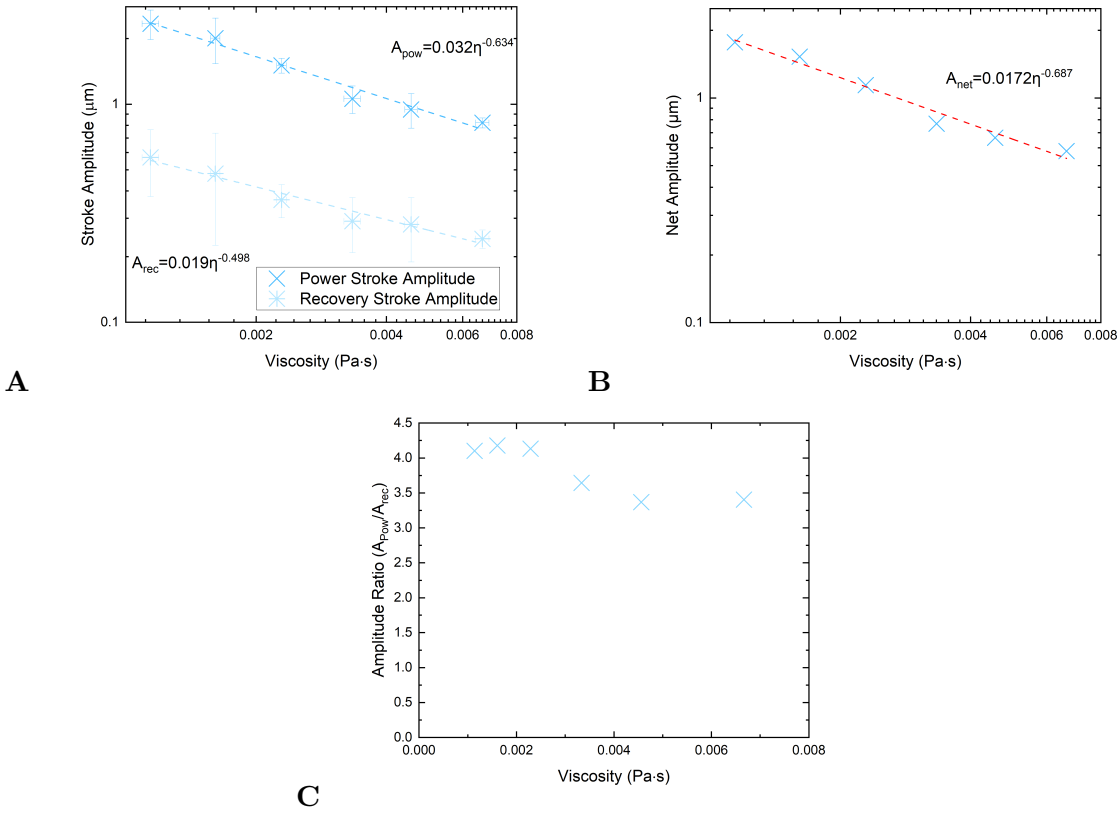

Figure 5.16: (A) Average distance travelled (A_{pow}&A_{rec}) through the power and recovery stroke as a function of viscosity. Error bars relate to rheological error and standard deviation across population analysed (B) Average amplitude (A_{net}) covered in a single stroke against medium viscosity follows a power-law of ($A_{net} \propto \eta^{-0.687}$). (C) Ratio of power to recovery amplitude with viscosity showing only slight variations across viscosity ranges.

5.5.5 Local mean square displacement

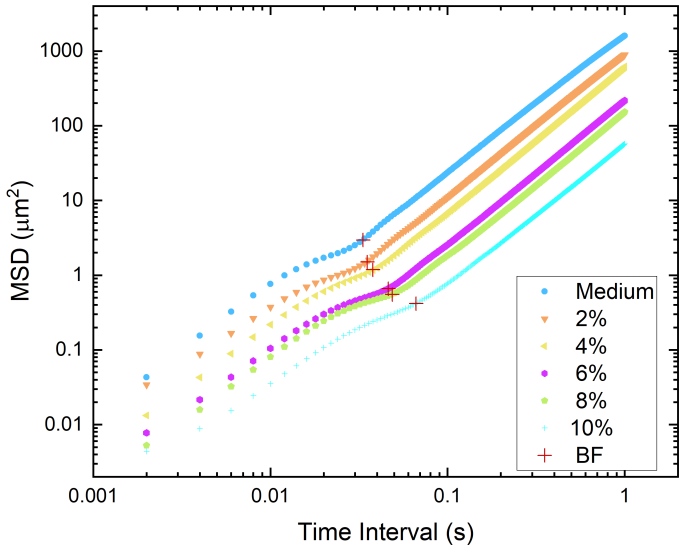

Figure 5.17: Local MSD across varying Ficoll concentrations. A clear distinction between local and net motion is observed, with a transition period in between which relates to the inverse of the beating frequency. The red crosses denote the beating period calculated by FFT methods.

As discussed in Section 4.2.3.5 the localised MSD provides extra detail of the swimming strokes at reduced timescales. Figure 5.17 shows the localised MSD across the viscosity range. As with the net MSD, viscosity decreases the apparent diffusion of the swimming population. In all cases, a clear distinction between the two regimes discussed previous with a transition region in between is notable. Further, it is notable that the transition region is shifted towards increasing time intervals as viscosity is increased. This is due to the decrease in beating frequency associated with the increase in viscosity. The red crosses mark the beat period calculated though FFT methods. All cases seem to lie at the point of initiation of net motion and the end of the transition region.

5.6 Overview of viscous effects

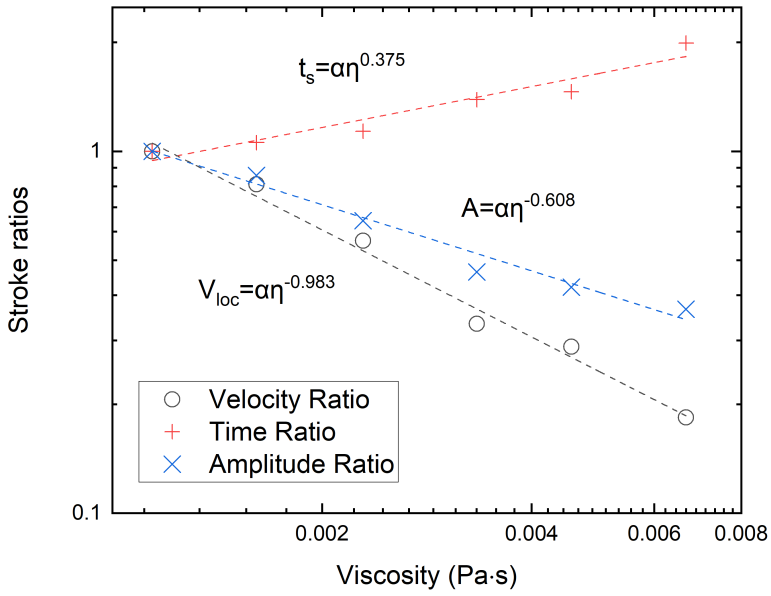

Figure 5.18: Velocity (V_{loc}), amplitude (A_{loc}) and time (t_s) scaled in relation to parameters taken in swimming medium across viscous variations. This allows for a comparison between three parameters and the different power-law fits.

Figure 5.18 shows how velocity, time and body amplitude varies with viscosity scaled to the relative value found in the medium. This graph, therefore, shows the difference within the scaling of the different parameters and how viscosity effect each individually. The three parameters react to the effects of viscosity with different trends: the velocity follows an inverse power-law relating to the constant thrust production and the amplitude and time, reduce and increase respectively, following varied trends that if combined produces the overall velocity decrease. This variation in characteristic trends, displays a complex interaction to changes in fluid dynamics that is not apparent if purely analysing the velocity.

In terms of the flagella, the time per stroke calculated through the body can be related to the flagella and should remain very similar. The same cannot be stated about the body

and flagella amplitude. Despite this, through the analysis of viscous drag and described by simple RFT methods, it is apparent that the body and flagella velocity decreases linearly with increasing viscosity, leading to constant drag of the body and thus constant thrust produced by the flagella. This is assuming the normal and tangential components maintain relative similarities to each other across viscosity ranges. As the stroke time increases following $t_s \propto \eta^{0.375}$, to maintain constant thrust produced by the flagella it would be assumed the flagella amplitude would follow the decrease of that of the body amplitude to satisfy the flagella velocity linearity (Section 5.5.2).

The variation in flagella beat time and amplitude cannot be described by simple RTF methods and the fluid viscosity increases, and must be a dynamic induced by the increased work to move the flagella through a higher viscous fluid. The reasoning behind the differences in beating frequency and flagella amplitude are unknown, and likely are influenced by the internal energy production and distribution across the flagella. A possible explanation relates to the internal elastic properties of the flagella as well as the external viscous forces [24, 52, 299–301]. Despite this, it is apparent that the gait modulation is intrinsic to the constant thrust produced by the flagella.

5.6.1 Simple model

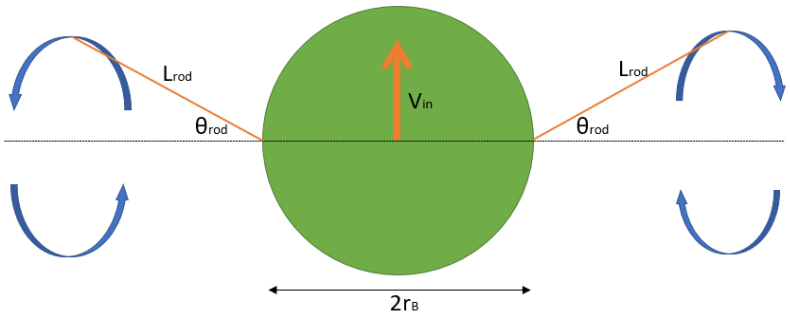

Figure 5.19: Schematic diagram of model representing swimming alga. Model definitions are shown. Flagella are represented by an orange rod and with blue arrows denoting their motion through the stroke.

The swimming dynamics observed in Newtonian fluids can be captured by a simple analytical model. This provides a greater understanding of the effects of viscosity, confirming some theories already mentioned such as the reduction of flagella velocity. The model was primarily developed by Debasish Das, and thanks goes to him for his support in its generation. A spherical body is assumed with cylindrical rods protruding at each side representing the flagella, as in Figure 5.19. The flagella movement is controlled by θ_{rod} which is denoted relative to the horizontal axis. Thus, in the power stroke, $\triangle\theta_{rod} < 0$ and $\triangle\theta_{rod} > 0$ for the recovery. Non-reciprocal motion is incorporated by imposing varying rod lengths between the strokes, i.e. large in power, small in recovery. The resultant force balance equation can be solved to attain the body velocity

$$-6\pi\eta r_B v_{in} - 2L_{rod}v_{in}(C_N sin^2\theta_{rod} + C_T cos^2\theta_{rod}) + \omega_{rod}C_T l_{rod}^2 cos\theta_{rod} = 0 \qquad (5.5)$$

where v_{in} relates to the velocity at that instant, C_N and C_T the normal and tangential resistance coefficients (Equations 5.1 and 5.2), ω_{rod} the angular velocity, l_{rod} the rod length and θ_{rod} the angle of the rod relative to the horizontal direction [77].

The first term of the force balance relates to the body viscous drag as in Equation 4.13, the second the viscous drag produced by the rod as is moves through the fluid and the final term the angular drag of the rod [302, 303].

Assigning the angle swept by the filament as $\theta_{rod}(t) = A_{rod}sin(2\pi f_{rod}t)$, the angular velocity as $\omega_{rod}(t) = 2\pi f_{rod}A_{rod}cos(2\pi f_{rod}t)$ and the change in filament length as $l_{rod}(t) = cos(2\pi f_{rod}t) + 2r_B$ and solving, the velocity with respect to time can be calculated and thus the velocity features as described in Section 4.2 can be recovered. Figure 5.20 shows the inputs with respect to time, relating closely to the flagella dynamics observed in *D. salina* in the medium.

There are some key assumptions and draw backs integrated with this model. A 50/50 power/recovery stroke time is inputted, which is a dynamic not observed in the experi-

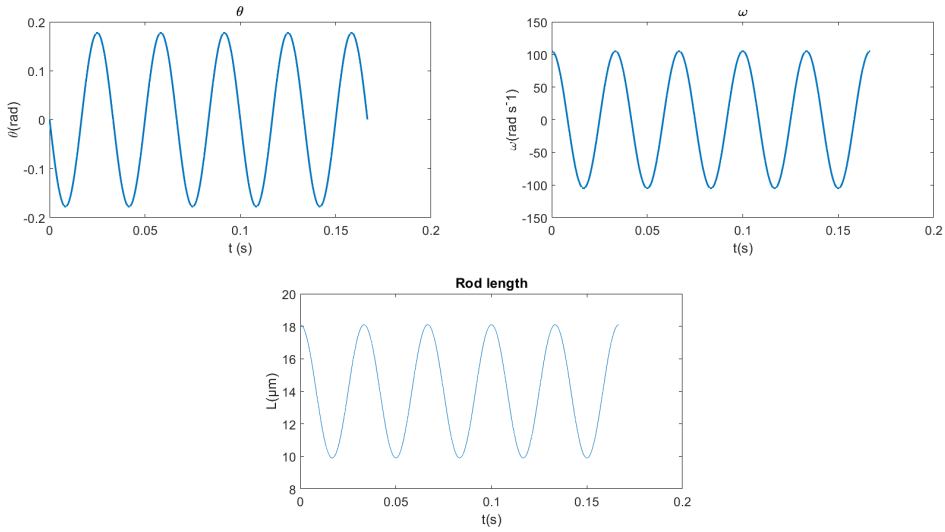

Figure 5.20: Inputs into model covering flagella angle, angular velocity and the rod (flagella) length. All vary with time and are approximated to represent flagella motion of *D. salina*.

mental observations. Furthermore, a straight rod of fix rigidity is imposed with no ability to bend or match the stroke of *D. salina*. Therefore, there are likely some inconsistencies present in the model, such as the relation between power and recovery stroke. While the model gives an approximate understanding for viscous effects and simplified dynamics, it by no means attempts to capture the full dynamics of the swimming patterns of *D. salina* and is purely a representative model.

The resultant velocity spectrum of the alga in the medium is displayed in Figure 5.21. Despite the simplicity of the model, the model output qualitatively lies close to the experimental results found in the medium displayed in Figure 4.11.

In terms of the effects of viscosity, in Equation 5.5 the viscosity terms cancel out. Therefore, with the above model, purely altering the viscosity does not produce the velocity variations observed for *D. salina*. To produce the decay in velocity observed, the rod dynamics must be altered. To satisfy the constant thrust production, the flagella velocity

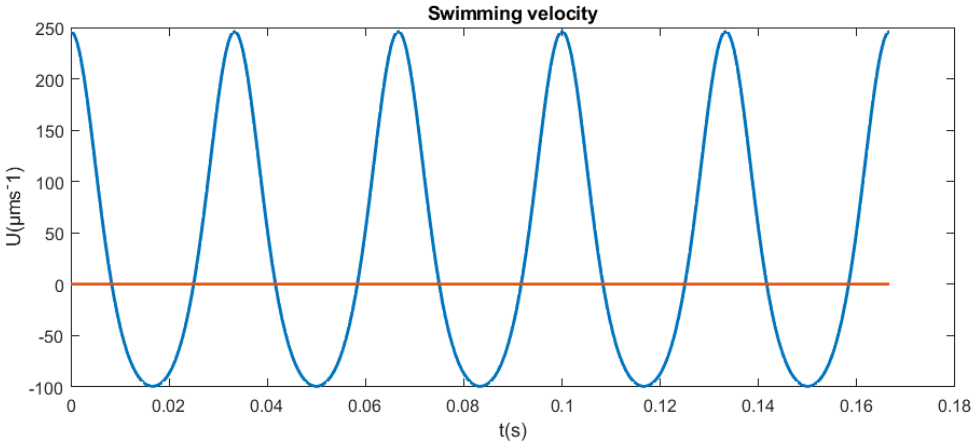

Figure 5.21: Velocity output spectrum for model alga swimming in the medium, matches close to experimental spectrum displayed in Figure 4.11.

must maintain a velocity that decreases to the power of -1. It has been observed that the flagella time increases to the power 0.375 with viscosity, and thus stated that the amplitude of the flagella follows to the power -0.687. Inputting these decay trends into the model, (A_{rod} for amplitude and f_{rod} for frequency) the motion of the swimmer in viscous fluids should be recovered. The results of the calculated velocities are displayed in Figure 5.22.

It is clear from the resultant graphs (Figure 5.22) that the model captures the decay in velocities well, with all velocities following the same overall decay trends. One exception is the net velocity which is under-represented, which is likely due to the recovery stroke having a larger proportion of the stroke than found experimentally. These results give backing to the reduction in flagella velocity following a power-law to the -1 as with the body. However, the model does not give details into the reduction of the beating frequency, amplitude and the variation in the two rates. This is likely due to internal dynamics along the flagella, but would be an interesting follow up to understand this variation [24, 52, 299–301].

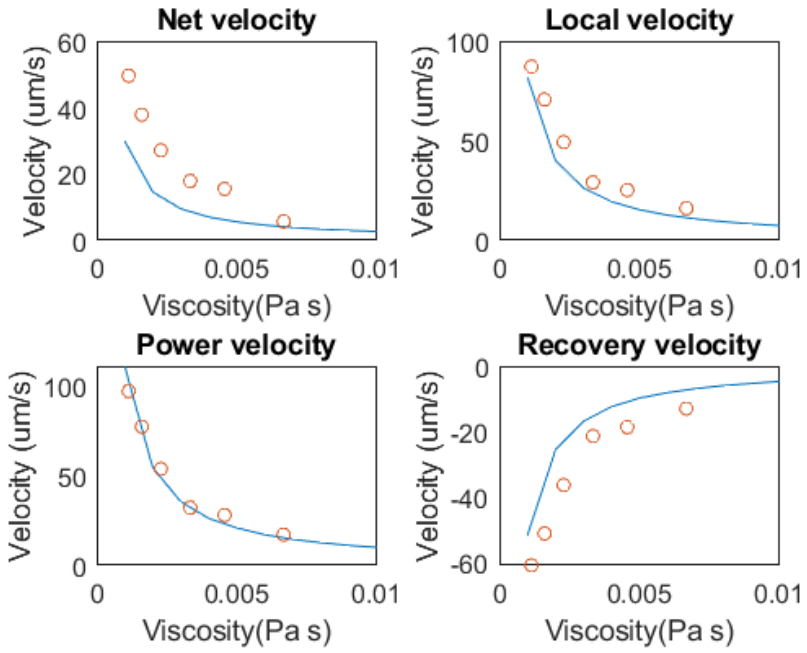

Figure 5.22: Resultant velocities dependent on fluid viscosity controlled by frequency and amplitude (blue line) and experimental observations (orange circles).

5.6.2 Velocity dependence on body size

During an alga's life cycle, their body shape alters as they grow and develop. Generally starting off small, then increasing and becoming more spherical throughout their lifetime. As discussed in the Section 4.3.3, the diameter is integral to the viscous drag on a body moving through a fluid. It has been stated that across the population the viscous drag remains constant independent of viscosity. However, the size of an alga is not universal. Here, a closer look into swimming velocity and body size is carried out on an individual basis.

Figure 5.23 shows a plot of swimmer's equivalent diameter versus velocity normalised by a multiplication of the solution viscosity. This allows for a comparison of swimmers under different viscous influences. As viscosity has been shown to have no influence on the ratio of the power and recovery stoke, and the power of the swimmer remains constant

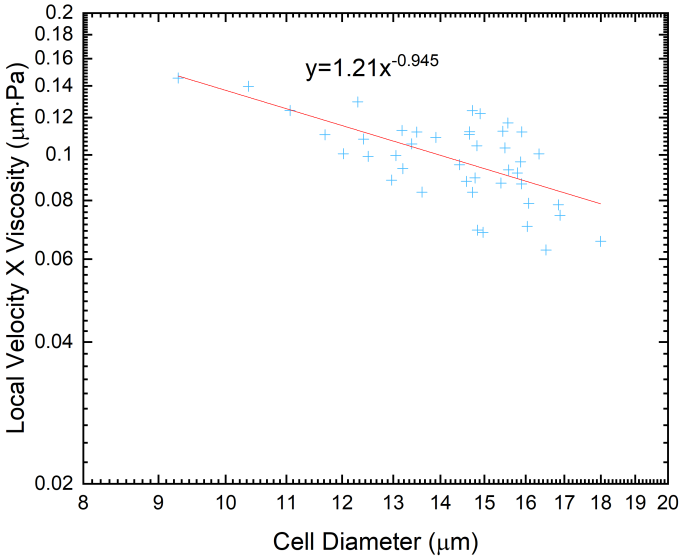

Figure 5.23: Viscous swimming velocity against equivalent cell diameter with power-law fit. Each cross represent an individual alga.

regardless of viscous changes, it is deemed acceptable to compare the data in this way. The local velocity is used in the calculation to capture the full stroke.

D. salina display a tendency for the swimming velocity to be related to the diameter, where large swimmers swim with a reduced velocity and vice versa for smaller swimmers. The decrease also follows a scaling linked to a power-law ($V_{loc} \propto r_B^{-1}$), very similar to the velocity and viscous drag calculations.

From the previous calculations and discussion into viscous drag, this might seem a trivial observation. The smaller the swimmer, the less drag, the faster it swims. However, looking at a swimmer on an individual basis shows some interesting dynamics. What is apparent from this data is that the swimming velocity of *D. salina* is dominated by the cell size. Furthermore, in the most part, as the body size may change across the population, the flagella will produce the same thrust regardless. This also has a bearing on the spread of velocities and lack of spread of the beat frequencies (Figure 4.21). It has also been noted

anecdotally through experimentation, that flagella length seems to be mostly maintained across population, which may also be a factor of the discussed results. Other factors will affect velocity such as turning etc. but the dominant metric is clearly the cell size. This raises the interesting proposition that algae motility is primarily controlled by age and the relative size of the algae and has no influence on the power produce by the flagella, only the drag of the body. The result of these dynamics for *D. salina* shows an independence of beating dynamics on the physiology of the swimmer and across an algae population the flagella dynamics do not seem to change no matter the age, size or circumstances of a particular alga.

5.7 Conclusion

The swimming dynamics of *Dunaliella salina* are inherently linked to the viscous forces present within the medium they are motile within. With increases in the viscosity of the medium, the swimming velocity of the algae is found to reduce. The algae have no method of increasing thrust either actively or passive and the viscosity has a marked impact on the swimmer's velocity.

The swimming velocity decrease followed an approximate power-law decrease to the power of -1 with viscosity, implying the swimmer produces constant thrust. Using a simplification of a sphere moving through a fluid, the viscous force produced by the swimmer was calculated across the viscous ranges and was found to remain constant ($\sim 15\,\mathrm{pN}$). The local velocity was used in the calculation of this data, as it better captures the full stroke dynamics and does not hide the recovery stroke of the beating cycle. Analysis of the beating frequency likewise showed a decrease with an increase in viscosity, while not following the same power-law observed in the velocity. The modulation of the gait seems not to affect the flagella velocity response to changes in viscosities, maintaining constant thrust. Furthermore, the relative stroke dynamics between recovery and power stroke remained notable similar across viscosity ranges examined.

The concept of constant thrust is well known across similar types of swimmers, and from this analysis of the swimming size and velocity it would seem that the force *D. salina* produces is independent of size or physiology of the swimmer. Further, the apparent lack of change in beating frequency across the population quantifies the independence of beating and flagella dynamics from algae physiology. Therefore, all algae seem to produce a constant thrust and similar beat pattern, but the primary factor affecting their swimming efficiency is their size and viscosity of the medium they are within.

Chapter 6

Swimming in shear thinning fluids

6.1 Chapter overview

The following chapter analyses the response of the swimming organism to shear thinning fluid properties of its medium. Initially, the fluid properties are defined, such as the levels of shear thinning within each fluid (power-law index). Once established, the swimming dynamics in a shear thinning fluid are quantified, initially focusing on the net velocity and then moving to focus on the stroke dynamics response to such fluids. After, the swimming response to shear thinning properties is discussed in detail, and finally a discussion into the use of an effective viscosity as a method of comparing the swimming response in complex fluids is conducted.

6.2 Rheology of modified medium with Xanthan gum

Xanthan gum (XG) was the rheological agent used to import shear thinning properties to the medium. It is a water-soluble polysaccharide produced by the bacterium Xanthomonas campestris during its fermentation processes [229, 232, 304]. Xanthan gum is a widely used pseudoplastic agent in food, health, cosmetic, petroleum and research industries as discussed in Section 3.3.2.3 [305–307] and has not been shown to react with algae or other

forms of microscopic swimmers bar any rheological changes .

Xanthan Gum rheology has been found to be independent of the concentration of sodium chloride below a cross-over concentration. Depending on the literature the cross-over point ranges from 0.1% to 1% of XG and the consensus is that below these limits the effects of additional salts are negligible [305]. Across the critical concentration, the polymer backbone acquires a helical conformation, stabilising the polymer from a disordered to ordered state, leading to the shear viscosity and shear thinning levels lowering compared to a salt-free solution. All solutions used for this work have sodium chloride concentration that fall well below the mentioned critical concentrations (Section 3.2.1).

Table 6.1: Power-law index (n) and flow consistency index (m) for Xanthan gum solutions taken from a fit of rheological data using a power-law model.

Solution Concentration (XG - Ficoll)	**XG concentration**	**Ficoll concentration**	**n**	**m**
250PPM	0.025% (250PPM)	0%	0.856	0.0039
250PPM - 2%	0.025% (250PPM)	2%	0.857	0.0058
250PPM - 4%	0.025%(250PPM)	4%	0.857	0.0093
500PPM	0.05% (500PPM)	0%	0.752	0.0109
500PPM - 1%	0.05% (500PPM)	1%	0.746	0.0136
500PPM - 2%	0.05% (500PPM)	2%	0.765	0.015
750PPM	0.075% (750PPM)	0%	0.653	0.0282

Xanthan gum was added to the original medium or the medium with Ficoll at different concentrations (Section 3.3.2.5) to give a range of modified medium with different viscosities and shear thinning levels.

Solutions of Xanthan gum with concentrations of 250PPM, 500PPM and 750PPM in the medium were used in the analysis. These provided base shear thinning solutions where the viscosity was primarily controlled by the XG concentration. Further, XG solutions with added Ficoll were also experimentally examined. The addition of Ficoll increased the viscosity of the solution, while the power-law index remained very close to the base solutions with no Ficoll. This allowed for a comparison to be drawn between solutions

with similar shear thinning properties, but with increased viscosity. An overview of the different solutions utilised can be viewed in Table 6.1.

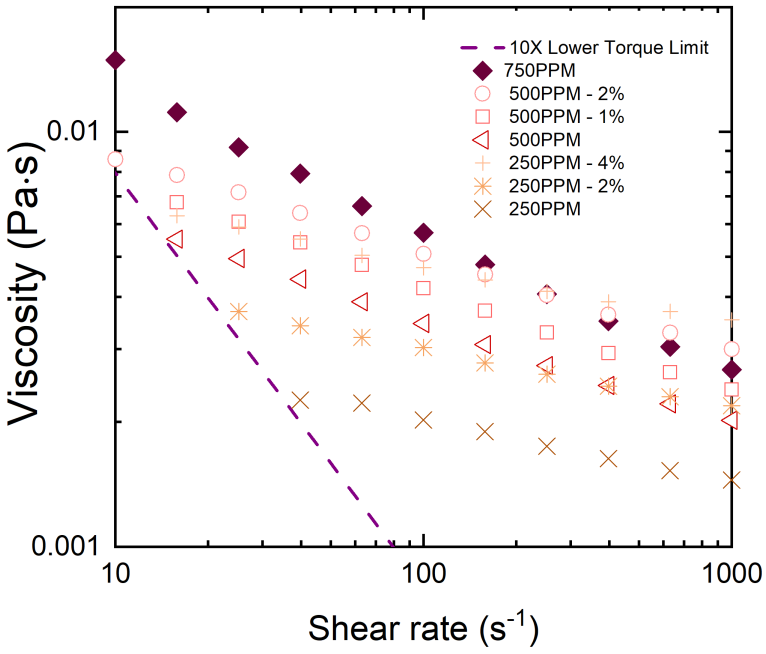

Figure 6.1: Flow curves showing the steady shear viscosity of all Xanthan Gum solutions measured. All show varying shear thinning and viscous properties. Three concentrations of Xanthan gum solutions were examined, which displayed varying power-law indices. To enhance the viscosity of these three base solutions, concentrations of Ficoll were added. This is noted by the percentage succeeding the Xanthan gum concentration in the legend and denotes the percentage weight of Ficoll within the solutions. The minimum measurable torque represented by the purple dashed line is calculated from Equation 3.10.

The shear flow curves of the medium with added shear thinning (XG) and viscous (Ficoll) agents can be seen in Figure 6.1. A more pronounced shear thinning behaviour is clearly visible with increases in concentration. Furthermore, solutions with additional Ficoll can be seen to have increased viscosity but similar levels of shear thinning behaviour (power-law index). All solutions were fitted to the power-law model as defined as in Appendix C.1. Table 6.1 shows the values of the flow consistency index and power-law

index for all Xanthan gum solutions.

6.3 Swimming response to shear thinning fluids

To quantify any swimming dynamic changes in a shear thinning fluid, a comparison to a Newtonian solution is often drawn by means of calculation of an effective viscosity of the swimmer. As discussed in Section 2.4.1 defining a single characteristic viscosity experienced by the swimmer can be complex and can lead to inconsistencies. Instead, to avoid the uncertainties within this method, the analysis that follows draws comparison to Newtonian solutions through different methods such as comparing variations in stroke dynamics. In Section 6.5 the method of defining an effective viscosity is reviewed in the context of the results observed and conclusions drawn to the effectiveness of this method.

For quantification of the shear thinning response the same experimental methodologies were utilised as for the Newtonian fluids discussed in Chapter 4 and 5 with velocities, beating frequencies and individual stroke dynamics all captured. The number of algae examined for each concentration followed close to that described in Table 3.5.

Initially, to introduce the shear thinning response, the variation of the net swimming velocity with concentration is discussed. With increasing XG concentration, the algae display a clear decrease in their swimming velocity (Figure 6.2). The reduction in swimming velocity is likely dominated by the increases in viscosity in the XG concentrations. This is also observed with the solutions of added Ficoll which display a reduced velocity on their base solutions. While the data presented thus far gives initial insight into the swimming response to shear thinning fluids, it is not possible to determine the effects of shear thinning from viscous responses.

To begin the comparison to Newtonian viscous fluids, the swimming dynamics are broken down into their simplest form, that being the body amplitude (A_{pow} & A_{rec}) and time taken in the individual strokes (t_{pow} & t_{rec}) as seen in Figure 6.3 for the power (A) and for recovery (B) strokes. The Newtonian response is included and follows a decreasing

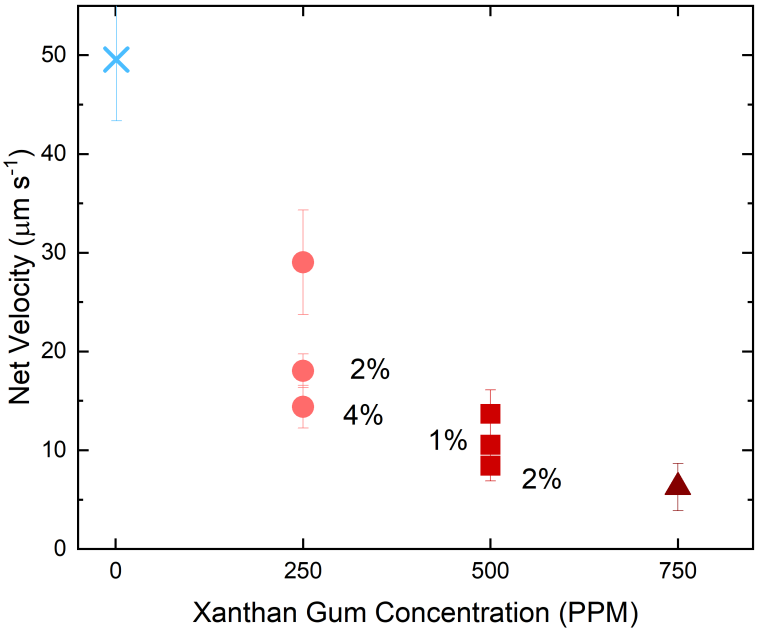

Figure 6.2: Swimming velocity as a function of Xanthan gum concentration for solutions analysed. Percentage notes additional Ficoll concentrations. Increased concentrations leads to an overall decrease in the swimming velocity. Error bars denote standard deviation across population analysed.

distance achieved per stroke and increasing time per stroke, with increasing viscosity. The ratio between power and recovery stroke velocities, time and amplitude all remain relativity similar.

With the addition of shear thinning fluid properties, the stroke dynamics do not follow similar trends as the response in Newtonian solutions. For the base XG solutions, in the case of the power stroke, an apparent reduction in both the amplitude and stroke time is seen in relation to the Newtonian cases. Conversely, for the recovery, an apparent increase in both these variables is seen. This shows that the shear thinning properties of the fluid are indeed altering the swimming dynamics of *D. salina* and the power and recovery strokes are displaying different responses.

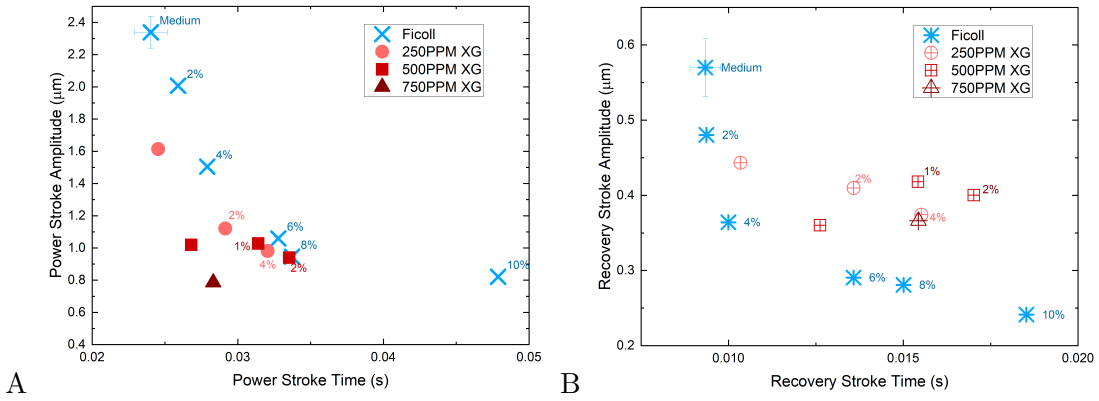

Figure 6.3: (A) Average stroke amplitude (A_{pow}) and time (t_{pow}) for power stroke in shear thinning and Newtonian solutions. Percentage represent concentration of Ficoll added to shear thinning solutions (red) and Ficoll concentrations in Newtonian solutions (blue). Example error representative of entire data set is displayed on medium data point, relating to standard deviation of population. Each point consists of data from between 8 - 15 algae representing approximately 10000 data points. (B) Recovery stroke.

The addition of Ficoll to the base shear thinning fluid concentrations display a shift in the response, with the power stroke lying closer to the Newtonian cases and recovery further away from Newtonian.

To characterise the differences in dynamics displayed between the power and recovery stroke in a shear thinning fluid, it is possible to relate the average power stroke amplitude/time to the net amplitude/time (t_{pow}/t_s & A_{pow}/A_{net}). Figure 6.4 shows this in the context of a single averaged stroke. The start and end of the stroke are normalised to a single point, and by plotting the power stroke amplitude/time over the net values, the difference in these values relative to each other and to the recovery stroke are seen. The Newtonian cases are included as a reference (Figure 6.4 (B)) and due to similarities in response from both the power and recovery with increasing viscosity, all concentrations conform to similar dynamics.

The stroke dynamics in the shear thinning fluids show a clear and obvious change in response to the Newtonian cases, with both the amplitude and stroke time experiencing a separation from that seen in the Newtonian cases. In terms of the amplitude, the ratio

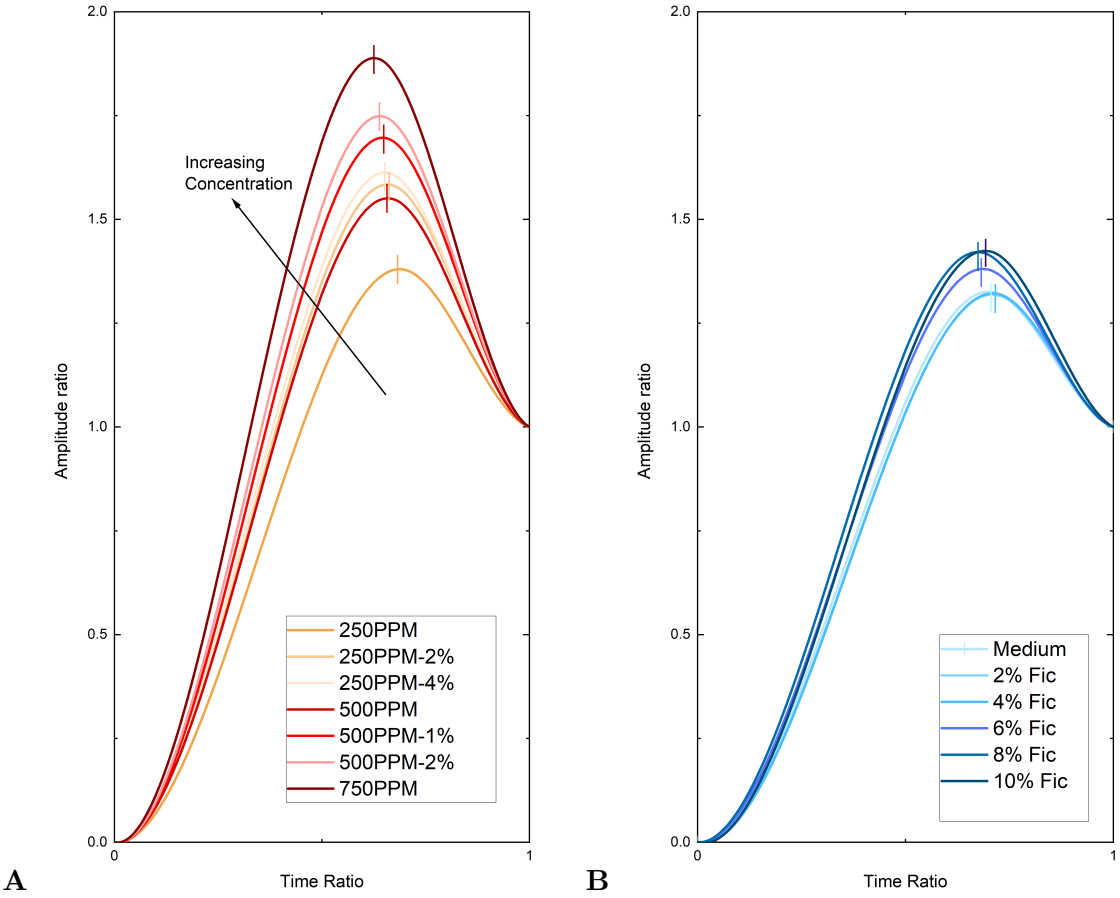

Figure 6.4: (A) Stroke data scaled to the relative values of a full completed stroke for shear thinning fluids. Crosses denote t_{pow}/t_s & A_{pow}/A_{net}. Any variation represents a shift in stroke response relative to each other (B) Newtonian scaled data.

between the power and recovery stroke increases, denoting a shift in favour of the recovery stroke (for relative increases in stroke velocities). On the other hand, the time per stroke ratio decreases, leading to a favourable shift towards the power stroke. It seems apparent the amplitude shift experiences a greater separation in response from Newtonian than that in time, which may indicate a relative increase in the velocity of the recovery stroke to the power. The separation from the Newtonian cases are increased in the cases with additional Ficoll from their relative base case.

Upon analysis of the stroke velocity ratios (V_{Pow}/V_{Rec}) displayed in Figure 6.5 the

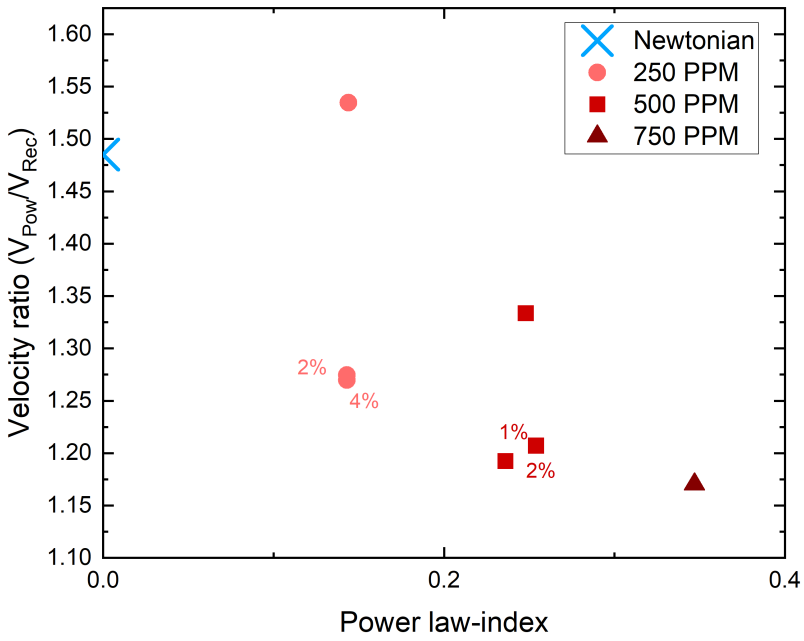

Figure 6.5: Velocity stroke ratio (V_{Pow}/V_{Rec}) for shear thinning and Newtonian solution. Newtonian solutions are represented by a single point, as the variation in velocity ratio is minor. With the addition of shear thinning properties, the velocity ratio is shifted in favour in the recovery stroke, a response that is enhanced by the addition of Ficoll to the solution.

response to a shear thinning fluid seems to promote a relative increase in the recovery stroke velocities over the power stroke, as hinted at in Figure 6.4. In the Newtonian solutions, the stroke ratios remain relatively constant and are represented by a single averaged point in Figure 6.5. However, with the addition of shear thinning properties, the velocity ratio decreases with solution concentration. This velocity ratio shift seems to be driven by differences in amplitudes and time between the power and recovery strokes seen in Figure 6.4. With the effective shift in favour of recovery stroke, the swimmer in a shear thinning fluid would seem to lose efficiency in its gait as more effort is converted to moving the swimmer backwards through the stroke.

Furthermore, solutions with additional added Ficoll display a further decrease in the stroke velocity ratio. Thus reducing the stroke efficiency by an even greater margin. This is

of particular note, as increases of viscosity in Newtonian Ficoll solutions lead to no changes in the stroke velocity ratios. Therefore, this dynamic may be related to other factors such as the solvent viscosity, as this will differ between solutions. Furthermore, it seems that the added Ficoll reaches a limiting point, as both 2% and 4% in 250PPM 1% and 2% in 500PPM show similar velocity ratios. This may purely be experimental error or a limit of the recovery stroke enhancement. An interesting question would be if it was possible to alter the solution rheology sufficiently to shift the velocity ratio below unity and induce stationary or even backwards swimming.

To sum up, a clear and obvious dynamical change in the beating dynamics were found once shear thinning properties were added to the medium. A reduction in amplitude and time was found in the power stroke and the opposite dynamics observed in the recovery stroke relative to the Newtonian response. Upon analysis of the stroke velocities, it is apparent that there is a shift in favour of the recovery stroke velocity, decreasing the overall apparent efficiency of the stroke. Shear thinning solutions with similar power-law indices and increased viscosities show relative increases in both power and recovery stroke time and amplitude on the base cases. This attributes to an additional shift in the stroke velocity ratios in favour of the recovery stroke, posing the question of the effects of different rheological properties.

6.3.1 Swimming orientation

Further to the stroke dynamics, the swimmers' orientation and preferred paths can be analysed to asses the effects of shear thinning solutions.

As in Section 4.2.2.4 the velocity data for the shear thinning cases were fitted to a mean-squared displacement model to extract the apparent diffusion coefficients and exponents for all concentration analysed. The diffusion coefficient is seen to reduce with the increase in solution concentration, as with the increase in drag associated with the increased viscosity. Interestingly, the exponent seems to reduce with increasing XG concentrations following the

Table 6.2: Shear thinning power-law fit of local MSD, with diffusion coefficient and exponent extracted from the fit.

Fluid Concentration	**Power-law fit**	**Diffusion Coefficient**	**Diffusion Exponent**
250PPM	$y = 745.6x^{1.895}$	745.6	1.895
250PPM−2%	$y = 348.3x^{1.896}$	348.3	1.844
250PPM−4%	$y = 186.3x^{1.855}$	186.3	1.855
500PPM	$y = 151.1x^{1.836}$	151.1	1.836
500PPM−1%	$y = 96.5x^{1.824}$	96.5	1.824
500PPM−2%	$y = 53.8x^{1.829}$	53.8	1.829
750PPM	$y = 23.9x^{1.786}$	23.9	1.786

power-law index. It is unknown whether this effect is due to the influence of shear thinning properties increasing turning events of the algae or by experimental error. However, As the exponents all fall within the varying ranges seen in the Newtonian cases (Table 5.1) it is difficult to state for definite this is a response to shear thinning properties.

6.4 Effects of shear thinning fluids

It is clear from the observable results, the stroke of *D. salina* under shear thinning influences experiences a marked change in its dynamics. In this section, the possible reasoning behind the observed stroke changes are discussed.

6.4.1 Viscosity variation across swimmer

The swimming stroke of *D. salina* will inherently produce varied shear rates with its fast moving very thin flagella compared to a relative slower moving large body. Due to the increased velocity and much decreased diameter of the flagella, it is a fair to assume that they will produce a much greater shear rate onto the fluid than the body of the swimmer. Therefore, in a shear thinning fluid, the flagella should be experiencing lower viscosities

than the body.

This shift in viscosity ratio may be reasoning behind the dynamics observed for the power stroke in Figure 6.3 where a decrease in both stroke time and amplitude is apparent compared to the Newtonian cases. The relativity lower viscosity at the flagella should allow the flagella to beat faster, thus reasoning for the reduced stroke time. Then for the body, it feels an increased viscosity compared to the flagella and the faster beating does not translate to the amplitude. It may even be possible that the flagella produce such a great shear rate that they are experiencing a value close to the solvent viscosity through part of their stroke. This is possibly seen in solutions with additional Ficoll, as the solvent viscosity is increased on the base solutions, which leads to an increase in beating frequency. Furthermore, the solvent viscosity may be driving the reduction in stroke velocity ratios (Figure 6.5).

The recovery stroke in the shear thinning solutions experiences the opposites dynamics to that of the power, with an increase in stroke time and amplitude observed. Unlike the power stroke, this dynamical change cannot be explained simply by the viscosity changes across flagella and body. In fact, the opposite of what may be expected is true. Thus, it is apparent that other methods induced by shearing properties are affecting the recovery stroke.

6.4.1.1 Body viscous drag

Thus far in the analysis the focus has been primarily based on the variation between stroke dynamics, mainly the stroke time and amplitude. To provide further understanding and to add further comparison between the shear thinning and Newtonian strokes, it is possible to relate the body effective viscosity to the swimming velocity.

For *D. salina*, the body can be assumed to be spherical and thus possible to relate its motion to experiments of falling spheres [174, 175]. Therefore, the effective shear rate of the body can be approximated by

$$\dot{\gamma_B} = \frac{V_{loc}}{2r_B} \tag{6.1}$$

where V_{loc} is the localised velocity and r_B is the equivalent radius of the body. For each shear thinning solution, the estimated body shear rate can be viewed in Table 6.3. It should be noted this expression denotes an average shear rate exerted by the body and the shear rate will vary through the stroke dependent on the instantaneous velocity at that moment. The local velocity was used in this calculation to achieve the shear rate related to the overall stroke.

Table 6.3: Local velocity and effective body shear rate of XG fluids, calculated with Equation 6.1.

Solution Concentration (XG - Ficoll)	**Local Velocity ($\mu m\,s^{-1}$)**	**Effective Body Shear rate (s^{-1})**
250PPM	58.9	4.21
250PPM - 2%	35.7	2.55
250PPM - 4%	28.5	2.04
500PPM	35.0	2.50
500PPM - 1%	30.9	2.20
500PPM - 2%	26.5	1.89
750PPM	26.3	1.87

Using the body shear rates defined in Table 6.3 in combination with Equation C.1 (Appendix C.1) the effective viscosity dependent on the body can be calculated. The body effective viscosity acts only as a tool for comparing the relative changes experienced by the body and is by no means an overriding effective shear rate for the swimmer as a whole.

Relating the local body velocity to the effective body viscosity, as seen in Figure 6.6 (A) a clear shift is observed from the Newtonian solutions. For the shear thinning solutions, an increased local velocity is present in relation to the Newtonian solutions for similar effective body viscosities. This dynamic would seem to be driven by the variation in viscosity felt by the flagella and body. From Equation 5.5 with the flagella feeling lower viscosities, an

imbalance is present.

This is further presented in Figure 6.6 (B) where the effective viscosity around the swimmer's body is inputted to Equation 4.13 to calculate the effective viscous drag of the swimmer. With increasing shear thinning properties, the apparent viscous drag calculated using the relative body viscosity increases with shear thinning properties. This seems to be as the flagella produce the thrust associated with low viscous solutions which is not balanced by the drag of the body due to the viscous imbalance (Equation 5.5). Therefore, an apparent thrust increase from a simple Newtonian fluid is present in relation to the body.

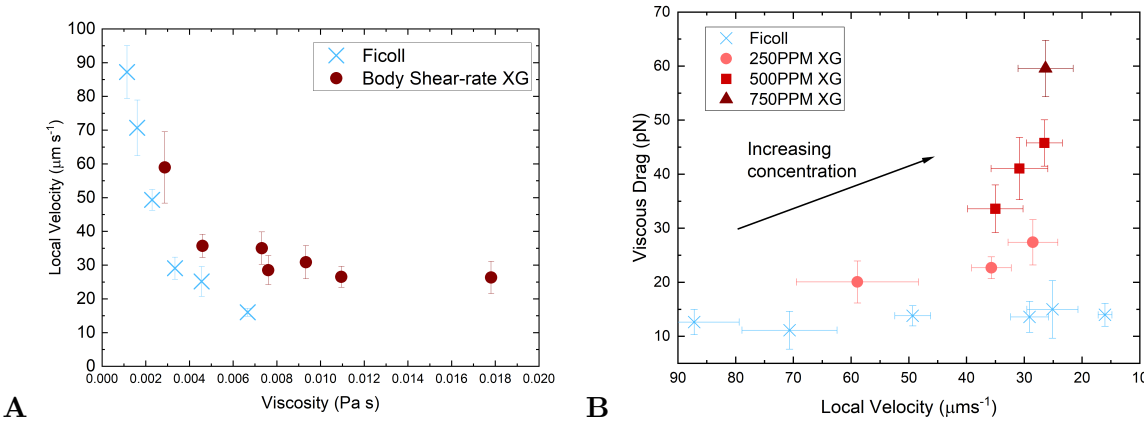

Figure 6.6: (A) Local velocity varying with the calculated body shear rate for shear thinning and Newtonian solutions. A clear separation is observed, primarily driven by the reduced viscosity felt by the flagella due to increased produced shear rates. Error bars denote standard deviation across population analysed (B) The variation between flagella and body viscosities relates to an apparent viscous drag increase calculated by inputting the body viscosity and local velocity into equation 4.13.

Thus, it seems the presence of the shear thinning solutions induces a viscous imbalance across the swimmer, allowing the flagella to beat as if they were in a medium of low viscosity. The body is then constrained to relatively higher viscosities. This has the two-fold effect of reducing the beating frequency and increasing the amplitude of the stroke, as seen in figure 6.3.

6.4.2 Flagella gait

An assumption made through the previous section is a consistent flagellum beating pattern through the stroke. It seems that this is true for the Newtonian cases, as the stroke dynamics remain relatively constant between the power and recovery strokes, and has been seen in another puller algae [24]. However, several studies have found fluids with shear thinning properties to alter the motion of the flagella through their beat [24, 33, 34], although most have elastic properties on top of shear thinning properties. Unfortunately, sufficient quality images for enhanced flagella tracing was not available in this research, as discussed in Section 3.6.2.2.

Of particularly note is the recovery stroke change found in *C. reinhardtii* in which the recovery stroke sees notable alteration in its pattern, returning closer to the body and increasing the time spent in this stroke under the influences of a shear thinning viscoelastic fluid [24]. In *D. salina*, the time spent in the recovery stroke was found to increase with shear thinning properties, possibly hinting at changes in flagella gait as seen in *C. reinhardtii*. If the gait of the recovery stroke was found to alter, it may be reasoning behind the variation in responses between the power and recovery stroke. This is an area of this research that could be added to in future research.

6.4.3 Viscous gradients

With the presence of a shear thinning fluid, viscosity gradients will be present as the swimmer applies a shearing force to the fluid. Gomez et al. [163] argue that an increased helix velocity in a shear thinning fluid was related to confident like effects due to viscosity stratification around the swimmer.

Table 6.2 may hint to an influences of shear thinning viscous gradients, with the MSD diffusion exponent reducing with increasing power-law. Thus, the swimmer is seen to tend towards random walk motion with increasing power-law of the fluid. If viscous gradients are seen to influence the swimmer, they may be a cause of this response due to viscotaxis

at a very local scale.

Furthermore, viscous gradients may be in part behind the changes seen between power and recovery stroke. In the power stroke, the flagella pull the swimmer though the fluid. However, in the recovery stroke, the algae become effectively a pusher swimmer, with the flagella acting as a motor at the back of the swimmer propelling the swimmer backwards [60, 62, 308]. Thus, through the stroke the body "follows" the flagella in the power stroke and "leads" the flagella in recovery. In terms of the viscous gradient present, the direction of the viscosity gradient will alter, relative to the direction of travel through each stroke. Therefore, potentially affecting the two strokes in different manners.

6.4.4 Non-Newtonian wake

Another hypothesis could involve non-Newtonian wake that has been built up behind the body or flagella as they move through it. As Xanthan gum solutions are inelastic at these concentrations, memory effects are likely very small or non-existent. Furthermore, analysis of a helical swimmer ruled out these effects in a shear thinning fluid by altering the swimming direction of their helix, where no change was found [163]. Therefore, it is likely these influences in this regard are not a driving factor in the case descried here. However, it is very possible that this will occur when viscoelastic fluids are analysed in the following chapter. Even with the very little time dependence of the shear thinning fluid, residual stresses or similar may still be present in the previously sheared fluids by the flagella that the body would feel in the power stroke as it is "following" the flagella through this fluid. However, in the recovery stroke this would not be apparent as the swimmer becomes an effective pusher.

6.4.5 Polymer interactions

A further interaction that may be influencing the stroke is the flagella interacting with individual polymers. The assumption has been made thus far that all interactions in the

fluids are in the continuum. However, the length scales of the polymer strands within Xanthan gum are not too dissimilar for the flagella characteristics. The diameter of the flagella (200 nm) [101, 102], is similar to the radius of gyration of Xanthan gum, which is 241 nm [309]. Therefore, it may be possible for the flagella to be interacting with the individual polymers with the polymers potentially tangling in the flagella or simply making it harder for the flagella to move through the fluid [179, 310].

Furthermore, V. Martinez et al. stated the possibility of the flagella of *E. coli* to pass through the polymers, not interacting with them and not causing them to stretch or create a shear response [27]. *D. salina's* flagella are larger than *E. coli's*. However, it is possible the flagella like in E.coli could be passing by the polymers, having little influence on their stretching profile. If true, the flagella, rather than shearing the fluid and feeling low viscosities in this regard, would simply pass by the polymers essentially feeling close to the base solution (medium or medium with Ficoll) and thus presenting a different reasoning behind the response in Figure 6.3 and discussed in Section 6.4.1. The primary shear thinning response would then be controlled by the body as it moved through the fluid as it stretched the polymers.

6.4.6 Passive vs active swimming

One question that can be posed and has been discussed in the literature with no definitive answer [24, 141] is whether a change in stroke dynamics is passive or active. Active stroke change is when the swimmer changes its stroke actively to counter new complex fluids and passive when the swimmer has no control in the presence of complex fluids. Another possibility is that the stroke pattern of the swimmer has been developed through the evolutionary process so it can work in both a Newtonian and complex fluid as efficiently as possible.

The question of whether *D. salina* have the ability to alter their stroke to overcome complex fluid interactions to maintain efficiency is primarily a biological one. From the

data, it is apparent a shift is seen in favour of the recovery stroke, seemingly reducing the effectiveness in terms of the velocity ratio relative to the power stroke. It cannot be stated for certain, but the fact the swimmers' efficiency is decreased it would be suspected that the swimmer does not have active control of its stroke to maintain efficiency though these fluids. However, the stroke could potentially be altering to make the movement "less worse" or there may be an overall increase to both power and recovery strokes.

In their natural habitat *D. salina* would not come across complex fluids of this nature, so it would seem strange for the swimmer to possess an ability to actively respond to changing fluid stimuli. A biological method of active swimming has not been observed to our knowledge, and the fact the swimming stroke reduces in efficiency would lead us to believe that the response observed is passive and driven by the changes in fluid around the flagella and body of the algae.

6.5 Defining an effective shear rate

In the work thus far, defining an effective shear rate of the swimmer and using it as a tool for comparison to Newtonian solutions has been avoided to remove the uncertainties with this method. The dialogue that follows discusses the effective shear rate the algae exert and how appropriate it is as an approximation of swimming characteristics in complex fluids. A comparison is drawn between the shear thinning results at different effective shear rates based on approximate values of the body and flagella shear rates as often conducted within the literature. The definition of an effective viscosity and examples used in the literature can be found in Section 2.4.1.

The effective body shear rate calculated by Equation 6.1 of the swimmer in different shear thinning solutions can be viewed in Table 6.3. An effective shear rate to define the characteristic beating is often more complex to calculate. In the case of *D. salina* this is related to the shear rate produced by the flagella. Many propositions have been discussed in defining a characteristic beat effective shear rate [24, 311] for such a swimmer and with

the complex stroke pattern of the flagella, it can be difficult to gain an accurate estimate. For the following, a nominal high shear rate ($1000\,s^{-1}$) is examined. This high shear value was chosen from experimental observations and is by no means representative, it purely aims to give a rough approximation of the flagella shear and a comparison range to compare to the body effective shear rate.

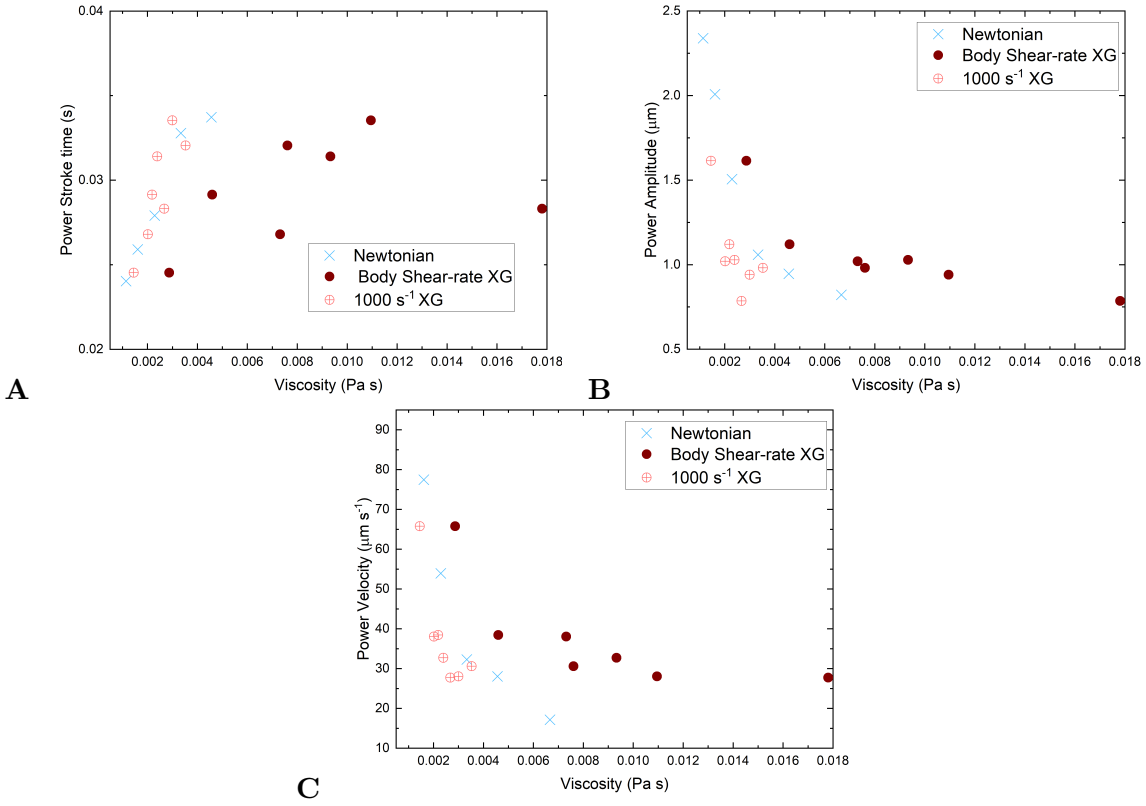

Figure 6.7: (A) Power stroke time plotted assigned body effective viscosity and $1000\,s^{-1}$ giving an effective viscosity for comparison to Newtonian solutions, (B) power amplitude, (C) power stroke velocity.

Calculating the viscosity based on the defined body and flagella effective shear rates and plotting for each individual swimming attribute as shown in Figure 6.7 for the power stroke, shows the variation in the body and flagella shear. The stroke times for all cases lie close to the Newtonian cases at a shear rate of $1000\,s^{-1}$ (Figure 6.7 (A)) showing the

apparent large shear rate produced by the flagella. Whereas the amplitude is presented differently, with Newtonian cases lying in-between the calculated flagella and body effective viscosities (Figure 6.7 (B)). Similarly, the Newtonian power stroke velocity as viewed in Figure 6.7 (C) lies in-between the XG results at effective viscosities corresponding to body and flagella velocities.

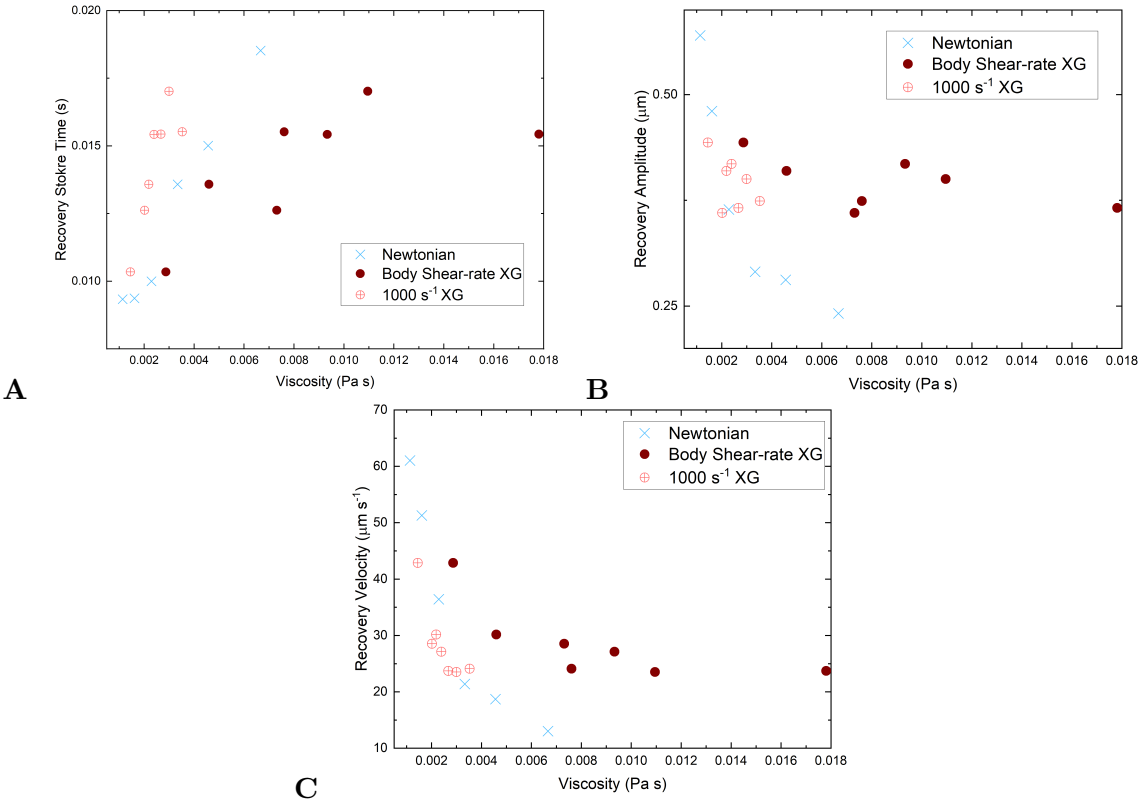

Figure 6.8: (A) Recovery stroke time plotted assigned body effective viscosity and $1000\,\mathrm{s}^{-1}$ giving an effective viscosity for comparison to Newtonian solutions, (B) recovery amplitude, (C) recovery stroke velocity.

In regard to the recovery stroke, calculating estimates of the effective viscosity do not follow the same dynamics as those found in the power stroke. As previously discussed (Section 6.3) the recovery stroke follows very different behaviour to the power stroke, with an apparent increase in stroke time and amplitude in relations to Newtonian swimming.

For the time spent in the recovery stroke (Figure 6.8 (A)), the XG results based on the effective viscosity from the body velocity lie closer to the Newtonian data than was observed for the power stroke, while the amplitude (Figure 6.8 (B)) follows closer to the apparent defined high flagella shear rate.

These results for both the power and recovery stroke show clear differences in the effective viscosity calculation in terms of the stroke dynamics captured through this work. While it may be possible to capture individual dynamics, a single effective viscosity does not capture the full stroke dynamics across both power and recovery strokes, assessed in this work. Furthermore, it is apparent there is a large spread in shear rates present across the stroke with, in the power stroke, the flagella seemingly exhibiting very high shear rates and body much lower.

6.5.1 Challenges of defining an effective shear rate

In the following section, the challenges plus some other considerations will be discussed in regard to calculating an effective viscosity of a swimmer of this nature.

1. Difficulties in the flagella shear approximation

    - The flagella is a complex structure and calculation of a reasonable effective shear rate possess many challenges. For swimmers of this type, the beating frequency has been used in previous works [24]. In Figure 6.7 (A) it seems the power stroke beating time matchs shear rates close to $1000\,\mathrm{s}^{-1}$, significantly higher than the beating frequency approximation. Thus, it would seem a more complex method of defining the shear rate produced by the flagella is needed.

      Riley and Lauga propose an average shear rate across a waving flagellum to be defined as [311]

$$\dot{\gamma}_f = \frac{C_N V_f}{2\sqrt{2} r_f \pi \eta} \tag{6.2}$$

$$V_f = \sqrt{V_N^2 + 2\frac{C_T^2}{C_N^2} \times V_T^2} \tag{6.3}$$

where V_f is the flagellum velocity, C_T and C_N the normal and tangential resistance coefficients and V_T and V_N the normal and tangential flagella velocity components. This function is highly dependent on the flagellum dimensions and velocities [311], values that require in-depth analysis of the flagellum beat pattern and characteristic dimensions. This analysis, due to equipment limitations, could not be conducted sufficiently in this work. Of particular challenge is capturing the normal and tangential velocity components of the stroke across the full range of solutions measured.

2. Large changes in shear rate

   - The large changes in the shear rates produced by the flagella and the body lead to difficulties approximating an average between the two. Convention is the average between the body and flagella shear rates is taken as the effective shear rate. While it is possible to estimate both these values with varying degrees of validity depending on methods, it seems clear that the variation between the two is large for *D. salina*. Therefore, if one has a dominant effect over the other, taking the average between these values will not capture this change. Furthermore, trying to capture the two vastly different shear rates with a single overall shear rate is inherently unrepresented of the whole swimming stroke.

3. Stroke decoupling

   - Another challenge to assigning a body and flagella shear rate is the link between the two, with both sharing an inherent reliance of the other. Any changes to the body dynamics will affect the flagella and vice versa.

4. Polymer interaction

- Finally, the effects of polymer interactions have not been sufficiently quantified to include or discard their influences on any effective shear viscosity. If the flagella do pass by the polymers [27] having little influence on the stretching profile of the polymer, the defined effective shear rate of the flagella would have to incorporate this, with potentially the body being the primary driver of a true shear thinning response.

Taking all these uncertainties into account, it is clear that defining a singular effective shear rate for a swimmer of this type provides many challenges and deep knowledge into many dynamics of the swimmer's stroke should be undertaken beforehand. Even with an accurate effective shear rate of the body and the flagella, difficulties still arise in the interaction between the two and the dominance on either on the swimming stroke. For swimmers where the characteristic beating shear rate and body shear rate are close such as *C. elegans* the effective shear rate calculation may simplify, but for a swimmer such as *D. salina* it may not be an applicable method of comparison.

6.6 Effect of shear thinning properties on swimming velocity

Defining whether shear thinning properties have a positive or negative effect on the swimming velocity is difficult to conclude from the data obtained through this work. A definition of the changes to velocity relies on a comparison to a Newtonian case, as it is heavily influenced by the viscosity of the fluids. Shear thinning fluids make this difficult due to the viscosity dependence on shear rate.

If compared to the zero-shear viscosity, shear thinning properties will always likely lead to increases in velocity as the viscosities are always decreased across the swimmer compared to the polymer-free medium. However, to increase swimming velocities it may not be as simple as adding a shear thinning agent to a medium and increasing velocities, as the addition of any agent will inherently increase the viscosity of the fluid.

Compared to the body shear rate, the swimmer showed an increased velocity and an apparent thrust increase (Figure 6.6). This is as a result of the flagella feeling a reduced viscosity relative to the body. If compared to the flagella shear rate, the velocity will likely always be reduced. Convention dictates that an effective shear rate can be taken as the average between the flagella and body effective shear rates, and this may prove to be an efficient measurement to define velocity increases or decreases from non-trivial viscosity swimming dynamic changes. However, as mentioned, this method presents many difficulties in its calculation.

Through analysis of the stroke dynamics, it was apparent that shear thinning fluid properties led to a shift in favour of the recovery stroke in terms of the velocity ratio between the two. This was increased with the power-law index of the fluid and increased viscosity. Therefore, it would seem that the overall efficiency of the stroke is decreased and thus, that the swimmer would swim slower in a shear thinning fluid. However, it is not possible to determine the quantitative change in swimming rate at a specific viscosity without a way to determine the appropriate Newtonian and shear-thinning cases to compare.

6.6.1 A note on artificial swimming

For the application of designing an artificial swimmer that may need to navigate shear thinning fluids, it would generally be desirable to produce a swimmer with the greatest efficiency. The results presented in this work show challenges in using the dynamics to increase the efficiency in the stroke. If the dynamics of the recovery stroke relative velocity enhancement can be understood, utilised and reversed, so they apply to the power stroke such that the velocity ratio enhancement between the two favours the power stroke, it may be possible to increase the swimming efficiency of such type of swimmer. This may be as simple as placing the flagella at the rear of the body and pushing the swimmer through the power stroke rather than pulling. However, much greater detailed work would have to be conducted to fully quantify this.

6.7 Conclusion

To conclude, a marked change in stroke dynamics has been observed under the influences of a shear thinning fluid. The power stroke was found to experience a reduction in both the amplitude and time spent in the stroke, an attribute that was related to the flagella feeling a reduced viscosity of the body either by its larger produced shear rate or by passing the polymers within the solution. In contrast, the recovery stroke experienced the opposite, with an increase in amplitude and stroke time relatively. The recovery stroke changes could not be attributed to simple viscous changes, and therefore must be a method of some other non-trivial factors. Furthermore, the recovery stroke experienced an enhancement in terms of the stroke velocity, compared to the power stroke and thus the swimming efficiency seems to decrease in a shear thinning fluid. The addition of viscosity seems to increase this favourable shift towards the recovery stroke. From this analysis it has been shown that the power-law exponent is a poor defining characteristic of shear thinning properties and the viscosity and possible the solvent viscosity play an important role.

At the start of this work, it was hoped an effective shear rate could be quantified. However, as the analysis progressed, it became apparent this method was not practical due to difficulty defining the flagella shear rate and the large variations in shear rate across the body and flagella. Therefore, this method was deemed unfit for this analysis as detailed flagella imaging would have to be undertaken, which was not possible.

Chapter 7

Swimming in viscoelastic fluids

7.1 Chapter overview

This chapter focuses on the effects of viscoelasticity on the swimming kinematics of *D. salina*. Firstly, the fluid rheology is introduced giving a description of the key rheological parameters such as viscosity curves, relaxation times and the critical concentration. The chapter then moves focus to the swimming kinematics, starting with the swimming velocities captured with a conventional camera. Thereafter, the stroke dynamics are presented in the presence of viscoelastic fluids and a discussion conducted into the effects of these fluids on the swimming characterisation.

7.2 Fluid properties of modified medium with Polyacrylamide

Polyacrylamide (PAA) is a long chain polymer known for its viscoelastic time dependant properties when diluted into an aqueous solution (Section 3.3.2.4) [312, 313]. These properties are utilised in the characterising of *Dunaliella salina's* response to viscoelastic effects of their medium. High molecular weight Poly(acrylamide/sodium acrylate) [70:30] (Polysciences) was used as the polymer of choice throughout this work ($MW = 18\,000\,000$). PAA was added to the medium as described in Section 3.3.2.5 creating solutions of varying

viscoelasticities.

7.2.1 Shear rheology of modified medium with PAA

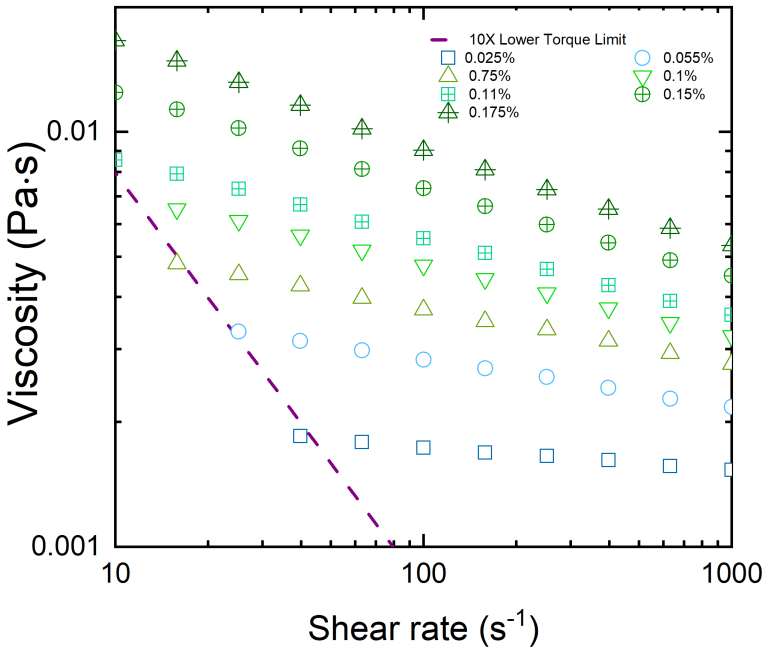

Figure 7.1: Flow curves showing the steady shear viscosity of polyacrylamide solutions. All the fluids show varying shear thinning properties. The minimum measurable torque represented by the purple dashed line is calculated from Equation 3.10.

The shear viscosity flow curves are plotted in Figure 7.1 for the viscoelastic solutions analysed. As well as viscoelasticity, the solutions are seen to exhibit shear thinning behaviour. It should be noted that in this work, PAA solutions are notated in terms of % concentration and XG by parts per million.

As discussed in Section 3.2.1, *D. salina* are a halophilic alga meaning they live in salty environments and to mimic their natural habitat the medium contained a large concentration of salt (Section 3.2.1). Unlike Xanthan gum, which shows no interaction with salts, the properties of polyacrylamide solutions are significantly altered by its presence. Sodium

ions in the salts, cause the polymer chains to coil which in turn decreases their hydrodynamic volume. This has the two-fold result of reducing the viscosity as well as the elastic properties of the polymer solutions [234, 235, 314, 315]. All rheological measurements were conducted with the medium as the base solution and thus have the full salt concentrations.

7.2.2 Extensional rheology of medium with PAA

As well as the shear rheology, the extensional rheology of the PAA solutions was quantified to characterise the elastic response of the fluids under extension. This was carried out using the CaBER as described in Section 3.3.4. The PAA solutions showed an increase in relaxation time with increasing concentrations (Table 7.1) increasing from 25.8 ms in the lowest concentrated solution to 188 ms in the highest.

Table 7.1: Extensional rheology data of PAA solutions with the longest extensional relaxation times determined from CaBER measurements.

PAA concentration	**Relaxation time λ (ms)**	**STDEV**
0.025%	25.8	2.69
0.055%	49.5	2.27
0.075%	60.9	2.8
0.1%	69.1	5.1
0.11%	72.2	3.2
0.15%	94.5	3.5
0.175%	96.8	2.9
0.5%	188	2.1

7.2.3 Critical overlap concentration of PAA

A further important characteristic measurement of a polymer solution, such as the ones used in the work here is, the critical overlap concentration (c*), the transition from the dilute regime [314,316]. This definition is of significance, as a worm type swimmer has been observed to gain a significant enhancement in velocity after the cross-over point is reached, albeit the solutions reached a fully concentrated state [26]. The critical concentration can

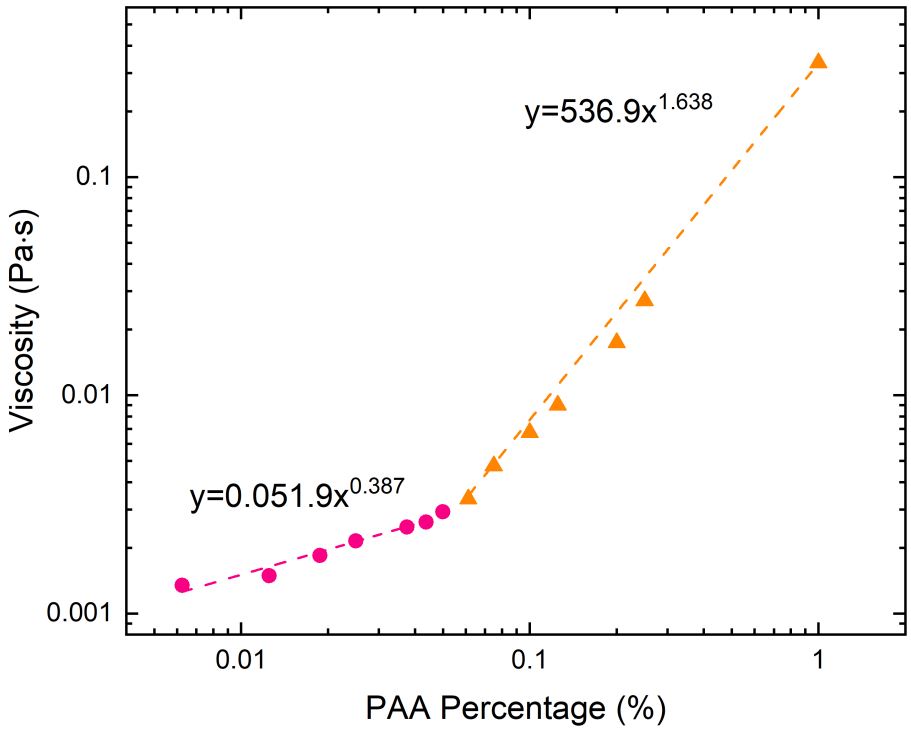

Figure 7.2: Viscosity variation with PAA concentration showing the point of critical overlap concentration, with regimes denoted by pink circles and orange triangles (1% solutions is included for line fit). Critical concentration is calculated from intersection of power fits (viscosity measurements taken at $15s^{-1}$).

be visualised by plotting the polymer concentration against the viscosity in log-log (Figure 7.2). The cross-over point was calculated at the intersection of the two regimes and was found to be 0.061% at a shear rate of $15s^{-1}$. The range of PAA concentrations used in this work varies from $0.025\% - 0.5\%$, thus crosses this critical concentration threshold.

7.2.4 Weissenberg number

The Weissenberg number as defined in Section 1.3.2 is an important dimensionless number used when non-linear elastic effects are present.

Here, the Weissenberg number is defined as the product of the characteristic shear rate produced by the swimmer and the relaxation characteristic of the fluid ($Wi = \lambda\dot{\gamma}$). As shown in Chapter 6, *D. salina* produce shear rates that vary significantly across its flagella and body, and thus the Weissenberg number will also vary across the swimmer. The body shear rate for the analysed solutions is calculated using Equation 6.1 and was found to be below unity for all cases examined. As for the flagella, as discussed in Section 6.5.1 it was estimated the characteristic shear rate to be in the region of 1000s^{-1} from the stroke times in a shear thinning fluid. From this very simple analysis, it becomes clear that the flagella will experience much higher Wi numbers than the body (Table 7.2). Therefore, it is likely the response to viscoelasticity will primarily be caused by the flagella.

Table 7.2: Body and flagella Wi numbers defined as $Wi = \lambda\dot{\gamma}$, where the shear rate is taken as the approximate shear rate at the body and flagella.

Solution Concentration	**Body Wi**	**Flagella Wi**
0.025%	0.234	25.81
0.055%	0.377	49.53
0.075%	0.370	60.92
0.11%	0.291	69.07

7.3 Swimming velocities in viscoelastic fluids

A summary of the recent work into the effects of viscoelasticity on the swimming of microorganisms is provided in Section 2.2 with often the overriding question being whether elastic effects aid or hinder such swimmer's motion. However, no clear definition suitable for all microswimmers has been proposed, and the effects vary depending on swimmer type, motility method and type of polymer.

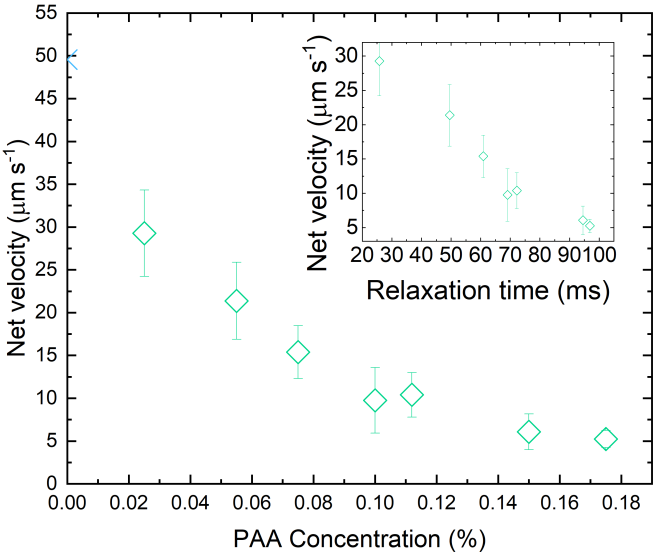

Figure 7.3: Net swimming velocity as a function of PAA solution concentration. Swimming velocity decrease is primarily due to increases in viscous forces with increasing solution concentration. The inset shows velocity in relation to the relaxation times of the viscoelastic fluid.

As with the previous analysis carried throughout in this work, the first step taken is to analyse the global net motion of the swimmer, as defined in Section 4.2.2.2. Figure 7.3 shows the change in swimming velocity in regard to the concentration of the PAA within the medium. A clear reduction in velocity is seen with increasing concentration. This would be expected as it follows the increase in viscous forces with concentration increase. The inset of Figure 7.3 shows the change with respect to the relaxation time of the fluid with similar findings, again following a decrease with increasing relaxation times.

From the initial data, no clear and obvious change in gait is determinable at the critical cross-over point (0.061%) with the data following the expected trend.

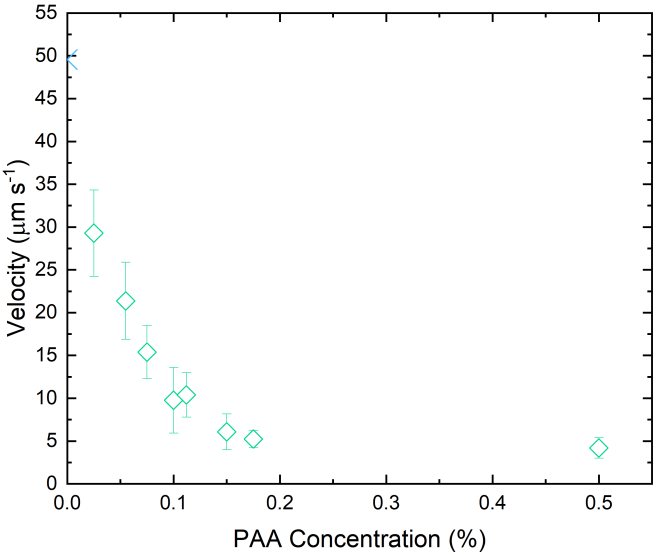

Figure 7.4: Net swimming velocity in highly elastic solution, showing little deviation from overall trend and observations in Newtonian highly viscous fluid.

7.3.1 Swimming at very high relaxation times

The discussions thus far have focused on the lower end of the viscosity spectrum below the point non-swimming as defined in Section 5.4.2. Further to this analysis, it is important to look at higher concentrations to discern any highly elastic effects and ascertain if they can become dominant over the viscosity. Therefore, a solution of 0.5% PAA was analysed with a relaxation time of 188ms.

Figure 7.4 extends the plot in Figure 7.3 to include the data for 0.5% PAA. The data lines up very closely to that of the highly viscous case in Section 5.4.2 with the velocity sitting slightly above the defined point of non-motility. Therefore, it can be stated that for this concentration, elastic effects do not overcome the viscous forces.

7.3.2 Shear thinning decoupling

As seen in Chapter 6, *D. salina* are influenced by shear thinning properties of the medium. As aqueous PAA solutions are shear thinning, it is important to decouple the effects of shear thinning and viscoelasticity throughout the analysis. Therefore, the analyses completed in Chapter 6 will be drawn upon throughout the next sections in an attempt to decouple any viscoelastic responses from shear thinning.

Ideally, a viscous comparison would be drawn to the Newtonian cases, but as discussed previously this was avoided due to the inconsistencies with the definition of an effective viscosity (Section 6.5.1). Therefore, to decouple the two responses, the rheological properties of the shear thinning and viscoelastic solutions need to be understood and related through the analysis.

When a rheological comparison is drawn with the XG and PAA solutions, some notable solutions of comparable rheological are found. The PAA solution of concentration 0.075% shares a similar power-law index ($n \sim 0.857$ (XG) $vs\, n = 0.864$ (PAA)) than that of the 250PPM XG solutions and in terms of viscosity, the PAA solution (0.075%) lies halfway between 250PPM-2% and 250PPM-4% (Figure 7.5). Therefore, if purely in regard to the shear thinning properties, in this solution, the algae should exhibit a response that lies between the two XG solutions. Another further comparison could be drawn between 250PPM-2% and 0.055% which display very similar rheological properties, with the Xantham gum solution displaying a slightly higher power-law index ($n \sim 0.857$ (XG) $vs\, n = 0.864$ (PAA)).

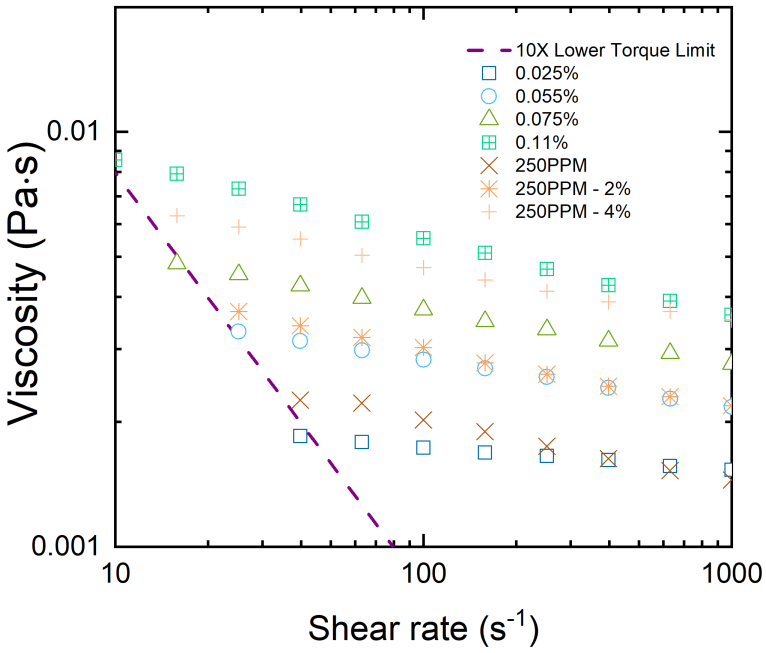

Figure 7.5: Comparison of the shear rheological data of the PAA solutions with that of the 250PPM Xanthan Gum. Particular note should be taken of 0.055% PAA / 250PPM−2% and 0.075% as it has similar power-law index as 250PPM XG and lies in between 250PPM−2% and 250PPM−4% in terms of viscosity.

7.3.3 Swimming in solutions of comparable rheology

For this stage of the analysis, the different algae dynamics in the solutions of comparable rheological properties (as disused in the previous Section, Section 7.3.2) are compared. A comparison of the velocity distributions are plotted in Figure 7.6 where 0.055% PAA and 250PPM−2% XG-Fic share similar rheology and 0.075% lies in between 250PPM−2% and 250PPM−4%. For both these comparisons, a clear difference between PAA and XG swimming is present, with both the power and recovery stroke velocities for the viscoelastic solutions appearing higher than the shear thinning. In relation to the stroke amplitude and beating frequency (Figure 7.6 inset) the algae in the PAA solutions maintain a much greater beating frequency and the amplitude is similar to the comparable XG case for

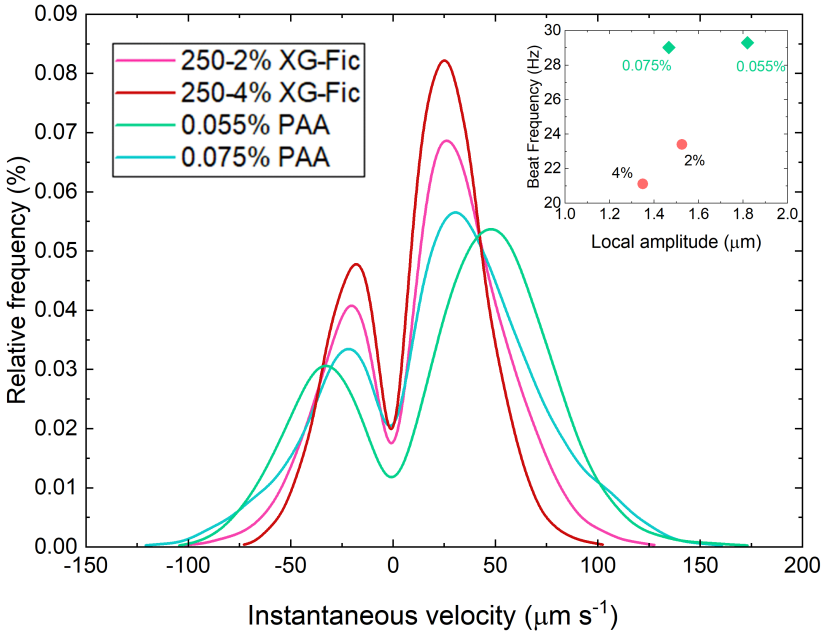

Figure 7.6: Velocity distributions of algae in solutions of comparable rheology (0.055% PAA / 250PPM−2% and 0.075% between 250PPM−2% and 250PPM−4%). Inset shows the beating frequency and amplitude of the solutions, showing that the increased velocity is mostly driven by the increased frequency. Percentages relate to PAA concentration and additional Ficoll in XG solutions.

0.075% PAA. The increase in amplitude in 0.055% on the comparable XG case may be due to the difference in viscosity at the body shear rate due to the slightly different power-law indices. Therefore, it seems that this velocity enhancement is primarily driven by the increased beating frequency in the viscoelastic solutions.

However, for these solutions, one property that has not been maintained is the solvent viscosity. The Xanthan gum solutions used in this analysis include additional Ficoll which would be assumed to increase the solvent viscosity from the base, which is not the case in the PAA solutions as they do not possess the extra Ficoll. As discussed previously (Section 6.4.1), the flagella (either by producing a very large shear rate or passing by the polymers) seem to feel the (or very close to the) solvent viscosity of the fluid they are immersed in. If true, this may be the reasoning behind the differences in beating

frequency in the comparable solutions discussed as the flagella are feeling significantly lower viscosities in the PAA solutions, thus showing the response is not entirely dependent on the viscoelasticity. Therefore, it is not possible to attribute the differences in dynamics purely to elastic properties of the fluid.

7.3.4 Stroke dynamics in a viscoelastic fluid

To further analyse the response to viscoelastic fluids, similar analysis methods are conducted as previously undertaken in the shear thinning fluid cases (Section 6.3).

The first stage of this process is to analyse the average amplitudes and stroke times for the power and recovery stroke in relation to their Newtonian counterparts, reducing the stroke down to its simplest form (Figure 7.7). In regard to the power stoke (Figure 7.7 (A)), the data follows similarly to the response observed in the shear thinning solutions without any additional Ficoll. For the solutions with low PAA concentration, the stroke times stay remarkably close to that displayed by swimmers in the medium with no rheological agents. In some solutions a stroke time less than that in the medium is displayed. However, this is likely due to experimental uncertainties rather than a physical response.

The recovery stoke, in the most part, shows similar data to the shear thinning solutions. However, there are notable disparities in the data, with the viscoelastic solutions displaying a varied response across the solutions analysed. However, within the error it is difficult to denote a significant deviation from the shear thinning trend.

To provide further insight, the relative scaled stroke dynamics in reference to a full stroke are analysed (t_{pow}/t_s & A_{pow}/A_{net}) as displayed in Figure 7.8. For the viscoelastic solutions, displayed in green, as would be expected, a relative shift in amplitude and time is observed. This follows the trends found in shear thinning solutions (Section 6.3) and it may be suggested that the dynamics presented are dominated by the shear thinning properties of the viscoelastic fluid. From the data thus far, it is difficult to note swimming dynamics that can be purely attributed to an elastic response, as the responses observed

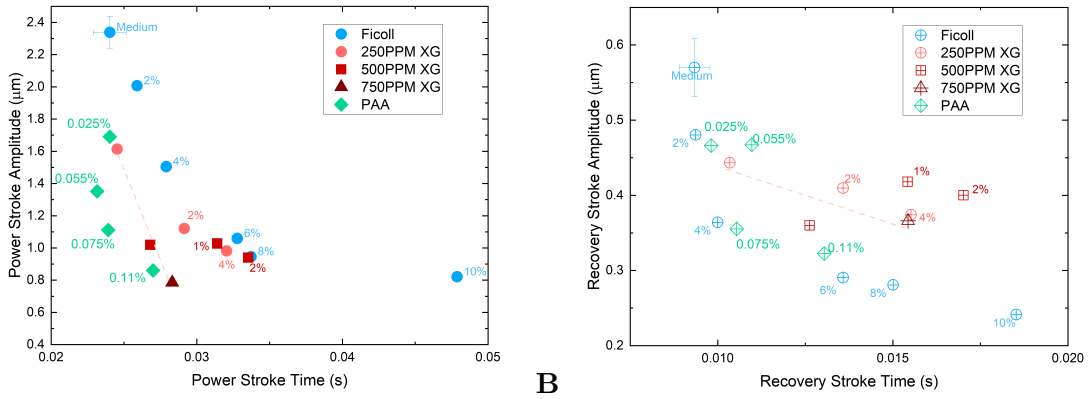

Figure 7.7: (A) Average stroke amplitude and time for power stroke in shear thinning, viscoelastic Newtonian solutions. Percentages relate to the addition of Ficoll in shear thinning solutions (red), PAA concentrations (green) and Ficoll concentrations (blue). Example error representative of entire data set is displayed on medium data point, relating to standard deviation of population. Each point consists of data from between 8 - 15 algae representing approximately 1000 data points. (B) Recovery stroke.

can be attributed to the shear thinning properties of the medium.

The ratio of the power and recovery stroke velocities is plotted in Figure 7.9. It is apparent that the velocity ratio (V_{pow}/V_{rec}) in the viscoelastic solutions decreases in favour of the recovery stroke with increasing concentration. A factor likely in part induced by the shear thinning nature of the fluid. However, the viscoelastic solutions feel the reduction in stroke efficiencies at a lower power-law index than the shear thinning fluids without Ficoll. As the visoelastic solutions should share similar solvent viscosities to the base shear thinning solutions, this may not be the reasoning behind the reduced velocity ratio, and it is possible the elasticity in the solutions are partly responsible for this change. However, difficulties are still present, as differences in the viscosity of the solutions may also be influencing this change, as seen in XG solutions with Ficoll.

Thus far it has not been possible to relate any of the apparent stroke dynamics changes to a purely viscoelastic response, as the variation in strokes observed could also be related to variations in the solvent viscosity. The analysis has focused on decoupling the shear thinning and elastic responses. However, total decoupling of shear thinning effects from

viscoelastic presented challenges as the power-law index, general viscosity and solvent viscosity all seem to play a part in the stroke response. In an attempt to combine the features into a single metric, the effective body shear viscosity was calculated as in Section 6.4.1.1. This can be viewed in Figure 7.10 (A) plotted against the local swimming velocity. The viscoelastic solutions again display similar characteristics to shear thinning solutions. Thus, it is likely that for the solutions analysed the response observed of the swimmer in viscoelastic solutions is primarily dominated by the shear thinning properties of the solutions rather than elastic elements. Furthermore, the calculation of the viscous drag in Figure 7.10 (B) shows the expected trend, following the analysis of the shear thinning solutions. Therefore, from the data presented, it is not possible to relate specifically any of the swimming dynamics purely as a response to elastic elements with the fluid.

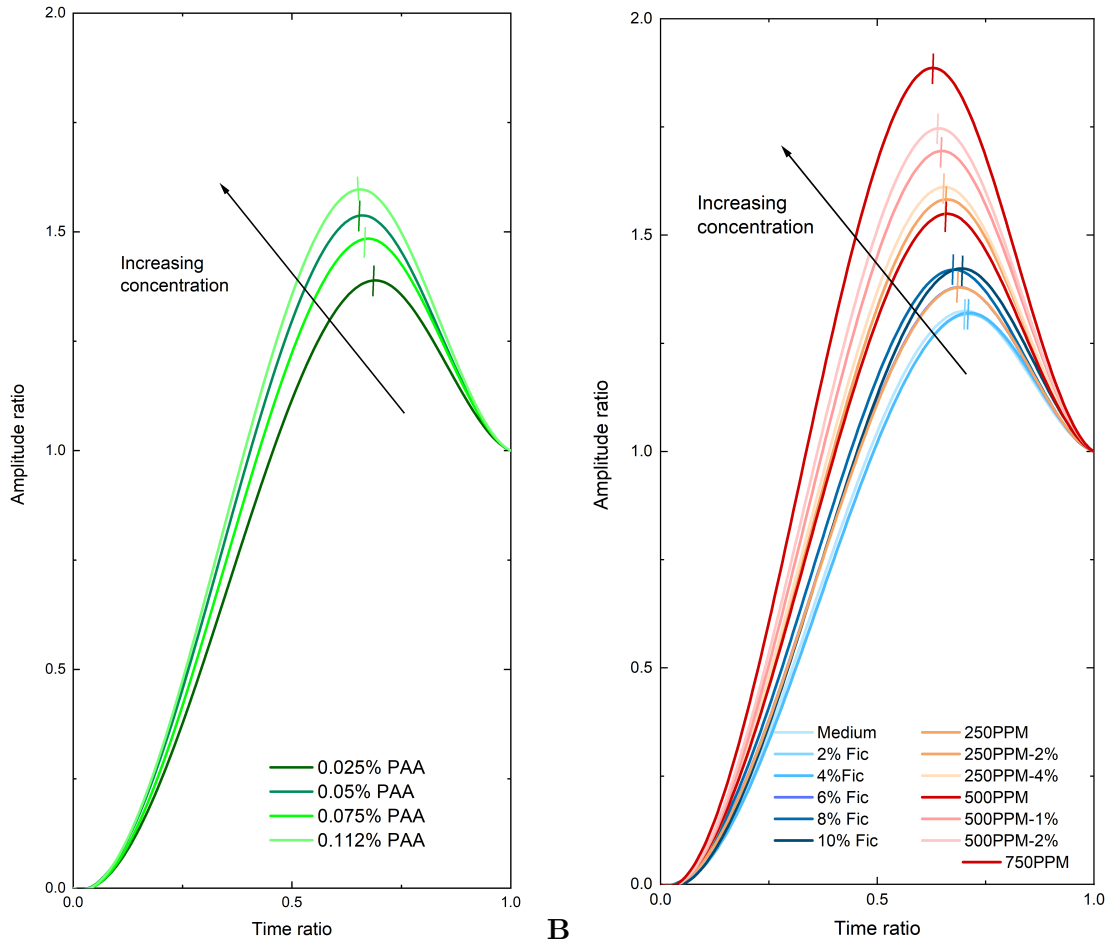

Figure 7.8: (A) Stroke data scaled to the relative values of a full completed stroke for viscoelastic cases. Crosses denote t_{pow}/t_s & A_{pow}/A_{net}. (B) Shear thinning and Newtonian cases for comparison

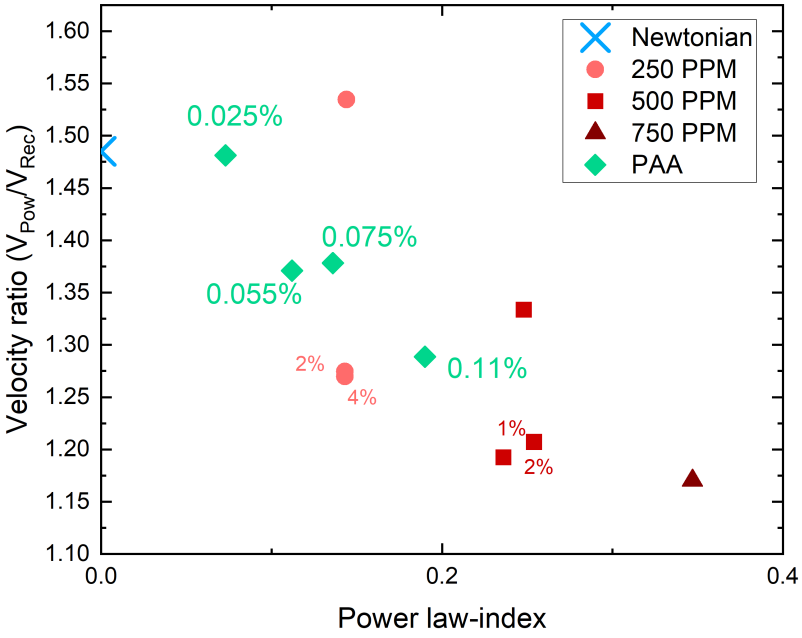

Figure 7.9: Ratio of velocities between power and recovery stroke relative to the power-law index of the fluid the swimmer is immersed in. Newtonian solutions are represented by a single point, as the variation in velocity ratio is minor. Percentages relate to the addition of Ficoll in shear thinning solutions (red) and viscoelastic concentrations (green).

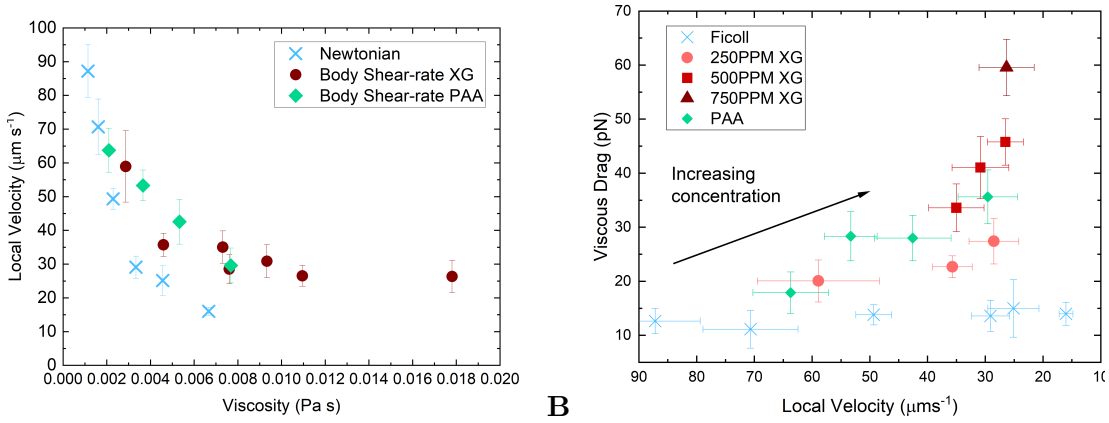

Figure 7.10: (A) Local velocity varying with the calculated body shear rate for shear thinning, viscoelastic and Newtonian solutions. Error bars denote standard deviation across population analysed (B) Viscous body drag for three different solutions measured. Viscoelastic solution follows experted trend from its shear thinning properties.

7.3.4.1 Swimming orientation

Table 7.3: Viscoelastic power-law fit of local MSD with diffusion coefficient and exponent extracted from the fit.

Fluid Concentration	**Power-law fit**	**Diffusion Coefficient**	**Diffusion Exponent**
0.025%	$y = 750.8x^{1.869}$	750.8	1.869
0.055%	$y = 361.1x^{1.842}$	361.1	1.842
0.075%	$y = 171.9x^{1.832}$	171.9	1.832
0.11%	$y = 94.36x^{1.85}$	94.36	1.850

The swimming orientation dynamics was analysed as in Section 4.2.2.4 for the swimmers in viscoelastic solutions. The MSD results can be viewed in Table 7.3. In comparison to the Newtonian and shear thinning cases, no significant notable shift in the dynamical swimming properties was observed. The diffusion exponent and characteristic times fall in the similar ranges observed in the other solutions. Therefore, it seems by this analysis viscoelasticty does not affect the swimming orientation of *D. salina* by the metrics analysed.

7.4 Discussion

As the power-law index, general viscosity and solvent viscosity all seem to influence the swimmer's response to complex fluids, full decoupling of these effects from any viscoelastic responses is challenging. For the viscoelastic solutions analysed, any variation from the Newtonian base seem to primarily be controlled by the shear thinning properties of the solutions with some hints of an elastic response. That being said, a response to viscoelastic solutions has been observed in a number of swimming species and models, as discussed in Section 2.2, and it is possible that the viscoelastic response is being masked or working in unison with the response to shear thinning properties.

The following section discusses the possible elastic influences on the swimmer. It should be noted that this list is not definitive, and many complex interactions could be present around the swimmer.

1. Elastic stresses

    - The build-up of elastic stress around the flagella is a mechanism that has been discussed and modelled previously. It has been predicted that regions of concentrated stresses can build up near the tips of swimming appendages and can have significant bearing on the active forces of the filament [24, 72, 167, 168]. Furthermore, elastic stress have been shown to accumulate along the tangential flagella axis, potentially affecting the ratio between normal and tangential resistance coefficients of the flagella [167]. These elastic forces have been shown to produce an increase in velocity in both power and recovery stroke, but weighted in favour of the recovery stroke. It is possible the same dynamics are seen in this work and the boost in recovery stroke velocity over the power in viscoelastic fluids (Figure 7.9) is by the mechanisms disused by Li [24, 167]. From this it may be apparent that in terms of the velocity ratio between strokes, the shear thinning properties give an initial boost in favour of the recovery stroke with the viscoelastic solutions adding to this boost with an additional increase.

2. Non-Newtonian wake

    - The build-up and subsequent relaxation of elastic stresses is pronounced for swimming organisms as it is possible for the relaxation time to become comparable to the beating frequency and thus leading to Deborah numbers close to unity ($De = \lambda/t_s$, Section 1.3.2). These values for this experimental work can be viewed in Table 7.4. It is clear that the longest relaxation time of the fluid calculated using the CABeR is in proportion to the beating time for the majority of cases.

Table 7.4: Comparison of beating times and the fluid relaxation time present in viscoelastic solutions. The two metrics are comparable, with De number increasing with solution concentration.

Solution Concentration	**Relaxation time** (ms)	**Stroke time** (ms)	Deborah number
0.025%	25.8	33.8	0.76
0.055%	49.5	34.1	1.45
0.075%	60.9	34.4	1.77
0.11%	72.2	40.0	1.80

Therefore, the flagella and the body may be moving through regions of non-Newtonian wake where region of residual stresses are still prevalent. These regions of non-Newtonian wake would be most prevalent at the onset of each individual stroke. i.e. as the swimmer moves from the power to recovery stroke. It is possible they may be a factor in the slight variation in the flagella power stroke beating frequencies (Figure 7.7) as it may provide a mechanism of easing swimmer's flagella and body movement though the fluid [163].

3. Polymer interactions

- As discussed in Section 6.4.5 under shear thinning influences, the flagella interactions with individual polymer strands is a possibility that cannot be ruled out without detailed analysis. The radius of gyration of PAA (140 nm) as with XG is comparable to the swimmer's flagella diameter($\sim$ 200 nm) . Furthermore, the effects of salts altering the polymer makeup may be influencing polymer interactions, and are a possible reasoning behind the lack of clear swimming variation in the elastic fluids.

  Further, as with Xanthan gum (Section 6.4.5) it may be possible for the flagella of the algae to pass the polymers having little influence on their stretch profile. Thus, the flagella would not be influenced to a large extent by the polymer and the primary response to the fluid would be controlled by the body which as seen

in Table 7.2 are under the influence of relatively small Weissenburg numbers. Hence, this could provide possible explanation behind the dominance of the shear thinning behaviour.

4. Other influences

   - Further to the points discussed, there may be other unknown influences on the changes observed in swimming dynamic. Some of these influences were discussed previously in Section 6.4 and may be a factor such as passive vs. active stroke dynamics, flagella shape and viscosity gradients.

7.5 Does viscoelasticity improve swimming velocities

The question of efficiency and whether elasticity will enhance swimming velocities under viscoelastic influences is difficult to answer under the conditions examined. Defining the effects of elastic solutions has been difficult for the cases examined, with no notable stroke variations for the fluids examined. Therefore, for the experimental set-up it seems that elastic influences have very little influence on the swimming stroke. Of greater importance seems to be the shear thinning properties of the fluid, and this has a dominant influence on the swimming dynamics. As seen in many other swimmers, these results are apparent for this particular swimmer and fluids analysed, varying the swimmer or type of fluid may alter these findings and could lead to be better understanding of the dominant effects.

7.6 Conclusion

To sum up, the stroke dynamics observed in a viscoelastic fluid display a clear and obvious shift in dynamics from Newtonian solutions. The stroke time and amplitudes are found to be reduced in the power stroke and increased in the recovery stroke, and a favourable shift in favour of the recovery stroke was observed. However, due to the confounding effects of

elasticity and shear thinning it is not possible to see dynamics clearly driven by elasticity and the primary response seems to be driven by the shear thinning properties within the solutions. This is not to say that elastic influences are not present, but that shear thinning properties in this case seem to be dominant in defining the swimmers' stroke response. Further work would need to be conducted on the flagella beat pattern or altering fluid properties to ease the shear thinning/viscoelastic decoupling process to fully quantify the effects of viscoelasticity on the swimming dynamics of such a swimmer.

Chapter 8

Interaction with solid surfaces

8.1 Chapter overview

All the measurements presented in the above results sections are based on algae swimming in microfluidic chambers with solid boundaries, but focus on the swimming behaviour in bulk. In this chapter, however, the alga interactions with solid boundaries are examined, as in many applications and natural scenarios algae and other swimmers will be close to and interact with similar boundaries. Initially, the methodologies used for data collection and analysis is described, giving details about the types of interactions and their defining characteristic. The analysis that follows is based on the statistical observations on alga wall interactions based of characteristic variables on approach, escape and at the wall's surface. From these observations, suggestions on the likely dynamics behind such interactions will be discussed. Here, only algae swimming in their original medium (HWMM) are analysed, thus complex fluids or fluids with different viscosities are not examined.

8.2 Methodology of wall response

The process of the collection of data for the wall interaction analysis followed very similar processes as descried in Chapter 3 for the collection of data in complex fluids. However,

only the algae in the vicinity of the boundary side walls ($50\,\mu m > y > 350\,\mu m$) were considered. The algae location was captured and tracked on their approach to, interaction with and scattering from the boundary, which were used as input for a homebuilt MATLAB code to analyse the data, determining approach and scattering angles and velocities, as well as the velocity, displacement and time spent at the wall. The analysis was conducted with the algae in the unmodified HWMM of Newtonian rheology.

8.2.1 Channel properties

For the analysis of wall interactions, a channel with a depth of $\sim 20\,\mu m$ (Figure 8.1) was used to produce a quasi 2D geometry for the algae, in-line with previous work using *C. reinhardtii* [45]. The width of the channel was maintained at $\sim 400\,\mu m$ as in previous chapters, and a 10X objective was used. Example wall bounce interactions are shown in Figure 8.2.

While this method provided a suitable platform to visualise side wall interactions, it also meant increased interaction with the upper and lower walls of the channel due to the narrow depth [43, 77]. This is discussed in more detail in Appendix F.

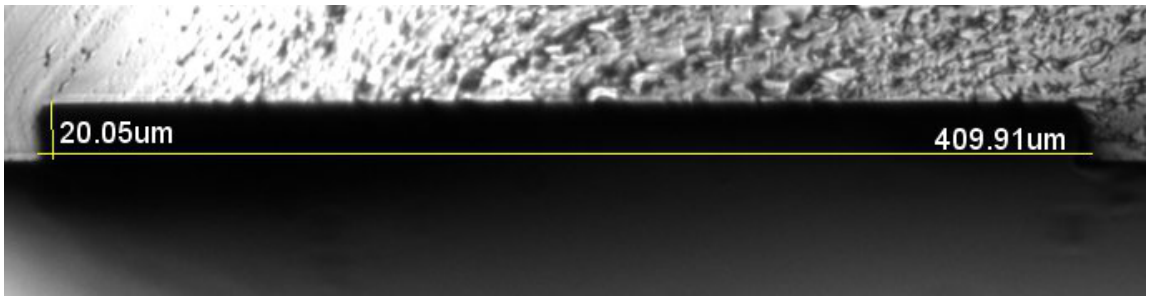

Figure 8.1: Microscope image of shallow (quasi-2D) channel cross-section (displaying height (δ) and width (w)) used to study *D. salinas* interaction with solid boundaries.

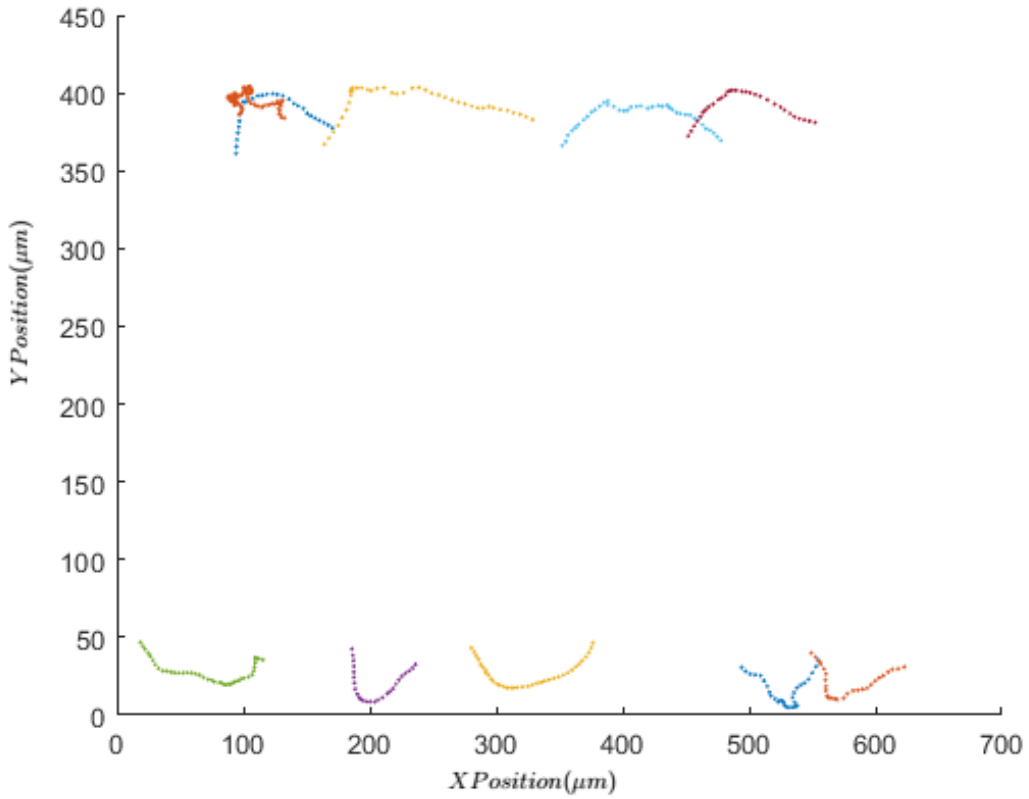

Figure 8.2: Sample bounce interactions with walls taken from the dataset. The walls are approximately located at $y = 0\,\mu\text{m}$ and $y = 400\,\mu\text{m}$ with iterations taken at the centre plane. The approach (defined as 5 frames preceding reaching the wall), wall interaction (when the algae were under 1 body length distance away from the wall) and escape (defined as 5 frames post leaving the wall interaction) are all plotted.

8.2.2 Wall interaction defining characteristics

For a discussion of wall interactions, specific defining dynamics and features must be determined. These could then be used to prescribe a particular type of wall interaction.

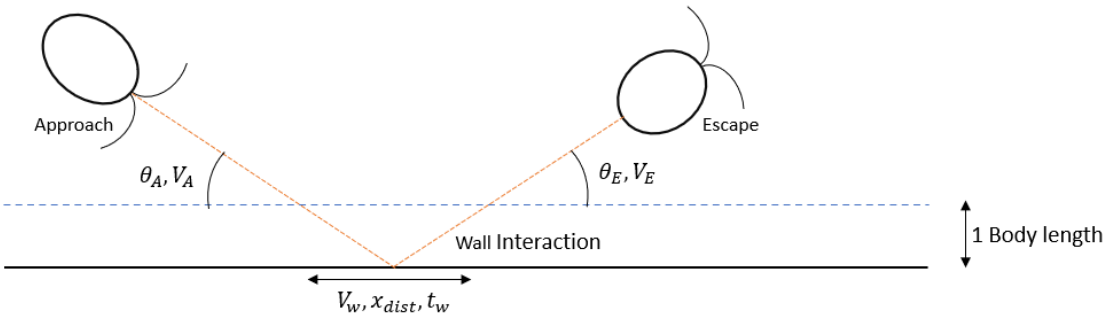

Figure 8.3: Schematic representation of the defining characteristics used to define interactions with a solid boundary. A classic bouncing interaction is displayed, highlighting the incidence and scattering angles (θ_A, θ_E) and velocities (V_A, V_E). Further, when the algae remain within the region of 1 body length distance perpendicular to the wall (blue dashed line) the time at the wall (t_w), distance travelled at the wall (x_{dist}) and the wall velocity (V_W) are collated. Please note, the schematic is not to scale.

In this work, a swimmer was defined as under the wall's influence when the centroid position of the swimmer was less than 1 body length away from the specific wall. The approach and escape, to and from the wall were characterised by two defining characteristics, the approach (incidence) and escape (scattering) angles (θ_A, θ_E) and corresponding velocities (V_A, V_E). On approach, the angles to the wall and velocities of approach were defined as the average of the corresponding instantaneous values of the 5 frames preceding the algae reaching 1 body length distance from the wall. The escape velocities and angles were defined as the average of the 5 frames subsequent to the algae reaching a distance greater than 1 body length from the wall. A schematic diagram of the definitions of wall dynamics can be viewed in Figure 8.3. The approach and escape angles were calculated in relation to the direction the algae approached the wall, such that θ_A is always less than 90°. Thus, the approach angle is independent of the direction of travel (left or right) or which wall the interaction took place at. If the algae were to approach as seen in the

Figure 8.3 and escape in the same direction as the approach, the escape angle would still be referenced in the same manner and thus would be greater than 90°. This was defined as a reverse bounce.

Further characteristics were measured while the swimmer was seen to be in contact with the wall (defined here as within 1 body length from the wall) to give a description of the dynamics while under the wall's influence. These values were the average wall velocity (V_w) which was calculated as the average of the instantaneous velocity between frames across the full time the algae was in this region, the time spent at the wall (t_w) and the entrapment length (x_{dist}) which was defined as the x distance between the point of entry to escape. It should be noted that the entrapment length was irrespective of the time and velocity at the wall, and was purely calculated as the distance between the points of escape and approach.

These parameters allow for a global discussion into how a particular swimmer interacts when in proximity to a solid interface. The full list of defining characteristics can be viewed in Table 8.1. Local interactions such as flagellum contact and the beating frequencies are known to be critical in the process [44, 45] but were not possible to capture using the methods employed in this work.

Table 8.1: Defining characteristics of wall interactions.

Location	**Characteristic**	**symbol**	**Unit**	**Description**
Approach	Angle	θ_A	°	Angle of approach to the wall
	Velocity	V_A	$\mu m\,s^{-1}$	Velocity on approach to wall
Wall	Time	t_w	s	Time spent at wall
	Entrapment length	x_{dist}	µm	x distance between approach and escape
	Velocity	V_w	$\mu m\,s^{-1}$	Average of V_{in} at the wall
Escape	Angle	θ_E	°	Angle after escaping the wall
	Velocity	V_E	$\mu m\,s^{-1}$	Velocity at escape

8.2.3 Types of wall interactions

In this work, the interactions according to the behaviours captured in each video were classified. These behaviours are illustrated in Figure 8.4 and include:

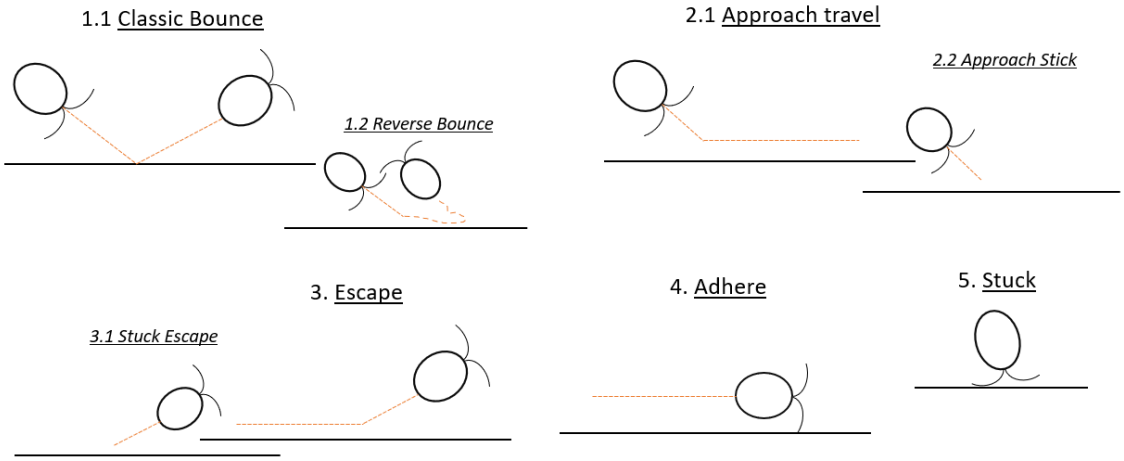

Figure 8.4: Schematic illustrations of the different types of wall interactions. Interactions are displayed, with specific sub interactions also defined.

1. Bounce event

   - To be defined as a bounce event, the alga must approach the interface, come within 1 body length, and then after its interaction with the wall escape from the wall's influence (1 body length distance).

     During the time spent at the wall, a number of different scenarios could occur. A classic bounce was defined as a bounce that approached from one side and escaped from the other such that $\theta_E < 90°$ (Figure 8.4 (1)). Further to a classic bounce, it was possible for the algae to escape in the same direction as the approach ($\theta_E > 90°$), defined as an reverse bounce (Figure 8.4 (1.1)).

2. Approach event

- An approach event was defined as an alga approaching the wall and attaching to the wall with no escape detected (Figure 8.4 (2)). After the contact, the alga may have remained in the same position (Approach stick) or moved along the wall (Approach travel).

3. Escape event

- An escape event was given the definition of when an alga had no approach event captured in the video, but escaped from the wall (Figure 8.4 (3)). This may be as a result of the alga being located at the wall before the onset of the video, or if it was stuck at the wall and managed to escape its influence.

4. Adhere event

- An adhere event was defined as an alga remaining in the vicinity of the wall but with the ability to travel along the wall (Figure 8.4 (4)).

5. Stuck event

- An alga with no movement at the wall was defined as an alga stuck at the wall (Figure 8.4 (5)).

For the definition of wall travel in the case of approach travel (2.1), stuck escape (3.1) and adhere (4) the alga must travel at least 100 µm along the wall.

It was possible that through the methods used, some genuine bounces could be defined as an approach followed by an escape event, splitting the bounce into two separate interactions. This would be presented if the track was lost within the wall region. It was particularly common if two algae came in contact with each other at the wall's surface. To reduce the likelihood of these errors, each track was analysed to ensure any loss of tracks were either combined or removed from the analysis.

Further difficulties appeared as it was possible for algae to swim in and out of the field of view while at the wall. This occurred at the edges of the video frame and through this action, it was possible for a bounce event to appear as purely an escape or an approach interaction. Algae displaying this behaviour were removed from the analysis.

For the experimental set up used, the length of the video had an impact on the interactions. As the video times were relativity short (1 minute), the interactions were thus related to this short time frame. For example, an alga coming into contact with the wall and spending over a minute at the wall before escaping may be seen as a stuck alga by the methods conducted. Thus, the determination of the wall interactions may be influenced by the experimental set-up and some interactions under or over-represented compared to a sufficiently longer system.

8.3 Wall Interactions

This section introduces and discusses the probability of the type of interactions displayed by the algae in contact with a microfluidic geometry boundary for the experimental set up described.

Figure 8.5 displays the range of interactions observed across the full population of algae in regard to the approach to the wall. The highest proportion of interaction represents algae that come into contact with the wall and proceed to bounce away from the wall's influence (79.3% of interactions) in-line with what has been observed with *C. reinhardtii* [45]. The remainder of the interactions were either an approach stick or an approach travel. With the limitation of the video length, it is possible that the percentage of wall bounce presented is slightly under-represented of the real value, as a proportion of the algae at the walls at the onset or termination of the video may be misrepresented.

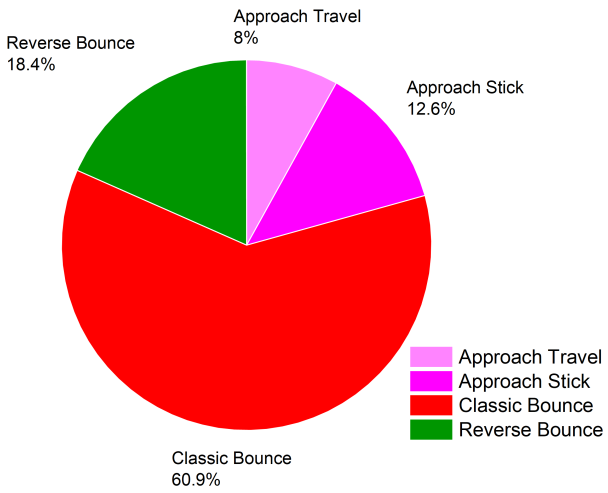

Figure 8.5: Probability of interaction events as *D. salina* approached the wall.

8.3.1 Bounce interactions

As the dominant interaction of the algae is to bounce from the wall's surface, the majority of the analyses that follows focuses on these events, detailing the defining characteristics and dynamics observed. For reference, the defining characteristic of a bounce event can be viewed in Table 8.1.

Approach/escape angle:

Perhaps the most applicable metric for wall interactions is the approach and escape angles, which are plotted in Figure 8.6 for individual bounce events with a density plot in the background. The red points denote a classic bounce and green points a reverse bounce, which can also be discerned by an escape angle greater than 90°.

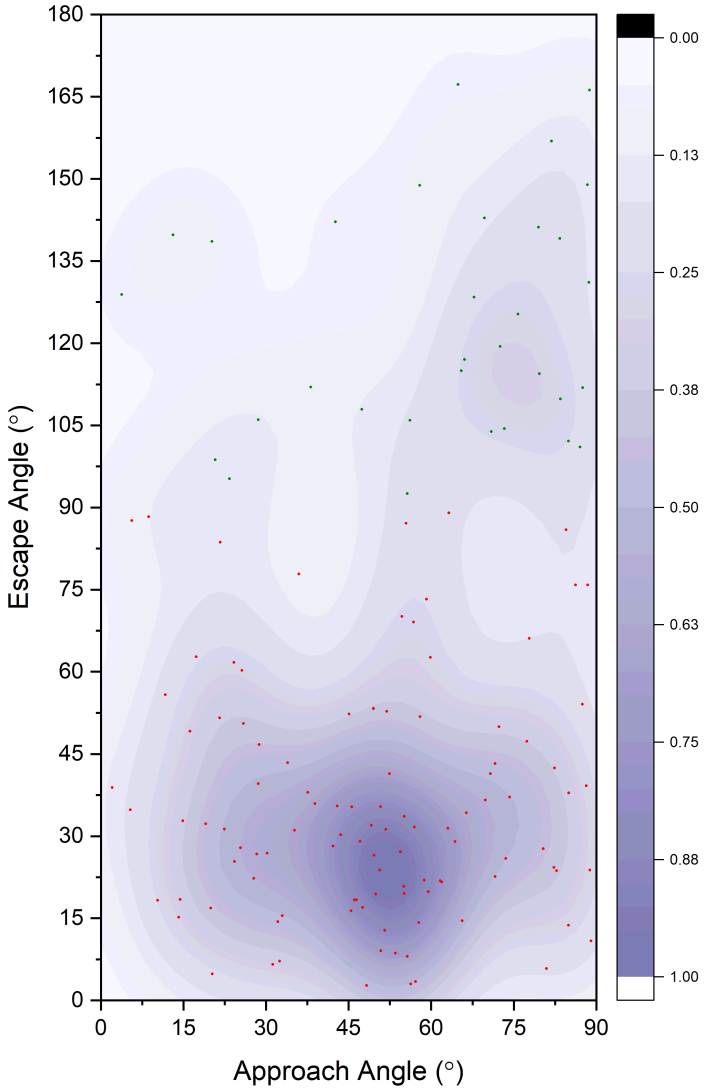

Figure 8.6: Approach and escape angles of *D. salina* with density plot overlayed beneath. Each point represents a bounce event with an approach and escape angle. Red points denote a classic bounce, while green points show a reverse bounce.

The approach angle of the algae forms a generally random distribution with a tendency to approach close to the median (45°) with an average of $\theta_A = 52.2°$, slightly above this median value. An approach angle of close to the median value may be expected to satisfy

a random approach. However, due to difficulties for the swimmer in maintaining a very small angle (close to 0°) on approach to the wall, the average approach angle is seen to be slightly greater than the median. On the other hand, the algae are seen to scatter from the walls at significantly lower angles, with the average escape angle of a classic bounce found to be 35.7°, notably below 45°. Similar results have been previously seen in *C. reinhardtii* [45] and have been shown to be linked to the morphology of the flagellum and longitudinal rotation of the body [186].

Upon analysis of the relation between approach and escape angles, it is apparent that the two appear not to be linked such that the approach angle cannot predict how the algae escape from the wall. The one exception to this observation is in large approach angles, which increase the likelihood of a reverse bounce occurring ($\theta_E > 180°$). Upon observation of these interactions it seems in the majority of cases this is caused by the algae spinning inwards towards the wall, resulting in the algae facing the same direction as entry.

Approach/escape velocity:

The average velocity on approach to the wall for a classic bounce was found to be $V_A = 59.1\,\mu\mathrm{m\,s^{-1}}$ which is greater than the approximate channel velocity calculated in Appendix F. This is expected as faster swimming algae have an increased likelihood of interact with the wall.

The escape velocity ($V_E = 56.5\,\mu\mathrm{m\,s^{-1}}$) was again found to be higher than the overall bulk swimming velocity, but slightly smaller than the approach velocity. This suggests that through the wall interaction, the algae velocity was reduced slightly, and they did not recover fully to their approach velocity in the time frame analysed. However, with only a slight drop in velocity, it seems there are little lasting effects from the wall on the swimmer after leaving its influence. This is confirmed in Figure 8.7 where the majority of the velocities lie on, or close to the slope of unity representing no change between the approach and escape velocity.

Further to the approach and escape velocities, the velocity along the wall was found to be $V_w = 51.1\,\mu\mathrm{m\,s^{-1}}$ for a classic bounce. This value is lower than both approach and

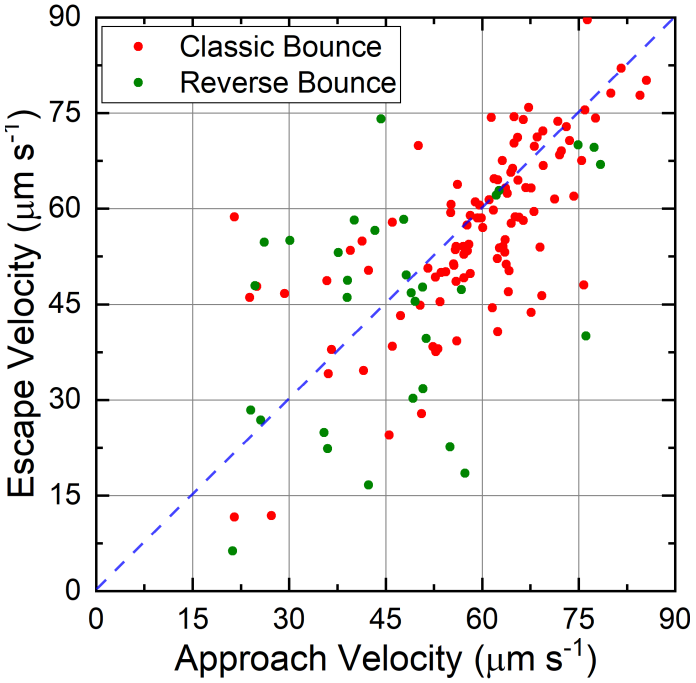

Figure 8.7: Velocity of approach and escape from a wall bounce. Each point represents an individual dynamic, with red denoting a classic bounce and green a reverse bounce. The blue dashed line shows a slope of unity, denoting an equal approach and escape velocity.

escape velocities, albeit only by a small amount. Thus, it seems the algae can navigate along the wall with ease, only displaying a slight reduction in velocity.

With a reverse bounce interaction, the velocity data is more stochastic (Figure 8.7), showing less correlation between escape and approach. Further, the velocity at the wall is reduced compared to a classic bounce. These dynamics are possibly as a result of the algae spinning in towards the wall (an interaction that has been observed for the majority of reverse bounces) meaning the algae are facing the barrier, thus slowing them down.

Wall distance travel and time:

During a classic bounce interaction, the algae spent on average $t_w = 2.63\,\text{s}$ under the influence of the wall before escaping and the average distance between entry and escape was $x_{dist} = 94.7\,\mu\text{m}$. The standard deviation of wall travel was $72.1\,\mu\text{m}$, showing the non

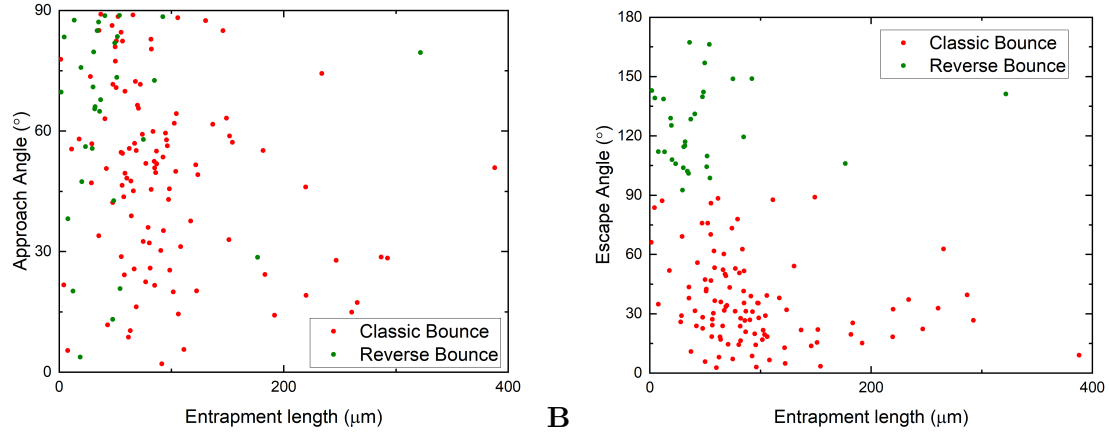

Figure 8.8: (A) Distance travelled along x-axis in relation to the angle of approach to the wall and (B) Angle of escape.

uniformity in interactions.

The approach angles influence on the entrapment length (Figures 8.8 (A)) leads to no obvious trends in the data present, and it seems apparent the approach angle has little influence on the entrapment length. Despite this, there is a very slight tendency for shallow approaches to induce longer distance wall travel, with a number of longer wall travels relating to a shallow angle. This is discussed in greater detail in Section 8.3.2.

In regard to the question whether the wall distance travelled influences the escape angle, a clearer picture is observed (Figure 8.8 (B)). It is apparent that at larger wall travel distances, the likelihood of a shallow escape angle is greatly increased. Above approximately 100 µm of wall travel, with the exception of a couple of outliers, the escape angle is found to always be below 45°. Therefore, it can be stated that for significant wall travel, the escape angle tends to be low and for a short travel or "glance" the escape angle can vary across the full spectrum of escape angles ($0° < \theta_E < 180°$).

On analysis of reverse bounce interactions, the wall distance travel is relatively small compared to a classic bounce. Thus, generally in a reverse bounce, the algae stay in a region close to entry at the wall before escaping in the same direction as the incidence.

Summary:

A summary of all the defining characteristic average values is displayed in Table 8.2. There are notable differences between a classic bounce and a reverse bounce which, is discussed further in the following section.

Table 8.2: Wall bounce average defining characteristics and corresponding standard deviation.

Location	**Characteristic**	**Symbol**	**Classic Bounce**	**Reverse Bounce**
Approach	Angle	θ_A	$49.1°$	$61.5°$
	Velocity	V_A	$59.1\,\mu m\,s^{-1}$	$47.1\,\mu m\,s^{-1}$
Wall	time	t_w	$2.63\,s$	$4.0\,s$
	Entrapment length	x_{dist}	$94.7\,\mu m$	$61.6\,\mu m$
	Velocity	V_w	$51.1\,\mu m\,s^{-1}$	$39.5\,\mu m\,s^{-1}$
Escape	Angle	θ_E	$35.7°$	$123.8°$
	Velocity	V_E	$56.5\,\mu m\,s^{-1}$	$44.7\,\mu m\,s^{-1}$

8.3.2 Approach interactions

The following section discusses the impact of wall interactions and the process of the algae attaching to the wall, bouncing or instigating wall travel. To visualise this, the relative frequency of interaction type dependence on the angle (Figure 8.9 (A)) and velocity (B) are plotted. For this analysis, a long bounce is defined as the swimmer travelling more than $100\,\mu m$ along the wall's surface.

Upon analysis of the approach angle, there are some general trends in the data with some notable jumps at specific angle bins (Figure 8.9 (A)). These outliers (specifically $50 - 60°$) are felt to be purely statistical rather than physical. This aside, some general trends are observed. At lower approach angles ($0 - 30°$) the tendency for the algae to travel further along the wall seems to be increased, which was also hinted at in Figure 8.8 (A). As the angles increase ($30 - 60°$) a classic short bounce becomes more prominent and at the higher angles ($60 - 90°$) the reverse bounce increases in likelihood.

In regard to the chances of an alga approaching the wall and becoming stuck to its surface, at the lower approach angles it seems very unlikely for the algae to become stuck, but as the approach angle increases the likelihood increases slightly. As with a bounce event, it seems lower angle approaches increases the tendency for wall travel.

Perhaps surprisingly, reverse bounce interactions show a high dependence on the approach velocity, with lower velocities displaying a much greater likelihood of a reverse bounce to take place (Figure 8.9 (B)). The mechanisms behind this observation are unknown, but may be due to morphology variability or flagellum interactions. A slight dependence for wall travel with faster swimming velocities is also present, which is likely a result of greater swimmer velocities present at the wall, increasing wall travel. The chance for the alga to become stuck at the wall remains remarkably uniform across the velocity ranges.

Therefore, on an approach to a wall some interactions see an increased likelihood depending on certain conditions, such as a reverse bounce becoming much more likely with a high angle and low velocity. Further, the chance of becoming stuck at the wall increases with increasing approach angles and long bounces seem to have a greater likelihood with low approach angles.

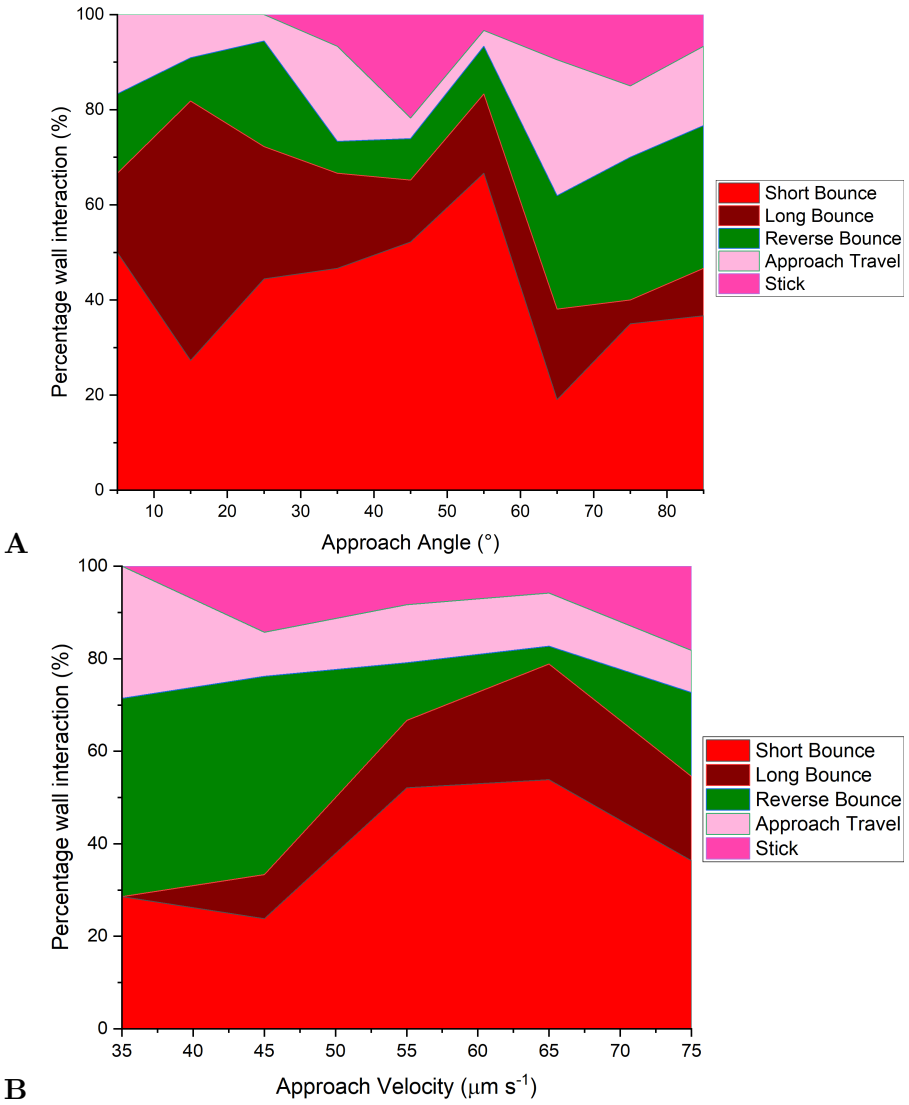

Figure 8.9: Likelihood of different wall interactions depending on (A) approach angle, (data is grouped into bins of 10°) and (B) approach velocities (data is grouped into bins of $10\,\mu\mathrm{m\,s^{-1}}$.)

8.4 Discussion

From the observations of wall interactions, the classification of the response to a boundary can be split into three approximate regimes. How the algae approach the wall can give a predictive factor to which regime they will conform to, although this is by no means wholly inclusive and only forms an increased likelihood of such a reaction:

1. The algae scatter off the wall soon after contacting with its surface with little wall travel or time at the wall, bouncing away at any angle below 90° (short travel classic bounce). This reaction is often induced by shallow approach angles and slower velocities.

2. The algae adhere to the wall and travel along its surface before escaping from the wall's influence with a shallow angle, generally below 45° (long travel classic bounce). The chance of a longer bounce increased with greater velocity of the swimmer and primarily occurs at shallow approach angles.

3. The algae attach to the wall, spinning towards the wall's surface and thereafter either escape the wall at any angle (generally a reverse bounce) or becoming stuck at the wall. This reaction has possibly the largest dependence on the approach to the wall, with low velocities and high approach angles in the most part leading to this type of wall reaction.

Often, factors such as morphology and flagellum contact that have not been examined in this work are likely important in understanding algae wall behaviours. These factors likely depend on the characteristics described and work in concert to initiate the responses observed. They are discussed in the following:

- The flagella are the first part of the swimmer to come in contact with the wall, and it has been shown in previous works the escape angles to be highly dependent on flagellum length [45]. Thus, how the flagella interact to the wall is likely key in the response.

For the observed reverse bounces and algae spinning towards the wall in these interactions, the greater approach angles may lead to the flagellum further away from the wall becoming more influential, possibly influencing the algae spin. Further, at what point in their stroke the algae are in when first contact with the wall may be of importance. However, this is purely speculation and more work would need to be conducted into how the flagella of the algae interact with the wall.

- The morphology of the swimmer such as the effects of body shape, size and flagellum length are expected to be important. It would likely follow for *D. salina* of that which has been proposed in *C. reinhardtii* [45] for the flagellum length to influence the escape from the wall, with slight changes across the algae population leading to variations in the wall escape. Furthermore, the body size of the algae as well as being linked to the velocity may influence how the algae responded to a boundary contact.

- Finally, the longitudinal rotation of the swimmer has been discussed as a method of wall escape [186]. The frequency of this rotation may be an indication of wall travel length and possibly an explanation in the shallow angle taken when escape from the wall.

It is likely to truly predicting how an alga interacts with the wall, a knowledge of a combination of the discussed dynamics is needed.

8.5 Conclusion

In summary, the response to a solid boundary of *D.salina* has been experimentally analysed by confining the algae to a quasi 2D domain (shallow channel) with approach, escape and wall characteristics determined. *D. salina* was found to favour bouncing from the wall. From the analysis, certain predictive factors were found such as low velocities and high approach angles were more likely to induce a reverse bounce and for the algae to get stuck at the wall. On the other hand, shallow angles induced more classic bounces with

increased velocity increasing the travel distance in the bounce. On analysis of the escape, it was found that the wall travel distance had a significant bearing on the escape angle, with the algae tending to escape with a shallow angle after travelling along the wall. Soon after escaping from the wall, the swimmer recovered to its pre-interaction swimming dynamics, and in general the algae did not lose significant motility while swimming at the wall's surface. Despite these findings, a full characterisation of wall interactions would benefit from analysis of other effects such as flagellum contact, which are expected to be influential on the alga's response. It is hoped that the details from this work could be used in the development of bio photo-reactors or in species concentration or separation.

Chapter 9

Conclusion and future work

9.1 Conclusion

In this thesis, the swimming dynamical response of *Dunaliella Salina* has been characterised in a range of simple and complex fluids, including: water-like (Chapter 4), Newtonian viscous (Chapter 5), shear thinning (Chapter 6) and viscoelastic (Chapter 7). Furthermore, the interaction with a boundary wall was studied (Chapter 8). The hope is that with this research a clearer picture will have been developed of microswimmer navigation. This will hopefully aid in the development of artificial microswimmers, novel methods of utilising microorganisms and commercial alga methods.

Utilising velocimetry and microscopy methods, the swimming dynamics of *D. salina* were recovered as they swam in a microfluidic channel. The net velocity and orientation observed with a conventional frame rate was captured, as well as the beating frequency of the swimmers' back and forth cycle and the respective stroke dynamics captured with a high speed camera. The initial work focused on the algae swimming in their unmodified medium with the swimming characteristics found matching the literature ($V_{net} = 49.55\,\mu\mathrm{m\,s^{-1}}, f_{BF} = 29.97\,\mathrm{Hz}$) [43, 106], but differed from that of *C. reinhardtii* which is on occasion referenced for *D. salina*. On analysis of the individual stroke dynam-

ics, *D. salina* was found to spend approximately $2/3^{rds}$ of their time in the power stroke and $1/3^{rds}$ in the recovery. This time shift and an increased velocity through the power stroke lead to a displacement efficiency per stroke of 4.1 in favour of the power stroke.

With the effects of viscosity, a monotonic decease in velocity was observed with increasing viscosity. Overall no definitive non-motile viscosity was found and even at the highest viscosity (0.04 Pa s) motility was still present, albeit very minimal. The velocity of the swimmer decayed with a power-law index to the -1 with respect to the viscosity, which indicts the swimmer operates at a constant thrust [24, 67]. Furthermore, the extra viscous forces seemed to have no significant influence on the stroke dynamics, as seen by the power and recovery stoke dynamics reducing in-line with the expected decrease following constant thrust production. Moreover, the ratio between power and recovery stroke dynamics (velocity, time and amplitude) all remained relatively constant. The beating frequency and stoke amplitude were found to decay with power-laws to the -0.375 and -0.687 respectively. This was attributed to a flagella velocity reduction in-line with the body velocity decay.

When shear thinning fluid properties were added to the medium, (an arguably overlooked property in the favour of viscoelastisty) it was shown to have great influence on the swimming behaviour of *D. salina*. The nature of the swimmer in question, with large disparities in size and velocity between the body and flagella seemed to lead this response. In general, it was proposed that the flagella would feel a reduced viscosity to the body, either by its large shear rate or simply passing by the polymers. Thus, in the power stroke, the beating of the flagella was found to be much faster than in Newtonian cases for comparable stoke amplitudes. However, the recovery stroke did not prescribe to these dynamics exhibiting the opposite response. The variation in response across the power and recovery stroke lead to a significant enhancement in the recovery stroke relative to the natural viscous velocity decay, and thus likely reducing the efficiency of the swimmers' gait. The addition of a viscous element, while maintaining the power-law index of the solution, but increasing the viscosity, gave notable variations in the swimmers' response. Both the

power and recovery stroke exhibited a shift in their dynamics, as well as a further boost in the velocity ratio in favour of the recovery stroke. This hinted at the solvent viscosity being an important metric and the flagella would feel close to this value. It was hoped that through this work, an effective viscosity for this particular swimmer could be defined for comparison to a Newtonian viscous case. However, it was deemed that this method was not sufficient to encompass the full range of stroke variations displayed by the swimmer in a shear thinning solution.

The addition of a viscoleastic element provided difficulties in defining a viscoelastic response. By the nature of the fluid used, it possessed shear thinning properties, and thus a decoupling of the shear thinning or viscoelastic response was needed. Upon analysis of the visocoelastic response, the algae followed similar trends as if in an inelastic shear thinning solution such as the velocity ratio shift in favour of the recovery stoke and variation in stroke times and amplitudes. However, some hints of a response to the elastic properties were present, such as a stroke velocity ratio decrease for comparable power-law indices compared to the shear thinning cases. Despite this, from this work, due to the confounding effects of elasticity and shear thinning it was not possible to state conclusively the influence of visoelasticity on the swimming dynamics of *D. salina* and shear thinning properties seem to be dominant in the cases discussed.

Additionally, to the analysis in complex fluids, the algae interactions with a solid microfluidic channel boundary were analysed and quantified. To create a quasi 2D platform, a shallow channel was manufactured and utilised with the wall characteristic such as approach and escape angles and velocities as well as the specific wall dynamics all defined. It was found that *D. salina* have a high preference to bounce off from a solid boundary, and predetermining the wall interactions was difficult from the approach characteristics. Despite this, the algae displayed a slight tenancy to induce a reverse bounce with a high approach angle and low velocities. The escape from the wall was shown to be dependent on the methods of swimming at the wall, such as algae travelling along the wall tended to escape with a shallow angle. Furthermore, it was found that the wall had very little

influence on the algae velocity, with the algae returning close to their approach velocity soon after the wall event. The swimming velocities when the algae were in contact with the wall were found to be reduced, but only by a limited amount.

9.2 Future work

The analysis conducted through this work has aimed at aiding and developing the picture of microswimmers immersed in complex media. While answering some of these questions and displaying new novel swimming dynamics, there still remain many questions to fully understanding the response to the fluids analysed:

Understanding of beating frequency and amplitude decay It was found through the work (Section 5.6) that the flagella beat frequency and amplitude decreased at different rates with increasing viscosities. A behaviour that could not be attributed to simple viscous fluid changes. The mechanism responsible for this reduction is unknown, and understanding why the beat dynamics react as such to display the different decay trends for the beating frequency and amplitude would be of great interest. It is possible that understanding the internal dynamic of the flagella (which likely need significant biological, modelling and computational abilities) may shed light on this swimming response.

Response under flow A further topic of interest would be the alga response under flow, and further the response under flow in complex fluids. *D. salina's* ability to respond to different flow conditions and strengths may help in the development of photo bio reactors in which the algae are constantly mixed. This topic was briefly researched within this work, with an interesting velocity reduction at low flow rates observed. Furthermore, with the addition of complex fluids, particularly shear thinning fluids potentially adding a lifting force from the walls surface, may lead to interesting discoveries such as the algae avoiding the walls.

Flagella beat in complex fluids One area of research that would lead to increased understanding of the results observed is enhanced visualisation and tracking of the flagella

shape across all cases studied. With the right set up (Section 3.6.2.2), quantifying the flagella gait would allow for a greater understanding of the variations observed in shear thinning and viscoelastic solutions, and possibly give further insight to the algae swimming response. Furthermore, it may help shed light on the flagella interaction with individual polymers, as well as allowing for modelling of the flagella stroke with a prescribed beat to be undertaken.

Response to complex fluids Within this work, it has been shown the algae stroke is influenced by shear thinning properties, the solvent viscosity and viscoelasticity. With this knowledge, future works could focus on attempting to decouple these rheological properties through modelling or experimental methods. This would hopefully highlight the individual influences and potentially asses the dominant properties in the different responses observed.

Effects of complex fluids on wall response A further area of interest may combine the response of complex fluids and solid boundaries to understand if complex fluids vary wall interactions. For example, with the presence of shear thinning fluids at a boundary, an extra lift force from the wall may be present as a result of shear gradients. With significant research, the possibility of controlling wall interactions with fluid properties could be obtained, leading to increased sorting possibilities of such a swimmer.

Appendix A

Procedure of media production

In this appendix, the procedure for the preparation of the Hejazi and Wijffels growth medium is described.

What is needed

A 2 L flask, chemicals (section 3.2.1), a spatula, a 50 mL beaker, 1 L bottle, plastic vials/containers for weighting the chemicals, antibacterial disinfectant, lab gloves, a micropipette, a pHmeter, a fume hood

Preparing the medium

- Pour 800 mL of distilled water in the 2 L flask.
- Weigh 70.13 g of Sodium chloride [NaCl] and add it to the water.
- Using the spatula, mix the solution in order to eliminate the precipitate,
- Add 0.34 g of Sodium nitrate [NaNO3],
- Add 0.99 g of Magnesium sulfate heptahydrate [MgSO4 7H2O],
- Add 0.06 g of Potassium chloride [KCl],
- Add 0.035 g of Calcium chloride dihydrate [CaCl2 2H2O],

- Add 0.67 g of Sodium bicarbonate [NaHCO3],
- Add 9.72 g of a compound called Tris-base [THAM Tris(hydroxymethyl)aminomethane],
- For the remaining chemicals, work should be conducted under the fume hood. Wearing lab gloves, clean the fume hood surface using the antibacterial disinfectant,
- Add 0.08 mL of the trace elements solution (called f/2 medium), through a micropipette,
- Add 0.4 mL of a 0.15 M Boric acid solution [H3BO3],
- At this point, you need to adjust the pH of the medium using a 1 M solution of HCl. The pH must be around 7.5,
- After adjusting the pH, transfer the solution to the 1 L bottle,
- The solution should then be sterilised at 121 $^{\circ}$C for 30 minutes in the autoclave, to avoid contamination. The lid of the bottle should be placed on the bottle, but loosened. The solution must cool down to room temperature before continuing,
- After the sterilising process, you need to work under the fume hood again and add 0.8 ml of 0.1 M Monosodium phosphate solution [NaHPO4].

Storage of the growth medium

The medium must be kept in the fridge, and it maintains its property for a few months.

Appendix B

Preparation and storing of the algae suspensions

In this Appendix, the procedure for the preparation and the storage of the *D. salina* suspensions is described in detail.

What is needed

A suspension of living algae, growth medium (Section 3.2.1), 4-5 flasks, antibacterial disinfectant, cotton will, tin foil, plastic disposable pipettes, a fume hood, lab gloves, an autoclave.

Preparing the suspensions

- Wash the flasks with tap water and a test tube brush, in order to remove any previous algal deposit,
- Sterilise the flasks and the cotton by autoclaving them at 121° for 30 minutes, to avoid contamination.
- Wait until the flasks and the cotton cool down to room temperature,
- Wearing the lab gloves, clean the fume hood surface using the antibacterial disinfectant, to avoid contamination,

Appendix B. Preparation and storing of the algae suspensions

- Working under the fume hood, pour 50 ml of the fresh growth medium in each flask and inoculate roughly $2-3$ ml of the living algal suspension, using the plastic pipette,
- Cork the flasks using the cotton wool and the tin foil,
- Wash the flasks with tap water in order to remove some salts that may have deposited on the flasks surface, after the sterilising process. This must be done to make sure that the light path is not affected.

Storing the suspensions The *D. salina* suspensions must be stored in the algae hut (Figure 3.1), in order to prevent *D. salina* from being affected by light pollution. Moreover, the suspensions must be exposed to two fluorescent lights, using a 12/12 light/dark cycle to simulate daylight cycle, at room temperature. Since *D. salina* is a good swimmer, the cultures can be grown without being mixed. For continual experiments, alga should be replenished every 2 weeks by this method.

Appendix C

Fluid models

C.1 Power-Law model

The Power-law model or the Otswald-de Awele relationship is the simplest form to describe a generalised Newtonian fluid [216]. It gives a basic relationship between the strain rate and viscosity

$$\eta(\dot{\gamma}) = m\dot{\gamma}^{n-1} \tag{C.1}$$

where m is the flow consistency index and is related to the magnitude of viscosity and n is the power-law index which defines the rate of change of viscosity and shear rate. Based on the power-law index, the behaviour of the fluid is described as:

- $0 < n < 1$ – The fluid shows shear thinning properties, with smaller values of n denoting a greater level of shear thinning
- $n = 1$ – The fluid shows Newtonian behaviour
- $n > 1$ – The fluid shows shear thickening properties, with greater values of n denoting a greater level of shear thickening

The power-law model's advantages lie within its simplicity and ease of describing a fluid's state. However, it is only valid over a limited range of shear rates. Therefore, must be taken from shear rates that the fluid exhibiting power-law behaviour.

C.2 Carreau-Yasuda model

A model that attempts to remove some limitations of the power-law model is the five-parameter Carreau-Yasuda model [216]. By incorporating the zero and infinite shear to describe the fluid, it is valid over very low and high shear rates. The Carreau-Yasuda model is described as follows

$$\eta(\dot{\gamma}) = \eta_\infty + (\eta_0 - \eta_\infty)[1 + (\lambda_{cy}\dot{\gamma})^{\alpha_{cy}}]^{\frac{n-1}{\alpha_{cy}}} \tag{C.2}$$

where η_∞ is the infinite shear viscosity, η_0 the zero-shear viscosity, λ_{cy} the 'relaxation time' which describes the shear rate at the transition between the solvent plateau and power-law regions and α_{cy} the exponent which describes the shape of the transition regions between the zero-shear plateau and power-law like region. A Carreau fluid behaves like a Newtonian fluid at low and high shear rates and a power-law fluid in between, with transition regions joining each region. This can be viewed in Figure C.1. The Carreau-Yasuda model fits most viscosity vs shear rate data on the assumption that all 5 parameters are available to the model [214, 216].

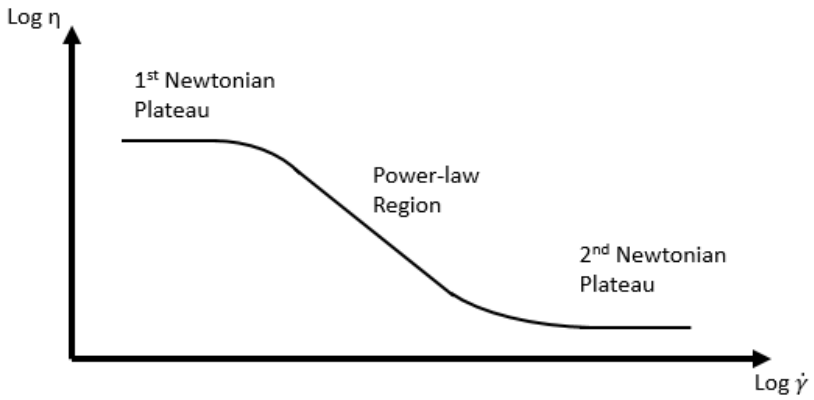

Figure C.1: Example Carreau-Yasuda model fit displaying different regions of interest. Power-law index is recovered from power-law region. The first plateau is related to the zero shear viscosity and second to the infinite or solvent viscosity. Image adapted with permissions from [317].

Appendix D

Effects of viscosity on velocity

Here, representative velocity functions in time domain of individual algae are shown for algae in the medium with various Ficoll concentrations (Figure D.1). A – E corresponds to Medium, $4\%, 6\%, 8\%, 10\%$ respectively.

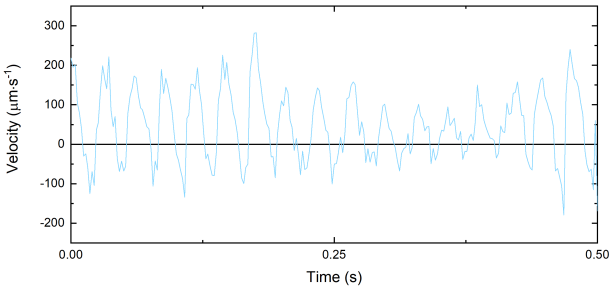

A

Appendix D. Effects of viscosity on velocity

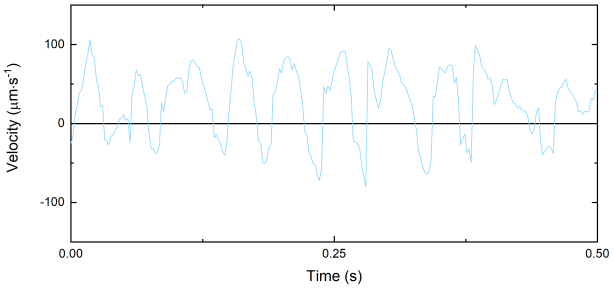

B

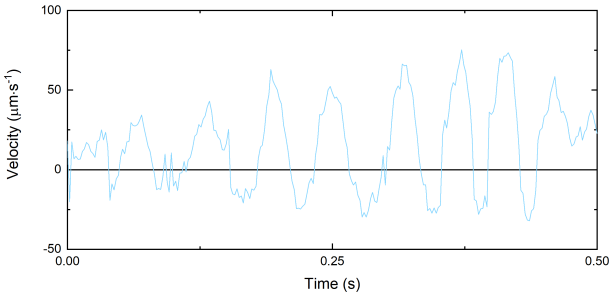

C

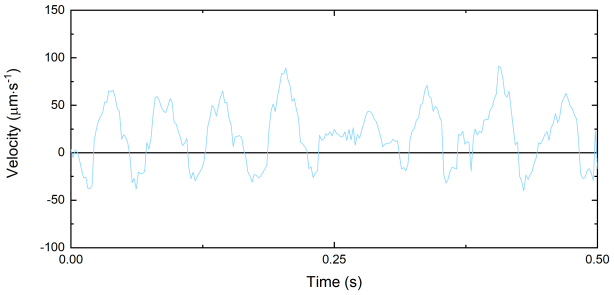

D

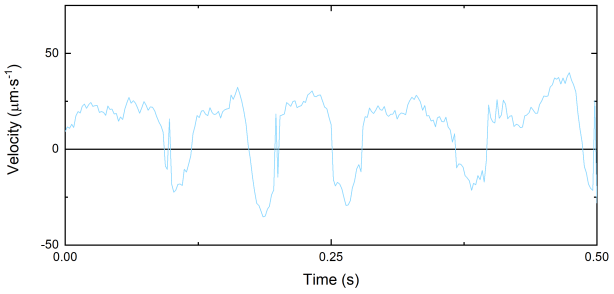

E

Appendix E

Algae response to glycerol

In this work, in addition to Ficoll, glycerol was also tested as a viscosity enhancer. However, unlike Ficoll, glycerol was seen to interact with the swimmers' chemistry and caused the velocity results to become skewed.

Glycerol is a sweet tasting hygroscopic liquid that occurs naturally, but can also be produced synthetically. It is colourless and odourless and is used in a significant range of industrial and commercial applications [126, 224] as well as in microfluidic research [225].

For this analysis, glycerol solutions of 10%, 20% and 30% were used with viscosities ranging from $1.44 - 3.22\,\mathrm{mPa\,s}$. Figure E.1 shows the flow curves for the three solutions, with all exhibiting Newtonian behaviour.

When comparing the responses to the increases in the viscosity of the medium between Ficoll (Chapter 5) and glycerol, a significant shift in swimming velocities was observed (Figure E.2). Rheologically, the two types of solutions are similar, showing Newtonian behaviour with increasing viscosity with concentration. However, the swimming velocities observed were found to be markedly different for similar viscosities. Algae swimming in glycerol showed a sharp decrease in velocity with increases in viscosity and reached a point of apparent non-motility at values of viscosity of $3\,\mathrm{mPa\,s}$, while in the Ficoll modified medium, the swimming velocity was seen to decreases slowly with no defined non-motility

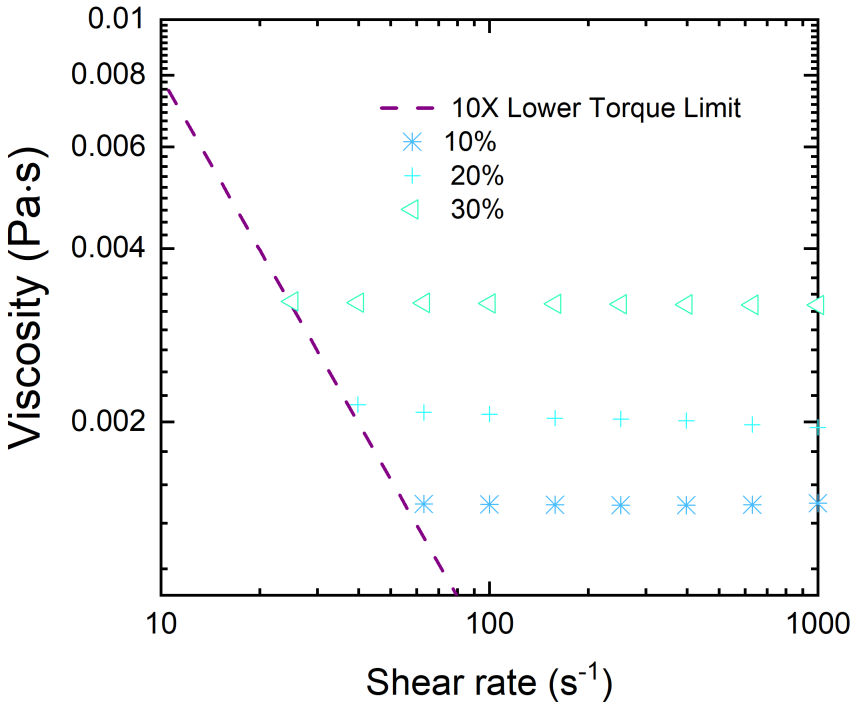

Figure E.1: Flow curves showing the steady shear viscosity of the medium solutions with different glycerol concentrations used in experiments. The minimum measurable torque represented by the purple dashed line is calculated from Equation 3.10. All the medium solutions with added glycerol display Newtonian behaviour with increasing viscosity with concentration.

viscosity observed for the ranges of viscosities measured.

This obvious and distinct variation to the algae reaction to viscous effects could be seen as quite intriguing if it is assumed the algae interaction with the fluid is purely rheologically based. However, on examination of the algae, it was noticed that the algae body shape in the high glycerol concentration solutions was misshaped. Rather than a normal spherical body, the algae shapes were distorted (Examples of distorted algae can be viewed in figure E.3). This change coincided with the point of non-motility and seemingly an indication of an interaction between solution and the algae. As mentioned in Section 1.4.1.1 *D. salina* produce glycerol within the cell which is used to maintain osmotic equilibrium, allowing this

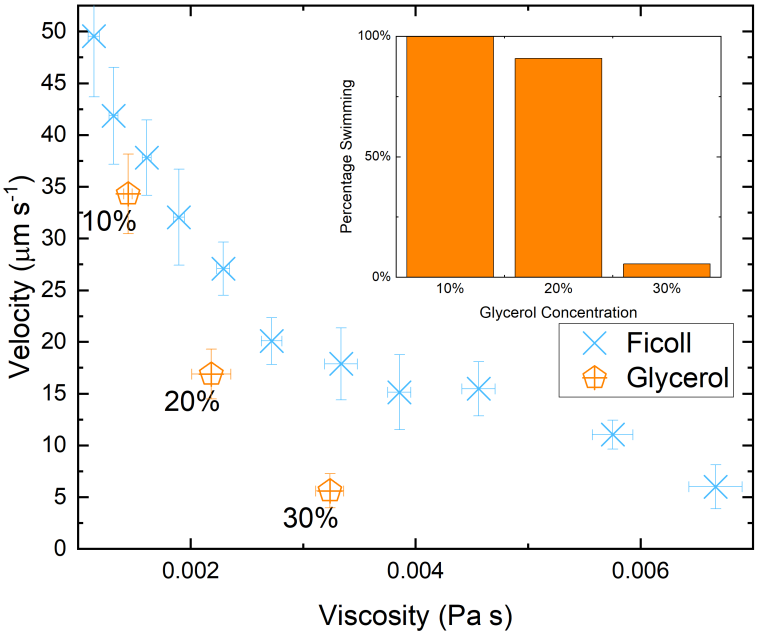

Figure E.2: Net velocity of Newtonian solutions analysed with increasing viscosity. A clear separation is observed for solutions of similar rheology, with glycerol displaying much reduced velocities. Horizontal error bars relate to the experimental error in rheological measurements (Section 3.3.3.3) and vertical the standard deviation across population analysed. The inset shows number of algae swimming above non-swimming value ($3\,\mu m\,s^{-1}$) with the remaining being classed as non-motile.

specific alga to live and thrive at high salinity levels [296,318]. Thus, it seems the addition of glycerol within the medium disturbs this balance, passing through the cell barrier and as a result causing the cell to become hypo-glycerol. Essentially, incapacitating the cell and voiding it of any movement. Therefore, despite possessing similar rheology, the swimming response to these solutions is controlled by this reaction, voiding any possible conclusions to be drawn from rheological induced behaviours.

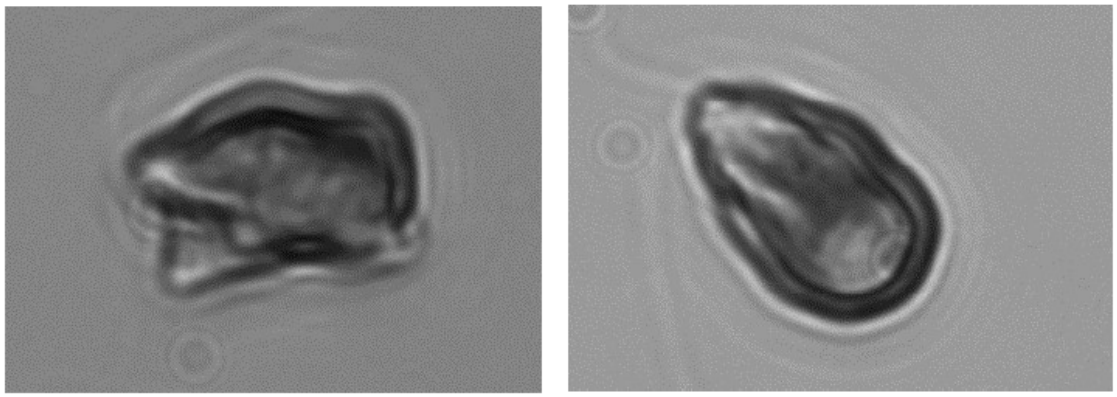

Figure E.3: Distorted alga shape as a result of increased glycerol concentration of the medium. Both images show non-motile algae in 30% glycerol.

Appendix F

Channel depth influence on wall interactions

To provide a proportion of quantitative data to the effects of a shallow channel ($\delta \sim 20\,\mu m$) the swimming dynamics were compared and contrasted to that in the deep channel ($\delta \sim 84\,\mu m$) (Section 4.3). The experimental techniques were conducted in line with that described in Chapter 3, the only disparity being the changes in channel height.

An uncontrolled parameter between the two channels was the fact that the camera captured purely 2D motion. This was likely to cause a slight under-representation of the swimming velocity in the deeper channel, as any z velocity components would not be captured. However, in the "2D" channel the algae were restricted to a quasi-single plane, thus could not swim with a z velocity component. Therefore, perhaps "truer" representation of the algae swimming velocity would be captured in the shallow channel, albeit with an increased local wall presence.

The net velocity of the algae swimming in the shallow channel was found to be $V_{net\_shal} = 46.77\,\mu m\,s^{-1}$ a value slightly lower than that found in the deeper $84\,\mu m$ channel ($V_{net} = 49.55\,\mu m\,s^{-1}$). Both values fall within the experimental error range as descried in Section 5.4.2.

Appendix F. Channel depth influence on wall interactions

Further analysis can be drawn from the distributions of the swimming velocities (Figure F.1). The distributions are not too dissimilar, with similar maximum velocities and similar peaks close to the mean velocity. However, there are some notable differences that shed light on the changes induced by the shallower channel. The peak distribution of the shallow channel shows two distinct phases, the first a plateau region at a velocity below the mean, followed by an increased peak at higher velocities. Furthermore, compared to the 84 µm channel, there is a greater probability for slower swimming and the high velocity peak is narrower.

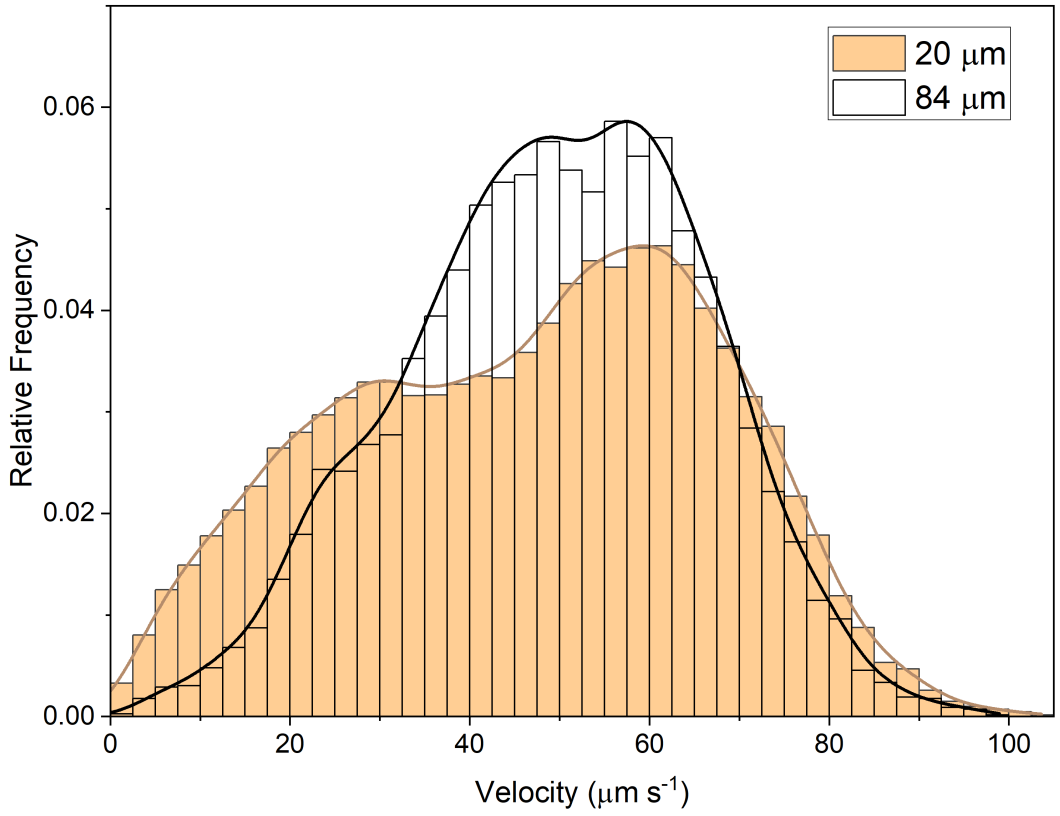

Figure F.1: Instantaneous velocity distribution of shallow (20 µm) and deep channels (84 µm). Shallow channel represented with orange columns and deep by clear.

The increased likelihood of slower swimming is likely down to wall contact as the

presence of the wall is in close contact with the swimmer, increasing drag on both the flagella and body. Further it is possible that the flagella can get caught on the wall, distorting the swimming stroke and changing the velocity of the swimmer.

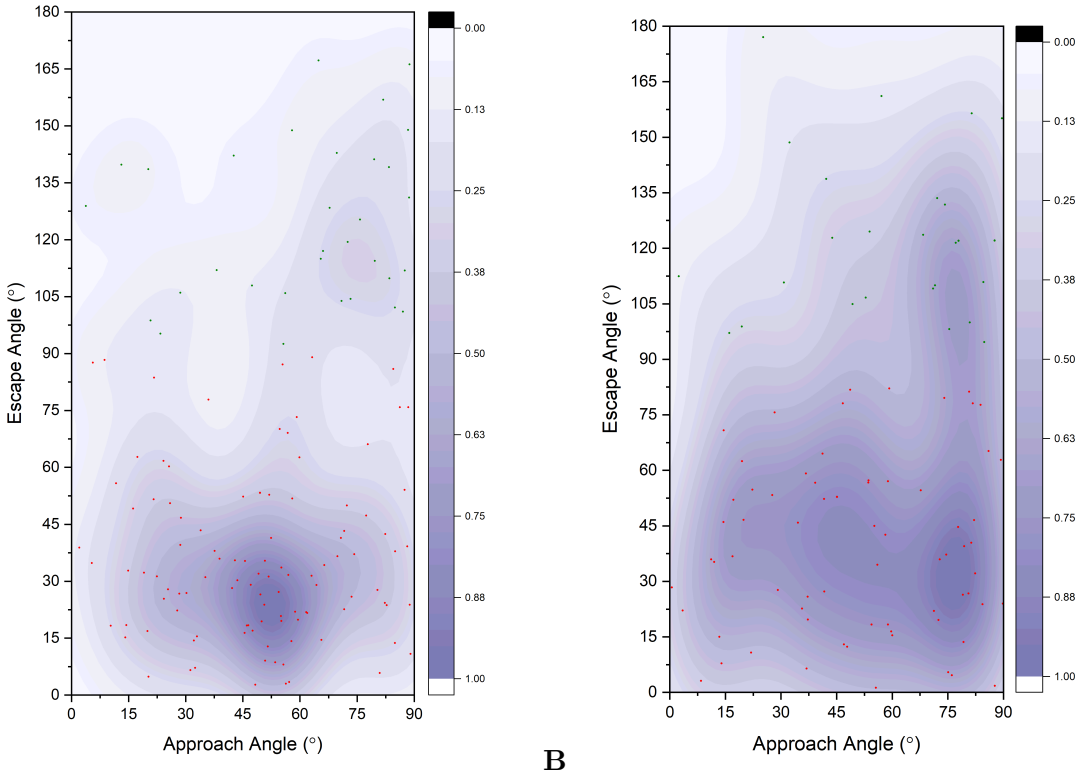

Figure F.2: (A) Approach and Escape angles when swimmers' are confined to a shallow channel (20 µm) (B) and deep channel (84 µm).

The narrowing of the upper peak close to the mean velocity is likely down to the 2D effects discussed earlier. The algae swimming at this velocity are likely not under the wall's influence and therefore are propelling themselves at their natural velocity. The peak is narrower than the deep channel, as the velocities are under-represented due to vertical components in the z direction not being captured in this case. This peak in the shallow channel is therefore likely a truer representation of the normal free-swimming velocity of *D. salina*.

Appendix F. Channel depth influence on wall interactions

Further to the velocity analysis, to assess the changes in channel depth on the definition of wall interaction, a comparison between the shallow and deep channel is quantified as discussed in Chapter 8. The only variation between methods was the channel depth, with the visualisation methods staying consistent. The greater channel depth will inevitably lose accuracy due to the increased surface for wall interactions and lack of 2D visualisation plane. However, an analogy will allow for a comparison between methods and a discussion of the effectiveness of this method. Furthermore, if this method is deemed acceptable to capture wall events, a discussion into the effects of complex fluids can be conducted as this data was captured during this work during the complex fluid analysis.

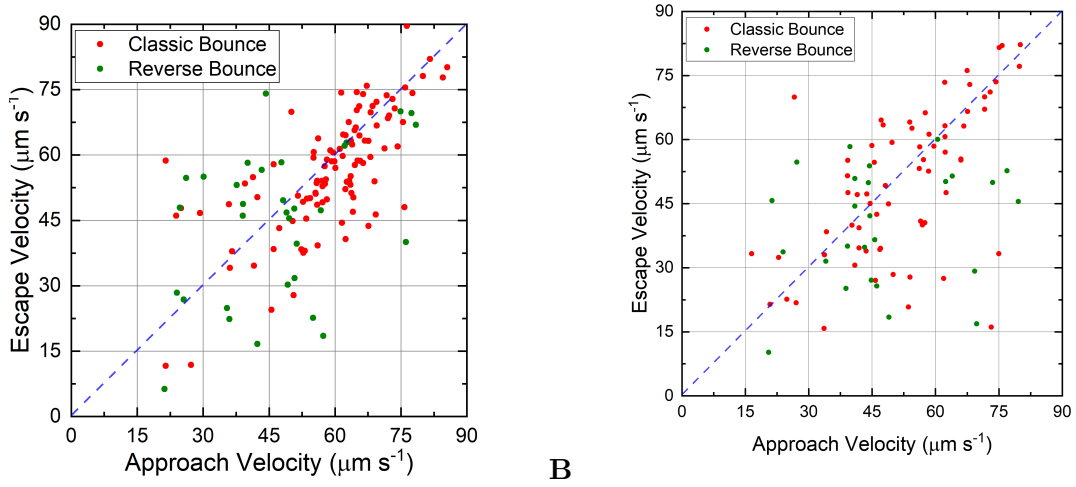

Figure F.3: (A) Approach and Escape velocities of swimmers' in a shallow channel (20 µm) (B) and deep channel (84 µm).

Figure F.2 shows the angle scatter for the 20 µm (A) and 84 µm (B) channels. In comparison between the two graphs, the general distribution of the data is fairly similar with a tendency for swimmers' to escape with lower angles and a mostly even distribution across the approach angles. However, the spread of data is much more erratic in the deeper channel, with less concentration around the lower escape angle. This is likely due to the imaging set up not capturing the correct angles due to the vertical components of the algae

swimming.

In terms of the approach and escape velocities of the two channels, displayed in Figure F.3, as with the previous scatter diagram the data in the deeper channel follows a similar trend to the shallow channel. However, the spread of the data is much larger and scattered from the line of unity. The general trends of the data is captured as found in the shallow channel, but by itself the data does not present a detailed picture of the dynamics at the wall.

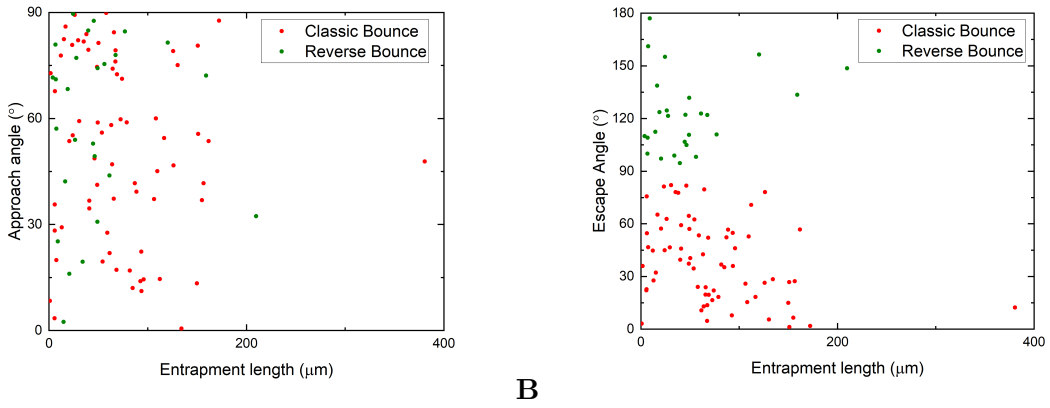

Figure F.4: (A) Approach angle relative to wall travel distance in deep channel (84 µm). (B) Escape angle related to wall distance travel distance in deep channel (84 µm).

Finally, a comparison between the entrapment length and scattering angles is drawn in Figure F.4. In this regard, the data conforms slightly closer to that observed in the shallow channel (Figure 8.8). However, certain details are lost such as long wall travel and the reduction in escape angle with wall travel is more obvious when analysis in undertaken in the shallow channel. With the deeper channel, the added surface area of the wall as well as possible interactions with the corners of the channels are likely influencing the results.

To conclude, while undertaking this type of analysis in the deeper channel displays some similar trends as that of the shallow channel, the data is much more erratic and spread out. Without a comparison of the quasi 2D channel, difficulties would arise over the interpretations and legitimacy of the data. Therefore, it is clear that without sufficient

supporting evidence, analysis of the swimmers' interaction with the walls in this manner is not significantly rigours and lacks scientific quantification. Taking this observation and the fact with increasing viscosities reduces the quantity of captured data through slower swimming, it was decided not to continue with the analysis for wall interactions in complex fluids as was hoped.

Bibliography

[1] V. A. Vladimirov, M. S. Wu, T. J. Pedley, P. V. Denissenko, and S. G. Zakhidova, "Measurement of cell velocity distributions in populations of motile algae," *J Exp Biol*, vol. 207, no. Pt 7, pp. 1203–16, 2004. [Online]. Available: https://www.ncbi.nlm.nih.gov/pubmed/14978061

[2] A. Hope, "Particles in oscillatory flows jamming of concentrated particulate suspensions and the response of swimming algae," Thesis, 2014. [Online]. Available: http://oleg.lib.strath.ac.uk/R/?func=dbin-jump-full&object_id=24396

[3] A. Chengala, M. Hondzo, and J. Sheng, "Microalga propels along vorticity direction in a shear flow," *Phys Rev E Stat Nonlin Soft Matter Phys*, vol. 87, no. 5, p. 052704, 2013. [Online]. Available: https://www.ncbi.nlm.nih.gov/pubmed/23767563

[4] S. Jung, "Caenorhabditis elegans swimming in a saturated particulate system," *Physics of Fluids*, vol. 22, no. 3, p. 031903, 2010. [Online]. Available: ⟨GotoISI⟩://WOS:000276212200006http://aip.scitation.org/doi/pdf/10.1063/1.3359611

[5] T. D. Montenegro-Johnson, D. A. Gagnon, P. E. Arratia, and E. Lauga, "Flow analysis of the low reynolds number swimmer c. elegans," *Physical Review Fluids*, vol. 1, no. 5, p. 053202, 2016. [Online]. Available: ⟨GotoISI⟩://WOS:000390230000001

[6] D. A. Gagnon, N. C. Keim, and P. E. Arratia, "Undulatory swimming in shear-thinning fluids: experiments with caenorhabditis elegans," *Journal of Fluid Mechanics*, vol. 758, 2014. [Online]. Available: ⟨GotoISI⟩://WOS:000343757900003

[7] H. Gadêlha, P. Hernández-Herrera, F. Montoya, A. Darszon, and G. Corkidi, "Human sperm uses asymmetric and anisotropic flagellar controls to regulate swimming symmetry and cell steering," *Science Advances*, vol. 6, no. 31, 2020. [Online]. Available: https://advances.sciencemag.org/content/6/31/eaba5168

[8] J. F. Jikeli, L. Alvarez, B. M. Friedrich, L. G. Wilson, R. Pascal, R. Colin, M. Pichlo, A. Rennhack, C. Brenker, and U. B. Kaupp, "Sperm navigation along helical paths in 3d chemoattractant landscapes," *Nature communications*, vol. 6, no. 1, pp. 1–10, 2015.

[9] J. R. Blake and M. A. Sleigh, "Mechanics of ciliary locomotion," *Biological Reviews*, vol. 49, no. 1, pp. 85–125, 1974. [Online]. Available: https://onlinelibrary.wiley.com/doi/abs/10.1111/j.1469-185X.1974.tb01299.x

[10] M. Sleigh, J. Blake, and N. Liron , "The propulsion of mucus by cilia," *The American review of respiratory disease*, vol. 137, pp. 726–41, 04 1988.

[11] I. Priyadarshani and B. Rath, "Commercial and industrial applications of micro algae – a review," *J. Algal Biomass*, vol. 3, no. 4, pp. 89–100, 2012. [Online]. Available: https://www.academia.edu/23887786/Commercial_and_industrial_applications_of_micro_algae_A_review

[12] O. Pulz and W. Gross, "Valuable products from biotechnology of microalgae," *Appl Microbiol Biotechnol*, vol. 65, no. 6, pp. 635–48, 2004. [Online]. Available: https://www.ncbi.nlm.nih.gov/pubmed/15300417

[13] K. Y. Show, Y. G. Yan, and D. J. Lee, *Chapter 7 - Algal biomass harvesting and drying*. Elsevier, 2019, pp. 135–166. [Online]. Available: http://www.sciencedirect.com/science/article/pii/B978044464192200007X

[14] M. Hannon, J. Gimpel, M. Tran, B. Rasala, and S. Mayfield, "Biofuels from algae: challenges and potential," *Biofuels*, vol. 1, no. 5, pp. 763–784, 2010. [Online]. Available: https://www.ncbi.nlm.nih.gov/pubmed/21833344

[15] X. Z. Chen, M. Hoop, F. Mushtaq, E. Siringil, C. Z. Hu, B. J. Nelson, and S. Pane, "Recent developments in magnetically driven micro- and nanorobots," *Applied Materials Today*, vol. 9, no. Supplement C, pp. 37–46, 2017. [Online]. Available: ⟨GotoISI⟩://WOS:000417805400005

[16] L. Stricker, "Numerical simulation of artificial microswimmers driven by marangoni flow," *Journal of Computational Physics*, vol. 347, no. Supplement C, pp. 467–489, 2017. [Online]. Available: ⟨GotoISI⟩://WOS:000408045500023

[17] Z. Wu, Y. Chen, D. Mukasa, O. S. Pak, and W. Gao, "Medical micro/nanorobots in complex media," *Chemical Society Reviews*, 2020.

[18] C. Bechinger, R. Di Leonardo, H. Löwen, C. Reichhardt, G. Volpe, and G. Volpe, "Active particles in complex and crowded environments," *Reviews of Modern Physics*, vol. 88, no. 4, p. 045006, 2016. [Online]. Available: ⟨GotoISI⟩://WOS:000388631900001https://journals.aps.org/rmp/abstract/10.1103/RevModPhys.88.045006

[19] S. S. Suarez and X. Dai, "Hyperactivation enhances mouse sperm capacity for penetrating viscoelastic media," *Biol Reprod*, vol. 46, no. 4, pp. 686–91, 1992. [Online]. Available: https://www.ncbi.nlm.nih.gov/pubmed/1576267

[20] C. K. Tung, C. Lin, B. Harvey, A. G. Fiore, F. Ardon, M. Wu, and S. S. Suarez, "Fluid viscoelasticity promotes collective swimming of sperm," *Sci Rep*, vol. 7, no. 1, p. 3152, 2017. [Online]. Available: https://www.ncbi.nlm.nih.gov/pubmed/28600487

[21] M. Backholm, A. Kasper, R. Schulman, W. Ryu, and K. Dalnoki-Veress, "The effects of viscosity on the undulatory swimming dynamics of c. elegans," *Physics of Fluids*, vol. 27, p. 091901, 09 2015.

[22] E. Nader, S. Skinner, M. Romana, R. Fort, N. Lemonne, N. Guillot, A. Gauthier, S. Antoine-Jonville, C. Renoux, M.-D. Hardy-Dessources *et al.*, "Blood rheology: Key parameters, impact on blood flow, role in sickle cell disease and effects of exercise," *Frontiers in physiology*, vol. 10, p. 1329, 2019.

[23] B. W. Park, J. Zhuang, O. Yasa, and M. Sitti, "Multifunctional bacteria-driven microswimmers for targeted active drug delivery," *ACS Nano*, vol. 11, no. 9, pp. 8910–8923, 2017. [Online]. Available: https://www.ncbi.nlm.nih.gov/pubmed/28873304

[24] B. Qin, A. Gopinath, J. Yang, J. P. Gollub, and P. E. Arratia, "Flagellar kinematics and swimming of algal cells in viscoelastic fluids," *Sci Rep*, vol. 5, p. 9190, 2015. [Online]. Available: https://www.ncbi.nlm.nih.gov/pubmed/25778677

[25] A. E. Patteson, A. Gopinath, M. Goulian, and P. E. Arratia, "Running and tumbling with e. coli in polymeric solutions," *Sci Rep*, vol. 5, p. 15761, 2015. [Online]. Available: https://www.ncbi.nlm.nih.gov/pubmed/26507950

[26] D. A. Gagnon, X. N. Shen, and P. E. Arratia, "Undulatory swimming in fluids with polymer networks," *EPL (Europhysics Letters)*, vol. 104, no. 1, p. 14004, 2013. [Online]. Available: ⟨GotoISI⟩://WOS:000327448900010

[27] V. A. Martinez, J. Schwarz-Linek, M. Reufer, L. G. Wilson, A. N. Morozov, and W. C. Poon, "Flagellated bacterial motility in polymer solutions," *Proc Natl Acad Sci U S A*, vol. 111, no. 50, pp. 17 771–6, 2014. [Online]. Available: https://www.ncbi.nlm.nih.gov/pubmed/25468981

[28] S. Spagnolie, *Complex Fluids in Biological Systems*, ser. Biological and Medical Physics, Biomedical Engineering. Springer-Verlag New York, 2015, vol. 1. [Online]. Available: //www.springer.com/gb/book/9781493920648

[29] A. Hope, O. A. Croze, W. C. K. Poon, M. A. Bees, and M. D. Haw, "Resonant alignment of microswimmer trajectories in oscillatory shear flows," *Physical Review Fluids*, vol. 1, no. 5, p. 051201, 2016. [Online]. Available: ⟨GotoISI⟩://WOS:000390234700001

[30] Z. Qu, F. Z. Temel, R. Henderikx, and K. S. Breuer, "Changes in the flagellar bundling time account for variations in swimming behavior of flagellated bacteria in viscous media," *Proc Natl Acad Sci U S A*, vol. 115, no. 8, pp. 1707–1712, 2018. [Online]. Available: https://www.ncbi.nlm.nih.gov/pubmed/29434037

[31] X. N. Shen and P. E. Arratia, "Undulatory swimming in viscoelastic fluids," *Phys Rev Lett*, vol. 106, no. 20, p. 208101, 2011. [Online]. Available: https://www.ncbi.nlm.nih.gov/pubmed/21668264

[32] J. G. White, E. Southgate, J. N. Thomson, and S. Brenner, "The structure of the nervous system of the nematode caenorhabditis elegans," *Philos Trans R Soc Lond B Biol Sci*, vol. 314, no. 1165, pp. 1–340, 1986. [Online]. Available: https://www.ncbi.nlm.nih.gov/pubmed/22462104

[33] T. Hyakutake, K. Sato, and K. Sugita, "Study of bovine sperm motility in shear-thinning viscoelastic fluids," *Journal of Biomechanics*, vol. 88, pp. 130 –

137, 2019. [Online]. Available: http://www.sciencedirect.com/science/article/pii/S0021929019302271

[34] T. Hyakutake, H. Suzuki, and S. Yamamoto, "Effect of non-newtonian fluid properties on bovine sperm motility," *Journal of biomechanics*, vol. 48, p. 2941, 08 2015.

[35] D. J. Smith, E. A. Gaffney, H. Gadelha, N. Kapur, and J. C. Kirkman-Brown, "Bend propagation in the flagella of migrating human sperm, and its modulation by viscosity," *Cell Motil Cytoskeleton*, vol. 66, no. 4, pp. 220–36, 2009. [Online]. Available: https://www.ncbi.nlm.nih.gov/pubmed/19243024

[36] A. Maude, "Non-random distribution of bull spermatozoa in a drop of sperm suspension," *Nature*, vol. 200, no. 4904, pp. 381–381, 1963.

[37] H. A. Guidobaldi, Y. Jeyaram, C. Condat, M. Oviedo, I. Berdakin, V. Moshchalkov, L. C. Giojalas, A. Silhanek, and V. I. Marconi, "Disrupting the wall accumulation of human sperm cells by artificial corrugation," *Biomicrofluidics*, vol. 9, no. 2, p. 024122, 2015.

[38] K. Ishimoto and E. A. Gaffney, "Fluid flow and sperm guidance: a simulation study of hydrodynamic sperm rheotaxis," *Journal of The Royal Society Interface*, vol. 12, no. 106, p. 20150172, 2015.

[39] H. H. Tuson and D. B. Weibel, "Bacteria–surface interactions," *Soft matter*, vol. 9, no. 17, pp. 4368–4380, 2013.

[40] M. C. Moura, T. H. Napoleão, P. M. Paiva, and L. Coelho, "Bacterial biofilms: Structure, development and potential of plant compounds for alternative control," *Advances in medicine and biology*, pp. 1–34, 2017.

[41] R. S. Friedlander, H. Vlamakis, P. Kim, M. Khan, R. Kolter, and J. Aizenberg, "Bacterial flagella explore microscale hummocks and hollows to increase adhesion," *Proceedings of the National Academy of Sciences*, vol. 110, no. 14, pp. 5624–5629, 2013.

[42] I. S. Chronakis, A. N. Galatanu, T. Nylander, and B. Lindman, "The behaviour of protein preparations from blue-green algae (spirulina platensis strain pacifica) at the air/water interface," *Colloids and Surfaces A: Physicochemical and Engineering Aspects*, vol. 173, no. 1-3, pp. 181–192, 2000.

[43] V. Infante, "Fluid dynamic behaviour of dilute dunaliella salina suspensions in contraction-expansion microfluidic devices : potential implications for tubular phototbioreactors," NonPeerReviewed, 2019. [Online]. Available: https://ethos.bl.uk/OrderDetails.do?uin=uk.bl.ethos.793463

[44] M. Contino, E. Lushi, I. Tuval, V. Kantsler, and M. Polin, "Microalgae scatter off solid surfaces by hydrodynamic and contact forces," *Phys Rev Lett*, vol. 115, no. 25, p. 258102, 2015. [Online]. Available: https://www.ncbi.nlm.nih.gov/pubmed/26722946

[45] V. Kantsler, J. Dunkel, M. Polin, and R. E. Goldstein, "Ciliary contact interactions dominate surface scattering of swimming eukaryotes," *Proc Natl Acad Sci U S A*, vol. 110, no. 4, pp. 1187–92, 2013. [Online]. Available: https://www.ncbi.nlm.nih.gov/pubmed/23297240

[46] A. Sokolov, M. M. Apodaca, B. A. Grzybowski, and I. S. Aranson, "Swimming bacteria power microscopic gears," *Proceedings of the National Academy of Sciences*, vol. 107, no. 3, pp. 969–974, 2010.

[47] M. Lisicki, E. Lauga *et al.*, "The bank of swimming organisms at the micron scale (boso-micro)," *Plos one*, vol. 16, no. 6, 2021.

[48] C. Brennen and H. Winet, "Fluid mechanics of propulsion by cilia and flagella," *Annual Review of Fluid Mechanics*, vol. 9, no. 1, pp. 339–398, 1977.

[49] A. S. Utada, R. R. Bennett, J. C. Fong, M. L. Gibiansky, F. H. Yildiz, R. Golestanian, and G. C. Wong, "Vibrio cholerae use pili and flagella synergistically to effect motility switching and conditional surface attachment," *Nature communications*, vol. 5, no. 1, pp. 1–8, 2014.

[50] S. O'Malley, "Bi-flagellate swimming dynamics," Thesis, 2011. [Online]. Available: http://theses.gla.ac.uk/2706/

[51] C. B. Lindemann, "The geometric clutch as a working hypothesis for future research on cilia and flagella," *Annals of the New York Academy of Sciences*, vol. 1101, no. 1, pp. 477–493, 2007. [Online]. Available: https://nyaspubs.onlinelibrary.wiley.com/doi/abs/10.1196/annals.1389.024

[52] R. H. Dillon and L. J. Fauci, "An integrative model of internal axoneme mechanics and external fluid dynamics in ciliary beating," *Journal of Theoretical Biology*, vol. 207, no. 3, pp. 415–430, 2000.

[53] J. Elgeti, R. G. Winkler, and G. Gompper, "Physics of microswimmers–single particle motion and collective behavior: a review," *Rep Prog Phys*, vol. 78, no. 5, p. 056601, 2015. [Online]. Available: https://www.ncbi.nlm.nih.gov/pubmed/25919479

[54] T. Qiu, T. C. Lee, A. G. Mark, K. I. Morozov, R. Munster, O. Mierka, S. Turek, A. M. Leshansky, and P. Fischer, "Swimming by reciprocal motion at low reynolds number," *Nat Commun*, vol. 5, p. 5119, 2014. [Online]. Available: https://www.ncbi.nlm.nih.gov/pubmed/25369018

[55] U. K. Cheang, F. Meshkati, H. Kim, K. Lee, H. Fu, and M. J. Kim, "Versatile microrobotics using simple modular subunits," *Scientific Reports*, vol. 6, p. 30472, 07 2016.

[56] J. R. Gomez-Solano, A. Blokhuis, and C. Bechinger, "Dynamics of self-propelled janus particles in viscoelastic fluids," *Phys Rev Lett*, vol. 116, no. 13, p. 138301, 2016. [Online]. Available: https://www.ncbi.nlm.nih.gov/pubmed/27082004

[57] H. Su, C.-A. H. Price, L. Jing, Q. Tian, J. Liu, and K. Qian, "Janus particles: design, preparation, and biomedical applications," *Materials today bio*, vol. 4, p. 100033, 2019.

[58] F. Qiu and B. J. Nelson, "Magnetic helical micro- and nanorobots: Toward their biomedical applications," *Engineering*, vol. 1, no. 1, pp. 021–026, 2015. [Online]. Available: ⟨GotoISI⟩://WOS:000422301300010

[59] K. E. Peyer, L. Zhang, and B. J. Nelson, "Bio-inspired magnetic swimming microrobots for biomedical applications," *Nanoscale*, vol. 5, no. 4, pp. 1259–1272, 2013.

[60] G. S. Klindt and B. M. Friedrich, "Flagellar swimmers oscillate between pusher-and puller-type swimming," *Physical Review E*, vol. 92, no. 6, p. 063019, 2015.

[61] A. Brown, I. Vladescu, A. Dawson, T. Vissers, J. Schwarz-Linek, J. Lintuvuori, and W. Poon, "Swimming in a crystal," *Soft matter*, vol. 12, 10 2015.

[62] A. Daddi-Moussa-Ider, B. Nasouri, A. Vilfan, and R. Golestanian, "Optimal swimmer can be puller, pusher, or neutral depending on the shape," *arXiv preprint arXiv:2104.13607*, 2021.

[63] E. Lauga and S. Michelin, "Stresslets induced by active swimmers," *Physical review letters*, vol. 117, no. 14, p. 148001, 2016.

[64] V. A. Martinez, E. Clément, J. Arlt, C. Douarche, A. Dawson, J. Schwarz-Linek, A. K. Creppy, V. Škultéty, A. N. Morozov, H. Auradou *et al.*, "A combined rheometry and imaging study of viscosity reduction in bacterial suspensions," *Proceedings of the National Academy of Sciences*, vol. 117, no. 5, pp. 2326–2331, 2020.

[65] J. Gachelin, G. Mino, H. Berthet, A. Lindner, A. Rousselet, and É. Clément, "Non-newtonian viscosity of escherichia coli suspensions," *Physical review letters*, vol. 110, no. 26, p. 268103, 2013.

[66] L. Jibuti, W. Zimmermann, S. Rafai, and P. Peyla, "Effective viscosity of a suspension of flagellar-beating microswimmers: Three-dimensional modeling," *Phys Rev E*, vol. 96, no. 5-1, p. 052610, 2017. [Online]. Available: https://www.ncbi.nlm.nih.gov/pubmed/29347779

[67] S. Rafai, L. Jibuti, and P. Peyla, "Effective viscosity of microswimmer suspensions," *Phys Rev Lett*, vol. 104, no. 9, p. 098102, 2010. [Online]. Available: https://www.ncbi.nlm.nih.gov/pubmed/20367014

[68] V. O. Adesanya, D. C. Vadillo, and M. R. Mackley, "The rheological characterization of algae suspensions for the production of biofuels," *Journal of Rheology*, vol. 56, no. 4, pp. 925–939, 2012. [Online]. Available: ⟨GotoISI⟩://WOS:000304305700011

[69] A. Wileman, A. Ozkan, and H. Berberoglu, "Rheological properties of algae slurries for minimizing harvesting energy requirements in biofuel production," *Bioresour Technol*, vol. 104, no. Supplement C, pp. 432–9, 2012. [Online]. Available: https://www.ncbi.nlm.nih.gov/pubmed/22133605

[70] A. Bolhouse, "Rheology of algae slurries," Thesis, 2010.

[71] A. Poddar, A. Bandopadhyay, and S. Chakraborty, "Near-wall hydrodynamic slip triggers swimming state transition of micro-organisms," *Journal of Fluid Mechanics*, vol. 894, 2020.

[72] B. Thomases and R. D. Guy, "Mechanisms of elastic enhancement and hindrance for finite-length undulatory swimmers in viscoelastic fluids," *Phys Rev Lett*, vol. 113, no. 9, p. 098102, 2014. [Online]. Available: https://www.ncbi.nlm.nih.gov/pubmed/25216008

[73] E. M. Purcell, "Life at low reynolds number," *American Journal of Physics*, vol. 45, no. 1, pp. 3–11, 1977. [Online]. Available: ⟨GotoISI⟩://WOS:A1977CS64300001

[74] J. S. Guasto, R. Rusconi, and R. Stocker, "Fluid mechanics of planktonic microorganisms," *Annual Review of Fluid Mechanics*, vol. 44, no. 1, pp. 373–400, 2012. [Online]. Available: ⟨GotoISI⟩://WOS:000304647800016

[75] "Analysis of the swimming of microscopic organisms," *Proceedings of the Royal Society of London. Series A. Mathematical and Physical Sciences*, vol. 209, no. 1099, p. 447, 1951. [Online]. Available: http://rspa.royalsocietypublishing.org/content/209/1099/447.abstract

[76] G. Taylor, "The action of waving cylindrical tails in propelling microscopic organisms," *Proceedings of the Royal Society of London. Series A. Mathematical and Physical Sciences*, vol. 211, no. 1105, pp. 225–239, 1952. [Online]. Available: ⟨GotoISI⟩://WOS:A1952XZ71800005http://rspa.royalsocietypublishing.org/content/royprsa/211/1105/225.full.pdf

[77] E. Lauga and R. P. Thomas, "The hydrodynamics of swimming microorganisms," *Reports on Progress in Physics*, vol. 72, no. 9, p. 096601, 2009. [Online]. Available: http://stacks.iop.org/0034-4885/72/i=9/a=096601

[78] J. Gray, "The movement of sea-urchin spermatozoa," *Journal of Experimental Biology*, vol. 32, no. 4, pp. 775–800, 1955. [Online]. Available: ⟨GotoISI⟩://WOS:A1955WX11500012

[79] J. Lighthill, "Flagellar hydrodynamics," *SIAM Review*, vol. 18, no. 2, pp. 161–230, 1976. [Online]. Available: ⟨GotoISI⟩://WOS:A1976BM13300001http://epubs.siam.org/doi/10.1137/1018040

[80] J. Gray and H. W. Lissmann, "The locomotion of nematodes," *J Exp Biol*, vol. 41, no. 1, pp. 135–54, 1964. [Online]. Available: https://www.ncbi.nlm.nih.gov/pubmed/14161604

[81] D. F. Katz, J. R. Blake, and S. L. Paveri-Fontana, "On the movement of slender bodies near plane boundaries at low reynolds number," *Journal of Fluid Mechanics*, vol. 72, no. 3, p. 529–540, 1975.

[82] L. Zhu, E. Lauga, and L. Brandt, "Self-propulsion in viscoelastic fluids: Pushers vs. pullers," *Physics of Fluids*, vol. 24, no. 5, p. 051902, 2012. [Online]. Available: ⟨GotoISI⟩://WOS:000304826100002

[83] N. C. Keim, M. Garcia, and P. E. Arratia, "Fluid elasticity can enable propulsion at low reynolds number," *Physics of Fluids*, vol. 24, no. 8, p. 081703, 2012. [Online]. Available: ⟨GotoISI⟩://WOS:000308417000003

[84] R. Poole, "The deborah and weissenberg numbers," *The British Society of Rheology - Rheology Bulletin*, vol. 53, pp. 32–39, 06 2012.

[85] E. Lauga, "Enhanced diffusion by reciprocal swimming," *Physical review letters*, vol. 106, no. 17, p. 178101, 2011.

[86] A. Shipunov, *Introduction to Botany*, shipunov, alexey ed. Minot State University, 2017.

[87] L. Barsanti and P. Gualtieri, *Algae: Anatomy, Biochemistry, and Biotechnology, Second Edition*. Taylor and Francis, 2014. [Online]. Available: https://books.google.co.uk/books?id=AZClAgAAQBAJ

[88] M. D. Guiry, "How many species of algae are there?" *J Phycol*, vol. 48, no. 5, pp. 1057–63, 2012. [Online]. Available: https://www.ncbi.nlm.nih.gov/pubmed/27011267

[89] Y. Sekerci and S. Petrovskii, "Mathematical modelling of plankton-oxygen dynamics under the climate change," *Bull Math Biol*, vol. 77, no. 12, pp. 2325–53, 2015. [Online]. Available: https://www.ncbi.nlm.nih.gov/pubmed/26607949

[90] M. A. Borowitzka and C. J. Siva, "The taxonomy of the genus dunaliella (chlorophyta, dunaliellales) with emphasis on the marine and halophilic species," *Journal of Applied Phycology*, vol. 19, no. 5, pp. 567–590, 2007. [Online]. Available: ⟨GotoISI⟩://WOS:000249205500024

[91] A. Oren, "A hundred years of dunaliella research: 1905-2005," *Saline Systems*, vol. 1, p. 2, 2005. [Online]. Available: https://www.ncbi.nlm.nih.gov/pubmed/16176593

[92] ——, "The ecology of dunaliella in high-salt environments," *Journal of Biological Research-Thessaloniki*, vol. 21, no. 1, pp. 1–8, 2014.

[93] A. Ramos, J. Polle, D. Tran, J. Cushman, E. Jin, and J. Varela, "[review] the unicellular green alga dunaliella salina teod. as a model for abiotic stress tolerance: genetic advances and future perspectives," *ALGAE*, vol. 26, no. 1, pp. 3–20, 2011. [Online]. Available: https://doi.org/DOI:10.4490/algae.2011.26.1.0http://www.e-algae.org/journal/view.php?number=2618

[94] M. Avron and A. Ben-Amotz, *Dunaliella : physiology, biochemistry, and biotechnology*. Boca Raton: CRC Press, 1992.

[95] X. Garcia, S. Rafai, and P. Peyla, "Light control of the flow of phototactic microswimmer suspensions," *Phys Rev Lett*, vol. 110, no. 13, p. 138106, 2013. [Online]. Available: https://www.ncbi.nlm.nih.gov/pubmed/23581381https://journals.aps.org/prl/abstract/10.1103/PhysRevLett.110.138106

[96] H. Chen, J. G. Jiang, and G. H. Wu, "Effects of salinity changes on the growth of dunaliella salina and its isozyme activities of glycerol-3-phosphate dehydrogenase," *J Agric Food Chem*, vol. 57, no. 14, pp. 6178–82, 2009. [Online]. Available: https://www.ncbi.nlm.nih.gov/pubmed/19548674

[97] A. A. Chengala, "Microalgal swimming in fluid environments: experimental and numerical investigations," Thesis or Dissertation, 2013. [Online]. Available: https://conservancy.umn.edu/handle/11299/160753

[98] A. Hosseini Tafreshi and M. Shariati, "Dunaliella biotechnology: methods and applications," *J Appl Microbiol*, vol. 107, no. 1, pp. 14–35, 2009. [Online]. Available: https://www.ncbi.nlm.nih.gov/pubmed/19245408

[99] O. Croze and F. Peaudecerf, "G.i. taylor and the physics of swimming," *News from the Cavendish Laboratory*, no. 15, pp. 4–5, 2016.

[100] T. Wang, Y. Liang, X. Wang, S. Ning, and T. Li, "Screening algae strains of chlorella sp. and dunaliella salina with resistance to oil pollution and their lipid enrichment by using petroleum hydrocarbons," *Cahiers de Biologie Marine*, vol. 56, pp. 195–203, 01 2015.

[101] I. H. Riedel-Kruse, A. Hilfinger, J. Howard, and F. Jülicher, "How molecular motors shape the flagellar beat," *HFSP Journal*, vol. 1, no. 3, pp. 192–208, 2007, pMID: 19404446. [Online]. Available: https://doi.org/10.2976/1.2773861

[102] B. Chakrabarti and D. Saintillan, "Spontaneous oscillations, beating patterns, and hydrodynamics of active microfilaments," *Physical Review Fluids*, vol. 4, 04 2019.

[103] C. Lakshmanan, "Biogeochemical studies for increased salt production in the tuticorin coast tamil nadu," Ph.D. dissertation, 2008. [Online]. Available: http://shodhganga.inflibnet.ac.in/handle/10603/43205

[104] I. S. Aranson, *Physical Models of Cell Motility*, ser. Biological and Medical Physics, Biomedical Engineering. Springer International Publishing, 2016, vol. 1. [Online]. Available: //www.springer.com/gb/book/9783319244464

[105] M. Melkonian, *Algal Cell Motility*. Springer US, 1991, vol. 1. [Online]. Available: http:////www.springer.com/gb/book/9781461596851

[106] Y. I. Posudin, N. P. Massjuk, and G. G. Llilitskaya, "Photomovement of two species od dunaliella teod. (chlorophyta)."

[107] M. Garcia, S. Berti, P. Peyla, and S. Rafaï, "Random walk of a swimmer in a low-reynolds-number medium," *Physical Review E*, vol. 83, no. 3, p. 035301, 2011. [Online]. Available: https://link.aps.org/doi/10.1103/PhysRevE.83.035301

[108] D. B. Weibel, P. Garstecki, D. Ryan, W. R. DiLuzio, M. Mayer, J. E. Seto, and G. M. Whitesides, "Microoxen: microorganisms to move microscale loads," *Proc Natl Acad Sci U S A*, vol. 102, no. 34, pp. 11 963–7, 2005. [Online]. Available: https://www.ncbi.nlm.nih.gov/pubmed/16103369

[109] K. Y. Wan and R. E. Goldstein, "Coordinated beating of algal flagella is mediated by basal coupling," *Proceedings of the National Academy of Sciences*, vol. 113, no. 20, pp. E2784–E2793, 2016.

[110] T. Pedley, "Hydrodynamic phenomena in suspensions of swimming microorganisms," *Annual Review of Fluid Mechanics*, vol. 24, no. 1, pp. 313–358, 1992. [Online]. Available: ⟨GotoISI⟩://WOS:A1992GY97300013

[111] M. A. Bees and O. A. Croze, "Mathematics for streamlined biofuel production from unicellular algae," *Biofuels*, vol. 5, no. 1, pp. 53–65, 2014. [Online]. Available: https://doi.org/10.4155/bfs.13.66http://www.tandfonline.com/doi/pdf/10.4155/bfs.13.66?needAccess=true

[112] H. V. Ramírez-Gómez, V. J. Sabinina, M. V. Pérez, C. Beltran, J. Carneiro, C. D. Wood, I. Tuval, A. Darszon, and A. Guerrero, "Sperm chemotaxis is driven by the slope of the chemoattractant concentration field," *Elife*, vol. 9, p. e50532, 2020.

[113] O. A. Croze, R. N. Bearon, and M. A. Bees, "Gyrotactic swimmer dispersion in pipe flow: testing the theory," *Journal of Fluid Mechanics*, vol. 816, pp. 481–506, 2017. [Online]. Available: ⟨GotoISI⟩://WOS:000396196300003

[114] M. S. Jones, L. L. Baron, and T. J. Pedley, "Biflagellate gyrotaxis in a shear flow," *Journal of Fluid Mechanics*, vol. 281, no. -1, pp. 137–158, 2006.

[115] P. Spolaore, C. Joannis-Cassan, E. Duran, and A. Isambert, "Commercial applications of microalgae," *J Biosci Bioeng*, vol. 101, no. 2, pp. 87–96, 2006. [Online]. Available: https://www.ncbi.nlm.nih.gov/pubmed/16569602

[116] E. Rajaei, K. Mowla, A. Ghorbani, S. Bahadoram, M. Bahadoram, and M. Dargahi-Malamir, "The effect of omega-3 fatty acids in patients with active rheumatoid arthritis receiving dmards therapy: double-blind randomized controlled trial," *Global journal of health science*, vol. 8, no. 7, p. 18, 2016.

[117] G. López, C. Yate, F. A. Ramos, M. P. Cala, S. Restrepo, and S. Baena, "Production of polyunsaturated fatty acids and lipids from autotrophic, mixotrophic and heterotrophic cultivation of galdieria sp. strain usba-gbx-832," *Scientific reports*, vol. 9, no. 1, pp. 1–13, 2019.

[118] Y. H. Cui, C. X. Jing, and H. W. Pan, "Association of blood antioxidants and vitamins with risk of age-related cataract: a meta-analysis of observational studies," *Am J Clin Nutr*, vol. 98, no. 3, pp. 778–86, 2013. [Online]. Available: https://www.ncbi.nlm.nih.gov/pubmed/23842458

[119] S. A. Paiva and R. M. Russell, "Beta-carotene and other carotenoids as antioxidants," *J Am Coll Nutr*, vol. 18, no. 5, pp. 426–33, 1999. [Online]. Available: https://www.ncbi.nlm.nih.gov/pubmed/10511324

[120] C. N. Holick, D. S. Michaud, R. Stolzenberg-Solomon, S. T. Mayne, P. Pietinen, P. R. Taylor, J. Virtamo, and D. Albanes, "Dietary carotenoids, serum beta-carotene, and retinol and risk of lung cancer in the alpha-tocopherol, beta-carotene cohort study," *Am J Epidemiol*, vol. 156, no. 6, pp. 536–47, 2002. [Online]. Available: https://www.ncbi.nlm.nih.gov/pubmed/12226001

[121] N. Mezzomo and S. R. Ferreira, "Carotenoids functionality, sources, and processing by supercritical technology: a review," *Journal of Chemistry*, vol. 2016, 2016.

[122] O. Isler and P. Zeller, *Total Syntheses of Carotenoids*. Academic Press, 1957, vol. 15, pp. 31–71. [Online]. Available: http://www.sciencedirect.com/science/article/pii/S0083672908605075

[123] S. Emeish, "Production of natural beta-carotene from dunaliella living in the dead sea," *The Jordan J Earth Environ Sci*, vol. 4, pp. 23–7, 2012.

[124] M. Garcia-Gonzalez, J. Moreno, J. C. Manzano, F. J. Florencio, and M. G. Guerrero, "Production of dunaliella salina biomass rich in 9-cis-beta-carotene and lutein in a closed tubular photobioreactor," *J Biotechnol*, vol. 115, no. 1, pp. 81–90, 2005. [Online]. Available: https://www.ncbi.nlm.nih.gov/pubmed/15607227

[125] I. Michalak, A. Dmytryk, and K. Chojnacka, "Algae cosmetics," *Encyclopedia of Marine Biotechnology*, vol. 1, pp. 65–85, 2020.

[126] H. W. Tan, A. R. Abdul Aziz, and M. K. Aroua, "Glycerol production and its applications as a raw material: A review," *Renewable and Sustainable Energy Reviews*, vol. 27, pp. 118–127, 2013. [Online]. Available: ⟨GotoISI⟩://WOS:000325954500011

[127] M. Xu, Q. Zeng, H. Li, Y. Zhong, L. Tong, R. Ruan, and H. Liu, "Contribution of glycerol addition and algal–bacterial cooperation to nutrients recovery: a study on the mechanisms of microalgae-based wastewater remediation," *Journal of Chemical Technology & Biotechnology*, vol. 95, no. 6, pp. 1717–1728, 2020.

[128] H.-J. Choi and S.-W. Yu, "Influence of crude glycerol on the biomass and lipid content of microalgae," *Biotechnology & Biotechnological Equipment*, vol. 29, no. 3, pp. 506–513, 2015.

[129] A. Chatterjee, S. Singh, C. Agrawal, S. Yadav, R. Rai, and L. Rai, *Role of Algae as a Biofertilizer*, 12 2017, pp. 189–200.

[130] C. Chen, L. H. Bai, D. R. Qiao, H. Xu, G. L. Dong, K. Ruan, F. Huang, and Y. Cao, "Cloning and expression study of a putative carotene biosynthesis related (cbr) gene from the halotolerant green alga dunaliella salina," *Mol Biol Rep*, vol. 35, no. 3, pp. 321–7, 2008. [Online]. Available: https://www.ncbi.nlm.nih.gov/pubmed/17562223

[131] Acsessed - 2019. [Online]. Available: https://corporate.exxonmobil.com/Research-and-innovation/Advanced-biofuels

[132] L. Idris, "Road map of the ultimate sustainable bio-fuel production from microalgae," Thesis, 2015.

[133] D. Aitken, "An assessment of the sustainability of bioenergy production from algal feedstock," Thesis, 2014.

[134] Y. Chisti, "Biodiesel from microalgae," *Biotechnol Adv*, vol. 25, no. 3, pp. 294–306, 2007. [Online]. Available: https://www.ncbi.nlm.nih.gov/pubmed/17350212

[135] "Oil(wti)," 2021. [Online]. Available: http://markets.businessinsider.com/commodities/oil-price?type=wti

[136] A. C. Tsang, E. Demir, Y. Ding, and O. S. Pak, "Roads to smart artificial microswimmers," *Advanced Intelligent Systems*, vol. 2, no. 8, p. 1900137, 2020.

[137] J. C. Love, B. D. Gates, D. B. Wolfe, K. E. Paul, and G. M. Whitesides, "Fabrication and wetting properties of metallic half-shells with submicron diameters," *Nano Letters*, vol. 2, no. 8, pp. 891–894, 2002. [Online]. Available: ⟨GotoISI⟩://WOS:000177485500021http://pubs.acs.org/doi/pdfplus/10.1021/nl025633l

[138] R. Dreyfus, J. Baudry, M. L. Roper, M. Fermigier, H. A. Stone, and J. Bibette, "Microscopic artificial swimmers," *Nature*, vol. 437, no. 7060, pp. 862–5, 2005. [Online]. Available: https://www.ncbi.nlm.nih.gov/pubmed/16208366

[139] U. K. Cheang, F. Meshkati, D. Kim, M. J. Kim, and H. C. Fu, "Minimal geometric requirements for micropropulsion via magnetic rotation," *Phys Rev E Stat Nonlin Soft Matter Phys*, vol. 90, no. 3, p. 033007, 2014. [Online]. Available: https://www.ncbi.nlm.nih.gov/pubmed/25314529

[140] U. K. Cheang and M. J. Kim, "Self-assembly of robotic micro- and nanoswimmers using magnetic nanoparticles," *Journal of Nanoparticle Research*, vol. 17, no. 3, p. 145, 2015. [Online]. Available: ⟨GotoISI⟩://WOS:000355017500004

[141] A. E. Patteson, A. Gopinath, and P. E. Arratia, "Active colloids in complex fluids," *Current Opinion in Colloid and Interface Science*, vol. 21, pp. 86–96, 2016. [Online]. Available: ⟨GotoISI⟩://WOS:000374357900010

[142] S. Tottori and B. J. Nelson, "Artificial helical microswimmers with mastigoneme-inspired appendages," *Biomicrofluidics*, vol. 7, no. 6, p. 61101, 2013. [Online]. Available: https://www.ncbi.nlm.nih.gov/pubmed/24396533

[143] K. Minhun, "Bots in the bloodstream," *Drexel University Research Magazine*, 2016. [Online]. Available: http://exelmagazine.org/article/bots-in-the-bloodstream/

[144] K. E. Peyer, L. Zhang, and B. J. Nelson, "Bio-inspired magnetic swimming microrobots for biomedical applications," *Nanoscale*, vol. 5, no. 4, pp. 1259–72, 2013. [Online]. Available: https://www.ncbi.nlm.nih.gov/pubmed/23165991

[145] A. M. Leshansky and L. M. Pismen, "Do small swimmers mix the ocean?" *Phys. Rev. E*, vol. 82, p. 025301, Aug 2010. [Online]. Available: https://link.aps.org/doi/10.1103/PhysRevE.82.025301

[146] K. Katija and J. Dabiri, "A viscosity-enhanced mechanism for biogenic ocean mixing," *Nature*, vol. 460, pp. 624–6, 08 2009.

[147] I. Houghton, J. Koseff, S. Monismith, and J. Dabiri, "Vertically migrating swimmers generate aggregation-scale eddies in a stratified column," *Nature*, vol. 556, 04 2018.

[148] J. Palacci, S. Sacanna, A. Preska Steinberg, D. Pine, and P. Chaikin, "Living crystals of light-activated colloidal surfers," *Science (New York, N.Y.)*, vol. 339, 01 2013.

[149] W. R. Schneider and R. N. Doetsch, "Effect of viscosity on bacterial motility," *J Bacteriol*, vol. 117, no. 2, pp. 696–701, 1974. [Online]. Available: https://www.ncbi.nlm.nih.gov/pubmed/4204439

[150] E. Lauga, "Propulsion in a viscoelastic fluid," *Physics of Fluids*, vol. 19, no. 8, p. 083104, 2007. [Online]. Available: ⟨GotoISI⟩://WOS:000249156500013

[151] O. S. Beveridge, O. L. Petchey, and S. Humphries, "Direct and indirect effects of temperature on the population dynamics and ecosystem functioning of aquatic microbial ecosystems," *J Anim Ecol*, vol. 79, no. 6, pp. 1324–31, 2010. [Online]. Available: https://www.ncbi.nlm.nih.gov/pubmed/20722873

[152] M. J. Orchard, S. Humphries, R. Schuech, and S. Menden-Deuer, "The influence of viscosity on the motility and sensory ability of the dinoflagellateheterocapsa triquetra," *Journal of Plankton Research*, vol. 38, no. 4, pp. 1062–1076, 2016. [Online]. Available: https://doi.org/10.1093/plankt/fbw004

[153] J. Pande, L. Merchant, T. Krüger, J. Harting, and S. Ana-Sunčana, "Setting the pace of microswimmers: when increasing viscosity speeds up self-propulsion," *New Journal of Physics*, vol. 19, no. 5, p. 053024, 2017. [Online]. Available: http://stacks.iop.org/1367-2630/19/i=5/a=053024

[154] D. M. Woolley and G. G. Vernon, "A study of helical and planar waves on sea urchin sperm flagella, with a theory of how they are generated," *J Exp Biol*, vol. 204, no. Pt 7, pp. 1333–45, 2001. [Online]. Available: https://www.ncbi.nlm.nih.gov/pubmed/11249842

[155] M. H. Sohn, S. Lim, K. W. Seo, and S. J. Lee, "Effect of ambient medium viscosity on the motility and flagella motion of prorocentrum minimum (dinophyceae)," *Journal of Plankton Research*, vol. 35, no. 6, pp. 1294–1304, 2013. [Online]. Available: https://doi.org/10.1093/plankt/fbt071

[156] B. Chaban, I. Coleman, and M. Beeby, "Evolution of higher torque in campylobacter-type bacterial flagellar motors," *Scientific Reports*, vol. 8, 01 2018.

[157] Y. Magariyama and S. Kudo, "A mathematical explanation of an increase in bacterial swimming speed with viscosity in linear-polymer solutions," *Biophys J*, vol. 83, no. 2, pp. 733–9, 2002. [Online]. Available: https://www.ncbi.nlm.nih.gov/pubmed/12124260

[158] T. Atsumi, Y. Maekawa, T. Yamada, I. Kawagishi, Y. Imae, and M. Homma, "Effect of viscosity on swimming by the lateral and polar flagella of vibrio alginolyticus," *J Bacteriol*, vol. 178, no. 16, pp. 5024–6, 1996. [Online]. Available: https://www.ncbi.nlm.nih.gov/pubmed/8759871

[159] A. A. Rizvi, M. I. Quraishi, V. Sarkar, C. DuBois, S. Biro, and J. Mulhall, "The effect of ph and viscosity on bovine spermatozoa motility under controlled

conditions," *International Urology and Nephrology*, vol. 41, no. 3, pp. 523–530, 2009. [Online]. Available: https://doi.org/10.1007/s11255-008-9493-x

[160] T. Hyakutake, H. Suzuki, and S. Yamamoto, "Effect of viscosity on motion characteristics of bovine sperm," *Journal of Aero Aqua Bio-mechanisms*, vol. 4, pp. 63–70, 2015.

[161] B. Liebchen, P. Monderkamp, B. ten Hagen, and H. Löwen, "Viscotaxis: Microswimmer navigation in viscosity gradients," *Physical Review Letters*, vol. 120, no. 20, p. 208002, 2018. [Online]. Available: https://link.aps.org/doi/10.1103/PhysRevLett.120.208002

[162] B. Liu, T. R. Powers, and K. S. Breuer, "Force-free swimming of a model helical flagellum in viscoelastic fluids," *Proc Natl Acad Sci U S A*, vol. 108, no. 49, pp. 19 516–20, 2011. [Online]. Available: https://www.ncbi.nlm.nih.gov/pubmed/22106263

[163] S. Gómez, F. A. Godínez, E. Lauga, and R. Zenit, "Helical propulsion in shear-thinning fluids," *Journal of Fluid Mechanics*, vol. 812, 2016.

[164] T. D. Montenegro-Johnson, D. J. Smith, and D. Loghin, "Physics of rheologically enhanced propulsion: Different strokes in generalized stokes," *Physics of Fluids*, vol. 25, no. 8, p. 081903, 2013. [Online]. Available: ⟨GotoISI⟩://WOS:000323946200004

[165] J. R. Vélez-Cordero and E. Lauga, "Waving transport and propulsion in a generalized newtonian fluid," 2014.

[166] T. D. Montenegro-Johnson, A. A. Smith, D. J. Smith, D. Loghin, and J. R. Blake, "Modelling the fluid mechanics of cilia and flagella in reproduction and development," *The European Physical Journal E*, vol. 35, no. 10, Oct 2012. [Online]. Available: http://dx.doi.org/10.1140/epje/i2012-12111-1

[167] C. Li, B. Qin, A. Gopinath, P. E. Arratia, B. Thomases, and R. D. Guy, "Flagellar swimming in viscoelastic fluids: role of fluid elastic stress revealed by simulations based on experimental data," *J R Soc Interface*, vol. 14, no. 135, 2017. [Online]. Available: https://www.ncbi.nlm.nih.gov/pubmed/28978746

[168] C. Li, B. Thomases, and R. D. Guy, "Orientation dependent elastic stress concentration at tips of slender objects translating in viscoelastic fluids," *Physical Review Fluids*, vol. 4, no. 3, Mar 2019. [Online]. Available: http://dx.doi.org/10.1103/PhysRevFluids.4.031301

[169] S. C. Lenaghan, C. A. Davis, W. R. Henson, Z. Zhang, and M. Zhang, "High-speed microscopic imaging of flagella motility and swimming in giardia lamblia trophozoites," *Proc Natl Acad Sci U S A*, vol. 108, no. 34, pp. E550–8, 2011. [Online]. Available: https://www.ncbi.nlm.nih.gov/pubmed/21808023

[170] D. A. Gagnon and P. E. Arratia, "The cost of swimming in generalized newtonian fluids: experiments with c. elegans," *Journal of Fluid Mechanics*, vol. 800, pp. 753–765, 2016. [Online]. Available: ⟨GotoISI⟩://WOS:000379846600029

[171] K. Drescher, K. C. Leptos, and R. E. Goldstein, "How to track protists in three dimensions," *Rev Sci Instrum*, vol. 80, no. 1, p. 014301, 2009. [Online]. Available: https://www.ncbi.nlm.nih.gov/pubmed/19191449

[172] T. S. Yu, E. Lauga, and A. E. Hosoi, "Experimental investigations of elastic tail propulsion at low reynolds number," *Physics of Fluids*, vol. 18, no. 9, p. 091701, 2006. [Online]. Available: ⟨GotoISI⟩://WOS:000240877600003http://aip.scitation.org/doi/pdf/10.1063/1.2349585

[173] B. Qian, T. R. Powers, and K. S. Breuer, "Shape transition and propulsive force of an elastic rod rotating in a viscous fluid," *Phys Rev Lett*, vol. 100, no. 7, p. 078101, 2008. [Online]. Available: https://www.ncbi.nlm.nih.gov/pubmed/18352599

[174] M. M. Mrokowska and A. Krztoń-Maziopa, "Viscoelastic and shear-thinning effects of aqueous exopolymer solution on disk and sphere settling," *Scientific reports*, vol. 9, no. 1, pp. 1–13, 2019.

[175] S. Malhotra and M. M. Sharma, "Experimental measurement of settling velocity of spherical particles in unconfined and confined surfactant-based shear thinning viscoelastic fluids," *JoVE (Journal of Visualized Experiments)*, no. 83, p. e50749, 2014.

[176] J.-S. Park, D. Kim, J. H. Shin, and D. A. Weitz, "Efficient nematode swimming in a shear thinning colloidal suspension," *Soft Matter*, vol. 12, no. 6, pp. 1892–1897, 2016.

[177] Z. Qu and K. S. Breuer, "Effects of shear-thinning viscosity and viscoelastic stresses on flagellated bacteria motility," *Physical Review Fluids*, vol. 5, no. 7, Jul 2020. [Online]. Available: http://dx.doi.org/10.1103/PhysRevFluids.5.073103

[178] C. Datt, L. Zhu, G. J. Elfring, and O. S. Pak, "Squirming through shear-thinning fluids," *Journal of Fluid Mechanics*, vol. 784, p. R1, 2015.

[179] A. Zöttl and J. M. Yeomans, "Enhanced bacterial swimming speeds in macromolecular polymer solutions," *Nature Physics*, vol. 15, no. 6, pp. 554–558, 2019.

[180] J. Teran, L. Fauci, and M. Shelley, "Viscoelastic fluid response can increase the speed and efficiency of a free swimmer," *Phys Rev Lett*, vol. 104, no. 3, p. 038101, 2010. [Online]. Available: https://www.ncbi.nlm.nih.gov/pubmed/20366685

[181] S. E. Spagnolie, B. Liu, and T. R. Powers, "Locomotion of helical bodies in viscoelastic fluids: enhanced swimming at large helical amplitudes," *Phys Rev Lett*, vol. 111, no. 6, p. 068101, 2013. [Online]. Available: https://www.ncbi.nlm.nih.gov/pubmed/23971615

[182] M. Dasgupta, B. Liu, H. C. Fu, M. Berhanu, K. S. Breuer, T. R. Powers, and A. Kudrolli, "Speed of a swimming sheet in newtonian and viscoelastic fluids," *Physical Review E*, vol. 87, no. 1, p. 013015, 2013.

[183] H. C. Fu, T. R. Powers, and C. W. Wolgemuth, "Theory of swimming filaments in viscoelastic media," *Phys Rev Lett*, vol. 99, no. 25, p. 258101, 2007. [Online]. Available: https://www.ncbi.nlm.nih.gov/pubmed/18233558

[184] B. Thomases and R. D. Guy, "The role of body flexibility in stroke enhancements for finite-length undulatory swimmers in viscoelastic fluids," *Journal of Fluid Mechanics*, vol. 825, p. 109–132, Jul 2017. [Online]. Available: http://dx.doi.org/10.1017/jfm.2017.383

[185] S. Campuzano, B. E.-F. De Ávila, P. Yanez-Sedeno, J. Pingarron, and J. Wang, "Nano/microvehicles for efficient delivery and (bio) sensing at the cellular level," *Chemical science*, vol. 8, no. 10, pp. 6750–6763, 2017.

[186] E. Lushi, V. Kantsler, and R. E. Goldstein, "Scattering of biflagellate microswimmers from surfaces," *Phys Rev E*, vol. 96, no. 2-1, p. 023102, 2017. [Online]. Available: https://www.ncbi.nlm.nih.gov/pubmed/28950627

[187] E. Lauga, W. R. DiLuzio, G. M. Whitesides, and H. A. Stone, "Swimming in circles: Motion of bacteria near solid boundaries," *Biophysical Journal*, vol. 90, no. 2, p. 400–412, Jan 2006. [Online]. Available: http://dx.doi.org/10.1529/biophysj.105.069401

[188] L. Lemelle, J.-F. Palierne, E. Chatre, and C. Place, "Counterclockwise circular motion of bacteria swimming at the air-liquid interface," *Journal of bacteriology*, vol. 192, no. 23, pp. 6307–6308, 2010.

[189] J. Hu, A. Wysocki, R. G. Winkler, and G. Gompper, "Physical sensing of surface properties by microswimmers–directing bacterial motion via wall slip," *Sci Rep*, vol. 5, p. 9586, 2015. [Online]. Available: https://www.ncbi.nlm.nih.gov/pubmed/25993019

[190] E. Teodoresco, "Organisation et développement du dunaliella, nouveau genre de volvocacée-polyblepharidée," *Beih z Bot Centralbl*, 1905.

[191] C. Hamburger, "Zur kenntnis der dunaliella salina und einer amöbe aus salinenwasser von cagliari," *Arch f Protistenkd*, vol. 6, pp. 111–131, 1905.

[192] M. A. Hejazi, E. Holwerda, and R. H. Wijffels, "Milking microalga dunaliella salina for beta-carotene production in two-phase bioreactors," *Biotechnol Bioeng*, vol. 85, no. 5, pp. 475–81, 2004. [Online]. Available: https://www.ncbi.nlm.nih.gov/pubmed/14760687

[193] E. Klimova, A. Bozhkov, E. Bychenko, E. Lavinskaya, N. Zholobak, and A. Korobov, "Characteristics of the response of the microalga (dunaliella viridis) to cerium compounds in culture," *Biosystems Diversity*, vol. 27, pp. 142–147, 2019.

[194] J. Thompson and A. Guy, "Mechanisms of osmoregulation in the green alga dunaliella salina," *Journal of Experimental Zoology*, vol. 268, no. 2, pp. 127–132, 1994. [Online]. Available: https://onlinelibrary.wiley.com/doi/abs/10.1002/jez.1402680209

[195] E. Chitlaru and U. Pick, "Regulation of glycerol synthesis in response to osmotic changes in dunaliella," *Plant physiology*, vol. 96, no. 1, pp. 50–60, 1991. [Online]. Available: https://pubmed.ncbi.nlm.nih.gov/16668185https://www.ncbi.nlm.nih.gov/pmc/articles/PMC1080712/

[196] "Culture collection of algae and protozoa." [Online]. Available: https://www.ccap.ac.uk/

[197] 2006. [Online]. Available: https://genome.jgi.doe.gov/portal/DunsalStandDraft/DunsalStandDraft.info.html

[198] R. A. Ahmed, M. He, R. A. Aftab, S. Zheng, M. Nagi, R. Bakri, and C. Wang, "Bioenergy application of dunaliella salina sa 134 grown at various salinity levels for lipid production," *Scientific reports*, vol. 7, no. 1, pp. 8118–8118, 2017. [Online]. Available: https://pubmed.ncbi.nlm.nih.gov/28808229https://www.ncbi.nlm.nih.gov/pmc/articles/PMC5556107/

[199] L. Hernandez javier, *Iodine speciation in marine microalgae cultures: Isochrysis aff. galbana, Dunaliella salina, Chaetoceros gracilis and Phaeodactylum tricornutum*, 2016.

[200] N. Sathasivam, Ramaraj; Juntawong, "Modified medium for enhanced growth of dunaliella strains," Conference Proceedings.

[201] J. C. Goldman, D. B. Porcella, E. J. Middlebrooks, and D. F. Toerien, "The effect of carbon on algal growth—its relationship to eutrophication," *Water research*, vol. 6, no. 6, pp. 637–679, 1972.

[202] L. Ren, P. Wang, C. Wang, J. Chen, and J. Qian, "Algal growth and utilization of phosphorus studied by combined mono-culture and co-culture experiments," *Environmental Pollution*, vol. 220, 09 2016.

[203] J. McLachlan, "The culture dunaliella tertiolecta butcher a euryhaline organism," *Canadian Journal of Microbiology*, vol. 6, no. 3, pp. 367–379, 1960. [Online]. Available: https://doi.org/10.1139/m60-041

[204] M. A. Borowitzka, "The mass culture of dunaliella salina," 1990, Conference Proceedings.

[205] M. A. Hejazi and R. H. Wijffels, "Effect of light intensity on beta-carotene production and extraction by dunaliella salina in two-phase bioreactors," *Biomol Eng*, vol. 20, no. 4-6, pp. 171–5, 2003. [Online]. Available: https://www.ncbi.nlm.nih.gov/pubmed/12919794

[206] J. Fábregas, V. Vázquez, B. Cabezas, and A. Otero, "Tris not only controls the ph in microalgal cultures, but also feeds bacteria," *Journal of Applied Phycology*, vol. 5, pp. 543–545, 2004.

[207] S. Tadama and H. Shiraishi, "Growth of the edible microalga arthrospira platensis in relation to boron supply," *International Journal of GEOMATE*, vol. 12, no. 30, pp. 90–95, 2017.

[208] A. Nguyen, D. Tran, M. Ho, C. Louime, and D. Tran, "High light stress regimen on dunaliella salina strains for carotenoids induction," *Integr Food Nutr Metab 3*, 2016.

[209] Y. Xu, I. M. Ibrahim, and P. J. Harvey, "The influence of photoperiod and light intensity on the growth and photosynthesis of dunaliella salina (chlorophyta) ccap 19/30," *Plant Physiology and Biochemistry*, vol. 106, pp. 305–315, 2016. [Online]. Available: http://www.sciencedirect.com/science/article/pii/S0981942816301917

[210] C. Soccol, A. Pandey, and C. Larroche, *Fermentation Processes Engineering in the Food Industry*. Boca Raton: CRC Press, 2013.

[211] J. Dehghani, A. Movafeghi, A. Barzegari, and J. Barar, "Efficient and stable transformation of dunaliella pseudosalina by 3 strains of agrobacterium tumefaciens," *BioImpacts : BI*, vol. 7, no. 4, pp. 247–254, 2017. [Online]. Available: https://pubmed.ncbi.nlm.nih.gov/29435432https://www.ncbi.nlm.nih.gov/pmc/articles/PMC5801536/

[212] A. Paar, "Basics of rheology," 2021. [Online]. Available: https://wiki.anton-paar.com/en/basics-of-rheology/

[213] W. Richtering, "Understanding rheology," *Applied Rheology*, vol. 12, pp. 233–233, 2002.

[214] C. W. Macosko and R. G. Larson, *Rheology: principles, measurements, and applications*, ser. Advances in interfacial engineering series. New York, NY: VCH, 1994. [Online]. Available: //catalog.hathitrust.org/Record/002898314http://hdl.handle.net/2027/mdp.39076001479059

[215] J. Meadows, P. A. Williams, and J. C. Kennedy, "Comparison of the extensional and shear viscosity characteristics of aqueous hydroxyethyl cellulose solutions," *Macromolecules*, vol. 28, no. 8, pp. 2683–2692, 1995. [Online]. Available: https://doi.org/10.1021/ma00112a013

[216] H. A. Barnes, J. F. Hutton, and K. Walters, *An Introduction to Rheology*, ser. Annals of Discrete Mathematics. Elsevier, 1989. [Online]. Available: https://books.google.co.uk/books?id=B1e0uxFg4oYC

[217] M. Chellamuthu, D. Arora, H. Winter, and J. Rothstein, "Extensional flow-induced crystallization of isotactic poly-1-butene using a filament stretching rheometer," *Journal of Rheology - J RHEOL*, vol. 55, 2011.

[218] C. Hadinata, D. Boos, C. Gabriel, E. Wassner, M. Ruellmann, N. Kao, and M. Laun, "Elongation-induced crystallization of a high molecular weight isotactic polybutene-1 melt compared to shear-induced crystallization," *Journal of Rheology - J RHEOL*, vol. 51, 2007.

[219] S. Różańska, "Chapter 6 - extensional rheology in food processing," in *Advances in Food Rheology and Its Applications*, ser. Woodhead Publishing Series in Food Science, Technology and Nutrition, J. Ahmed, P. Ptaszek, and S. Basu, Eds. Woodhead Publishing, 2017, pp. 125–157. [Online]. Available: https://www.sciencedirect.com/science/article/pii/B9780081004319000061

[220] J. M. Krishnan, A. P. Deshpande, and P. B. S. Kumar, *Rheology of Complex Fluids*. Springer-Verlag New York, 2010, vol. 1. [Online]. Available: //www.springer.com/gb/book/9781441964939

[221] F. Irgens, *Rheology and Non-Newtonian Fluids*. Springer International Publishing, 2014, vol. 1. [Online]. Available: //www.springer.com/gb/book/9783319010526

[222] G. Healthcare, "Ficoll pm70/ficoll pm400 data file 18-1158-27 ab," 2007.

[223] K. Sankaranarayanan and M. Natarajan, "Micro-viscosity induced conformational transitions in poly-l-lysine," *RSC Adv.*, vol. 6, p. 74009, 07 2016.

[224] R. Christoph, B. Schmidt, U. Steinberner, W. Dilla, and R. Karinen, *Glycerol*, ser. In Ullmann's Encyclopedia of Industrial Chemistry, (Ed.)., 2006. [Online]. Available: https://onlinelibrary.wiley.com/doi/abs/10.1002/14356007.a12_477.pub2

[225] A. G. M. Ferreira, A. P. V. Egas, I. M. A. Fonseca, A. C. Costa, D. C. Abreu, and L. Q. Lobo, "The viscosity of glycerol," *The Journal of Chemical Thermodynamics*, vol. 113, pp. 162–182, 2017. [Online]. Available: http://www.sciencedirect.com/science/article/pii/S0021961417301817

[226] V. Lazar, "Quantification of bone using a 3.0 tesla clinical magnetic resonance scanner," Ph.D. dissertation, 12 2011.

[227] A. Jeanes, J. E. Pittsley, and F. R. Senti, "Polysaccharide b-1459: A new hydrocolloid polyelectrolyte produced from glucose by bacterial fermentation," *Journal of Applied Polymer Science*, vol. 5, no. 17, pp. 519–526, 1961. [Online]. Available: https://onlinelibrary.wiley.com/doi/abs/10.1002/app.1961.070051704

[228] K. Symes, "The relationship between the covalent structure of the xanthomonas polysaccharide (xanthan) and its function as a thickening, suspending and gelling agent," *Food Chemistry*, vol. 6, no. 1, pp. 63 – 76, 1980. [Online]. Available: http://www.sciencedirect.com/science/article/pii/0308814680900072

[229] I. Cottrell, "xanthan gum." *Handbook of water-soluble gums and resins.*, 1980.

[230] S. Abedinzadeh, M. Torbati, and S. Azadmard-Damirchi, "Some qualitative and rheological properties of virgin olive oil-apple vinegar salad dressing stabilized with xanthan gum," *Advanced pharmaceutical bulletin*, vol. 6, no. 4, p. 597, 2016.

[231] D. F. S. Petri, "Xanthan gum: A versatile biopolymer for biomedical and technological applications," *Journal of Applied Polymer Science*, vol. 132, no. 23, 2015. [Online]. Available: https://onlinelibrary.wiley.com/doi/abs/10.1002/app.42035

[232] G. O. Phillips, P. A. Williams *et al.*, *Handbook of hydrocolloids*. CRC press Boca Raton, FL, 2000.

[233] T. Quinten, T. De Beer, j. Remon, and C. Vervaet, "Overview of injection molding as a manufacturing technique for pharmaceutical applications," *Injection Molding: Process, Design, and Applications*, pp. 1–42, 01 2011.

[234] S. A. Ramezani, M. Nourman, and M. A. Emadi, "Rheological behaviour and hydrodynamic diameter of high molecularweight, partially hydrolysed poly(acrylamide) in high salinity and temperature conditions," *Iranian Polymer Journal (English)*, vol. 19, no. 2(116), pp. 105–113, 2010. [Online]. Available: http://www.sid.ir/en/VEWSSID/J_pdf/813201011607.pdfhttp://en.journals.sid.ir/ViewPaper.aspx?ID=167648

[235] R. O. Afolabi, "Effect of surfactant and hydrophobe content on the rheology of poly(acrylamide-co-n-dodecylacrylamide) for potential enhanced oil recovery application," *American Journal of Polymer Science*, vol. 5, no. 2, pp. 41–46, 2015. [Online]. Available: http://article.sapub.org/10.5923.j.ajps.20150502.02.html

[236] P. C. Sousa, F. T. Pinho, M. S. N. Oliveira, and M. A. Alves, "Efficient microfluidic rectifiers for viscoelastic fluid flow," *Journal of Non-Newtonian Fluid Mechanics*, vol. 165, no. 11-12, pp. 652–671, 2010. [Online]. Available: ⟨GotoISI⟩://WOS:000278564300010

[237] P. Worsfold, A. Townshend, C. F. Poole, and M. Miró, *Encyclopedia of analytical science*. Elsevier, 2019.

[238] B. Wessling, "Critical shear rate - the instability reason for the creation of dissipative structures in polymers," *Z. Phys. Chem.*, vol. 191, pp. 119–135, 1995.

[239] B. Xiong, R. D. Loss, D. Shields, T. Pawlik, R. Hochreiter, A. L. Zydney, and M. Kumar, "Polyacrylamide degradation and its implications in environmental systems," *npj Clean Water*, vol. 1, no. 1, p. 17, 2018. [Online]. Available: https://doi.org/10.1038/s41545-018-0016-8

[240] T. Roger, "Engineering rheology," vol. 2, p. 586, 2000.

[241] T. Instruments, "Discovery hybrid rheometer getting started guide," 2013. [Online]. Available: https://pages.mtu.edu/~fmorriso/cm4655/TAInstruments/2013TA_DHRGettingStartedGuide.pdf

[242] H. P. Sdougos, S. R. Bussolari, and C. F. Dewey, "Secondary flow and turbulence in a cone and plate device," *Journal of Fluid Mechanics*, vol. 138, pp. 379–404, 1984.

[243] L. E. Rodd, T. P. Scott, J. J. Cooper-White, and G. H. McKinley, "Capillary break-up rheometry of low-viscosity elastic fluids," *Applied Rheology*, vol. 15, no. 1, pp. 12–27, 2005.

[244] D. Vadillo, T. Tuladhar, A. C. Mulji, S. Jung, S. Hoath, and M. Mackley, "Evaluation of the inkjet fluid's performance using the "cambridge trimaster" filament stretch and break-up device," *Journal of Rheology - J RHEOL*, vol. 54, 2010.

[245] D. Sachsenheimer, "Capillary thinning of viscoelastic fluid filaments," Thesis, 2014.

[246] C. M. Collier, J. Nichols, and J. F. Holzman, *4 - Digital microfluidics technologies for biomedical devices*. Woodhead Publishing, 2013, pp. 139–164. [Online]. Available: http://www.sciencedirect.com/science/article/pii/B9780857096975500049

[247] J. Fidalgo, K. Zografos, L. Casanellas, A. Lindner, and M. Oliveira, "Customised bifurcating networks for mapping polymer dynamics in shear flows," *Biomicrofluidics*, vol. 11, 2017.

[248] G. M. Whitesides, "The origins and the future of microfluidics," *Nature*, vol. 442, no. 7101, pp. 368–373, 2006. [Online]. Available: https://doi.org/10.1038/nature05058

[249] D. Qin, Y. Xia, J. A. Rogers, R. J. Jackman, X.-M. Zhao, and G. M. Whitesides, *Microfabrication, Microstructures and Microsystems*. Berlin: Springer-Verlag, 1998, vol. 194, pp. 1–20.

[250] S. K. Mitra and S. Chakraborty, *Microfluidics and nanofluidics handbook: Fabrication, implementation, and applications*, 2016.

[251] J. C. McDonald, D. C. Duffy, J. R. Anderson, D. T. Chiu, H. Wu, O. J. Schueller, and G. M. Whitesides, "Fabrication of microfluidic systems in poly(dimethylsiloxane)," *Electrophoresis*, vol. 21, no. 1, pp. 27–40, 2000.

[252] S. K. Sia and G. M. Whitesides, "Microfluidic devices fabricated in poly(dimethylsiloxane) for biological studies," *ELECTROPHORESIS*, vol. 24, no. 21, pp. 3563–3576, 2003. [Online]. Available: https://doi.org/10.1002/elps.200305584

[253] Y. Xia and G. M. Whitesides, "Soft lithography," *Annual Review of Materials Science*, vol. 28, no. 1, pp. 153–184, 1998. [Online]. Available: https://doi.org/10.1146/annurev.matsci.28.1.153

[254] S. Schmid, *Electrostatically Actuated All-Polymer Microbeam Resonators—Characterization and Application*, 01 2009.

[255] S. Hamouni, O. Arous, D. Abdessemed, G. Nezzal, and B. Van der Bruggen, "Alcohol and alkane organic extraction using pervaporation process," *Macromolecular Symposia*, vol. 386, p. 1800247, 08 2019.

[256] W. I. Wu, P. Rezai, H. H. Hsu, and P. R. Selvaganapathy, *1 - Materials and methods for the microfabrication of microfluidic biomedical devices*. Woodhead Publishing, 2013, pp. 3–62. [Online]. Available: http://www.sciencedirect.com/science/article/pii/B9780857096975500013

[257] J. Fidalgo, "Microfluidics for assessing the behaviour of deformable biological objects," Ph.D. dissertation, University of Strathclyde, 2019.

[258] J. C. McDonald and G. M. Whitesides, "Poly(dimethylsiloxane) as a material for fabricating microfluidic devices," *Accounts of Chemical Research*, vol. 35, no. 7, pp. 491–499, 2002. [Online]. Available: https://doi.org/10.1021/ar010110q

[259] M. A. Eddings, M. A. Johnson, and B. K. Gale, "Determining the optimal pdms–pdms bonding technique for microfluidic devices," *Journal of Micromechanics and Microengineering*, vol. 18, no. 6, p. 067001, 2008. [Online]. Available: http://dx.doi.org/10.1088/0960-1317/18/6/067001

[260] C. Sheppard, "Advanced light microscopy. vol. 2. specialized methods," *Journal of Modern Optics*, vol. 37, pp. 1277–1278, 2007.

[261] P. Antony, C. Trefois, A. Stojanovic, A. S. Baumuratov, and K. Kozak, "Light microscopy applications in systems biology: opportunities and challenges," *Cell Communication and Signaling*, vol. 11, no. 1, p. 24, 2013. [Online]. Available: https://doi.org/10.1186/1478-811X-11-24

[262] J. S. Guasto, K. A. Johnson, and J. P. Gollub, "Oscillatory flows induced by microorganisms swimming in two dimensions," *Phys Rev Lett*, vol. 105, no. 16, p. 168102, 2010. [Online]. Available: https://www.ncbi.nlm.nih.gov/pubmed/21231018

[263] R. Wayne, A. Kadota, M. atanabe, and M. ruya, "Photomovement in dunaliella salina: Fluence rate-response curves and action spectra," *Planta*, vol. 184, pp. 515–524, 1991.

[264] "Understanding microscopes and objectives," 2020. [Online]. Available: https://www.edmundoptics.co.uk

[265] "Microscope calculations: Field of view, depth of field, numerical aperture." [Online]. Available: https://dovermotion.com/applications-capabilities/automated-imaging/microscope-calculations/

[266] M. Abramowitz and M. Davidson, "Numerical aperture and resolution." [Online]. Available: https://www.olympus-lifescience.com/en/microscope-resource/primer/anatomy/numaperture/

[267] C. Meinhart, S. Wereley, and M. Gray, "Volume illumination for two-dimensional particle image velocimetry," *Measurement Science and Technology*, vol. 11, p. 809, 05 2000.

[268] D. Kokkinos, H. Dakhil, A. Wierschem, H. Briesen, and A. Braun, "Deformation and rupture of dunaliella salina at high shear rates without the use of thickeners," *Biorheology*, vol. 53, no. 1, pp. 1–11, 2016. [Online]. Available: https://www.ncbi.nlm.nih.gov/pubmed/26967951

[269] K. W. Oh, K. Lee, B. Ahn, and E. P. Furlani, "Design of pressure-driven microfluidic networks using electric circuit analogy," *Lab Chip*, vol. 12, no. 3, pp. 515–45, 2012.

[270] D. Katritsis, L. Kaiktsis, A. Chaniotis, J. Pantos, E. P. Efstathopoulos, and V. Marmarelis, "Wall shear stress: Theoretical considerations and methods of measurement," *Progress in Cardiovascular Diseases*, vol. 49, no. 5, pp. 307–329, 2007. [Online]. Available: http://www.sciencedirect.com/science/article/pii/S0033062006001253

[271] [Online]. Available: http://www.phage.dk/plugins/download/wrMTrck.pdf

[272] C. Pedersem, "C. elegans motility analysed in imagej." [Online]. Available: https://silo.tips/download/c-elegans-motility-analysis-in-imagej-a-practical-approach

[273] V. K. Narayana, E. S. A Reddy, and M. S. Prasad, "A new method for gray level image thresholding using spatial correlation features and ultrafuzzy measure," Conference Proceedings.

[274] R. P. McCord, J. N. Yukich, and K. K. Bernd, "Analysis of force generation during flagellar assembly through optical trapping of free-swimming chlamydomonas reinhardtii," *Cell Motil Cytoskeleton*, vol. 61, no. 3, pp. 137–44, 2005. [Online]. Available: https://www.ncbi.nlm.nih.gov/pubmed/15887297

[275] T. J. Boddeker, S. Karpitschka, C. T. Kreis, Q. Magdelaine, and O. Baumchen, "Dynamic force measurements on swimming ¡i¿chlamydomonas¡/i¿ cells using micropipette force sensors," *Journal of The Royal Society Interface*, vol. 17, no. 162, p. 20190580, 2020. [Online]. Available: https://royalsocietypublishing.org/doi/abs/10.1098/rsif.2019.0580

[276] P. V. Bayly, B. L. Lewis, E. C. Ranz, R. J. Okamoto, R. B. Pless, and S. K. Dutcher, "Propulsive forces on the flagellum during locomotion of chlamydomonas reinhardtii," *Biophys J*, vol. 100, no. 11, pp. 2716–25, 2011. [Online]. Available: https://www.ncbi.nlm.nih.gov/pubmed/21641317

[277] E. Cuche, P. Marquet, and C. Depeursinge, "Simultaneous amplitude-contrast and quantitative phase-contrast microscopy by numerical reconstruction of fresnel off-axis holograms," *Applied optics*, vol. 38, no. 34, pp. 6994–7001, 1999.

[278] A. Gianfrancesco, "Technologies for chemical analyses, microstructural and inspection investigations," *Materials for Ultra-Supercritical and Advanced Ultra-Supercritical Power Plants*, pp. 197–245, 2017.

[279] M. L. Huber, R. A. Perkins, A. Laesecke, D. G. Friend, J. V. Sengers, M. J. Assael, I. N. Metaxa, E. Vogel, R. Mareš, and K. Miyagawa, "New international formulation for the viscosity of h2o," *Journal of Physical and Chemical Reference Data*, vol. 38, no. 2, pp. 101–125, 2009. [Online]. Available: https://doi.org/10.1063/1.3088050

[280] M. Polin, I. Tuval, K. Drescher, J. P. Gollub, and R. E. Goldstein, "Chlamydomonas swims with two "gears" in a eukaryotic version of run-and-tumble locomotion," *Science*, vol. 325, no. 5939, pp. 487–90, 2009. [Online]. Available: https://www.ncbi.nlm.nih.gov/pubmed/19628868

[281] [Online]. Available: https://www.mathworks.com/matlabcentral/fileexchange/47248-wind-rose

[282] J. Howse, R. Jones, A. Ryan, T. Gough, R. Vafabakhsh, and R. Golestanian, "Self-motile colloidal particles: From directed propulsion to random walk," *Physical Review Letters*, vol. 99, no. 4, p. 048102, 2007. [Online]. Available: https://link.aps.org/doi/10.1103/PhysRevLett.99.048102

[283] MIT, "Msd tutorial," 2018. [Online]. Available: http://web.mit.edu/savin/Public/.Tutorial_v1.2/

[284] M. V. Nadal, "Development of a brownian dynamics simulation code for enzymatic reaction-diffusion processes in crowded intracellular environments." Thesis, 2016.

[285] N. Tarantino, J. Tinevez, E. F. Crowell, B. Boisson, R. Henriques, M. Mhlanga, F. Agou, A. Israël, and E. Laplantine, "Tnf and il-1 exhibit distinct ubiquitin requirements for inducing nemo-ikk supramolecular structures," *Journay of Cell Biology*, vol. 204, no. 2, pp. 231–45, 2015.

[286] A. Callegari and G. Volpe, *Numerical Simulations of Active Brownian Particles*. Springer, 2019.

[287] J. Bewerunge, I. Ladadwa, F. Platten, C. Zunke, A. Heuer, and S. U. Egelhaaf, "Time and ensembleaverages in evolving systems: the case of brownian particles in random potentials," *Physical Chemistry Chemical Physics*, vol. 18, no. 28, pp. 18 887–18 895, 2016. [Online]. Available: http://dx.doi.org/10.1039/C6CP02559E

[288] F. Safaeifard, S. P. Shariatpanahi, and B. Goliaei, "A survey on random walk-based stochastic modeling in eukaryotic cell migration with emphasis on its application in cancer," *mcijournal*, vol. 2, no. 1, pp. 1–12, 2018. [Online]. Available: http://mcijournal.com/article-1-190-en.html

[289] S. Bo, F. Schmidt, R. Eichhorn, and G. Volpe, "Measurement of anomalous diffusion using recurrent neural networks," *Physical Review E*, vol. 100, no. 1, p. 010102, 2019. [Online]. Available: https://link.aps.org/doi/10.1103/PhysRevE.100.010102

[290] G. Randall, "Persistent random walks and the telegrapher's equation lecture 10," 2003.

[291] C. Maklin, "How to implement the fast fourier transform algorithim in python from stratch," 2019. [Online]. Available: https://towardsdatascience.com/fast-fourier-transform-937926e591cb

[292] S. Burrus, M. Frigo, S. G. Johnson, M. Pueschel, and I. Selesnick, *Fast Fourier Transforms*. [Online]. Available: http://cnx.org/content/col10550/1.22/

[293] P. Heckbert, *Fourier Transforms and the Fast Fourier Transform (FFT) Algorithm*, 1995, pp. 15–463. [Online]. Available: https://www.cytivalifesciences.co.jp/catalog/pdf/18115827.pdf

[294] D. Jia, J. Hamilton, L. M. Zaman, and A. Goonewardene, "The time, size, viscosity, and temperature dependence of the brownian motion of polystyrene microspheres," *American Journal of Physics*, vol. 75, no. 2, pp. 111–115, 2007.

[295] A. Prieto, J. Pedro Cañavate, and M. García-González, "Assessment of carotenoid production by dunaliella salina in different culture systems and operation regimes," *J Biotechnol*, vol. 151, no. 2, pp. 180–5, 2011.

[296] L.-n. Zhao, W.-f. Gong, X.-w. Chen, and D.-f. Chen, "Characterization of genes and enzymes indunaliella salinainvolved in glycerol metabolism in response to salt changes," *Phycological Research*, vol. 61, no. 1, pp. 37–45, 2013. [Online]. Available: https://onlinelibrary.wiley.com/doi/abs/10.1111/j.1440-1835.2012.00669.x

[297] G. S. Klindt, C. Ruloff, C. Wagner, and B. M. Friedrich, "Load response of the flagellar beat," *Phys Rev Lett*, vol. 117, no. 25, p. 258101, 2016. [Online]. Available: https://www.ncbi.nlm.nih.gov/pubmed/28036211

[298] B. Huner and R. G. Hussey, "Cylinder drag at low reynolds number," *The Physics of Fluids*, vol. 20, no. 8, pp. 1211–1218, 1977. [Online]. Available: https://aip.scitation.org/doi/abs/10.1063/1.862001

[299] S. Camalet and F. Jülicher, "Generic aspects of axonemal beating," *New Journal of Physics*, vol. 2, pp. 24–24, oct 2000. [Online]. Available: https://doi.org/10.1088/1367-2630/2/1/324

[300] X. Yang, R. H. Dillon, and L. J. Fauci, "An integrative computational model of multiciliary beating," *Bulletin of mathematical biology*, vol. 70, no. 4, p. 1192, 2008.

[301] S. Gueron and K. Levit-Gurevich, "Computation of the internal forces in cilia: application to ciliary motion, the effects of viscosity, and cilia interactions," *Biophysical journal*, vol. 74, no. 4, pp. 1658–1676, 1998.

[302] K. C. Leptos, M. Chioccioli, S. Furlan, A. I. Pesci, and R. E. Goldstein, "An adaptive flagellar photoresponse determines the dynamics of accurate phototactic steering in chlamydomonas," *BioRxiv*, p. 254714, 2018.

[303] E. E. Riley, D. Das, and E. Lauga, "Swimming of peritrichous bacteria is enabled by an elastohydrodynamic instability," *Scientific reports*, vol. 8, no. 1, pp. 1–7, 2018.

[304] A. M. Jamieson, J. G. Southwick, and J. Blackwell, "Dynamical behavior of xanthan polysaccharide in solution," *Journal of Polymer Science: Polymer Physics Edition*, vol. 20, no. 9, pp. 1513–1524, 1982. [Online]. Available: https://onlinelibrary.wiley.com/doi/abs/10.1002/pol.1982.180200901

[305] J. Lecourtier, G. Chauveteau, and G. Muller, "Salt-induced extension and dissociation of a native double-stranded xanthan," *International Journal of Biological Macromolecules*, vol. 8, no. 5, pp. 306–310, 1986.

[306] J. L. Zatz and S. Knapp, "Viscosity of xanthan gum solutions at low shear rates," *Journal of Pharmaceutical Sciences*, vol. 73, no. 4, pp. 468 – 471, 1984. [Online]. Available: http://www.sciencedirect.com/science/article/pii/S0022354915460617

[307] H. Y. Jang, K. Zhang, B. H. Chon, and H. J. Choi, "Enhanced oil recovery performance and viscosity characteristics of polysaccharide xanthan gum solution," *Journal of Industrial and Engineering Chemistry*, vol. 21, pp. 741 – 745, 2015. [Online]. Available: http://www.sciencedirect.com/science/article/pii/S1226086X14002020

[308] S. Gluzman, D. A. Karpeev, and L. V. Berlyand, "Effective viscosity of puller-like microswimmers: a renormalization approach," *Journal of The Royal Society Interface*, vol. 10, no. 89, p. 20130720, 2013. [Online]. Available: https://royalsocietypublishing.org/doi/abs/10.1098/rsif.2013.0720

[309] G. Berth, H. Dautzenberg, B. E. Christensen, S. Harding, G. Rother, and O. Smidsrød, "Static light scattering studies on xanthan in aqueous solutions," *Macromolecules*, vol. 29, pp. 3491–3498, 1996.

[310] Y. Zhang, G. Li, and A. M. Ardekani, "Reduced viscosity for flagella moving in a solution of long polymer chains," *Phys. Rev. Fluids*, vol. 3, p. 023101, Feb 2018. [Online]. Available: https://link.aps.org/doi/10.1103/PhysRevFluids.3.023101

[311] E. E. Riley and E. Lauga, "Empirical resistive-force theory for slender biological filaments in shear-thinning fluids," *Phys. Rev. E*, vol. 95, p. 062416, Jun 2017. [Online]. Available: https://link.aps.org/doi/10.1103/PhysRevE.95.062416

[312] S. Gou, S. Luo, T. Liu, P. Zhao, Y. He, Q. Pan, and Q. Guo, "A novel water-soluble hydrophobically associating polyacrylamide based on oleic imidazoline and sulfonate for enhanced oil recovery," *New J. Chem.*, vol. 39, pp. 7805–7814, 2015. [Online]. Available: http://dx.doi.org/10.1039/C5NJ01153A

[313] A. Thomas, N. Gaillard, and C. Favero, "Some key features to consider when studying acrylamide-based polymers for chemical enhanced oil recovery," *Oil & Gas Science and Technology–Revue d'IFP Energies nouvelles*, vol. 67, no. 6, pp. 887–902, 2012.

[314] L. F. Lopes and B. M. O. Silveira, "Rheological evaluation of hpam fluids for eor applications," *International Journal of Engineering and Technology*, vol. 14, no. 3, p. 6, 2014. [Online]. Available: http://citeseerx.ist.psu.edu/viewdoc/summary?doi=10.1.1.659.6456

[315] F. J. Galindo-Rosales, L. Campo-Deaño, P. C. Sousa, V. M. Ribeiro, M. S. N. Oliveira, M. A. Alves, and F. T. Pinho, "Viscoelastic instabilities in micro-scale flows," *Experimental Thermal and Fluid Science*, vol. 59, no. Supplement C, pp. 128–139, 2014. [Online]. Available: ⟨GotoISI⟩://WOS:000343843400015

[316] H. Perez, E. Andablo-Reyes, P. Díaz-Leyva, and J. Arauz-Lara, "Microrheology of viscoelastic fluids containing light-scattering inclusions," *Physical review. E, Statistical, nonlinear, and soft matter physics*, vol. 75, p. 041505, 05 2007.

[317] T. Zolper, A. Seyam, C. Chen, M. Jungk, A. Stammer, H. Stoegbauer, T. Marks, Y.-W. Chung, and Q. Wang, "Energy efficient siloxane lubricants utilizing temporary shear-thinning," *Tribology Letters*, vol. 49, 01 2013.

[318] N. Montazeri-Najafabady, M. Negahdaripour, M. Salehi, M. Morowvat, S. Shaker, and Y. Ghasemi, "Effects of osmotic shock on production of beta-carotene and glycerol in a naturally isolated strain of dunaliella salina," *Journal of Applied Pharmaceutical Science*, vol. 6, pp. 160–163, 2016.